Writing and Characterisation Methods for UV-Photosensitivity based Devices and their Applications

Filip Floreani

Doctor of Philosophy

Aston University

December 2004

Aston University

Writing and Characterisation Methods for UV-Photosensitivity based Devices and their Applications

Filip Floreani

Doctor of Philosophy

December 2004

Abstract

The underlying work to this thesis focused on the exploitation and investigation of photosensitivity mechanisms in optical fibres and planar waveguides for the fabrication of advanced integrated optical devices for telecoms and sensing applications.

One major scope is the improvement of grating fabrication specifications by introducing new writing techniques and the use of advanced characterisation methods for grating testing.
For the first time the polarisation control method for advanced grating fabrication has successfully been converted to apodised planar waveguide fabrication and the development of a holographic method for the inscription of chirped gratings at arbitrary wavelength is presented. The latter resulted in the fabrication of gratings for pulse-width suppression and wavelength selection in diode lasers.
In co-operation with research partners a number of samples were tested using optical frequency domain and optical low coherence reflectometry for a better insight into the limitations of grating writing techniques.

Using a variety of different fabrication methods, custom apodised and chirped fibre Bragg gratings were written for the use as filter elements for multiplexer-demultiplexer devices, as well as for short pulse generation and wavelength selection in telecommunication transmission systems.
Long period grating based devices in standard, speciality and tapered fibres are presented, showing great potential for multi-parameter sensing. One particular scope is the development of vectorial curvature and refractive index sensors with potential for medical, chemical and biological sensing. In addition the design of an optically tunable Mach-Zehnder based multi-wavelength filter is introduced.

The discovery of a Type IA grating type through overexposure of hydrogen loaded standard and Boron-Germanium co-doped fibres strengthened the assumption of UV-photosensitivity being a highly non-linear process. Gratings of this type show a significantly lower thermal sensitivity compared to standard gratings, which makes them useful for sensing applications. An Oxford Lasers copper-vapour laser operating at 255 nm in pulsed mode was used for their inscription, in contrast to previous work using CW-Argon-Ion lasers and contributing to differences in the processes of the photorefractive index change.

Key Words: Optical Fibre, Bragg Grating, Optical Telecommunication, Optic Sensor, Grating Fabrication

To Danijela, for all the support and patience evinced in the course of this work.

ACKNOWLEDGEMENTS

This thesis would not have been possible in the present form without the kind support, collaboration and friendship of a great number of people. First I would like to thank the members of the Photonics Research Group at Aston University, in particular Lin Zhang simply for being deservedly the most popular supervisor with all postgraduate students and a great person to work with. Many thanks also to Bert Biggs, without whom all work would grind to a halt and Ian Bennion for having me here in the first place. Thanks go to Xuewen Shu and Tom Allsop for introducing me into the fine art of FBG fabrications and LPG sensing, respectively, Yufang Hu and Igor Khrushchev who helped me promoting the scanning holographic fabrication set-up and provided valuable results for this thesis. Special thanks are due to George Simpson, helping me to push forward the experimental work on type IA gratings, and Andy Gillooly, Xianfeng Chen, Amos Martinez, and Michael Dubov for providing me with gratings for reference data.

Amongst all support staff I would like to mention particularly our group secretaries Helen Yard and Selena Teeling, Katy Barry from the school office, and Aston Guild's welfare manager Jill Wilson, who all were very helpful in settling down and get work done at Aston.

Acknowledgement is due to all my partners from the ODUPE Research Training Network, in particular to the groups in Hamburg, Paris and Lille for organising the ODUPE Training sessions and to the following persons:

It has been my pleasure to work with Rosa Romero from INESC Porto in a string of projects and the list of joint publications speaks for itself. The number of results owed to her collaboration is too large all to be presented in this thesis.

I also like to express gratitude to Hans-Jürgen Deyerl and Martin Kristensen from the DTU Lyngby for inviting me to work in their laboratories and for their superb supervision which did not stop the day I left the group. I owe thanks and an apology to Christophe Peucheret and Beata Zsigri for some complicated but successful WDM measurements of gratings.

Further contributions to this thesis in form of optical measurements were given by Christian Knothe and Sven Kieckbusch and their supervisors Ernst Brinkmeyer and Hagen Renner from the TU Hamburg-Harburg.

I am obliged to Karen Chisholm for always responding to my emergency calls when there was trouble with the FRED laser and to Kate Sudgen for the liberal access to Indigo Photonics equipment and to both of them for sharing their great expertise and knowledge on grating fabrication with others.

Last but not least I would like to thank Kazimierz Jedrzejewski from Warsaw University for his support with grating tapers and Edik Rafailov and Iain Cormack from St. Andrews University for the fruitful collaboration leading to two publications.

TABLE OF CONTENTS

FIGURE CAPTIONS

1 INTRODUCTION

1.1 Outline

The discovery of UV photosensitivity in doped Silica glasses by Hill in 1978 [*1*] opened a huge field of interest for the scientific and economic exploitation of this effect. With the development of huge industries working on optical glass fibre based telecommunication systems more and more aspects of photosensitivity in glass had to be investigated, starting from the mechanisms to its applicability in optical devices.

With a better understanding of the underlying chemical processes leading to photosensitivity effects, its optimisation and the progress of manufacturing processes for UV-written devices, which lead to better specifications and reproducibility of integrated optical components, this technology has made a breakthrough and great impact in the areas of optical telecommunications and networks, optical sensing, packaging and integration, and miniaturisation.

As an interim result of a development, which started in the late eighties, fibre optic technology enabled the evolution of the Internet and computer networks, on-demand cable TV and a dense and reliable telephone grid spanning around the globe, as we know them today. Since the very beginning of electronic data transmission in the 19th century, the performances of succeeding systems showed an exponential increase over the years. Ongoing research is pushing the performances of bit-rates in optical transmission systems ever further [*2*], making advanced fibre optic technology the ultimate solution for present and future commercial communications.

Further miniaturisation and development of passive and active planar waveguide components opens the way for integrated optical logic circuits, which may yield the next technological revolution in computer and multimedia technology, and entertainment electronics. Amongst the most promising future applications are so called optical MEMS structures offering "Lab-on-Chip" solutions for chemical, medical and bio sensing [3] or as optical switches for a broad field of applications [4].

Also of great interest is the integration of thin film technology into fibre based or integrated optics for chemical sensing. However, the degradation of the thin film materials due to gas absorption still is a major issue [5].

To date embedded fibre optic sensors are already in widespread use to monitor acute strains and temperatures in airplane wings, ship hulls and masts, or large scale constructions, as bridges and high-rise buildings. By developing and applying of more complex system designs

fibre optic devices also can be used as sensors for electric currents, pressure, vibration, magnetic fields and many other variables. Unlike electronic devices, which are susceptible to electromagnetic interference, glass-based fibre optic probes are feasible probes for multi-variable measurements that can be used in harsh environments, like great oceanic depths or nuclear reactors.

1.2 Thesis Overview

Following this outline, an introduction of the theoretical formalisms underlying the filter function of Bragg and long period gratings is given, as well as the correlation between the design considerations of gratings and their resulting filter spectra. The fundamentals of UV-writing of Bragg gratings and long period gratings in optical fibres and waveguides are described in the following sub-chapters. The first offers a short explanation about photosensitivity effects in germanium-doped glass, based on which all devices presented with this work are fabricated and is followed by a comprehensive overview on fabrication methods for the fabrication of gratings.

Following the introduction to fibre Bragg grating writing in ***Chapter 3***, two novel methods are presented, which were developed during the course of this project. The first enables high flexibility in wavelength selection of chirped fibre Bragg gratings, the second is an elegant approach for the writing of apodised planar Bragg gratings.

This is followed by an investigation of grating properties achieved by reflectometry based characterisation methods, mapping the strengths and flaws of two selected writing methods regarding their writing definition and resolution limits.

In both ***Chapter 2*** and ***Chapter 3*** special emphasis is put on those fabrication methods, which were used for the writing of the devices presented in the following **Chapter 4** and **Chapter 5**.

Chapter 4 focuses on device fabrication and testing for telecom applications. It covers topics such as multiplexer-demultiplexer designs, low dispersion grating filters for WDM, add-drop filters and chirped gratings for dispersion compensation, starting from the conceptualisation of each device and moving over design considerations of the gratings to their testing and finally showing the results obtained.

Another subchapter addresses to the application of gratings for the wavelength tuning and short-pulse generation from semiconductor lasers.

The conceptualisation and fabrication of smart structure devices for sensing and switching is discussed in ***Chapter 5***.

Complex sensor structures are achieved by writing gratings in non-cylindrical, tapered and modified standard fibre samples. Results are presented for their response to changes of

ambient refractive index, directional bending, temperature and strain. This work was done to pave the way for detectors useable in medical and bio-chemical applications, such as respiratory sensors and sensors for aqueous solutions.

In addition a multiple applicable modulator based on an in-fibre Mach-Zehnder interferometer concept is presented, performing temperature and refractive index measurement, as well as channel switching.

Not included in ***Chapter 5*** is the work on Type IA gratings, which are presented in a separate section, although their main application also lies in temperature sensing. ***Chapter 6*** gives a discussion about the writing of Type IA gratings using a pulsed 255 nm wavelength high power copper-vapour laser and the properties of the resulting gratings and covers aspects like growth dynamic during the writing process, grating decay processes due to annealing and sensitivity to temperature and strain in comparison to data obtained on Type IA gratings fabricated using 244 nm UV-sources.

Chapter 7 concludes this thesis and is followed by a publication list in ***Chapter 8*** and the list of references cited in this thesis in ***Chapter 9***.

This Ph.D. project has been financed by the Research Commission of the European Union (Contract N° HPRN-CT-2000 00045) and the work presented here has been done as part of a research effort within the ODUPE Network (Optical Devices Using Photosensitivity for their Elaboration). Parts of this thesis include results from collaborative work with partners from inside and outside the network, which are mentioned below.

For the fabrication of the gratings presented in ***Chapters 3.3***, ***3.5*** and ***4.2*** the polarisation control set-up at the COM centre of the Danmarks Tekniske Universitet (Technical University of Denmark, DTU) in Lyngby was used under the supervision of Dr. Hans-Jürgen Deyerl and Prof. Martin Kristensen. The detuning tolerance of the zero-dispersion gratings shown in ***Chapter 4.2*** was measured by Christophe Peucheret and Beata Zsigri.

For the reflectometry based grating characterisation, as introduced in ***Chapter 3.5*** additional gratings were supplied by my colleagues from Aston University, Andy Gillooly and John Mitchell. The results from reflectometry measurements were performed and provided by Christian Knothe, Sven Kieckbusch, Dr. Hagen Renner and Prof. Ernst Brinkmeyer from the Technische Hochschule Hamburg-Harburg (Technical University Hamburg-Harburg, TUHH), following a study into the compatibility of results obtained from different reflectometry methods, involving Philippe Giaccari, Dragan Ćorić and Prof. Hans Limberger, who were additional collaborators from the Ecole Polytechnique Federale de Lausanne (Federal Polytechnical School in Lausanne, EPFL).

Collaborative work with Rosa Romero and Prof. Paulo Marques from INESC Porto covered aspects of multiplexer designs for WDM, as presented in ***Chapter 4.1***. The gratings for these research projects were fabricated at Aston University and put into test at Porto. Further

collaborative work covered devices in tapered fibres, which were provided by INESC. Results from these projects are shown in ***Chapter 5.2*** and ***Chapter 5.4***.

From outside the Network Kazimierz Jedrzejewski from the Fibre Optic Institute of Warsaw University provided additional fibre tapers for the work on ***Chapter 5.4***.

Further results include the successful multiple wavelength tuning of laser diodes at St. Andrews University using fibre gratings written at Aston University. This work was done in collaboration with Edik Rafailov and Iain Cormack. The results are presented in ***Chapter 4.3.1***.

Chapter 4.3.2 is based on an internal cooperation at Aston University including Igor Khruschev and Yufang Hu, who measured the spectral filter-effects on the pulse-width of a diode laser, using fibre Bragg gratings.

2 FUNDAMENTAL PRINCIPLES OF UV-GRATING INSCRIPTION

2.1 Filter Response of Bragg and Long Period Gratings in Waveguides

2.1.1 Basic Principles of Guided Waves

The functioning principle of optical waveguides is based on total internal reflection of light travelling through them. This is achieved by surrounding the waveguide core with a refractive index n_{core} with a cladding of slightly lower index n_{clad}.

The simplest geometry of an optical fibre is the cylindrical step-index fibre, which has a core with uniform refractive index over its full radius R_{core} and a cladding with homogenous refractive index between R_{core} and R_{clad}. Using polar coordinates, this can be described as follows.

$$n(r,\phi,z) \underset{def}{=} n(r) = \begin{cases} n_{core} & for\ r \le R_{core} \\ n_{clad} & for\ R_{core} < r < R_{clad} \\ n_{out} & for\ r > R_{clad} \end{cases} \qquad \textbf{Equation 2.1-1}$$

A standard silicate telecommunications (SM 28) fibre has a core radius of < 4 µm and a full diameter of 125 mm. The index step from core to cladding is relatively low, typically around 0.01. In general, the cladding thickness is large enough that the whole electromagnetic field travelling through the core is confined within the fibre cross-section. However, as will be shown later, cladding modes can be excited in the fibre. These interact directly with the interface of the cladding with the surrounding medium and therefore the outer refractive index n_{out} becomes important.

Alternative fibre designs include graded index fibre, in which the transition between core and cladding refractive index is continuous, fibre cores with radial refractive index profiles, and non-cylindrical fibre cores, like elliptic and D-shaped structures.

Internal reflection at a planar and well-defined core to cladding interface is defined as such, that every incoming light ray is totally reflected if its angle of incidence is smaller than θ in *Equation 2.1-2*.

$$\theta = \arcsin\frac{n_{cl}}{n_{core}} \qquad \textbf{Equation 2.1-2}$$

Ray optics is a valid approach to describe light guidance in planar and rectangular structures, but reaches its limit for the description of waveguides with different geometry, like optical

fibres. A more general approach is given using the formalism of electromagnetic wave equations, starting from Maxwell's Equations of a propagating wave subjected to the boundary and continuity conditions of the waveguide. For optical fibres with cylindrical geometries the eigenvalues for supported electromagnetic modes are Bessel-Functions. An introduction in this topic and the derivation of the necessary formalisms can be found in standard text and reference books on this matter [*6,7*].

A general description of a planar electromagnetic wave, which is travelling along the z-axis, which is also the fibre axis, is given in *Equations 2.1-3*, using cylindrical coordinates.

$$\vec{E} = \vec{E}_0(r,\phi)e^{j(\omega t-\beta z)} \qquad \textbf{Equation 2.1-3a}$$

$$\vec{H} = \vec{H}_0(r,\phi)e^{j(\omega t-\beta z)} \qquad \textbf{Equation 2.1-3b}$$

These field vectors can be decoupled into their contributions of *r*, ϕ, *z* and *t*. An alternative formalism is the general wave equation, or Helmholtz equation for a uniform medium.

$$\nabla^2\vec{E} + k^2\vec{E} = 0 \qquad \textbf{Equation 21-4a}$$

$$\nabla^2\vec{H} + k^2\vec{H} = 0 \qquad \textbf{Equation 2.1-4b}$$

Under the assumption of "weak" guidance, all guided modes can be constructed from a set of linear polarised (LP-) modes of orthogonal electric and magnetic field components in the transverse plane. The weak guidance criterion is met if the difference between core and cladding refractive index Δn is only a small fraction of n_{core} and n_{clad}.

$$k_{clad} < \beta < k_{core} \qquad \textbf{Equation 2.1-5}$$

A wave is supported in the fibre under the above condition, with k_{clad} and k_{core} the propagation constants in the core and cladding medium, obtained by multiplication of their respective effective refractive index with the constant k_0 for wave propagation in vacuum.

The number of propagating modes in a fibre is determined by the *V*-number. This is directly reflecting the fundamental properties of the fibre, which appear as arguments of the eigenmode equations for the LP modes.

$$V = n_{core}R_{core}k_0\sqrt{2\Delta n} \qquad \textbf{Equation 2.1-6}$$

With the appropriate choice of fibre geometry and material, *V*, and thus the number of propagating modes evolving in a fibre can be restricted by setting a cut-off condition. For *V* numbers below 2.405, only the fundamental HE_{11} mode, approximated to be the LP_{01} mode, is permitted in a waveguide. In contrast to higher order modes, whose electric field is widely distributed over the core and cladding area of the fibre, the fundamental mode is well confined to the fibre core centre. In all following illustrations the higher order core modes in the pristine fibre region will be neglected.

2.1.2 Grating Structures in optic Fibres

A grating in an optical waveguide is a quasi-periodic perturbation of its refractive index n_{core}, respectively its dielectric constant ε_r in the particular core region. In general this can be a permanent index change due to the inscription with light from UV- or femtosecond lasers, or other power sources. Some of the mechanisms leading to such are described in the following ***Chapter 2.2***. But it can also occur as a temporal electro- or acousto-optic effect, result from a mechanical surface corrugation or material properties of the waveguide itself, as non-linear behaviour of the material [*8*].

Addressed here is the first case under the assumption that the fibre cladding stays unaffected by the writing process.

The profile of a waveguide grating can be described as a sinusoidal refractive index perturbation of the core by a general representation, replacing the upper term of *Equation 2.1-1* by:

$$n_{core}(z) = n_{core} + \delta n(z)\left[1 + m\cos\left(\frac{2\pi z}{\Lambda_0} + \phi(z)\right)\right] \qquad \textbf{Equation 2.1-7}$$

Again the assumption is made that inside the core the refractive index of both the unperturbed fibre sections and the grating does not change with radius. The refractive index is raised in average by $\delta n(z)$ and oscillating periodically with $2\pi/\Lambda_0$ by the amplitude $m \cdot \delta n(z)$ over the length z. Here m is a factor between 0 and 1 defining the modulation strength relative to $\delta n(z)$. In principle δn and the phase can vary over z, but for reasons of simplicity of the following derivations the first is defined to be constant and the latter zero. In this form *Equation 2.1-8* describes a uniform refractive index grating.

$$n(z) = n_0 + \delta n\left[1 + m\cos\left(\frac{2\pi z}{\Lambda_0}\right)\right] \qquad \textbf{Equation 2.1-9}$$

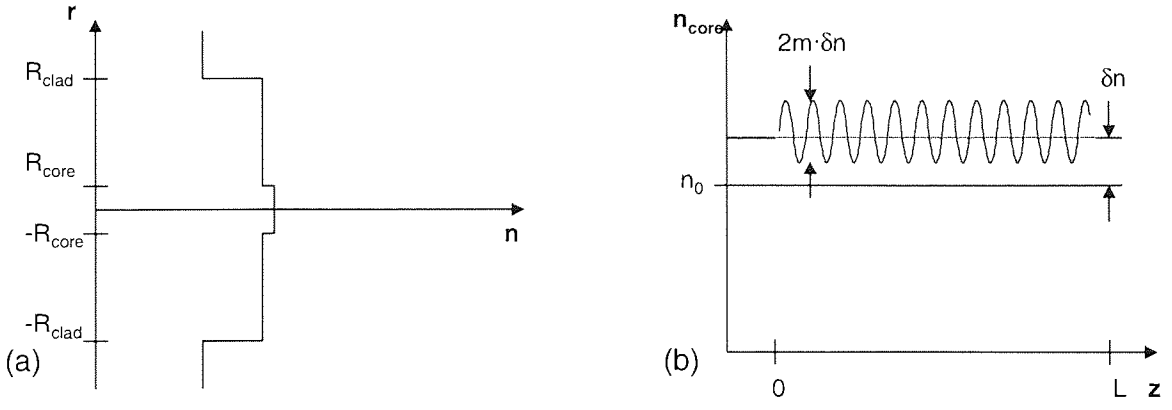

Figure 2.1-1: Radial refractive index profile in step-index fibre (a) and refractive index modulation in fibre core according to *Equation 2.1-1* and *Equation 2.1-9* (b)

The refractive index affects the propagation of the electric field component of a wave through ε_r, the electric permittivity of the material. The latter can be directly derived from the refractive index in the form $n^2=\varepsilon$. This term inserted into *Equation 2.1-8* yields:

$$\varepsilon(z)=\left[(n_0+\delta n)+\delta n m\cos\left(\frac{2\pi z}{\Lambda_0}+\phi\right)\right]^2 \qquad \textbf{Equation 2.1-9}$$

If the perturbation δn is very small compared to n_0, the induced modulated and non-modulated parts of the permittivity $\Delta\varepsilon_{AC}(z)$, and $\Delta\varepsilon_{DC}$, can be approximated by the first order of *Equation 2.1-9*.

$$\Delta\varepsilon_{AC}(z)=2n_0\delta n m\cos\left(\frac{2\pi z}{\Lambda_0}+\phi\right) \qquad \textbf{Equation 2.1-10}$$

$$\Delta\varepsilon_{DC}(z)=2n_0\delta n \qquad \textbf{Equation 2.1-11}$$

An electromagnetic wave incident on the area of perturbation will set up a modulated polarisation field $\vec{P}_{ac}$, which in return can affect the electric field.

$$\vec{P}_{ac}=\Delta\varepsilon(z)\vec{E} \qquad \textbf{Equation 2.1-12}$$

While the unperturbed fibre core is considered to be a single-mode waveguide, the perturbation of ε_r can change this property and allow additional modes to be induced by the present propagating wave.

The resulting electric field can be expressed in the same formalism as in *Equations 2.1-4*, but has to adhere to the new waveguide condition in the non-homogenous form.

$$\left[\nabla^2+\varpi^2\mu_0(\varepsilon_r+\Delta\varepsilon(z))\right]\vec{E}=0 \qquad \textbf{Equation 2.1-13}$$

As will be shown later, if a phase match between existing modes in the perturbation area occurs, their electric fields can exchange energy between each other due to a coupling mechanism. For two transverse modes, E_ν^t and E_μ^t, the coupling strength can be obtained from their overlap integral at any point of the grating section, again described in cylindrical coordinates.

$$K_{\nu\mu}^t(z)=\frac{\varpi}{4}\int_o^{2\pi}d\phi\int_0^{\infty}r\,dr\,\Delta\varepsilon(z)\vec{E}_\nu^t(r,\phi)\vec{E}_\mu^{t*}(r,\phi) \qquad \textbf{Equation 2.1-14}$$

By re-factoring the above Equation the standard expression for the coupling coefficient $\kappa_{\nu\mu}$ can be obtained.

$$\kappa_{\nu\mu}(z)=\frac{\delta n(z)}{n_{core}}K_{\nu\mu}^t(z) \qquad \textbf{Equation 2.1-15}$$

2.1.2.1 Generalised Coupled Mode Theory

Coupled mode theory has been identified to be a useful formalism for the description of electromagnetic waves in periodically perturbed waveguides even before the discovery of UV photosensitivity and the following development of refractive index modulated optical gratings [*8*]. Alongside a more recent and fundamental theory incorporating all relevant coupling effects by Erdogan [*9*], it is used as the main reference in the following.

The starting point is a LP_{01} mode incident in a perturbated region, which can be described by a function as in *Equation 2.1-3*.

In the grating region a part of its mode power, carried in the Poynting vector, can be transferred into other core or cladding modes. As the refractive index modulation is small compared to the refractive core index in its pristine state, the weak guiding approximation is still valid and the core modes are planar waves of constant polarisation. The supported cladding modes $\vec{E}^{clad}$ however, require a more elaborate derivation [*9,10*]. These conditions combined with *Equation 2.1-14* and *Equation 2.1-15* define the coupling between two LP_{01} core modes.

$$\kappa_{01-01}(z) = \frac{\varpi \varepsilon_0 n_{core}^2 \delta n}{2} \int_0^{2\pi} d\phi \int_0^{R_{core}} r dr \left(\left| \vec{E}_r^{core} \right|^2 + \left| \vec{E}_\phi^{core} \right|^2 \right) \qquad \textbf{Equation 2.1-16}$$

The coupling between the core mode with any first order cladding mode ν can be expressed accordingly. In general, the field distribution of cladding modes spans over all three waveguide layers for radial positions between 0 and ∞.

$$\kappa_{\nu-01}(z) = \frac{\varpi \varepsilon_0 n_{core}^2 \delta n}{2} \int_0^{2\pi} d\phi \int_0^{R_{core}} r dr \left(\vec{E}_r^{clad} \left\| \vec{E}_r^{core*} \right| + \left| \vec{E}_\phi^{clad} \right\| \vec{E}_\phi^{core*} \right| \right) \qquad \textbf{Equation 2.1-17}$$

The interaction between a given mode with all other modes in a waveguide perturbation can be described using generalised coupled mode equations, out of which relevant specific cases will be dealt with.

$$\frac{dA_\mu}{dz} = i \sum_\nu A_\nu \left(K_{\nu\mu}^t + K_{\nu\mu}^z \right) e^{i(\beta_\nu - \beta_\mu)z} + i \sum_\nu B_\nu \left(K_{\nu\mu}^t + K_{\nu\mu}^z \right) e^{-i(\beta_\nu + \beta_\mu)z} \qquad \textbf{Equation 2.1-18a}$$

$$\frac{dB_\mu}{dz} = -i \sum_\nu A_\nu \left(K_{\nu\mu}^t + K_{\nu\mu}^z \right) e^{i(\beta_\nu - \beta_\mu)z} - i \sum_\nu B_\nu \left(K_{\nu\mu}^t + K_{\nu\mu}^z \right) e^{-i(\beta_\nu + \beta_\mu)z} \qquad \textbf{Equation 2.1-18b}$$

$A_\mu(z)$ and $B_\mu(z)$ are amplitudes of transverse mode fields travelling in opposite directions through the waveguide. $K_{\nu\mu}^{\ t}$ and $K_{\nu\mu}^{\ z}$ are transverse and longitudinal coupling coefficients. The latter can be neglected in an approximation, as the core modes are nearly planar and the *z*-component of the cladding modes are also significantly smaller than the transverse components.

To further simplify the formalism, the number of modes to be admitted in the calculations has to be limited.

The following mode interactions are possible: coupling between the principal core mode with co- and counter-propagating core modes of the same order, and coupling of the core mode with co- and counter-propagating supported cladding modes, as well as with radiating cladding modes.

Out of these the three most important cases are:

- Counter-propagating core-core modes (Bragg gratings)
- Co-propagating core-cladding modes (long period gratings)
- Counter-propagating core-cladding modes (short wavelength loss in Bragg gratings)

Intuitively, it is also clear that only modes of near-matching phases will show resonant coupling. The phase-matching conditions for Bragg and long period gratings are functions of the wave propagation constants β_{01}, β_{ν} and the perturbation period Λ.

$$\delta_{01-01} = \tfrac{1}{2}\left(2\beta_{01} - \tfrac{2\pi}{\Lambda}\right) \qquad \textbf{Equation 2.1-19}$$

$$\delta_{\nu-01} = \tfrac{1}{2}\left(\beta_{01} + \beta_{\nu} - \tfrac{2\pi}{\Lambda}\right) \qquad \textbf{Equation 2.1-20}$$

Maximum resonance occurs when *Equation 2.1-19* and *Equation 2.1-20* are equal to zero.

2.1.2.1.1 Fibre Bragg Gratings

Substituting β_{01} by $2\pi n_{eff}/\lambda$ in *Equation 2.1-19* directly yields the Bragg condition of the first order for a beam incident perpendicularly on the reflecting plane.

$$\lambda = 2n_{eff}\Lambda_0 \qquad \textbf{Equation 2.1-21}$$

The power exchange between counter-propagating LP_{01} core modes simplifies to the form in *Equations 2.1-22.*

$$\frac{dA_{01}}{dz} = i\kappa_{01-01}A_{01} + i\kappa_{01-01}B_{01}e^{-2i\delta_{01-01}z} \qquad \textbf{Equation 2.1-22a}$$

$$\frac{dB_{01}}{dz} = -i\kappa_{01-01}B_{01} - i\kappa_{01-01}A_{01}e^{2i\delta_{01-01}z} \qquad \textbf{Equation 2.1-22b}$$

$$\frac{d}{dz}\left(A^2 + B^2\right) = 0 \qquad \textbf{Equation 2.1-22c}$$

Equation 2.1-22c postulates the conservation of power, which at all times is contained in the sum of both modes. Mode A_{01} arriving at the starting position, z=0, of a grating of length L will be at its full strength, whereas the counter-propagating mode B_{01} travels from the far end of the grating, z=L, and accumulates maximum power before leaving the grating at z=0.

The first terms on the right hand side of *Equation 2.1-22a* and *Equation 2.1-22b* are considered to be periodically varying with z, thus averaging to zero when integrated over z.

Only the phase match condition defined in *Equation 2.1-19* has to be corrected to

$$\delta_{01-01} + \kappa_{01-01} = 0 \qquad \textbf{Equation 2.1-23}$$

The boundary conditions for the remaining parts of the differential *Equations 2.1-22* can thus be set as $A_{01}(0)=1$ and $B_{01}(L)=0$, which yields the following solutions.

$$A_{01}(z) = \frac{A(0)e^{i\delta_{01-01}\beta z}}{-2\delta_{01-01}\beta\sinh\left(\frac{SL}{2}\right)+iS\cosh\left(\frac{SL}{2}\right)}\left\{2\delta_{01-01}\beta\sinh\left[\tfrac{S}{2}(z-L)\right]+iS\cosh\left[\tfrac{S}{2}(z-L)\right]\right\}$$

Equation 2.1-24a

$$B_{01}(z) = \frac{2i\kappa_{01}A(0)e^{-i\delta_{01-01}z}}{-2\delta_{01-01}\beta\sinh\left(\frac{SL}{2}\right)+iS\cosh\left(\frac{SL}{2}\right)}\sinh\left[\tfrac{S}{2}(z-L)\right] \qquad \textbf{Equation 2.1-24b}$$

The abbreviated term $S = 2\sqrt{\kappa^2 - \delta_{01-01}^2}$ was introduced into the above equations. Under phase-matching conditions from *Equation 2.1-19*, the formalism simplifies to *Equations 2.1-25*.

$$A_{01}(z) = A_{01}(0)\frac{\cosh[\kappa_{01}(z-L)]}{\cosh(\kappa_{01}L)} \qquad \textbf{Equation 2.1-25a}$$

$$B_{01}(z) = A_{01}(0)\frac{\kappa_{01}}{|\kappa_{01}|}\frac{\sinh[\kappa_{01}(z-L)]}{\cosh(\kappa_{01}L)} \qquad \textbf{Equation 2.1-25b}$$

The devolution of the mode propagation inside the grating under the boundary conditions is sketched in *Figure 2.1-2*.

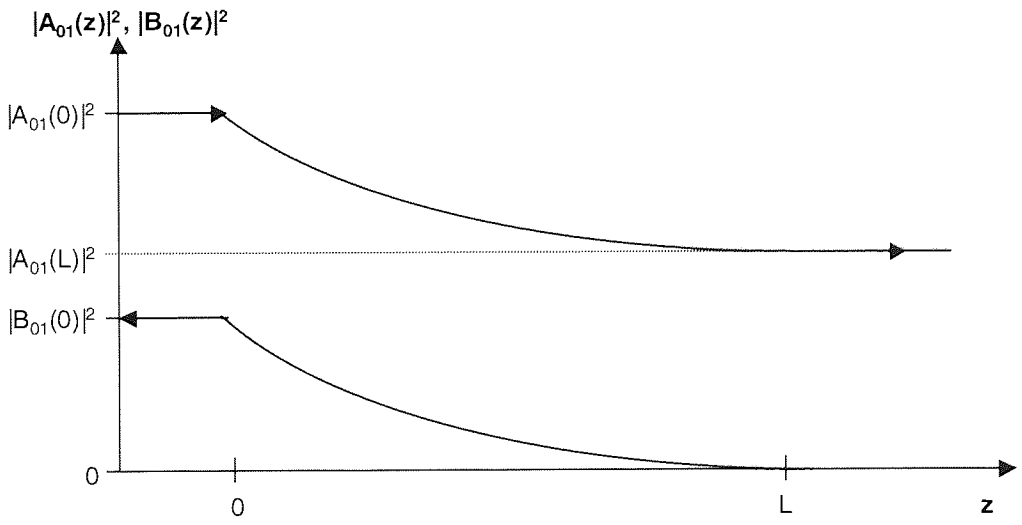

Figure 2.1-2: Mode power $|a_{01}(z)|^2$ and $|b_{01}(z)|^2$ in waveguide grating, as defined in *Equations 2.1-24*.

The reflectance of the fibre grating is defined as the ratio between the amplitudes of reflected and incident beams, which for the maximum value under phase matching condition is given as [*11*]:

$$R_{01}(0) = \left(\frac{B_{01}(0)}{A_{01}(0)} \right)^2 = \tanh^2(\kappa_{01} L) \qquad \textit{Equation 2.1-26}$$

The normalised spectral bandwidth of a grating filter can be approximated by the following term [*9*].

$$\frac{\Delta\lambda}{\lambda} \cong \frac{\lambda \kappa_{01}}{\pi n + \frac{1}{2}(n_{core} + n_{clad})} \sqrt{1 + \frac{\pi}{\kappa_{01} L}} \qquad \textit{Equation 2.1-27}$$

2.1.2.1.2 Complex Bragg Grating Structures

From Fourier optics it is known that a sinusoidal pulse of defined wavelength and finite duration will display a broadened spectrum showing side-lobes. In analogy to this the response spectrum of a weak waveguide grating based on a refractive index perturbation that is limited in length can be approximated by the Fourier transformation of its apodisation profile. The rectangular shaped envelope of the grating section therefore shows a sinc-shaped reflection spectrum centred around the wavelength of the Bragg condition. For optical telecommunication systems, where each wavelength carries the information of one data channel, this can lead to interference between neighbouring channels.

Using inverse Fourier transform formalisms, grating apodisation functions can be defined, which successfully suppress sidelobes [*10,11*]. Apodisation involves the variation of the coupling coefficient over the grating length by controlling the local amplitude of the refractive index modulation.

For some applications, gratings with aperiodic or arbitrary refractive index modulation are required. The most obvious design of the first category is the one for chirped gratings with a linearly progressing periodicity and linear phase-relation [*12,13,14*]. Besides changing refractive index modulation profile and period, some filters require local phase shifts in the grating structure [*15*].

The filter response of such grating devices cannot be obtained from analytical solutions, but has to be computed numerically.

For the simulation of these grating types the coupled mode theory has to be expanded by additional formalisms, as the Transfer Matrix Method [*13,15,16*] or the Riccati equations [*11,14*]. Using the former method requires the division of the grating into sections of quasi-constant wavelength and coupling coefficient, which then are concatenated by matrix multiplication. With the latter the spectrum is obtained from the solution of differential equations.

In *Equation 2.1-7* an exact description for arbitrary grating designs is given. The apodisation profile is defined by $\delta n(z)$, whereas $\phi(z)$ contains information about the z-dependence of chirp and local phase jumps.

2.1.2.2 Long Period Gratings

For coupling between core and cladding modes, the coupled mode formalism is somewhat different. Here the coupling between co-propagating modes shall be described. Using the definition of the phase-matching condition in *Equation 22*, the power transfer between the core mode A_{01} and all cladding modes A_ν in a long period grating is given by:

$$\frac{dA_{01}}{dz} = i\kappa_{01}A_{01} + i\sum_{\nu}\tfrac{m}{2}\kappa_{\nu-01}A_\nu e^{-2i\delta_{\nu-01}z} \qquad \textbf{Equation 2.1-28a}$$

$$\sum_{\nu}\frac{dA_\nu}{dz} = i\sum_{\nu}\tfrac{m}{2}\kappa_{\nu-01}A_{01}e^{-2i\delta_{\nu-01}z} \qquad \textbf{Equation 2.1-28-b}$$

Again, the first term in *Equation 2.1-28-a* describes a resonance wavelength shift due to the uniform increase of the core refractive index. From *Equation 2.1-20* the resonance condition can be approximated as:

$$\delta_{\nu-01} + \tfrac{1}{2}\kappa_{01} \underset{resonance}{=} 0 \qquad \textbf{Equation 2.1-29}$$

The factor of ½ is due to the fact, that only the core mode is affected by the uniform refractive index change.

For an exact solution of the differential equations above the mode field distribution and phase relation of the cladding modes has to be known.

The spectral width of a long period grating is approximately given as [*9*]:

$$\frac{\Delta\lambda}{\lambda} \cong \frac{\lambda}{\Delta nL}\sqrt{1+\tfrac{4\kappa_{\nu-01}}{\pi}} \qquad \textbf{Equation 2.1-30}$$

2.2 Photosensitivity Mechanisms

Despite all efforts to identify well-defined chemical and physical mechanisms of UV-photosensitivity, some aspects of this effect are still not clear. From the original experiment by Hill, who launched light of 488 nm wavelength through a boron-germanium co-doped fibre it was concluded that a two-photon process took place. All following experiments on this type of silica glasses using UV-light around 242 nm wavelength confirmed this theory [*17*].

Photosensitivity processes can be observed in a wide wavelength band between 180 and 350 nm, with the maximum absorption in the 240 nm range [*18*].

The main effect of UV-photosensitivity manifests in a change of the refractive index of the glass. To understand and describe this behaviour two theories are widely accepted as possible explanations: the colour centre model [*19,20,21*] and the density change model [*22*]. The change refractive index is explained by the rearrangement of chemical bonds in the first theory, respectively by locally induced density variations and stress in lattices of macroscopic size according to the latter.

For the description of a range of observed photorefractive effects the densification model gives reasonable explanations [*23,24,25*]. These densification effects can be measured as microscopic changes in stress and volume inside the fibre [*26,27*].

The colour centre model starts with the description of a Germanium-Silicate glass being composed of small regular lattices in which all Silicon (*Si*) and Germanium (*Ge*) atoms are tetra-coordinated and the Oxygen (*O*) atoms two-coordinated, linking a *Si*-atom to a neighbouring *Ge*-atom or two *Si*-atoms to each other. It is well known that silica glass is an amorphous material due to its intrinsic crystallisation properties, which means that these lattices are regular in very small areas only, containing a few hundreds of atoms at best. Scattered all over this structure are crystal defects of all kinds, of which so-called Germanium related Oxygen Deficiency Centres (GODC), or colour centres have been identified as one predominant source for UV-induced structural changes. These GODCs are classified in diamagnetic and paramagnetic defects, depending on whether an electron pair or a single electron is found at the site of the point defect. The most common diamagnetic defects are the neutral oxygen vacancy (NOV) centre in which the *O*-atom linking a *Si* and *Ge* atom is missing and the *Ge2+* defect, where a two-coordinated *Ge* is found instead of a tetra-coordinated one. All paramagnetic defects occur due to a defective bond consisting of a single electron only or due to non-bridging electrons embedded in the crystal matrix that act as electron traps. These include the *Ge*(1) defect between a germanium and an oxygen atom, the *GeE'* centre, in which a *Ge*-atom is linked to only three neighbouring oxygen atoms and the non-bridging oxygen hole centre (NBOHC), where an oxygen atom is linked to a *Ge* atom, but to no *Si*. An overview of these deficiency centres is presented in *Figure 2.2-1*.

Glass Network

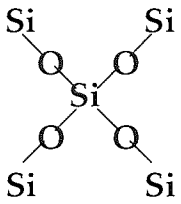

Classes of Defects in Ge-doped Glasses

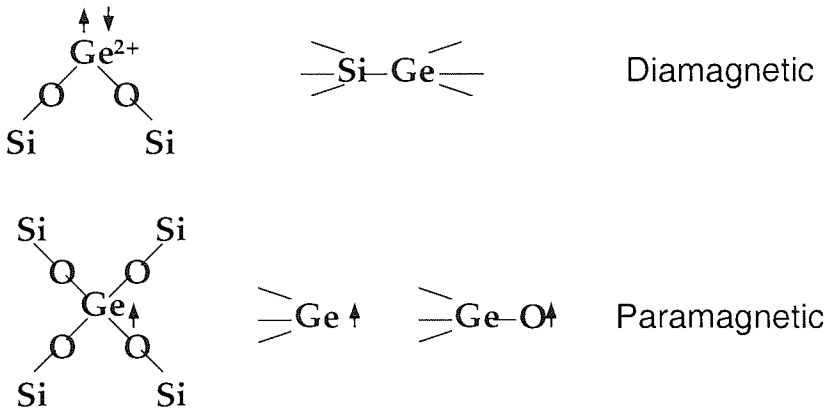

Figure 2.2-1: Chemical models of most common defect structures in Ge-doped silicate Glass (Ge^{2+}, NOV, Ge(1), GeE', NBOHC)

Based on the above assumptions and changes within the UV-absorption bands, the observed positive change of the effective refractive index can qualitatively be described by the Kramers-Kronig relation, as defined in *Equation 2.2-1* [*21,23*].

$$\Delta n(\omega') = \frac{c}{\pi} P \int_0^{\infty} \frac{\Delta\alpha(\omega) d\omega}{\omega^2 - \omega'^2} \qquad \textbf{Equation 2.2-1}$$

Here $\Delta\alpha(\omega)$ and $\Delta n(\omega)$ are changes in absorption and refractive index for a given optical frequency ω. The term c is the vacuum speed of light and P the principle part of the integral. Because this is the fundamental and most prominent UV-induced refractive index effect in germanium-silicate fibres, resulting gratings are called Type I gratings.

As for many standard fibre types the number of deficiency centres in a *Ge*-silica material is limited to the number of naturally occurring defects, so is the maximal refractive index change that can be achieved through UV-exposure. It is not always convenient to increase the dopant concentration within a fibre for reasons of increasing photosensitivity. Germanium is known to increase the refractive index and hence the numerical aperture of optical glass fibres, impairing their compatibility with standard fibre. Additional dopants, as boron, are used to both counteract these effects, as well as to increase the UV-sensitivity, but make the glass brittle and more difficult to handle.

This problem was solved by showing, that through additional hydrogenation of standard fibre with H_2 or D_2, almost all *Ge*-atoms in the glass structure can be turned into GODCs, allowing refractive index changes in the region of 10^{-2} with relatively moderate rates of *Ge*-doping. In the past this method has become a standard practice in research and industry whereby one differentiates between high pressure loading at room temperature [*28*] and the loading in a heat chamber [*29*]. One possible chemical process is shown in *Equation 2.2-2*, but different models have been suggested in the literature [*30,31*]. It shows the dissociation of a hydrogen molecule, followed by the reversible process using pure silica and the actual photosensitisation due to an existing Germanium site.

$$H_2 \rightarrow 2H$$

$$\equiv Si-O-Si\equiv + 2H \rightarrow \equiv Si-O-Si\equiv + H_2 \qquad \textbf{Equation 2.2-2}$$

$$\equiv Si-O\cdots \underset{\|}{Ge}\cdots O-Si\equiv + 2H \rightarrow 2 \quad \equiv Si-O-H + \dot{G}e=$$

A hydrogenation process prior to the UV-exposure requires a post-annealing of the samples over the duration of several days at a temperature above 120° C in order to out-diffuse the remaining hydrogen and stabilise the photorefractive effect [*32*]. The long-term prospects for the stability of gratings in hydrogen-loaded fibre after annealing can be obtained by continuous isochronal annealing experiments [*33*].

A second, less pronounced photorefractive effect is observed during overexposure of germanium co-doped fibres to the point where the saturation of the primary deficient centres is reached. A full or partial erasure of the Type I grating can be observed, followed by the growth of a secondary grating [*34,35*]. This kind of grating is defined as IIa type and exhibits wavelength shifts towards shorter wavelengths during inscription, indicating a negative refractive index change. Possible explanations for the occurring effect can be found in the theory of UV-induced *Ge(1)* and *Ge(2)* defect sites at 281 nm and 213 nm wavelength [*1*] and a multi-energy-level theory according to which more than just one meta-stable electron traps exist at different energy states of the crystal [*36*]. The formation of Type IIa gratings in hydrogen-loaded fibres has not been observed. Some research suggests that the hydrogen in the glass structure prevents the effects leading to negative refractive index changes [*37*].

It is obvious that because of the complex nature of photosensitivity a multitude of different models have evolved. Each of these formalisms describes a very limited set of parameters, regarding intrinsic material properties as dopant content and concentration, pre-treatment, assumed activation energies, densities and total number of the defect sites, as well as light wavelength, fluence and mode of operation of the UV source used for grating writing. Therefore different mechanisms are used to describe positive or negative refractive index changes. In conclusion UV absorption in *Ge*-Silicates has to be considered as a non-linear process. The fabrication of gratings showing highly non-linear and complex growth and

annealing characteristics will be discussed in ***Chapter 6***, presenting the formation of so-called Type IA gratings.

Recently the *UV dipole-quadrupole model* has been published in an attempt to describe the sum of photorefractive effects in *Ge*-glasses with a single formalism [*38,39*]. It combines well-known and documented data on colour centres in germanium-silicate glasses with a set of assumptions on further absorption processes, as expected from phenomenological observations. One promising aspect of this theory is the fact, that it describes the non-linearity of the UV-writing process as the simultaneous incidence of first and higher order positive and negative refractive index changes, as well as multi-photon and annealing processes with good accuracy. Unfortunately, so far it has only been validated for germanium doped fibre types. Proving its validity for more complex fibre compositions requires further thorough investigation.

In contrast to the pseudo-discrete electron transitions with UV-light of matching wavelength stand grating writing methods based on local melting and resolidification processes in a glass fibre core. The most classical example for grating inscription based on this principle are Type II, or damage gratings written by single excimer pulses which are diffracted by a phase mask [*40,41,42*]. More recently high power femtosecond lasers have become the subject of intensive research activity. Bragg and long period gratings are written using a strongly focused beam in a point-by-point approach [*43,44,45*] or an expanded beam through a phase-mask [*46*].

Refractive index changes can also be achieved applying an electric arc, as used for fibre splicing [*47*]. Because of the difficulty controlling the arc area, this method is limited to the fabrication of long period gratings only.

2.3 Fabrication Techniques for Fibre Bragg Gratings

In the experiment, which led Hill to discover the photosensitive property of *Ge*-doped Silica, a 488 nm laser beam of high intensity was launched into a fibre core [*1*]. Due to back-reflection of the light from the end-facet, a standing wave pattern was generated, which formed a permanent refractive index modulation along the full length of the fibre and thus a spectral filter blocking all light from passing through the fibre. Despite the fact that the observed effect could be explained very soon after this discovery, indicating that a periodic refractive index change took place due to a two-Photon effect, the relevance of this experiment became fully clear only after another decade. Using the initial method, the grating wavelength was defined by the wavelength of the light travelling through the fibre and it was impossible to influence the position, length or shape of the grating.

With growing importance of fibre optical systems and the need for the fabrication of well-defined fibre optical filters, a variety of more advanced fibre Grating fabrication methods has been developed, of which a few are going to be presented here. At the end of this chapter the advantages and drawbacks of these will be discussed.

2.3.1 Holographic FBG Writing

In 1989 Meltz et al came forward with a solution to overcome the problem restricting the grating design by introducing the side writing method [*48*]. In their experiment a frequency doubled 244 nm argon laser was used as the UV-source in an interferometer set-up, which is more suitable for the given task. The beam was separated in two fractions of identical power using a beam-splitter and brought to an overlap within the fibre core with two mirrors, as presented in *Figure 2.3-1*. The resulting Bragg wavelength λ_{FBG} is a function of the UV-wavelength λ_{UV}, the refractive index of the photosensitive waveguide core and the intersecting half-angle α of the two beams, the length L is given by the size of the overlap region and the refractive index modulation Δn_{mod} depends on the photosensitivity η of the fibre and the exposure time t. The function for the Bragg condition is shown below.

$$\lambda_{FBG} = \frac{n \cdot \lambda_{UV}}{\sin \alpha} \qquad \textit{Equation 2.3-1}$$

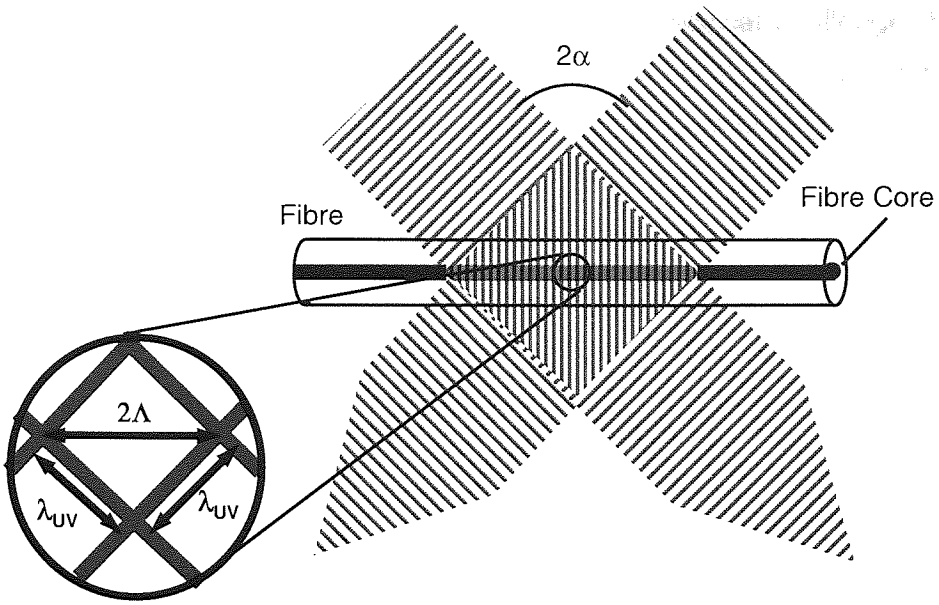

Figure 2.3-1: Principle of grating inscription by holographic imprint of 2-beam interference into fibre core

2.3.2 The phase-mask method

The growing demand of Bragg gratings with highly defined specifications means that a reliable tool for their mass production had to be found. Interferometer based systems with their free beam optical arrangements are no ideal solution for this task.

Therefore in 1993 the application of a phase-mask in the grating inscription process was reported for the fist time [*49*]. A phase-mask is a fused silica plate with a surface corrugation profile, which ideally diffracts a beam incident on its backside into a pattern of *+1* and *-1* order beams only. In a small area near to the corrugated surface these beams come to an overlap thus creating an interference pattern. The principle is depicted in *Figure 2.3-2*.

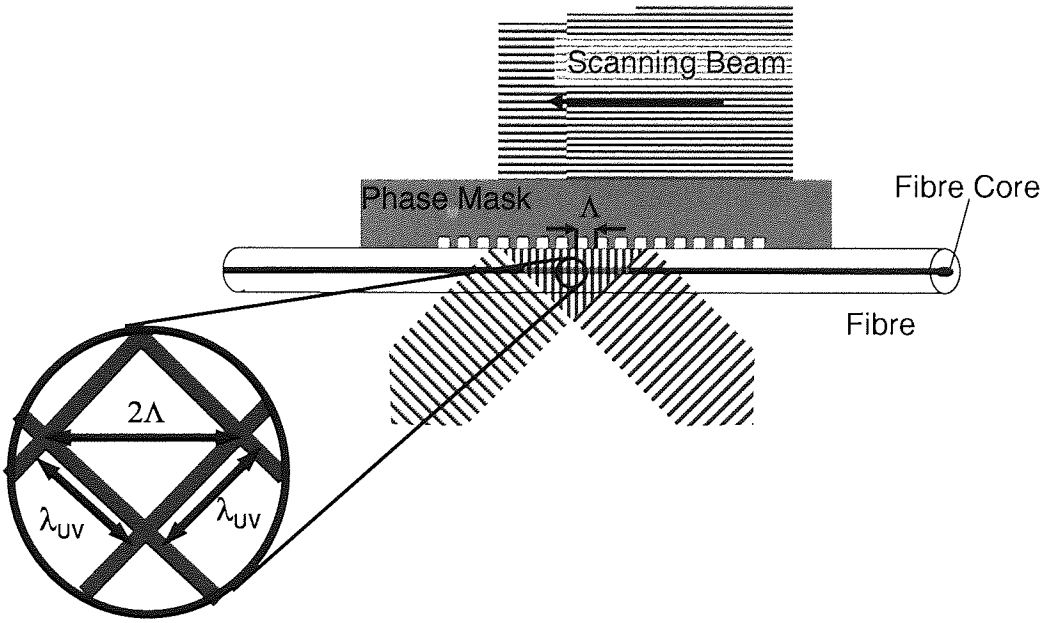

Figure 2.3-2: Grating inscription using interference pattern generated by a phase mask

The fabrication of high-quality phase-masks still is a technological challenge. For optimal diffraction efficiency, the accurate control of etch-depth, duty cycle and fringe profile is crucial. The required etch-depth is determined by the UV-wavelength the phase-mask is intended to be used with.

The resulting wavelength λ_B of a Bragg grating that is fabricated by illumination through a phase-mask is given by the period of its surface pattern Λ_{PM}, as shown in *Equation 2.3-2*, with n_{eff} as the effective refractive index of the fibre core.

$$\lambda_{FBG} = n\frac{\Lambda_{PM}}{2} \qquad \textbf{Equation 2.3-2}$$

It should be stated here that in literature with Λ_{PM} it is often referred to the period of the interference pattern, which will be denoted Λ here.

Another critical factor for the quality of a phase-mask is the local accuracy of Λ_{PM}. If electron-beam lithography is used in the fabrication process, so-called stitching errors can occur over the length of the phase-mask pattern. A section that can be written at once is only of sub-millimetre size, so in order to achieve a phase-mask of a practical length, a number of sections have to be concatenated. These errors manifest in unwanted reflection peaks in the final fibre Bragg grating spectrum [*50*].

The diffraction efficiency for the *±1*-oder beams reaches 40% in phase-masks of good quality with a suppression of the zero-order down to 1-2% of the total light power. Any contribution of light in orders except the *±1*-oder adds to a DC-offset of the induced refractive index change, thus reducing the amount of index modulation that can be achieved as a maximum. It also generates a disturbance of the interference pattern by adding higher order modulations.

Commercially available phase-masks come in lengths between 1 and 10 centimetres.

2.4 Alternative Fabrication Methods

Other standard grating fabrication set-ups are the Lloyd mirror [*51*] and a range of prism based configurations [*52,53,54*], of which one is shown in *Figure 2.4-1.*

In the first case a fibre is brought in contact with a bulk crystal at a right angle, which acts as a mirror for UV light. The beam grazes the mirror surface right at that point under a certain angle α in such a way, that half of the beam hits the fibre directly and the other half after reflection, as becomes apparent in the left half of *Figure 2.4-1.* Both fractions of the beam interfere in the fibre core and generate a grating. The resulting wavelength is in accordance with *Equation 2.3-1.*

The second mechanism works with a UV beam, which is incident on a prism. If the beam is well aligned to the prism, half of its width will propagate through it and the second fraction will

be deflected either by internal reflection or by refraction leading to a cross-over with the first. After propagation trough the prism both beam parts form an interference pattern within their crossover area. It is obvious that the main imitations of this set-up are the small region of beam overlap, restricting the grating length to half the beam size and the aligning of the beam to obtain two beam fractions of identical width.

The angle of the overlap is determined by the prism geometry, and the FBG wavelength again follows *Equation 2.3-1*.

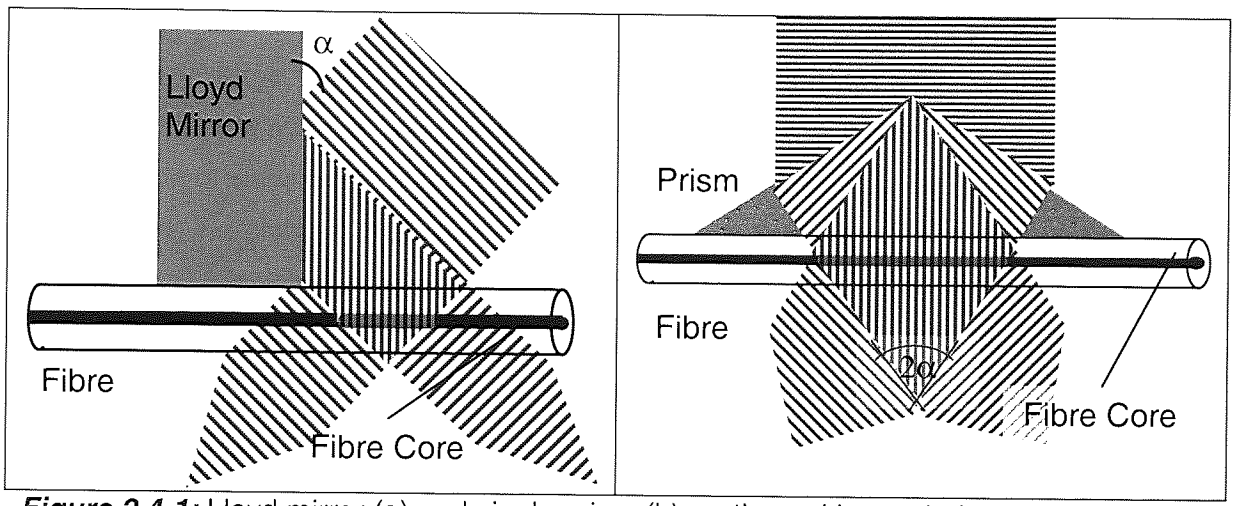

Figure 2.4-1: Lloyd mirror (a) and single prism (b) grating writing technique

One other approach, which does not rely on the diffraction pattern of expanded and coherent beams, is the Point-by-point method [*55*]. Here an incoming Gaussian beam is strongly focussed in the core of the fibre, using two cylindrical lenses, which are under a right angle to each other. While the beam is scanning over the length of the fibre, a shutter periodically opens and closes, setting the areas of the core, which are exposed or left unexposed.

2.5 Advanced Grating Fabrication

As pointed out in ***Chapter 2.1*** the filter function of a FBG can be optimised and tailored to preset specifications by applying an apodisation to the refractive index modulation profile. Apodisation of gratings leads to the suppression of side-lobes, which are characteristic for uniform gratings. This becomes important for the design of optical telecommunications networks with narrow channel spacing that is free of interference effects, so-called cross-talk, between neighbouring channels. In addition to that the design of a grating apodisation profile affects the dispersive properties of the device. One important aspect of add-drop filters in telecom applications for example is the conservation of the pulse form of the carrier wave to minimise bit errors within the system.

For these applications complex grating designs, such as those exhibiting a sinc-shaped modulation profile, in theory require both positive as well as negative refractive index changes over their length. In practice the straightforward control of writing conditions leading

to positive and negative refractive index changes is not possible. The envelope of a modulation profile resulting from UV-exposure always reflects the absolute value of the designed apodisation profile. Nevertheless the spectral response of a grating can be corrected to agree with its original design if π-phase shifts are introduced in the grating exactly at all positions where a transition between positive and negative refractive index change is due to take place.

Signal pulses travelling through long-haul transmission systems suffer degradation in shape due to the intrinsic dispersion of standard telecom fibres. In this case gratings can be used to reverse the effect of pulse broadening. Upon reflection within a linearly chirped Bragg grating, different spectral components of the light suffer different time-delays according to the distribution of wavelength selective reflecting sites within the grating. The chirp of a grating is defined as the change of local grating period per unit of length of the grating. In addition to the effect of side-lobe suppression, the apodisation of chirped gratings smoothens the time-delay response, by effectively reducing the symptomatic ripples of the curve [*56*].

In the following sections advanced writing techniques are introduced which make grating inscription as flexible and versatile as possible. They have all in common that they are based on the standard procedures as described above. Combination of these with additional process steps allows the production of gratings with virtually arbitrary apodisation, dispersion and time-delay profile.

2.5.1 Phase Masks with prefabricated Apodisation and Chirp

The most straightforward way to produce apodised fibre Bragg gratings is the application of an apodised phase mask in the writing process. In general, this will be a phase-mask with changing diffraction efficiency over its length, following a Gaussian function [*57*].

Nowadays Phase-masks with a linearly changing period over their length are standard tools for the fabrication of chirped fibre and waveguide Bragg gratings.

However, it is obvious that this method does not offer much flexibility for the grating writing process but is limited to the parameters of the phase masks used.

2.5.2 Double-scan technique

The easiest way to generate a non-uniform fringe pattern in a waveguide by exposure through a phase-mask is to control the beam power during the inscription scan. This can be achieved through external modulation of the UV beam. In this case however, not only the fringe visibility is a function of the applied apodisation profile, but also the mean refractive index, giving rise to an increased dispersion within the grating. In order to level out the envelope of the refractive index profile to a constant mean value, the phase-mask has to be

removed and a second scan with an inverse profile compared to the one of the first scan has to be applied [*58*]. The strength of this method is its simplicity and the fact that no costly additions have to be made to an existing set-up. The reproducibility of the grating inscription is fairly good. On the other hand only basic apodisation profiles can be achieved with this technique, in general of a Gaussian shape. A further drawback of this system is the strict requirement of linear photosensitivity of the waveguide core over time in order to achieve a undistorted function of the grating coupling coefficient κ.

2.5.3 Phase Mask Shifting Method

One of the most widespread procedures for the writing of advanced gratings is the shifting phase mask to fibre technique, which has was developed at Aston University in 1994 and the Optical Research Centre at Southampton University around the same time [*59,60*]. It basically comprises a standard phase mask writing set-up with the only difference that the phase mask is mounted on top of a piezoelectric transducer with its axis of movement aligned parallel to phase mask and fibre. A movement of the phase mask with the velocity v_{shift} during the inscription results in a shift of the effective period of the interference pattern seen by the fibre and the Bragg wavelength of the fibre grating according to

$$\frac{\Delta\Lambda}{\Lambda_0} = \frac{\Delta\lambda}{\lambda_0} = \frac{v_{shift}}{v_{scan}} \qquad \textbf{Equation 2.5-1}$$

At the same time the fringe visibility is depending on *Equation 2.5-2,* in which *d* is the beam diameter.

$$\Delta n_{\mathrm{mod}} = \frac{\lambda_0^2}{2n_{eff}\pi d\Delta\lambda}\sin\frac{2n_{eff}\pi d\Delta\lambda}{\lambda_0^2} \qquad \textbf{Equation 2.5-2}$$

It is obvious that the fringe visibility becomes zero, if the beam scanning velocity and phase mask shifting velocity match in such a way, that the beam passes with its full diameter over the length of one grating pitch in the same time, as the phase-mask is moved by one period. In this case a local π-phase shift is introduced in the grating. The matching condition can be expressed as follows:

$$\frac{d}{v_{SCAN}} = \frac{\Lambda_0}{v_{SHIFT}} \qquad \textbf{Equation 2.5-3}$$

In *Figure 5.2-1* this is illustrated in the left part of the schematic, where v_{shift} fits exactly the condition that phase mask moves half a period during the time $d \cdot v_{scan}^{-1}$, which the full beam requires to pass a given point on the phase mask surface. A shorter displacement time, as shown in the middle section results in a change of the effective grating period in the fibre core. The maximum fringe visibility is achieved for a static beam and the writing of a Bragg grating at the nominal wavelength, as shown in the right example.

It becomes clear that depending on the translation profile, this method allows the fabrication of both apodised, as well as chirped gratings using a uniform phase mask. The central wavelength of a grating can also be shifted with respect to the wavelength, for which the phase mask originally was designed, at the expense of the maximum achievable index modulation strength. One drawback of the latter two cases is the fact that the wavelength shift is interdependent with the fringe visibility over the beam dimension *d*. Because of the necessity of linear movements between fibre and phase-mask another restrictive aspect of the set-up is the translation range of the piezo-crystal. Nevertheless, it offers a highly flexible tool for wavelength selection and arbitrary profile tailoring in fibre Bragg gratings.

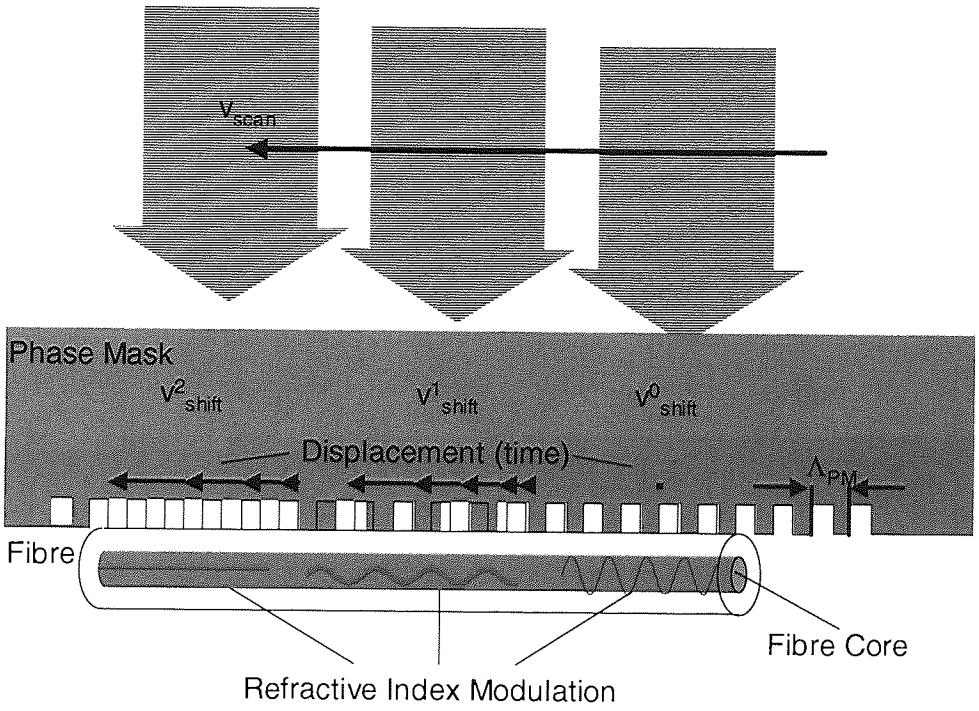

Figure 2.5-1: Concept of Bragg wavelength shift / apodisation with shifting phase–mask technique

The versatility of this set-up can be further enhanced using a modulated UV-beam, which illuminates the core of an optical fibre through a static phase-mask. Instead the fibre is moved parallel to the phase mask surface. The modulation frequency is fixed, while a computer system matches the fibre translation in order to achieve any required phase shift between mask and fibre grating. In this way the wavelength and modulation profile of the grating are tailored in the same manner, as using a continuous beam. In this case however, the grating length can be increased by concatenating an arbitrary number of grating sections with each other [*61*]. In the following this technique will be referred to as the Multiple Printing in Fibre (MPF) method.

2.5.4 Dithering Phase Mask Technique

Based on the same fabrication set-up as the shifting phase-mask method, this technique takes advantage of uniform and linear relative motion between phase mask and optic fibre [*62,63*]. An oscillation of the piezo-crystal during the grating inscription at a relatively low frequency of 20 Hz leads to the blurring of the fringe visibility within the fibre. If the shaking amplitude is set to equal the surface pattern of the phase mask Λ_{PM}, a complete erasure of the grating can be achieved. Control of the amplitude as a function of position along the fibre allows the superposition of arbitrary apodisation profiles over the grating modulation. Furthermore, local sections within the grating, in which the fringes have been eliminated completely act as local states with π-phase shifts, making this approach one of the most versatile methods for grating fabrication. The principle is described in *Figure 2.5-2*.

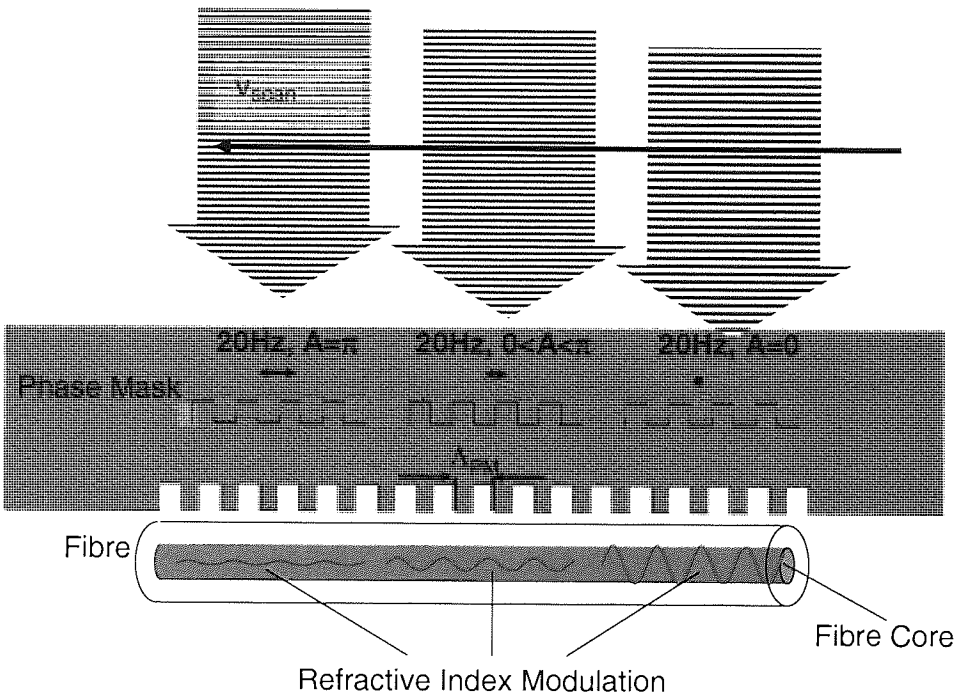

Figure 2.5.2: Apodisation by dithering phase mask method

In previous work the importance of the applied modulation format on the fringe effect has been evaluated, with the best results obtained with triangular [*64*] or stepped square [*65*] driving functions.

Between the phase mask dithering and shifting method the first one more convenient because it is easier to control and good results can be obtained at less efforts and cost. However, the shifting method offers better versatility and if controlled with good accuracy, can lead to better results.

2.6 Long Period Grating Fabrication

As the name suggests, long period gratings (LPGs) in first instance differ from fibre Bragg gratings due to the longer periods of their refractive index modulation. Typical periods can range between values from a few micrometers into the millimetre region. Their operating principles of these two grating types however differ significantly, as explained in ***Chapter 2.1***. The filter function of a fibre Bragg grating originates from the coupling between counter-propagating sets of modes in the fibre, whereas LPGs are defined by the coupling of co-propagating waves. Unlike FBGs, in which the light stays confined within the fibre core and the apparent propagation loss is due to reflection of certain parts of the light spectrum, LPGs are *adiabatic* loss filters. Light becomes coupled out of the core into the cladding. Some cladding modes are supported by the waveguide conditions, as long as the outer refractive index is lower than that of the cladding. Otherwise or when travelling through a fibre section where the outer coating has not been removed, these modes scatter out of the fibre. Their spectral sensitivity however make long period gratings the choice for a number of sensing applications, as they are highly sensitive to parameters as bending, temperature, strain, ambient refractive index [*66*] and load [*67*]. Another common application for LPGs is in gain equalisation for both fibre optic sensing and telecoms [*68*].

Depending on the required period, different methods can be used for LPG fabrication. For gratings with periods in the range of a few micrometers phase-masks can be used in the same way as described for FBG writing in ***Chapter 2.3.2***. More common is the use of amplitude masks with a periodic pattern of translucent and absorbing areas. For short LPGs these masks have to be done by a lithographic process in which chromium is deposited on a fused silica plate. In this case problems can arise due to diffraction on the edges of the pattern and damage of the chromium layer. For periods above 100 μm, gratings machined in Aluminium sheets can be used as amplitude masks. Another alternative is the point-by-point method, as featured in ***Chapter 2.3.4***, in which the UV laser beam, which is focussed in two orthogonal planes in the fibre core by using a vertical and horizontal cylindrical lens, is translated along the fibre and a computer-controlled shutter periodically exposes certain areas along the fibre [*69*].

The use of a phase-mask or amplitude mask offers a simple procedure for LPG inscription. The UV-beam only needs to be focussed in the plane of the fibre core. Amplitude masks are easier to fabricate and come at a lower cost than phase masks. However, the restrictions on the wavelength are even greater than those for Bragg gratings. Slight differences in the period of the mask have a big effect on the grating wavelength due to their coupling mechanism. This makes the appropriate use of an amplitude mask highly depending on the fibre type used.

The point-by-point fabrication principle offers the most flexible solution for setting the grating wavelength and choosing particular LPG modes to occur at the desired wavelength. A translation stage of fair scanning precision is required to control the duty cycle and refractive index modulation profile. The absolute positioning is also crucial, as the grating fabrication often requires multiple scans that match each previous one. The need of a second cylindrical lens for focussing the beam in lateral direction increases the set-up complexity with respect to alignment.

2.7 Summary

Most standardised fabrication techniques used today are based on the holographic and the phase mask method. Both provide the facility to write high quality gratings of 100% reflectivity. With the former method arbitrary wavelengths can easily be achieved. Its downsides are the limitation of grating by the size of the area in which the interfering beams overlap and the requirements with respect to beam coherence and mechanical stability. The application of a beam splitter crystal also means that the intersecting beams are of different polarisation, which in some cases has an adverse effect on the photosensitivity processes [*70*]. All of these points have implications of the fringe visibility in the fibre core.

The phase mask approach excels by high fabrication reproducibility. Very strong gratings of high quality and are written as standard. The main requirement to the laser source is its spatial coherence, as every part of the beam cross section has to adhere to the same diffraction condition on the phase mask surface. Special phase masks with apodised, chirped or otherwise altered diffraction pattern profiles over their length greatly improve the versatility of the method. Its main restriction is the limitation of the grating wavelength to a very narrow spectral area.

For reasons of higher flexibility each of the systems described above can be modified to obtain certain grating specifications, as shown in ***Chapter 2.5***. Combining the advantages of holographic and phase mask methods in one single set-up helps to overcome their major inherent draw-backs. In ***Chapter 3.2*** two novel techniques for advanced FBG fabrication are presented, which are relevant for the work done during this doctoral thesis.

Fabrication methods involving Lloyd mirrors and prisms offer as a main advantage high stability of the set-up, but face similar restrictions as the holographic method and require a high degree of accuracy of the beam alignment.

The point-by-point method in theory provides direct control over the writing of each single fringe of the grating with respect to period, duty cycle and modulation strength. However, under experimental conditions it is difficult to focus and control the beam within the fibre core with sub-micrometer precision. For this reason the method is mainly used for the inscription of long period gratings, where these issues are not as critical.

3 NOVEL FIBRE AND PLANAR BRAGG GRATING WRITING AND CHARACTERISATION TECHNIQUES

3.1 Fabrication of arrayed fibre Bragg gratings using phase mask shifting method

3.1.1 Introduction

In ***Section 2.5.3*** the principles of an advanced grating fabrication method was illustrated, which enables the apodisation and wavelength adjustment of fibre Bragg gratings by simultaneously moving a piezo translator on which the phase mask is mounted, during the scan with an UV-beam.

The practical application of this method is demonstrated by the fabrication of multiple grating arrays in fibres, the results of which are presented below.

3.1.2 Methodology and Set-Up

Ten gratings of different wavelengths have been written in different sections of two fibres, using the same uniform phase mask designed for grating inscription at 1560 nm. All gratings were written by scanning different 9 mm long sections of the phase mask, with their centres separated 10 mm from each other. In each of the two fibres a reference grating was written first with the piezo stage stationary during the scan. During the writing of the subsequent gratings the phase mask was shifted at a uniform speed different for each grating, resulting in a wavelength change.

The writing speed was 50 μm/s at a laser power of 125 mW. For the inscription of every subsequent grating, the shifting velocity of the piezo-crystal was increased by 9.6 μm/s. This, according to *Equation 2.5-3*, corresponds to a wavelength shift of 0.3 nm. For both fibres the phase mask was shifted with the same velocities, but in opposite directions, resulting in a wavelength increase in the one case, and gratings of shorter wavelength in the other case.

3.1.3 Results

The spectra from the resulting grating arrays are shown in *Figure. 3.1-1*. In the centre section, the two reference gratings with their 20 dB strong peaks at 1560.18 nm and 1560.35 nm are highlighted with a circle. Separated by approximately 0.3 nm from each other at their respective lower and higher wavelength side of the spectrum those gratings are

visible that were fabricated with a uniformly moving phase mask. With increasing wavelength shift away from the reference wavelength the grating strength decreases.

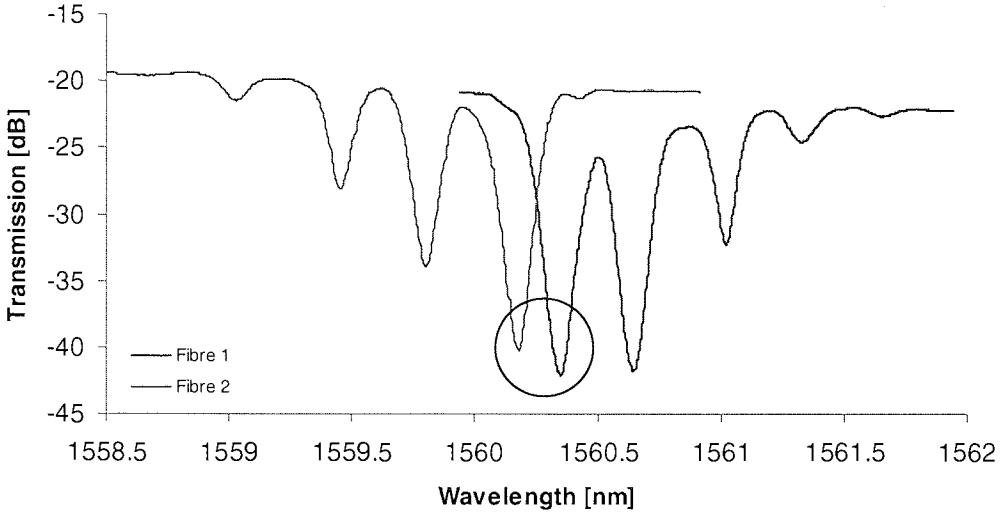

Figure 3.1-1: Demonstration of wavelength adjustability and apodisation effect using shifting phase-mask technique

An overview of the correlation between fabrication parameters and measured spectra of the resulting gratings is shown in *Table 3.1-1*. A maximum wavelength shift of 1.32 nm was obtained for the gratings in Fibre 1 and 1.13 nm for those in Fibre 2. Beyond these points the accumulated fringe pattern in the fibre core is erased, as described by *Equation 2.5-1*. The full range of the wavelength shift effect can be increased according to *Equation 2.5-2*, if the beam width is decreased.

	Fibre 1: λ_0=1560.35 nm, 20.3 dB				Fibre 2: λ_0=1560.18 nm, 19.9 dB			
Piezo Velocity [µm/s]	-9.6	-19.2	-28.6	-38.2	9.6	19.2	28.6	38.2
Expected Shift [nm]	0.30	0.60	0.90	1.20	-0.30	-0.60	-0.90	-1.20
Measured Shift [nm]	0.30	0.67	0.99	1.32	-0.38	-0.72	-1.13	
Insertion Loss [dB]	20.1	10.5	2.9	1.0	13.5	7.7	1.1	

Table 3.1-1: Wavelength shifts in theory and experiment using the phase-mask shifting technique

3.1.4 Discussion

From *Table 3.1.1* it can be seen, that the results obtained for positive wavelength shifts match the theoretical predictions better than for the opposite case, where the deviation from expected values is more than 20%. This can be explained by the fact that both the translation stage and the piezo-element have intrinsic errors of their actual velocity to the nominal

speed. This is even more significant, as there is a factor of 1000 between the values of both translation speeds. Another possible error source is the alignment of the fibre to phase mask gap. A misalignment can result in a dc-offset of the refractive index change at the expense of the fringe visibility. The slightly stronger reference grating in *Fibre 1* indicates the possibility of this case.

By estimation of the ordinates where the envelope of both grating arrays becomes zero and inversion of *Equation 2.5-2*, the approximate beam diameter used in this experiment can be calculated to be around 0.8 mm, which is in accordance with the estimated value.

Figure 3.1-2 shows a different approach, in which the curve defined by *Equation 2.5-2* has been fitted to the actual values of wavelength shift and grating strength obtained experimentally. A minimum value for the mean square root error was achieved for a beam diameter d of 0.68 mm. The graph shows the expected and measured grating transmission values alongside the fringe visibility.

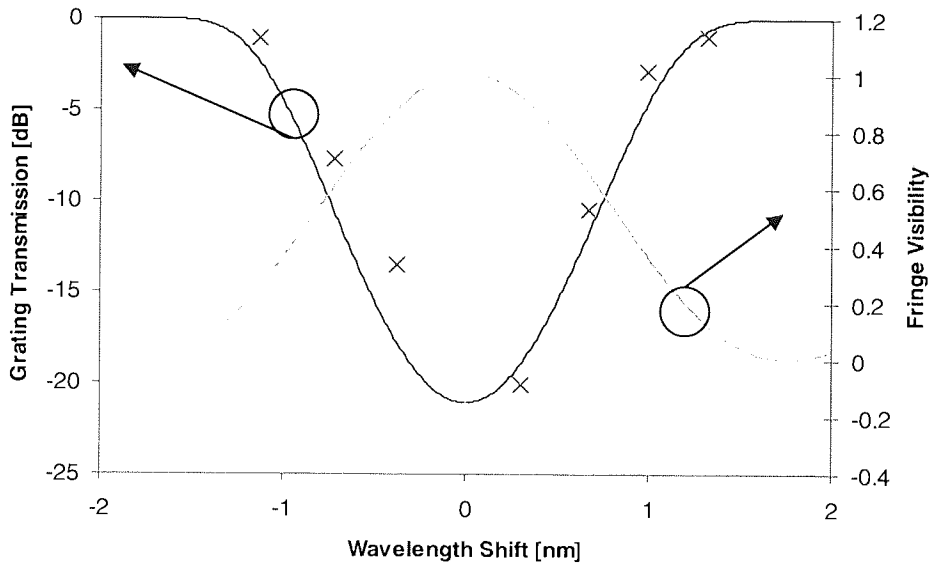

Figure 3.1-2: Comparison of experimentally obtained wavelength shift and apodisation effect with theoretical values according to *Equation 2.5.2*

3.1.5 Conclusions

Using the phase mask shifting method, fibre Bragg grating arrays were fabricated using a uniform phase mask. Positive and negative wavelength shifts were achieved up to 1.3 nm, at which point the simultaneous apodisation shows its full effect, practically erasing the grating fringes. From a fit of the obtained data with the predicted grating strengths, the active beam diameter was calculated. Knowing this parameter and the dynamic photorefractive response of the fibre enables writing multi-grating arrays of equalised transmission and reflection values by using a uniform phase-mask.

3.2 An advanced holographic Bragg Grating Inscription Method

3.2.1 Introduction and Motivation

As described in ***Chapter 2.3*** the use of holographic grating fabrication methods offers high flexibility in wavelength selection. However, standard holographic techniques lack the feasibility of writing apodised or chirped gratings, as well as gratings that are significantly longer than the beam width.

Chirped fibre Bragg gratings (CFBGs) are of huge interest for many applications, as dispersion management [*71*] and pulse-width suppression and ultra-short pulse generation [*72*] for telecom transmission systems, wavelength selection [*73*], reflection and gain flattening in fibre lasers and amplifiers [*74*], and wavelength encoding of measurands and demodulation in fibre optic sensing [*75*].

In particular for the use in telecom transmission systems, gratings with high side-lobe suppression and low time-delay ripples are desirable for a better performance of those, which is achieved by apodisation [*76*]. Another issue is the flexibility in wavelength selection and the cost-factor of a method for the inscription of such gratings.

Therefore various writing techniques offering wavelength selection for these types of gratings have been presented in the past. Farries et al. put cylindrical lenses in the beam paths of a holographic fabrication set-up, resulting in strongly chirped gratings due to the curvature of the distorted wave fronts [*77*]. Based on the same principle, a Talbot interferometer set-up has been proposed by Wang et al. [*78*]. For the fabrication of apodised chirped fibre Bragg gratings at arbitrary wavelength, Cortès et al. have presented a Sagnac interferometer in which the fine tuning of a rotatable mirror during the UV scan locally changes the wavelength along the fibre and gives rise to a chirp [*79*]. The apodisation effect is achieved by using a pulsed laser and the fact that the temporal overlap of the first order beams inside the fibre is depending on the optical path difference between the phase mask and the fibre [*80*].

Here a similar though simpler method is presented, which is based on a Talbot interferometer which was developed within the course of this work. It offers the same degree of wavelength selection as a classic holographic set-up based on a beam splitter crystal. Replacing the latter by a phase mask allows the writing of apodised and chirped gratings without the necessity to further manipulate any fraction of the beam by lenses or mirrors.

3.2.2 Experimental Set-Up

The experimental set-up used is shown in *Figure 3.2-1.* The Talbot interferometer uses a phase-mask as 50/50 beam-splitter and two mirrors M_1 and M_2, steering the diffracted ± 1-orders of the incoming beam to interfere at the core of the photosensitive fibre after

transmission through a cylindrical focussing lens, forming a fibre Bragg grating. The size of the fibre is emphasised with respect of the other elements.

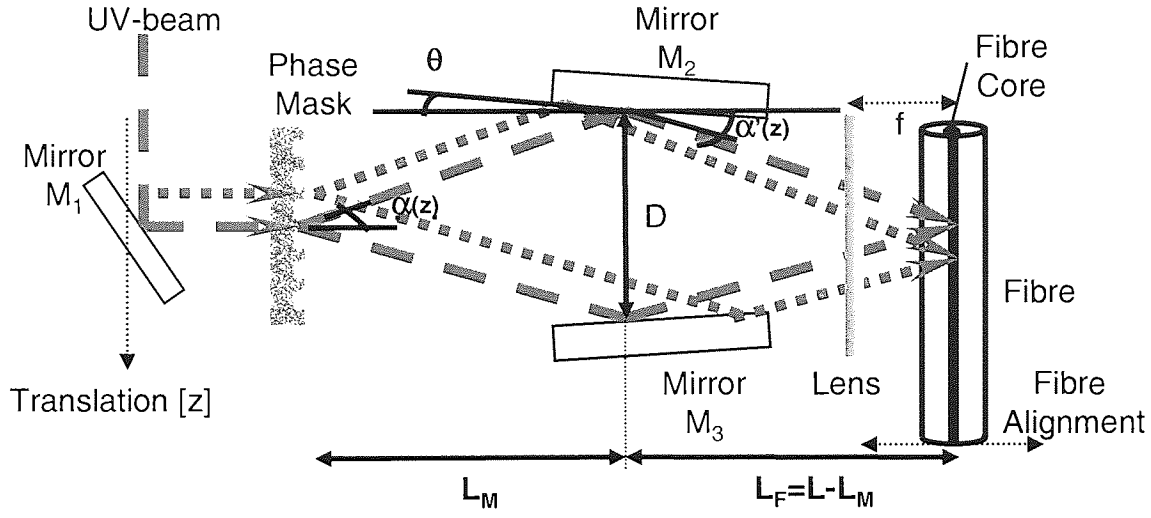

Figure 3.2-1: Schematic of scanning-holographic set-up

A CW laser beam with λ_{UV}=244 nm is scanned in *z*-direction along the static phase-mask at a constant speed, using a 45º mirror (M_1) mounted on a translation stage. For the reflection of the first order beams Al-coated mirrors have to be used for M_2 and M_3 in the interferometer to maintain a constant reflectivity at all angles of beam incidence that can be set for grating fabrication at different wavelength. In the graph the two dotted lines show the beam path at different positions along the phase-mask. The Mirrors M_2 and M_3 are mounted on rotational stages with their rotational centres separated by D from each other and placed at the distance L_M from the phase-mask.

At the distance L_F from these mirror centres the photosensitive fibre is mounted and aligned parallel to the phase-mask, as well as within the focal plane of a cylindrical lens that is fixed at the distance f in front of it.

The phase-mask and the mirrors are fixed in their positions. The fibre and the lens with the focal length f are mounted on a rail carrier that can be moved closer and further away from the phase mask. The wavelength is selected by adjustment of the mirror angles α and the distance L_F between fibre and mirror centres. With the help of a micrometer translation stage and a rotational stage the fine adjustment of the fibre position can be made, providing sub-nanometre precision for the resulting Bragg wavelength. According to geometric considerations it is clear that using a pair of 5 cm long Al mirrors and a phase mask with a pitch of Λ_{PM}=1065 nm in a well aligned set-up allows the writing of Bragg gratings of up to 1 cm length. This limitation is due to the small half angle of 7º at which the first diffraction orders of the beam are diverging. Another limitation is the length of the phase mask itself.

Depending on the geometric configuration the set-up magnifies or reduces the original image of the diffraction pattern by the phase mask in the plane in which the fibre is mounted. Thus using an apodised or chirped phase mask allows the fabrication of these grating types at almost arbitrary wavelength with this method.

In the following section the work principle of the set-up is explained in a general formalism covering uniform and chirped grating fabrication. The application of an apodised phase mask does not differ in any aspect from uniform grating fabrication apart from the beam power passing through the interferometer arms.

In contrast to the method of Cortès et al. [*80*], for chirped or apodised grating fabrication the interferometer mirrors do not have to be moved during the scan, as the chirp is provided by the phase-mask.

3.2.3 Functional Principle

For the exact determination of the beam path *Figure 3.2-2* sketches the trajectory of the *+1* diffraction order between phase mask and overlap section with the *-1* diffraction order beam.

The whole set-up is aligned symmetrically to the *L*-axis around a defined position z_0=0 on the phase-mask. If a chirped phase mask is used the local wavelength in this point sets the central wavelength of the resulting grating.

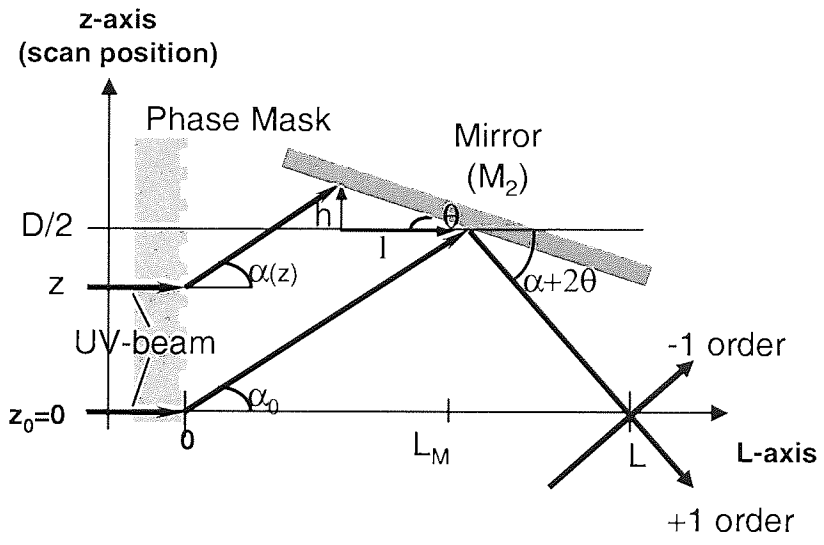

Figure 3.2-2: Schematic showing a detailed overview of the geometric principle with the example of +1 order beam trajectory

Considering all assumptions and definitions made above, the geometry of the set-up is defined by *Equation 3.2-1* and *Equation 3.2-2*.

$$L_M = \frac{D}{2\tan|\alpha(z_0)|} \qquad \textit{Equation 3.2-1}$$

$$L_F = \frac{D}{2\tan|\alpha'(z_0)|} \qquad \textit{Equation 3.2-2}$$

The diffraction angle α of the *±1* order beams is fixed by the period of the phase-mask pattern at the actual position of the beam-incidence according to *Equation 3.2-3*.

$$|\alpha(z)| = arc\sin\frac{\lambda_{UV}}{2\Lambda_0 + C\cdot z} \qquad \textit{Equation 3.2-3}$$

The constant *C* is a dimensionless factor of the chirp along the phase mask and Λ_0 is the period of the phase-mask pattern at its central point z_0. For a uniform phase mask, *C* has the value 0. For an effective refractive index of *n*, the fundamental mode in the fibre core, the angle α' and thus the resulting grating wavelength λ_{FBG} change in accordance with *Equation 3.2-4* and *Equation 3.2-5*.

$$|\alpha'(z)| = |\alpha(z)| + |2\theta| \qquad \textit{Equation 3.2-4}$$

$$\lambda_{FBG} = \frac{n\cdot\lambda_{UV}}{\sin|\alpha'(z)|} \qquad \textit{Equation 3.2-5}$$

The coordinates of incidence of the *±1* order beams on the two mirrors for an incoming beam at an arbitrary position *z* on the phase-mask are derived by basic geometric analysis of *Figure 3.2-2*.and are given in *Equation 3.2-6* and *Equation 3.2-7*. The equations for the positive and the negative order beam are indexed accordingly.

$$P_z^{\pm}(z) = \pm\frac{D}{2} + h(|\alpha(z)|) \qquad \textit{Equation 3.2-6}$$

$$P_L^{\pm}(z) = L_M \mp l(|\alpha(z)|) \qquad \textit{Equation 3.2-7}$$

An analogue approach is used for the calculation of the positions z_F^+ and z_F^- on the fibre, which the two beams hit after being deflected by the mirrors. Defining the angle θ to be positive for anticlockwise rotations of the mirror reflecting the *−1* order, and for clockwise rotations of the other mirror, yields *Equation 3.2-8*.

$$z_F^{\pm} = \pm\tfrac{D}{2} + l(z)\tan\theta \mp [L - L_M \pm l(z)]\cdot\tan\alpha'(z) \qquad \textit{Equation 3.2-8}$$

Because the angle of the diffracted $\pm1^{st}$ order beams changes while scanning over a chirped phase mask, the trajectory of the coordinates in which they fully overlap is tilted with respect to the fibre that is aligned parallel with the phase mask. Using the described experimental

set-up, it is possible to write a grating by scanning the fibre in regions where the two beams at least partially overlap in the fibre core, which depends on beam shape and diameter and the geometry of the set-up. Analogous to the temporal beam overlap described in [*79*], this leads to an apodisation profile directly related to the radial power distribution of the beams. The beams, which show a maximum of overlap in the plane of the fibre, when in central writing position z_0, separate according to a linear function of the scan position from this point. The function of overlap for two exemplary sets of parameters is shown in *Figure 3.2-3*. The phase mask period is Λ_{PM}=1065 nm and the chirp ratio 7.5 nm/cm. The curves shown apply to beam sizes of 1 mm and 2.5 mm for a set-up having a total length of 556 cm.

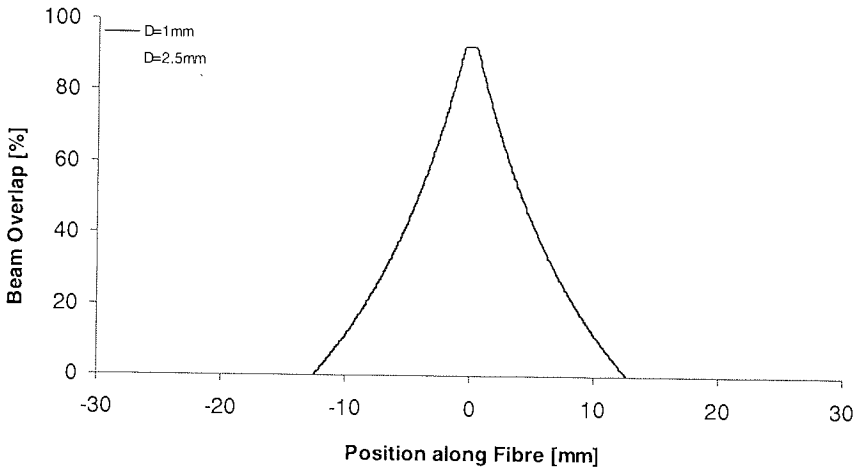

Figure 3.2-3: Normalised overlap function of interfering beams over scan length

This self-apodisation effect is desirable for side-lobe suppression of the reflection spectrum and smoothening of the time delay characteristic, but narrows the effective bandwidth of the grating. Tilting the fibre into the plane of the movement of the beam overlap will erase this apodisation function, but lead to slightly slanted gratings. Also the shortening of the effective grating section can be counter-balanced by using an expanded beam.

3.2.4 Chirped Grating Fabrication

One important step after the successful alignment of the set-up is the setting of the central scanning position, which has to match very accurately the point of the highest degree of overlap between the two interfering beams. In order to achieve this condition, the full scanning range was equally divided into 2 and 4 sections, in which subsequently partial gratings were written. The reflection spectra of the gratings from one set were pasted into one single graph from which the symmetry of each adjacent sub-grating could be assessed. If necessary, the central position was shifted to compensate for asymmetric behaviour of the gratings and a new set of test gratings was written.

Figure 3.2-4 shows the spectra of two imbalanced 5 mm and one 10 mm long chirped gratings, which were written for alignment purposes of the scanning holographic set-up. From the result it was concluded that the central wavelength had to be shifted further to the short wavelength side.

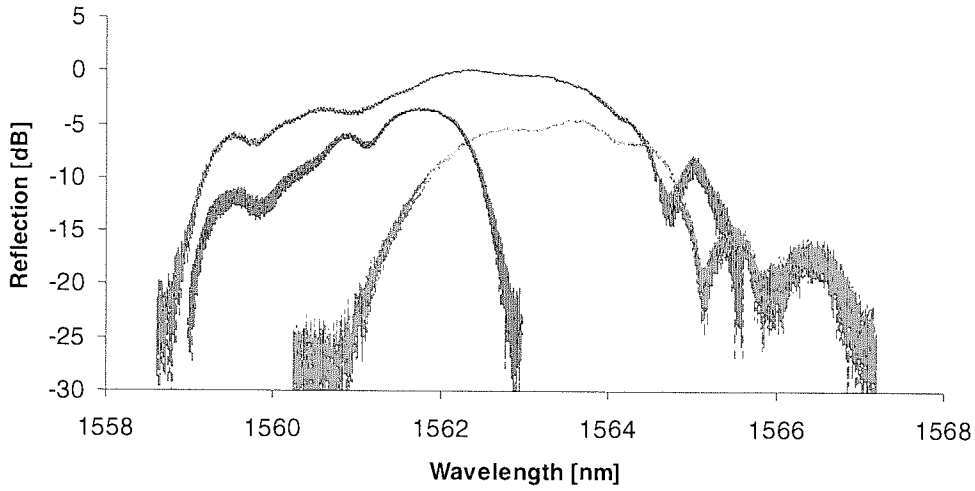

Figure 3.2-4: Spectra of test gratings written for alignment purposes of scanning holographic set-up

After the balancing procedure a set of three linearly chirped gratings of different length was written at 1560 nm wavelength using a cylindrical 2" phase mask with a chirp rate of 7.5 nm/cm. The central wavelength of the phase mask was 1544.4 nm. The applied wavelength was chosen to demonstrate the wavelength tunability without leaving the spectral range of the chromatic dispersion measurement facility at Aston University. Wavelength tuning was demonstrated for uniform and chirped gratings over a range from 780 nm to 1580 nm. The results from some of these gratings at lower wavelength are presented in ***Chapter 4.3***.

Figure 3.2-5 shows the transmission and reflection spectrum of a 7.5 mm long grating from this batch. The grating is 10 dB strong in transmission and the maximum power level of the reflected signal is only 0.6 dB below the reference level in transmission. At the short wavelength side the grating loss band abates gradually over a 10 nm wide region before the transmission power reaches the reference level. This effect was observed in a number but not all gratings and is probably due to a small tilt of the fibre during the writing process.

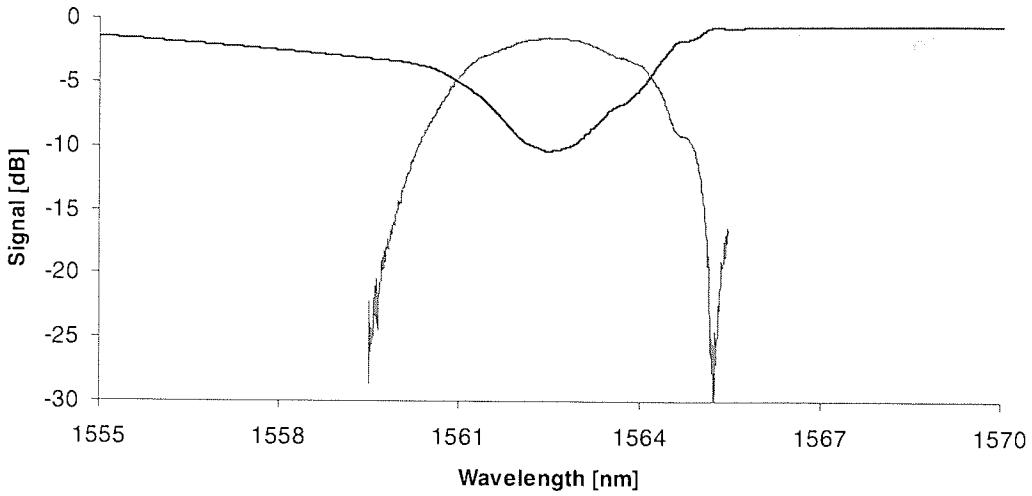

Figure 3.2-5: Transmission and reflection spectrum of 7.5 mm long chirped grating written with the scanning holographic set-up

3.2.5 Results

The reflection bandwidth and time delay curve of the above grating is compared to those from one 5 mm and one 10 mm long grating, shown in *Figure 3.2-6*. Apart from the change of length all other fabrication parameters were kept constant. It clearly shows that the bandwidth changes accordingly with the grating length, from 2.5 nm for the shortest grating to about 5 nm for the longest.

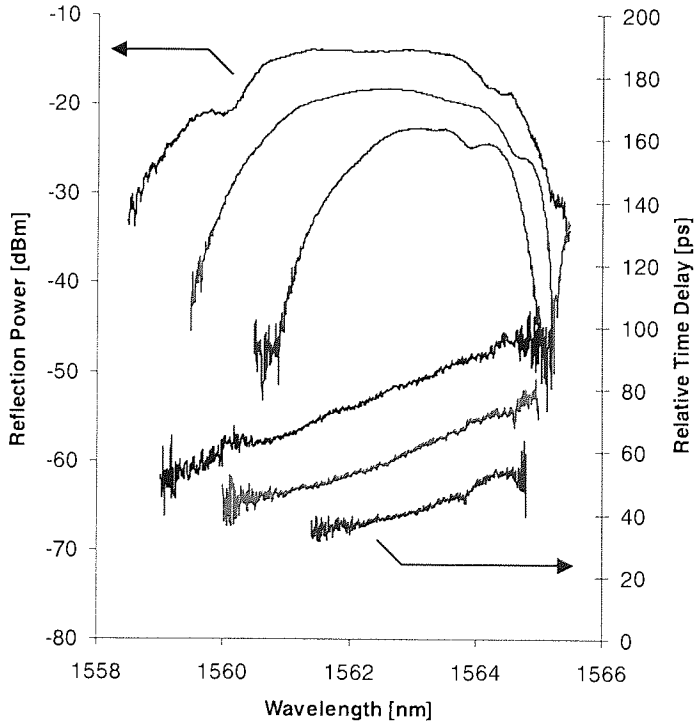

Figure 3.2-6: Reflection spectra and time delay curves of 5 mm, 7.5 mm and 10 mm long chirped gratings written by the scanning holographic method

The ripples on the time-delay curves are remarkably small, indicating the self-apodisation effect on the gratings. This feature is emphasised in *Figure 3.2-7*, which shows the reflection spectrum and time delay of the longest grating from above (a), compared to the spectra and time delay functions of a 5mm long conventionally fabricated grating with an added raised cosine apodisation profile (b) and a 10mm long non-apodised grating (c). In reflection, all these gratings are stronger than 25 dB and the slope of the time delay functions is 8.5±0.1 ps/nm.

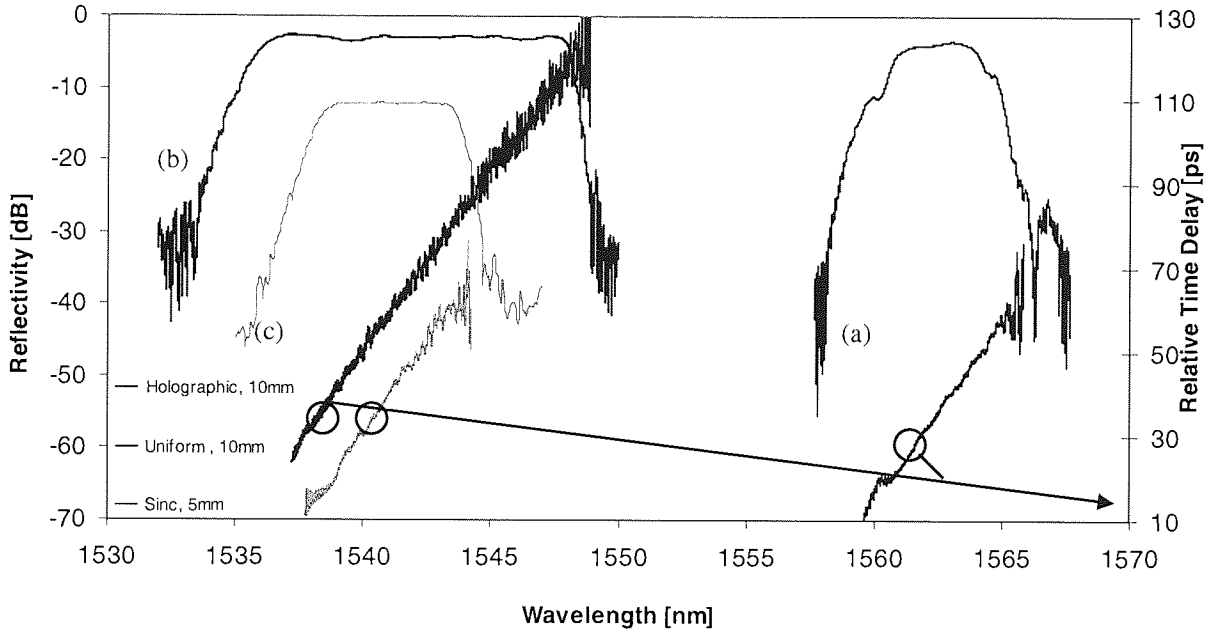

Figure 3.2-7: Reflection spectra and time delay curves of 10 mm long chirped grating written with the scanning holographic method in comparison to data obtained from 10 mm non-apodised chirped grating (b) and 5 mm sinc-apodised chirped grating (c)

Because of the apodisation of grating (a) and the shorter length of grating (c), the reflection bandwidth of their reflection spectra is narrowed compared to that of grating (b). The spectrum of (a) differs from the square shaped spectra of the conventionally written gratings. Looking at the time-delays, one can easily see that the intrinsically apodised grating (a) shows the smallest ripples, which are of a magnitude of around 2 ps. Grating (c) shows slightly larger ripple effect, with ripples up to 4 ps, whereas the ripples of the non-apodised grating (b) vary from 3 ps at the short wavelength–side to 6 ps at the long wavelength-side. One part of this effect can be attributed to the apodisation in the first two gratings. For the grating written with the scanning holographic method the fact that the grating is 10 dB weaker than the other two may also play a role.

3.2.6 Discussion and Conclusions

The presented results show the successful implementation of a novel hybrid phase-mask based holographic fabrication technique for the fabrication of uniform, chirped and apodised fibre Bragg gratings. In the previous sections the set-up, its working principles and the fabrication process with resulting grating spectra have been presented.

In accordance with the theoretical predictions intrinsically chirped gratings were fabricated using a chirped phase mask. The side-lobe suppression and low time delay ripples found in the gratings exemplify the apodisation effect and the grating bandwidths vary accordingly with the scan length applied to each grating.

It was not possible to simulate the spectra of the gratings written with the holographic method, because the overlap-function shown in *Figure 3.2-3* does not directly translate into the actual apodisation function. The power distribution along the beam diameter is not uniform, but of super-Gaussian shape. The refractive index change of the fibre is not necessarily linear with the beam fluence and as the tail of the one beam travelling ahead of the overlap section, a washing out effect of the photosensitivity in the fibre can be expected. Both effects can lead to a spectral narrowing of the grating because on a disproportionate refractive index change in the central section of the grating compared to the tails at both ends.

By changing the geometry of the set-up the grating wavelength could be changed and subsequently tuned with sub-nanometer precision. Using uniform or apodised phase masks with uniform period allows the fabrication of equivalent fibre gratings. A number of gratings fabricated using the presented set-up were successfully tested and used for various applications, which is shown in ***Chapter 4.3***.

3.3 Fabrication of apodised Planar Waveguide Gratings using the Polarisation Control Method

3.3.1 Introduction

During recent years planar waveguide gratings have become of great interest for various applications such as Mach-Zehnder Interferometers (MZI) based optical add-drop multiplexers in Wavelength Division Multiplexing (WDM) systems [*81*], optical filters [*82*], reflectors in external cavity semiconductor and Distributed Bragg Reflector (DBR) lasers [*83*]. These devices play an important role in modern optical telecommunication systems as tunable laser sources, add-drop multiplexers (OADMs) and optical cross-connects. Bragg gratings in integrated waveguides can be used as optical add-drop multiplexers to reduce the costs by avoiding expensive circulators in a FBG based WDM system [*84*].

Despite the fact that the fabrication methods for planar waveguide gratings are not yet as advanced as the techniques used for fiber Bragg gratings, planar waveguides are in direct competition with those. The main advantages of planar waveguide technology versus fiber-based devices are the high mechanical stability and the potential for dense packaging and mass-production.

As state of the art telecommunication systems require Bragg gratings of increasingly better quality, and higher complexity, in most cases fiber gratings are still the first choice to meet the defined specifications because of the flexibility given by standard fabrication methods. Apodisation is one important aspect of grating fabrication and for fiber gratings a large number of different techniques have been used [*59,64,85*] in order to reduce the channel spacing and interband cross-talk due to reflection side-lobes. At present, the most effective way to fabricate apodised planar waveguide gratings is the double-scan technique [*58*]. Presented here is the application of the polarisation control method for the fabrication of Gaussian apodised planar waveguide gratings, a single-scan technique that in future will allow the fabrication of advanced planar waveguide gratings with and without discrete phase-shifts.

3.3.2 Experimental Set-up

Although being a relatively new grating fabrication tool, the polarisation control method has been proven to be effective for the generation of complex grating structures [*86,87*]. It is based on the principle of two beams with tuneable power, which simultaneously inscribe two gratings with a π-phase shift into a fibre or waveguide. This can be achieved by splitting a circular polarised UV-beam into its *p*- and *s*-polarised fractions using a Wollaston prism. After geometrical considerations of the set-up, the condition to match a π-phase shift between the split beams can be summarised in a function of their divergence angle θ, the optical distance d_{tot} from the phase mask to the fibre core and the period of the refractive-index modulation, which is determined by the period of the phase mask Λ_{PM}. Suppression of one of the beam by control of a polarisation controller results in a grating written with full modulation depth, whereas the presence of both phase shifted beams of equal power at the same time results in the effective erasure of both simultaneously written gratings.

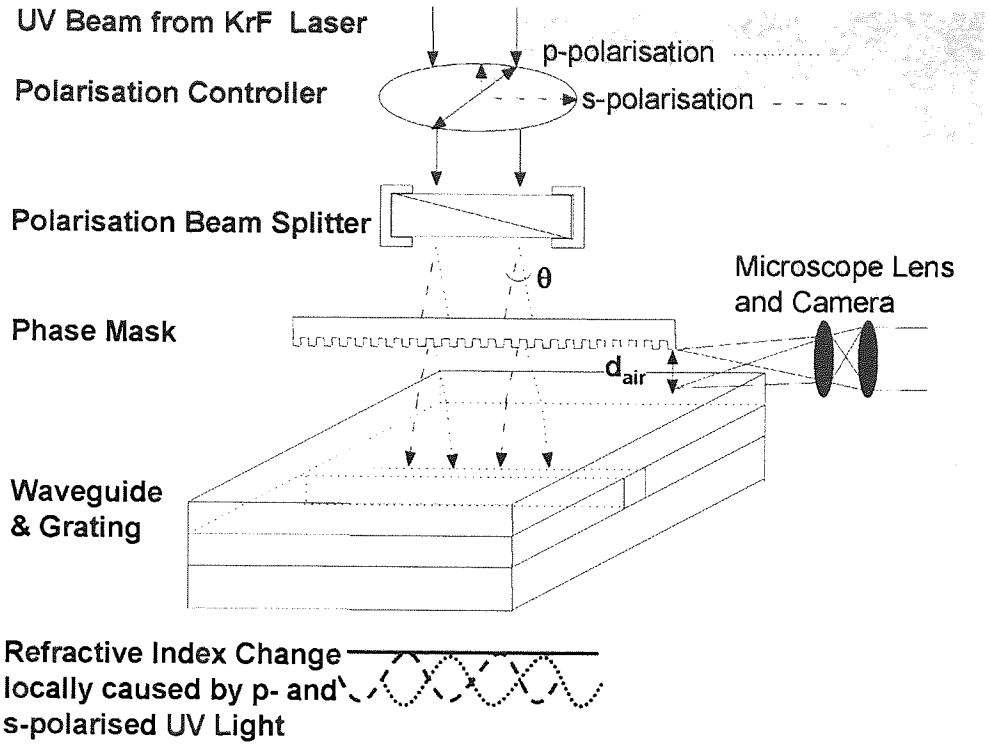

Figure 3.3-1: Polarisation control method set-up for fabrication of apodised planar waveguide gratings

A schematic of the set-up explaining its work principle is shown in *Figure 3.3-1*. In preliminary experiments, it has been shown that the accuracy for the alignment of the effective distance between waveguide and phase mask has to be within 1 μm.

Therefore a digital video camera with a microscope objective was used to establish the exact distance between waveguide and phase mask. The live image was projected on a TV screen, from which the gap between waveguide and its reflection from the lower phase mask surface was measured. The ratio of the physical distance to the image size was well-known at specific magnification levels. One such image, focused on the front edge of a chip is shown in *Figure 3.3-2*.

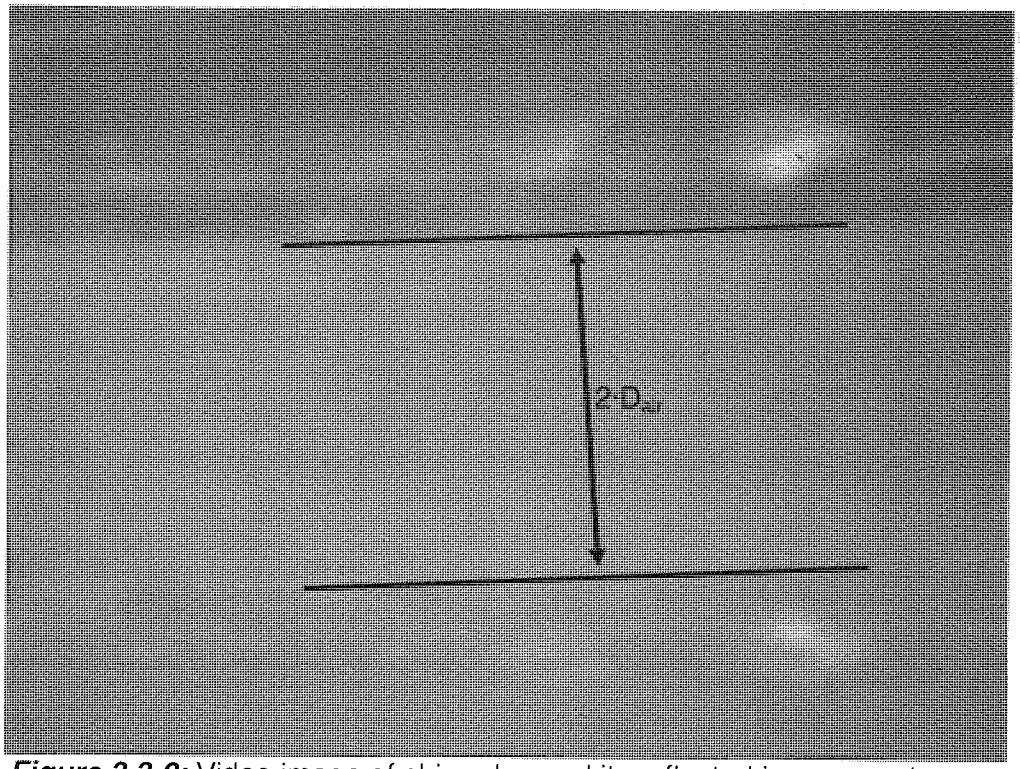

Figure 3.3-2: Video image of chip edge and its reflected image on phase mask surface used for alignment purposes

3.3.3 Operational Principle

In the case of an optical fibre, a first estimation of the required phase mask to core distance to achieve a π-phase shift between the beams of perpendicular polarisation in the core *Equation 3.3-1* can be used [*88*].

$$4\theta\left(d_{air}+\frac{d_{clad}}{n_{clad}}\right)=\Lambda_{PM} \quad \textbf{\textit{Equation 3.3-1}}$$

It needs to be pointed out that the optical distance consists of the distance that the light travels through air, d_{air}, and the effective distance across the fibre or waveguide cladding. The latter part is a function of cladding thickness d_{clad} and its refractive index n_{clad}. During the inscription process, the balance of the light power between the two light polarisation states can be tuned by setting the angle α of a Glan-Taylor polariser using computer control. If the reference angle is set correctly, at α=45° both gratings are written with the same light intensity, which yields a uniform refractive index change without modulation. This corresponds to a local π-phase shift in the grating. In the cases of α=0° and α=90° either of the polarisation states prevails completely with the other being fully suppressed, and a grating of maximum index modulation strength is written.

The resulting refractive index modulation of the gratings is described by *Equation 3.3-2* as a function of the waveguide photosensitivity (η), UV-fluence (F), scan position (z) and polariser angle (α).

$$\Delta n(z) = \eta F + \eta F \cos(2\alpha) \cos\left(\frac{2\pi z}{\Lambda_B} + \phi_0\right) \qquad \textbf{Equation 3.3-2}$$

The period of the index modulation profile is given by $\Lambda = \Lambda_{PM}/2$ and ϕ_0 is an arbitrary phase-offset.

Following *Equation 3.3-1* and the values in *Table 3.3-1*, the air gap d_{air} was calculated and set to 97 µm for the optical chips used. In the same way, as the full radius r_{fibre} is used for the calculation of the fibre cladding, the term d_{clad} includes half the core thickness of the waveguide.

	θ	r_{fibre}, d_{clad}	n_{clad} (248 nm)	Λ_{PM}	d_{air}
Fibre	0.14	62.5 µm	1.45	1070 nm	~ 66 µm
Waveguide	0.14	18.8 µm	1.45	1070 nm	~ 97 µm

Table 3.3-1: Optimal optical gap between phase mask and core for fibres and waveguides

3.3.4 Grating Fabrication

Two different types of waveguide chips have been used, one set provided by Ionas, a Photonics Technology company affiliated with the DTU, and a second one prepared by Haiyan Ou at the COM Research Institute itself. They were fabricated using a combination of UV-lithography reactive ion etching (RIE) and plasma-enhanced chemical vapour deposition (PCVD). The 5.5 x 5.5 µm waveguides were sandwiched between an 8 µm bottom and 16 µm top cladding layer. Their refractive indices at 244 nm were 1.4518 for the core and 1.4448 for the cladding layers. Photosensitivity was achieved by Deuterium loading at room temperature over a period of several weeks.

Unlike optical fibres, which can be aligned according to the transmitted diffraction pattern from the UV-laser projected on a screen, the means of aligning optical waveguides are more limited.

During alignment and UV exposure, the chip was fixed on a vacuum chuck. In a first step, the waveguide patterns were positioned parallel to the phase mask pattern by looking through the phase mask and aligning a reference waveguide with one edge of the phase mask area. *Figure 3.3-3* is a photograph showing the sample holder, phase mask mount and the assembly containing the Wollaston prism fixed on a motorised translation stage. First the beam is expanded using a telescope configuration, which is not shown in the image. Its final size and shape is the defined as it passes through two orthogonal sets of glass slits.

In two following steps, the chip surface had to be aligned parallel to the plane of the phase mask. For this the video camera was used, as shown in *Figure 3.3-2*. The chip edge at the

right hand side of the photograph was fixed first by comparing and levelling the chip to phase mask distance in an iterative procedure at two different points, using one of the two tilting stages at the phase mask holder. Once the first chip edge was put parallel, the procedure was repeated on the front edge. In this final step the gap between chip and phase mask was set to the appropriate value using a vertical translation stage.

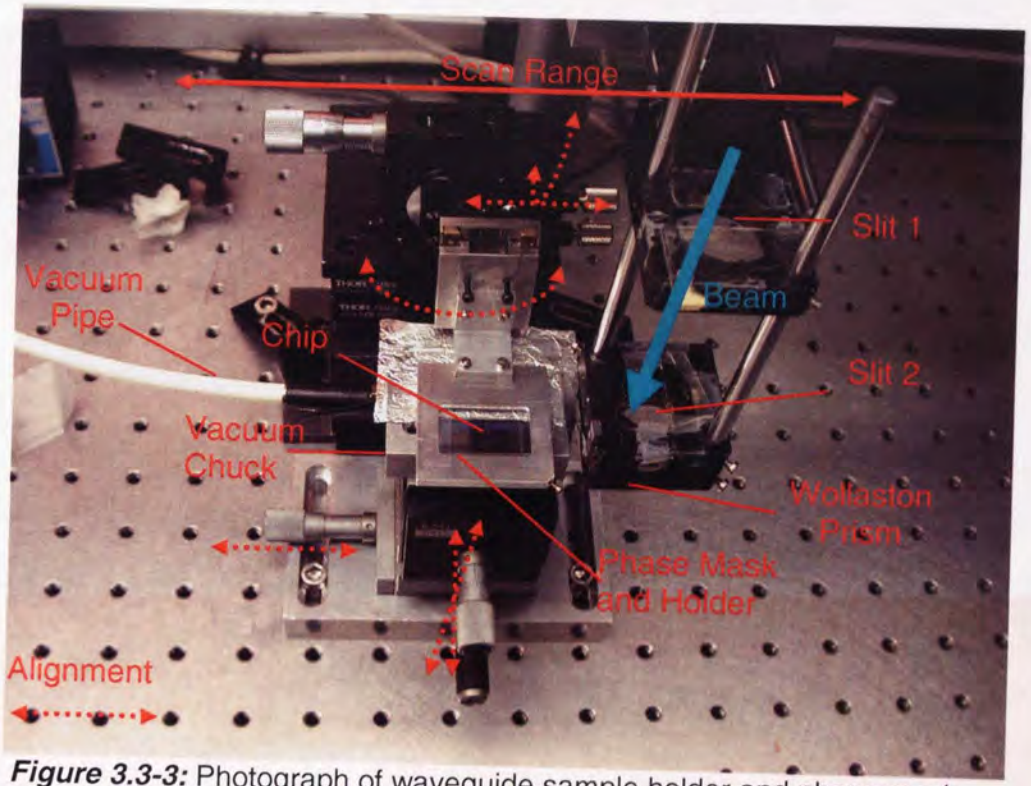

Figure 3.3-3: Photograph of waveguide sample holder and phase mask, demonstrating the alignment procedure

The expanded beam and the frame holding the two shaping slits are scanned by translation of a 45º mirror, which is not shown on the picture. For the sample alignment the phase mask is mounted on an x-translation stage and two orthogonal goniometer stages. The chip can be translated against the phase mask using three linear translation stages.

In a pre-alignment process, as described in the paper by Deyerl et al [*87*], the polariser angle was first reset to the exact point of origin at 45° to each of the polarisation states. The UV-source for the grating writing was a pulsed 248 nm KrF laser. The repetition rate could typically be set between 10 and 40 Hz. After equalisation of the quotient between *p*- and *s*-polarisation the output beam was collimated using a telescopic set-up comprising of four cylindrical lenses. The beam size was then further reduced and formed into a rectangle of approximately 6 x 0.7 mm by an aperture made from glass plates. This ensured an evenly distributed light power over the exposure area, which could cover 10-20 waveguides at one time. Before grating inscription the average pulse energy was measured and compared for different polarisation levels in order to set the total beam fluence of the exposure correctly.

The maximum tolerance for the deviation of energy between the polarisation states was set to be 2%.

3.3.5 Measurement Procedure

For characterisation all chips were placed on a vacuum chuck between two 3-dimensional linear manual translation stages, as shown in *Figure 3.3-4.*

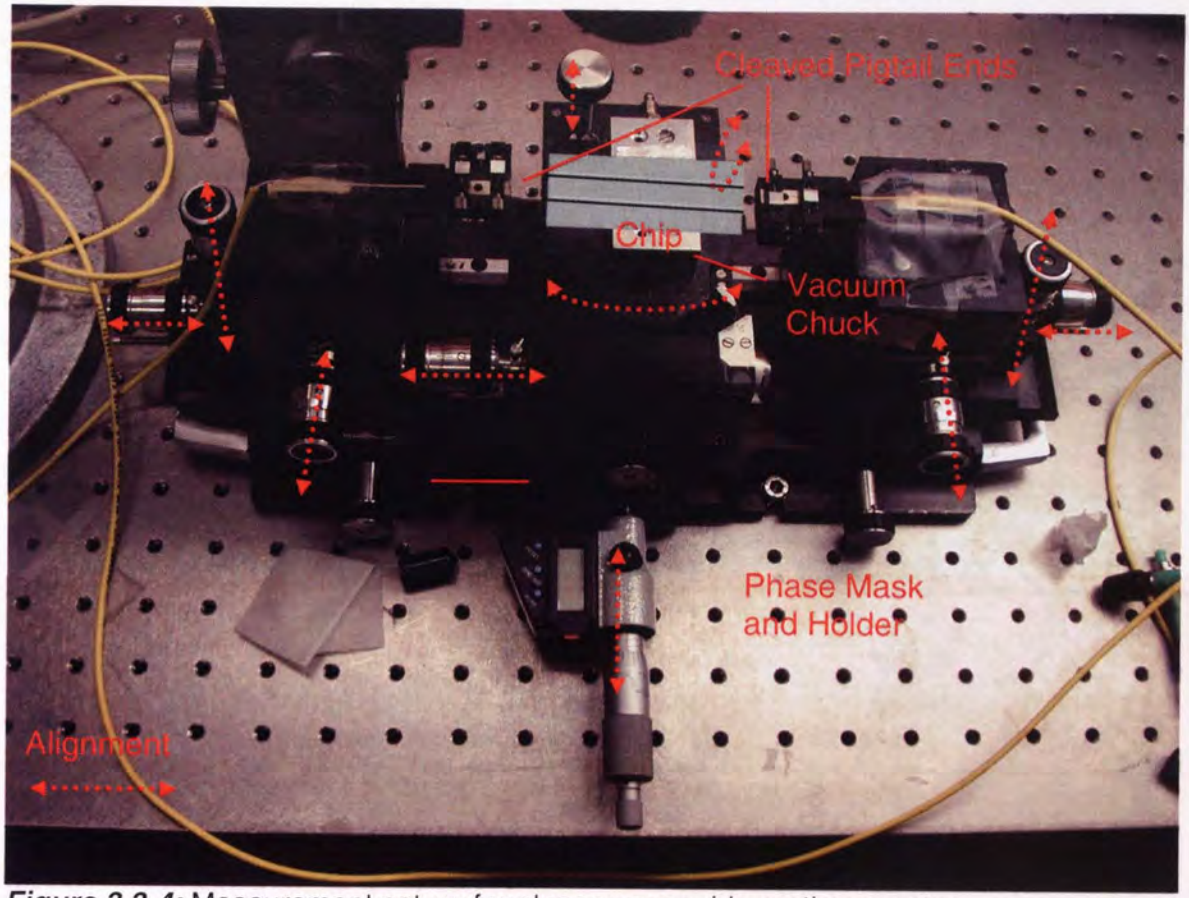

Figure 3.3-4: Measurement set-up for planar waveguide grating spectra

For coupling light into and out of the waveguides on the chip, the cleaved ends of two fibre pigtail cables were mounted in grooves on each of the translation towers. The chuck itself could be rotated in such a way to enable the waveguides to be aligned in line with the two pigtail ends which were finally brought into vicinity of the end facets of the waveguides, butt-coupling the light into the waveguide. In order to avoid the emergence of Fabry-Perot effects, between the fibre ends and waveguide end-facets, some index matching oil was added into the gap.

For the coarse alignment a 632 nm He-Ne laser was used. The alignment was finished by optimising the transmitted signal from an AQ 4321D tuneable laser to an AQ6317B optical spectrum analyser, both from Ando, with which the spectra were measured.

3.3.6 Results and discussion

With the described set-up planar waveguide Bragg gratings with different apodisation profiles were written. A first set of planar waveguide gratings was written with the phase mask placed on two different chips and no apodisation function applied. This was done to test the photosensitivity of the D_2 loaded chips and the quality of the gratings that can be written in waveguides of this kind.

The complexity of the task was then gradually increased with the fabrication of Gaussian and sinc-apodised grating.

The exact parameters used for the fabrication of all gratings presented here are given in *Table 3.3-2* alongside with the apodisation functions in *Equation 3.3-1* and *Equation 3.3-2*.

$$\exp\left[-\ln 2\left(\frac{2(z-L/2)}{A\cdot L}\right)^2\right] \qquad \textit{Equation 3.3-1}$$

$$\frac{\sin\left(\frac{2\pi(z-L/2)}{s\cdot L}\right)}{\left(\frac{2\pi(z-L/2)}{s\cdot L}\right)}\exp\left[-\ln 2\left(\frac{2(z-L/2)}{A\cdot L}\right)^2\right] \qquad \textit{Equation 3.3-2}$$

Grating	Length	Total Fluence	d_{air}	Gauss Factor	Sinc Factor
3.3-5	7 mm	2000 J/cm2	~ 0 µm		
3.3-6	14 mm	1500 J/cm2	~ 96 µm	A=0.45	
3.3-7	21 mm	1200 J/cm2	~ 111 µm	A=0.45	
3.3-8	16 mm	2000 J/cm2	~ 111 µm	A=7	s=0.25

Table 3.3-2: Fabrication Parameters of Planar Waveguide Gratings

3.3.6.1 Uniform Grating Fabrication

In *Figure 3.3-5* the transmission and reflection profiles of a uniform waveguide Bragg grating are shown and compared to the spectra obtained from numerical simulations using IFO Gratings 3.0.

The measured and calculated data are in good agreement for the transmission spectra, indicating that the polarisation state of the in-coupled light has been optimised using a polariser. For reflection the case is different, as some splitting of the experimental spectrum occurs, which could not be eliminated by changing the coupling condition between light source and waveguide.

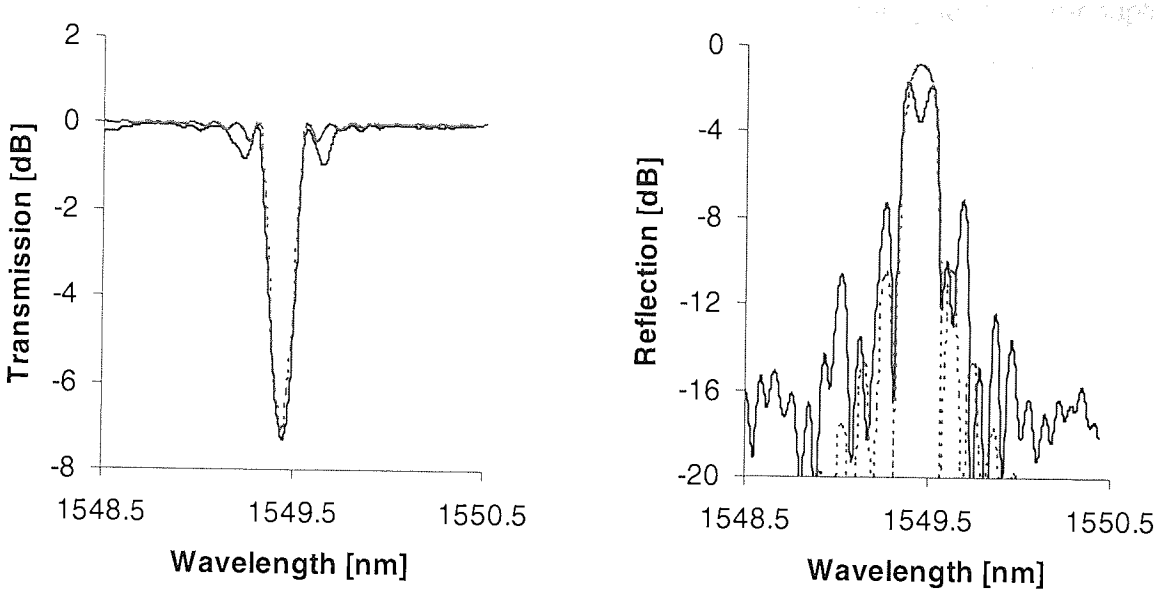

Figure 3.3-5: Measured (full line) and simulated (dotted line) of transmission (a) and reflection spectrum (b) of one uniform planar waveguide grating

Nevertheless the problem is likely to be an angle offset of the coupling condition or a birefringence effect. In general there is a good match between experimental and theoretical bandwidth, and the spectral position of side lobes, which in experiment appear to be larger than expected for both the transmission and reflection spectrum. The side lobe suppression in reflection is about -6 dB.

3.3.6.2 Gaussian Apodised Gratings

In accordance with the results of calculations made using *Equation 3.3-1* and *Table 3.3-1*, a first set of 14 mm long Gaussian apodised gratings was written into the waveguides of a chip. One of the resulting grating transmission spectra is shown in *Figure 3.3-6.*

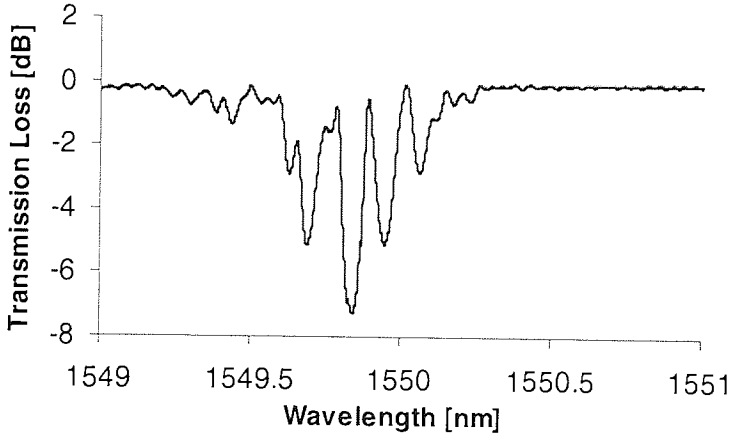

Figure 3.3-6: Transmission spectrum of Gaussian apodised planar waveguide grating fabricated under non-optimised alignment conditions

The quality of this spectrum could be enhanced neither by changing the in-coupling conditions, nor by manipulation of the polarisation of the light from the tunable laser.

The most obvious error source causing the splitting of the transmission spectrum is a wrong setting of the chip to phase mask distance d_{air}, resulting in the simultaneous writing of to arbitrarily offset gratings. For the writing of fibre Bragg gratings with the polarisation control method *Equation 3.3-1* gives a coarse value for d_{air}, which has to be determined more precisely in an experimental try-and error procedure [*87*].

Using a more intuitive approach by applying the rule-of-proportion rather than *Equation 3.3-1* for calculating d_{air} yielded a value of 111 µm instead of 96.5 µm, as used for the writing of the grating shown in *Figure 3.3-6*. It was assumed that for planar substrates the calculation of the optical path length perpendicular to the waveguide surface suffices. For the writing of apodised planar Bragg it appears that this approach is to be preferred to the one leading to *Equation 3.3-1*.

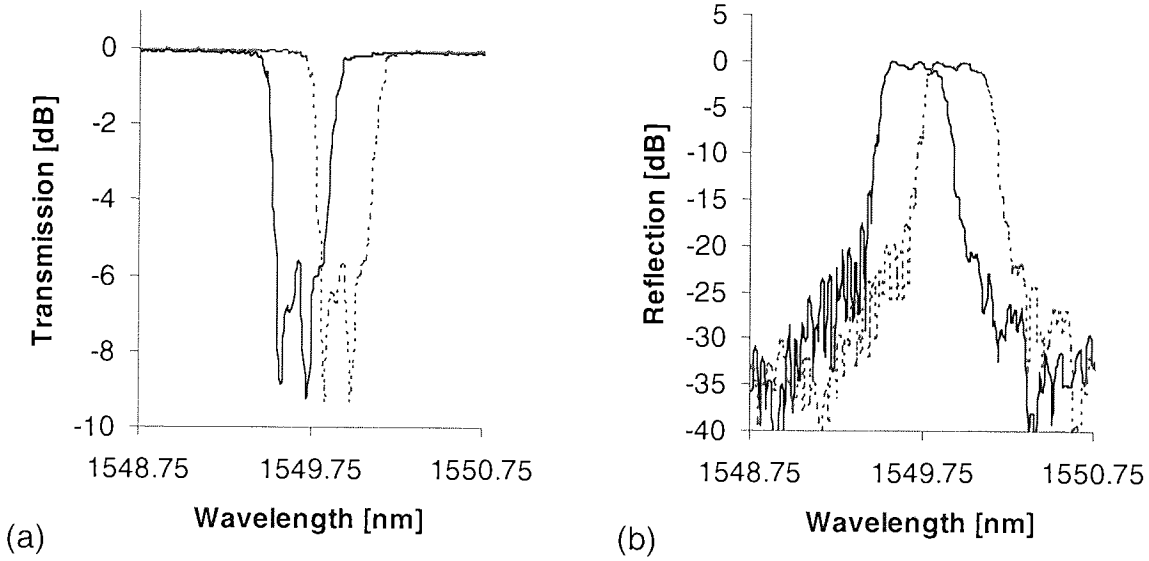

Figure 3.3-7: Transmission (a) and reflection spectrum (b) of Gaussian apodised planar waveguide grating for *p*- and *s*-polarised light

With the alignment set to this new value, the result obtained can be seen in *Figure 3.3-7*. It shows the spectrum of a 21 mm long Gaussian apodised planar waveguide grating.

By changing the polarisation state of the transmitted laser light it is possible to switch between two almost identical spectra separated by 0.27 nm, which indicates a birefringence of 7.4×10^{-5} between TE and TM mode. In reflection the successful side lobe reduction of below -20 dB could be proven.

Again a splitting of the spectrum was observed. The grating bandwidth of 0.2 nm is much higher than expected and calculated for a length of 21 mm. The dip in the transmission spectrum may be the result of a phase shift in the grating. The origins of this can be the inaccuracy of the gap set between phase mask and chip. Because of the limited number of

samples available it was not possible to perform an iterative pre-alignment in the same manner, as it is the standard for fibre Bragg grating fabrication. This is the more difficult, as the reference gratings that have to be written for the gap alignment are sinc-gratings with a number of phase-shifts. The writing of this type of gratings was planned as a step following the proof of principle on a single Gaussian grating. Although the exact refractive index change in the waveguide core is not known, the effect of a multi-mode spectral splitting is improbable, as it would show with larger wavelength separation.

Another flaw of the alignment procedure was the impracticality of measuring the gap at two points of each of the chip edges at the same time. When setting d_{air} under observation of the front edge it could happen that the chip tilts around the axis in the other dimension, resulting in the change of alignment distance in lateral dimension. The spectra taken from different waveguides on the same chip indicate that the gratings not only differ in strength due to a Gaussian envelope of beam power across the width of the scanned area, but often also significantly in quality.

Also a possible source of grating errors is the effect of back-reflections of the UV-beam from the planar bottom cladding into the core – a problem, which does not occur when working with fibres. If this adverse effect can be proven to happen, this problem can be addressed by incorporating an UV-absorptive layer below the bottom cladding during the fabrication of the waveguide chips.

By varying the gap d_{air} around the value used for the grating in *Figure 3.3-7* for subsequent samples it was tried to increase the accuracy of the alignment. However none of the experiments succeeded in writing gratings of a better quality, than the one shown above. Mainly the reasons therefore could be as described before.

A further unknown factor is the photosensitivity of the waveguide core. In theory, a large increase in refractive index could effect the transition from a single-mode waveguide to a multimode guiding condition, although this case is rather unlikely.

3.3.6.3 Sinc-Apodised Gratings

Besides uniform and Gaussian grating profiles, a sinc apodisation was applied during the writing of one planar Bragg grating set. The result is shown in *Figure 3.3-8*.

This grating was 16 mm long and has a Gaussian taper function superimposed over the sinc-apodisation profile. Like in the cases before, its profile also shows an asymmetric double peak. As known from the alignment procedure to determine the set points for polariser angle θ and d_{air}, a misalignment of θ leads to a well-centred peak or dip in the reflection spectrum, whereas d_{air} has a direct impact on the symmetry of the spectrum. The results from the grating shown are inconclusive because with 2 dB in transmission the grating is too weak and the side-lobe suppression in reflection is only 7 dB.

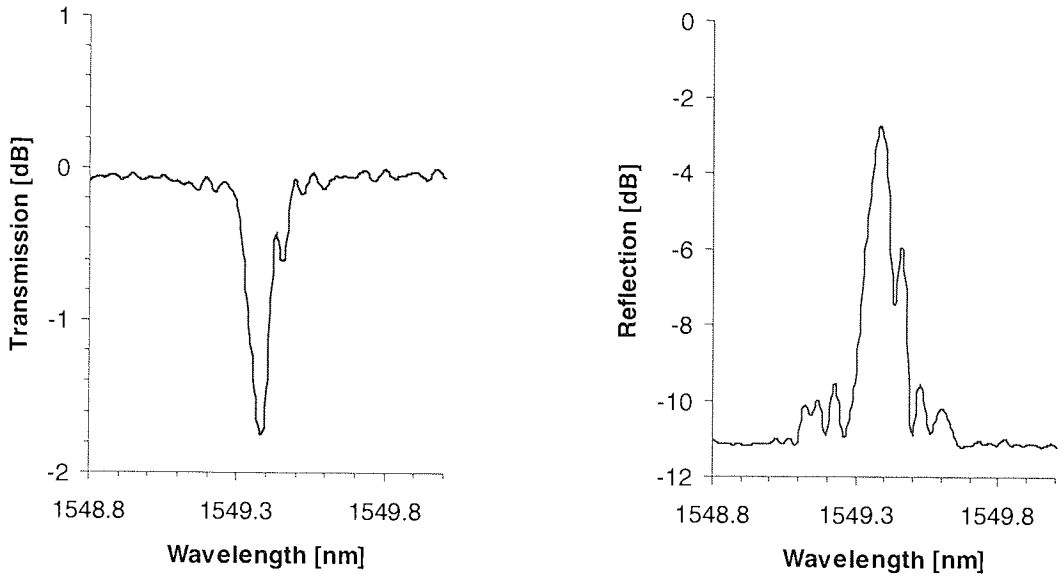

Figure 3.3-8: Transmission (a) and reflection spectrum (b) of sinc-apodised planar waveguide grating

3.3.6.4 Conclusions and Future Work

With the presented work it has been shown that the polarisation control method can be transferred from fibre technology to the fabrication of apodised planar waveguide gratings with considerably suppressed sidelobes in their reflection spectrum.

Uniform gratings and gratings with Gaussian and sinc apodisation profiles were written in buried germanium-silicate waveguides and their spectra compared to each other. In the Gaussian gratings the reflection sidelobes were successfully reduced to 14 dB less than those in the uniform gratings.

By changing between the *p*- and *s*-polarisation of the probing laser light the peak splitting of the Gaussian apodised grating spectra could be observed due to the birefringence of the waveguide. However, the grating bandwidth could not be matched with the expected value predicted by coupled mode theory. Possible reasons for this discrepancy may be inaccuracies in the setting of the optical gap between phase mask and waveguide and back-reflected light from the planar bottom cladding. This error can result in a tilt of the chip around an axis alongside the waveguides and the fact the necessity to determine a new formalism for calculating the correct value for planar geometries. The second error source can be eliminated by applying an anti-reflective bottom cladding for UV light.

Despite the observation of a reduced side-lobe effect, the results for sinc-apodised gratings were inconclusive because of their weak filter response and quality. Although the fabrication of sinc-gratings is more complex than the one for Gaussian apodised gratings, further results may yield the correct relation for setting the air gap between phase mask and chip surface, as sinc-gratings are used for the fine tuning of that distance for fibre grating fabrication.

3.4 Integrated Photonics Circuits

3.4.1 Introduction

Advancements in planar waveguide technology as presented in the previous chapter are only the first step towards the application of integrated photonics circuits in a wide range of applications. The potential for the telecoms sector has briefly been noted in ***Chapter 3.3.1***, where one of the main advantages is the simplicity of producing on-chip couplers, modulators and multiplexers [*89*].

The development of logic circuits fulfilling the tasks of nowadays-electronic chips is a long-term goal for the years to come [*90*]. Recent research shifts the emphasis more and more towards the newer field of chemical and bio sensing [*91*].

For all the mentioned applications one of the main arguments for planar optics is the miniaturisation due to integration, the possibility of guiding light over very small curvatures and the intrinsically high degree of mechanical stability, especially with respect to interferometric applications.

In collaboration with Indigo Photonics (now Insensys), first efforts have been made to have one foot in the door leading to this novel field of technology and research. Bragg gratings were written in planar samples containing a number of highly germanium doped buried waveguides with different geometries, which were subsequently tested.

3.4.2 Grating Fabrication

The optical chips provided by Indigo Photonics contained a number of single-mode and multimode waveguides that were fabricated using a standard combination of lithography with reactive ion etching (RIE) and plasma enhanced chemical vapour deposition (PECVD) techniques. The waveguide layer was about 6 μm thick and the width of the waveguides varied between 6 μm and 1 mm. Besides bunches of straight waveguides with different widths, some waveguides were bent, resulting in a lateral displacement of the outputs of 2-3 mm along the 20 mm long chip.

Similar to the fabrication of uniform gratings as described in ***Chapter 3.3.4***, the waveguide chip was stuck and aligned on a surface parallel to the phase mask and finally brought in a near contact position. A beam was then scanned along the phase mask pattern, inscribing gratings in several parallel waveguides simultaneously. Attention was given to expose only a straight part of the bent waveguides.

Gratings were written in both hydrogenated and non-hydrogenated samples, which was possible due to the high germanium content of the waveguide core.

3.4.3 Results and Discussion

Measurements on the gratings were taken using a set-up similar to the one introduced in ***Chapter 3.3-5***. The main differences are the fact, that instead of butt-coupling pigtail fibres to the waveguide facets, a free-beam approach was used. Light from a broadband or laser light source was coupled into the waveguides using a ball-lens patch-cord fibre and the out-coupling into a standard patch cord was done using a telescope set-up comprising of two microscope objectives. For the coarse alignment a visible He-Ne laser was used and after that the coupling conditions were optimised for infrared conditions using a broadband light source and a tuneable laser.

One result for grating inscription in a non-hydrogenated sample is shown in *Figure 3.4-1*. The graph shows a grating with a 1.1 dB transmission loss band and the equivalent reflection measured using a non-normalised spectrum from a broad-band light source.

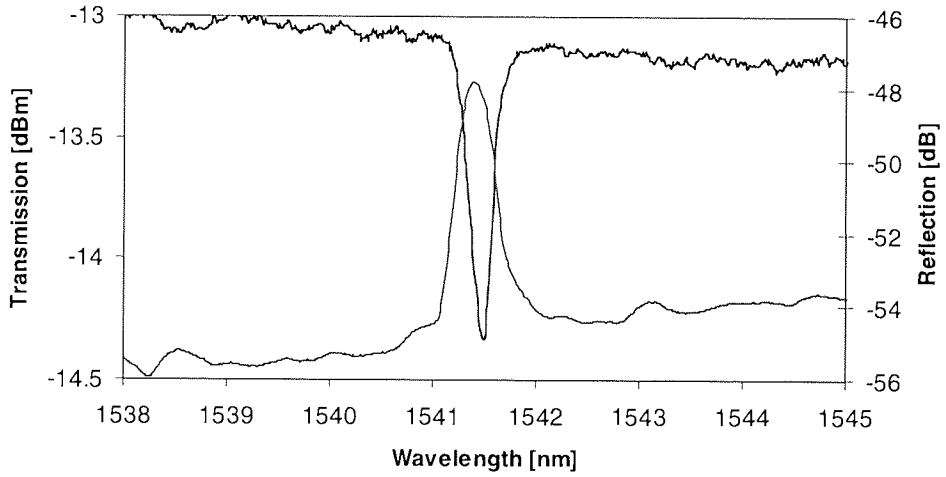

Figure 3.4-1: Transmission and reflection of Bragg grating written in non-hydrogenated germanium-doped planar waveguide

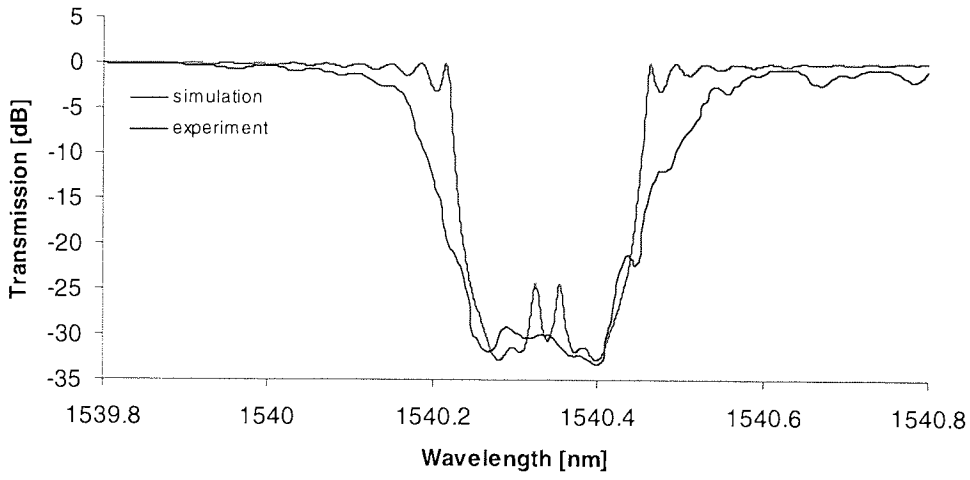

Figure 3.4-2: Measured and simulated transmission spectrum of Bragg grating written in hydrogenated waveguide

The effect of increasing the waveguide photosensitivity by hydrogen loading becomes apparent in *Figure 3.4-2*, showing a waveguide grating of over 30 dB in transmission. A simulated spectrum is overlaid, which was calculated using the parameters of the waveguide and grating and is in fair agreement with the measured spectrum. In the calculation orthogonal linear and circular light polarisation states were considered. Again, peak splitting is observed due to the high birefringence in the waveguide of oblong cross-section.

3.4.4 Conclusions and Future Work

The successful inscription and characterization of Bragg gratings in curved waveguides is presented. Test chips were provided with a variety of linear and curved highly germanium doped waveguides, in which the gratings were written after and without hydrogenation. Good wave-guiding properties were found in samples with curvatures of radii of about 6 mm. This is to highlight the feasibility of both the waveguide design as such as well as the grating inscription in these.

The next step to follow is the design and fabrication of waveguides and gratings for specific purposes. One possibility is the direct writing of waveguides in photosensitive planar substrates by focused UV-illumination at Aston University [*92*] or the purchase of specially designed waveguide chips from manufacturers using this technique or conventional methods involving lithography and PECVD.

3.5 Definition of High Resolution Limits of Grating Writing Techniques Using Optical Frequency Domain Reflectometry

Since the first steps in UV grating writing, inscription methods and grating designs have become more and more complex. Some standard writing set-ups for advanced Bragg grating fabrication in fibres and optical waveguides have been introduced in *Chapter 2* and the sections preceding this paragraph show some of the latest results in the development and improvement of fabrication techniques. Greatest attention has to be paid to the fabrication process. The resulting spectra and dispersion measurements of such gratings give a first indicator to the grating quality. As with increasing complexity the number of possible error sources increases, even slight perturbations in index modulation, phase errors or inaccuracies in the phase-mask used can manifest with great effect. It is therefore important to know the actual refractive index envelope and local periodicity of the grating, as well as the precise positions of induced phase-shifts. To eliminate error sources in the fabrication process, occurring errors have to be localised and their nature identified.

Optical reflectometry methods offer a powerful tool to measure local coupling strength and grating phase inside of fibre Bragg gratings with the highest possible resolution to date [*93,94*].

A number of gratings with complex apodisation profiles including multiple phase shifts of short separation lengths were fabricated using different writing techniques and tested using Optical Frequency Domain Reflectometry (OFDR). The results help to gain insight into the actual grating structure inside the fibre and to identify the strengths and weaknesses of the grating writing methods.

3.5.1 Introduction and Methodology

Advanced fibre Bragg gratings are used in a multitude of applications in the telecommunications sector, especially in high bit-rate transmission links and network nodes, as spectral filters for dense wavelength division multiplexing (DWDM) [*95*], chromatic dispersion compensation [*72,96*] and coding/encoding elements [*97*], pulse shaping [*98*], pulse width-suppression [*73*], wavelength selection [*74*], gain equalisation [75] and switching [*99*].

The efforts made by the present-day optical telecommunication industry in order to increase the efficiency in bandwidth utilisation and bit rates on our data highways and so to satisfy constantly soaring customer demand requires the application of increasingly complex electro-optical components and devices, and in particular grating designs, which must fulfil strictest specifications for optimal system performance.

Cross-talk between neighbouring transmission channels can greatly be reduced and the network bandwidth increased by using apodised grating filters. A multitude of different techniques for grating apodisation have successfully been presented in the past [*57,58*]. Of particular interest are techniques, which in addition offer the application of discrete phase-shifts with high position accuracy [*61,64,65,87,100*]. The realisation of sophisticated grating by use of these methods enables spectral shaping of the grating response for high bandwidth utilisation of the actual grating channel band and the fabrication of arbitrary dispersion profiles, as in low dispersion gratings for WDM filters [*101*] or for the generation of distinctive pulse formats or for encoding/decoding applications [*79*]. An example for the latter is presented in ***Chapter 4.3*** of this thesis.

The gratings tested in this project were fabricated using the Polarisation Control Method (PCM) at the DTU Lyngby and an advanced Multiple Printing in Fibre (MPF) method developed by Indigo Photonics (now Insensys) at Aston University based on a previously presented technique [*61*], in which arbitrary apodisation functions in gratings of unlimited length can be achieved by a controlled phase mask to fibre translation using synchronised UV pulses.

With each of the set-ups grating sets were written applying identical apodisation functions. These included Gaussian, sinc and a generic advanced apodisation format developed for the fabrication of fibre Bragg gratings of very low dispersion in the reflection band. The functional principle of the first grating is based on tailoring the local coupling coefficient only, whereas the two latter include up to ten π-phase shifts over their length.

Finally, for the grating characterisation, optical frequency domain reflectometry (OFDR) and optical low-coherence reflectometry (OLCR) [*94*] were used. The measurements were taken by Sven Kieckbusch and Christian Knothe the TUHH in Hamburg in the first case, and by Philippe Giaccari, Daniele Costantini and Dragan Ćorić at the EPFL in Lausanne as part of the ODUPE collaboration project.

First the gratings written with the polarisation control method were measured with the set-ups available at both institutes. This was done as a comparative study to determine the consistency of data obtained from the different approaches.

In a second step, the duplicate grating set fabricated with the sampling method were tested using the OFDR set-up only, to give a direct survey of the two writing methods.

Presented here are only results obtained from the OFDR measurements, as the raw data from the OLCR experiments were not made available. However, the results obtained with both methods were found to be in good agreement and a comparison study may still be published in the near future [*102*].

3.5.2 Measurement of local Coupling Coefficient and Grating Phase Shifts

One of the first approaches to measure the local coupling coefficients in gratings was the side diffraction method by Krug [*103*]. There, a He-Ne beam is focussed in and scanned along the fibre core containing a Bragg or long period grating. Because of the refractive index perturbation the beam will be diffracted. Depending on the angle of incidence with respect to the fibre axis and the strength and period of index modulation, the power of the angular power distribution of the diffracted beam measured at the other side of the fibre will vary.

Obvious downsides of this transversal beam set-up are difficulties of alignment and the restriction on measurements of coupling coefficients only, not including the possibility to obtain the grating phase.

In recent time techniques for the experimental determination of local complex coupling coefficients in waveguide gratings have greatly advanced thanks to the use of improved OFDR and OLCR measurement techniques and novel inverse scattering algorithms and layer-peeling methods [*104,105*], substituting the side-diffraction method and optical time domain reflectometry (OTDR) [*106*]. The latter method soon reached its limitations in

measurement accuracy due to the ultra-short pulses and time spans that needed to be measured with very high accuracy.

Both OFDR and OLCR are in-fibre solutions, meaning that the probing light is launched in the core of the fibre to be tested and therefore easier to control than transversal methods.

3.5.2.1 Optical Frequency Domain Reflectometry

The OFDR measurement set-up based on a double in-fibre Mach-Zehnder interferometer configuration using one tunable laser source (TLS) , as described by Kieckbusch [*93*]. The set-up is shown in *Figure 3.5-1*.

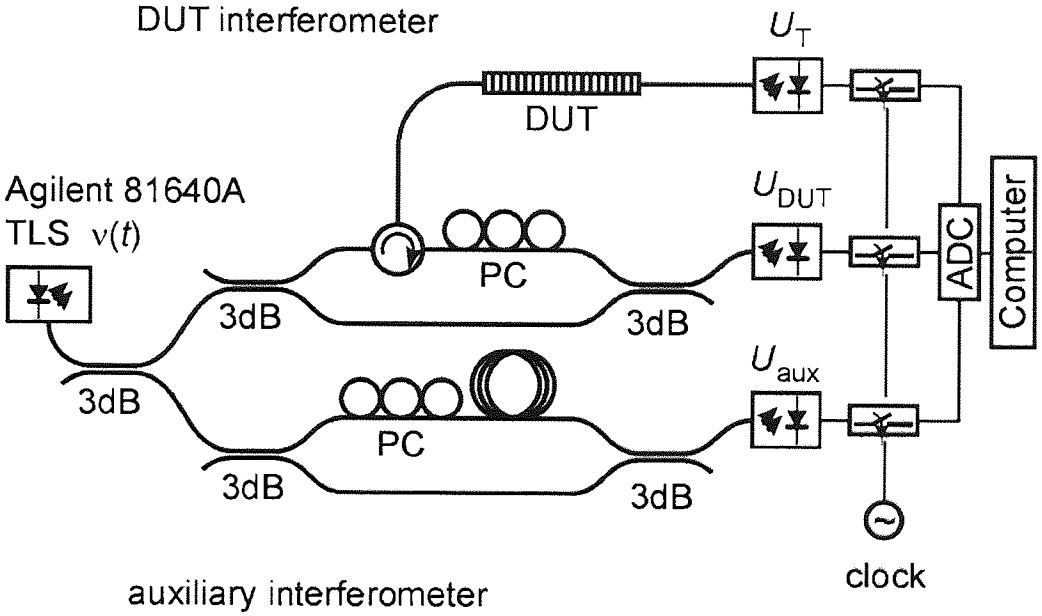

Figure 3.5-1: Set-up for fibre grating characterisation based on OFDR, taken from [*87*]

Shown in the set-up are five 3dB couplers, one circulator, two polarisation controllers (PC), three photo detectors (U_T, U_{DUT}, U_{aux}) and switches, an analogue to digital converter (ADC) and a computer. In the present case the device-under-test (DUT) is a fibre grating, but can be any device with spatially distributed reflection sites.

The main interferometer consists of the test arm with an optical circulator to which the grating under test is spliced, and a reference arm. During a measurement the TLS sweeps linearly over a wavelength range of 40 nm centred at the Bragg grating wavelength of the DUT with a rate of 40 nm/s. Any light reflected from the DUT is fed-back into the interferometer with a certain time-delay τ, equivalent to the position of the reflection site in the grating, and interferes at the output with the non-retarded wave from the reference arm due to the resulting phase offset. The detector measures the incoming oscillating signal with a sampling rate of typically 1-5 MHz.

To compensate for any non-linearity of the wavelength sweep, a secondary interferometer serves as a reference. It introduces an arbitrary and constant shift of optical path length in

one interferometer arm. An additional detector measures the time dependent signal of the interference signal coming from this output, providing the data for a function to eradicate errors in the main measurement. For calibration purposes a third detector measures the signal transmitted through the DUT. All three detectors are sampled using the same clock.
The main advantage of this method over OLCR is the high degree of system integration. All components are fibre based and no mechanical translation is required for the system tuning. The measurement of both, coupling coefficient and grating phase requires a single light source only and the measurement time is reduced significantly. The power of the light source also enables the characterisation of stronger gratings than OLCR.

3.5.2.2 Theoretical Principle

A fibre Bragg grating is completely defined by its refractive index modulation $n(z)$ or complex coupling coefficient $\kappa(z)$. An alternative formalism is the complex reflectivity responses $r(\nu)$ or $h(\tau)$. Both are equivalent because each is the Fourier transform of the other, translating from frequency domain into time domain and vice versa. The complex coupling coefficient $\kappa(z)$ can be obtained from $r(\nu)$ by applying a layer-peeling method. Due to their functional principle the OLCR method provides reflectivity data in the time domain and OFDR in the frequency domain, where ν directly corresponds to the light frequency at the output of the TLS.
Starting from an initial value ν_0, during the measurement the frequency $\nu(t)$ of the signal from the TLS is sweeping in time t across the central wavelength of the grating with a rate $\gamma(t)$, as shown in *Equation 3.5-1*.

$$\nu(t) = \nu_0 + \gamma(t) \qquad \textbf{Equation 3.5-1}$$

The time dependent optical field during the measurement can therefore be written as a function of optical frequency $\nu(t)$ and amplitude a_0:

$$a_0(t) = |a_0| e^{j2\pi\left[\nu_0 + \frac{\gamma}{2}t\right]t} \qquad \textbf{Equation 3.5-2}$$

Following *Equation 3.5-3*, in which λ is the central wavelength of the grating and n_{eff} the effective refractive index of the waveguide core for that specific mode and wavelength, a total sweep range of $\Delta\lambda$=40 nm automatically results in a longitudinal measurement accuracy of δz=20 µm [*107*].

$$\delta z \approx \lambda^2 / (2 n_{eff} \Delta\lambda) \qquad \textbf{Equation 3.5-3}$$

The measured intensity of the signal at the main detector in the interferometer is a superposition of the directly transmitted light wave with the retarded reflection from specific reflection sites inside the grating. For M reflection sites distributed over the length of the fibre

grating, the time dependent photo-detector signal can be formulated according to [*107*] as follows:

$$U_{PD}(t) = \sigma \left| a_0(t) + \sum_{m=1}^{M} r_{eff}^{m}\, a_0(t-\tau_m) \right|^2 \qquad \textit{Equation 3.5-4}$$

In this function, *m* is the index of each site with effective reflectivity *r* and corresponding time delay τ, and σ is the conversion efficiency factor of the detector.

Squaring the above function after insertion of *Equation 3.5-2* and out-factoring $U_0 = \sigma |a_0|^2$ yields the following result:

$$U_{PD}(t) = U_0 \left[1 + \sum_{m=1}^{M} \left| r_{eff}^{m} \right|^2 + 2 \sum_{m=1}^{M} \left| r_{eff}^{m} \right| \cos(2\pi\gamma\tau_m t + \phi_m) \right] \qquad \textit{Equation 3.5-5}$$

For the grating reconstruction only the oscillating part of the function is of interest, which includes the constant phase terms ϕ_m. Instead of using a time-dependent formalism, the oscillating term can easily be described as a frequency-dependent function, using *Equation 3.5-1*.

$$\tilde{U}(t) = 2U_0 \sum_{m=1}^{M} \left| r_{eff}^{m} \right| \cos(2\pi\nu\tau_m t + \Psi_m) \qquad \textit{Equation 3.5-6}$$

The impulse response is derived from Fourier transformation of this term.

$$h(\tau) = \int_{-\infty}^{\infty} \tilde{U}(\nu) e^{j2\pi\nu\tau} d\nu \qquad \textit{Equation 3.5-7}$$

For weak gratings, a second Fourier transformation into the spatial regime *h(z)* yields a good approximation of the complex coupling coefficient $\kappa(z)$, in the general case however, a layer peeling algorithm has to be applied.

Written in the form, as in *Equation 3.5-8*, it contains information on both, local coupling strength and grating phase.

$$\kappa(z) = |\kappa(z)| e^{j\phi_\kappa(z)} \qquad \textit{Equation 3.5-8}$$

3.5.3 Grating Fabrication

3.5.3.1 Polarisation Control Method

Using the Polarisation Control Method, three sets of grating pairs have been fabricated comprising of a Gaussian, a sinc-function and an apodisation profile developed and provided by Dr. L. Poladian and Dr. S. J. Madden from AOFR Pty. Ltd. (ADC Australia), which in the following will be referred to as the ADC format.

A KrF laser with an output at 248 nm was used as UV source, illuminating a hydrogenated highly non-linear fibre (HNLF) from OFS Denmark through uniform phase

masks from Ibsen, which were 23 mm and 50 mm long and had periods of Λ_{PM}=1073 nm and Λ_{PM} =1063 nm, respectively.

The Gaussian and sinc-shaped gratings were specifically produced for being tested using the presented OFDR and OLCR set-ups. Their reflectivity is between 6 and 13.5 dB, and all four were 23mm long.

The value of the *m*-parameter of the Gaussian apodisation function was chosen to be 0.4 in the case of purely Gaussian apodised gratings. A Gaussian shaped apodisation does not introduce any phase-shifts into the resulting gratings.

Over the apodisation profile of the sinc-gratings, a Gaussian taper function has been superimposed and the factor 7 was chosen for this function. For the function sinc-apodisation itself an *s*-factor of 0.167 was chosen, resulting in 10 phase-shifts distributed along the grating length.

As the third type of test gratings the previously introduced ADC design was chosen. To be used for these specific purposes, one ADC grating is 20mm long and 27 dB strong in transmission. Shown here is another ADC grating, which is 46mm long and shows a transmission dip of 23 dB.

This design shows a highly asymmetric apodisation in both strength of the coupling coefficient, as well as the distribution of the 7 phase-shifts along its length.

Because of its complex dynamics and high sensitivity to slightest phase errors, it puts both fabrication methods and the characterisation tools to the test. Results from tests of these gratings within a WDM system are presented in ***Chapter 4.2***.

The exact grating parameters and apodisation functions are displayed in *Table 3.5-1.* In the functions *L* denotes the total length of the grating and *x* any chosen position inside the grating.

Grating	Length [mm]	Phase Mask Period Λ [nm]	Transmission Loss [dB]	Index Modulation Δn_{mod}	Apodisation Function
PCM 1	23	1069	9.6	1.36×10^{-4}	$\kappa_{Gauss} = \exp\left(-\ln 2\left(\frac{2x-L}{mL}\right)^2\right)$
PCM 2	23	1073	11.5	1.72×10^{-4}	$\kappa_{Gauss} = \exp\left(-\ln 2\left(\frac{2x-L}{mL}\right)^2\right)$
PCM 3	23	1069	9.0	5.80×10^{-4}	$\kappa_{Sinc} = \sin c\left(2\pi\frac{x-\frac{L}{2}}{sL}\right)\cdot\exp\left(2\frac{x-\frac{L}{2}}{mL}\right)$
PCM 4	23	1069	6.7	5.30×10^{-4}	$\kappa_{Sinc} = \sin c\left(2\pi\frac{x-\frac{L}{2}}{sL}\right)\cdot\exp\left(2\frac{x-\frac{L}{2}}{mL}\right)$
PCM 5	46	1069	23.0	3.25×10^{-4}	ADC

Table 3.5-1: Parameters for Gratings written with the Polarisation Control Method

The value for the refractive index modulation shown as Δn_{mod} was obtained by matching the measured spectra to ones that were numerically calculated using IFO Gratings 3.0 [*108*]. The measured grating spectra are shown in the following chapter in direct comparison to the reconstructed spectra.

3.5.3.2 Grating Fabrication using Multiple Printing in Fibre (MPF) Method

A set of identical gratings as those described above was fabricated in SM 28 fibre using the multiple printing in fibre (MPF) method, as described in ***Chapter 2.5.3***, and were provided by Andrew Gillooly and John Mitchell from Aston University. The phase masks employed had periods of Λ_{PM}=1068.6 nm and 1070.0 nm.

Grating	Length [mm]	Phase Mask Period Λ [nm]	Transmission Loss [dB]	Index Modulation Δn_{mod}	Apodisation Function
MPF 1	23	1068.6	7.5	1.22×10^{-4}	$\kappa_{Gauss} = \exp\left(-\ln 2\left(\frac{2x-L}{mL}\right)^2\right)$
MPF 2	23	1068.6	8.5	1.31×10^{-4}	$\kappa_{Gauss} = \exp\left(-\ln 2\left(\frac{2x-L}{mL}\right)^2\right)$
MPF 3	23	1070.0	5.0	4.20×10^{-4}	$\kappa_{Sinc} = \sin c\left(2\pi\frac{x-\frac{L}{2}}{sL}\right)\cdot\exp\left(2\frac{x-\frac{L}{2}}{mL}\right)$
MPF 4	23	1070.0	5.0	4.55×10^{-4}	$\kappa_{Sinc} = \sin c\left(2\pi\frac{x-\frac{L}{2}}{sL}\right)\cdot\exp\left(2\frac{x-\frac{L}{2}}{mL}\right)$
MPF 5	23	1068.6	7.4	3.30×10^{-4}	ADC
MPF 6	23	1068.6	7.4	3.30×10^{-3}	ADC

Table 3.5-2: Parameters for Gratings written with the Multiple Printing in Fibre Method

The alignment and operation of this set-up shall not be explained in detail here because of its complexity, but the reader can refer to the theses of Andrew Gillooly [*109*] and John Mitchell [*110*].

After a thorough alignment procedure the fabrication for each grating takes typically 2-3 minutes. An overview of the grating parameters is given in *Table 3.5-2*.

3.5.4 Reflectometry Measurements and Results

Using OFDR, the reflectivity response for each grating was measured twice, once for each launching direction of the probing light into the fibre. This was done to eliminate measurement errors and double-check the results.

The wavelength sweep was 40 nm in all cases at a rate of 40 nm/s. The sampling rate of 1 MHz resulted in a step size of 0.040 pm between each two data points.

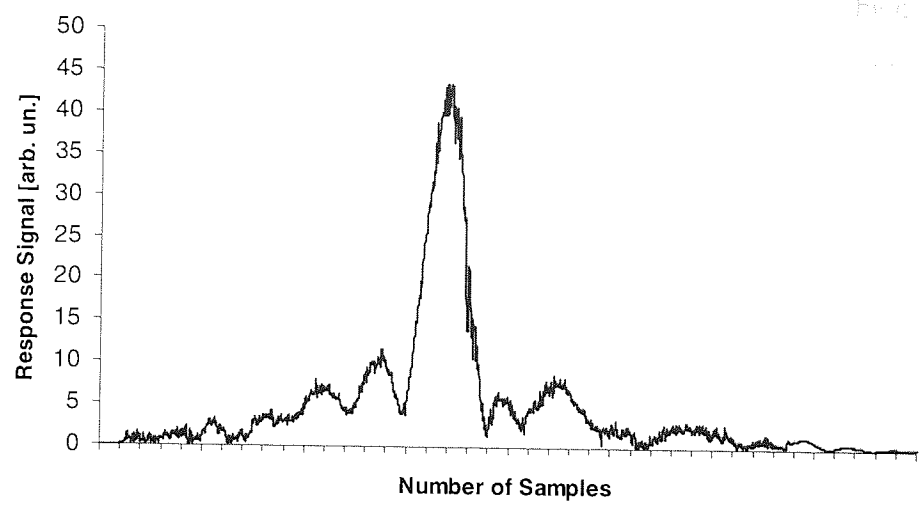

Figure 3.5-2: Reflectivity response from grating PCM3

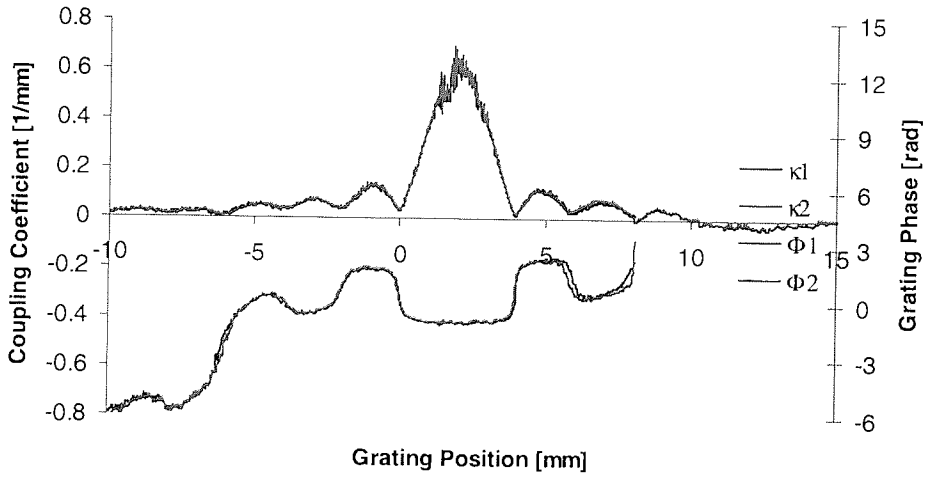

Figure 3.5-3: Match between reflectometry measurements on same grating taken from opposite directions

Figure 3.5-2 shows an example for a typical reflectivity response of an OFDR measurement taken from a sinc-apodised grating. The impact of changing the direction in which the light is launched into the fibre is highlighted in *Figure 3.5-3*, showing the coupling coefficient and grating phase calculated from the impulse response shown above and its counterpart, obtained from a measurement from opposite direction. The respective results are printed as black and red traces and show foridable agreement. The graph shows a coupling coefficient distribution, as expected from a sinc-apodised grating, having a main maximum in the grating centre, flanked by three side peaks of decreasing strength on both sides. At those grating positions, where κ reaches zero, the grating phase Φ follows the theory by showing 8 distinctive phase-shifts. These vary in magnitude, as the base line of Φ does not seem to follow a flat line along the grating length. Whether this is an intrinsic feature of the grating or due to underlying measurement and normalisation errors is not clear.

However, the good match of data obtained from applying opposite launching directions is observed throughout all measurements. In the following representations only one graph is presented for each grating.

3.5.4.1 Gaussian Gratings

In *Figure 3.5-4* the Gaussian apodised gratings PCM2 (a) and MPF2 (b) are directly compared to each other. Both measured apodisation profiles match well with the distinctive bell-shape of a Gauss function. Grating PCM2 displays a higher maximum value of κ. This corresponds well with the stronger reflectivity of that grating. Its transmission loss at the Bragg wavelength is with 11.5 dB higher than the 8.5 dB of MPF 2. The phase of both gratings follows the typical concave shape over their lengths. A striking feature of grating MPF2 are the fringes in the κ-function. Most pronounced is the sharp dip in the grating centre, showing some effect on the grating phase.

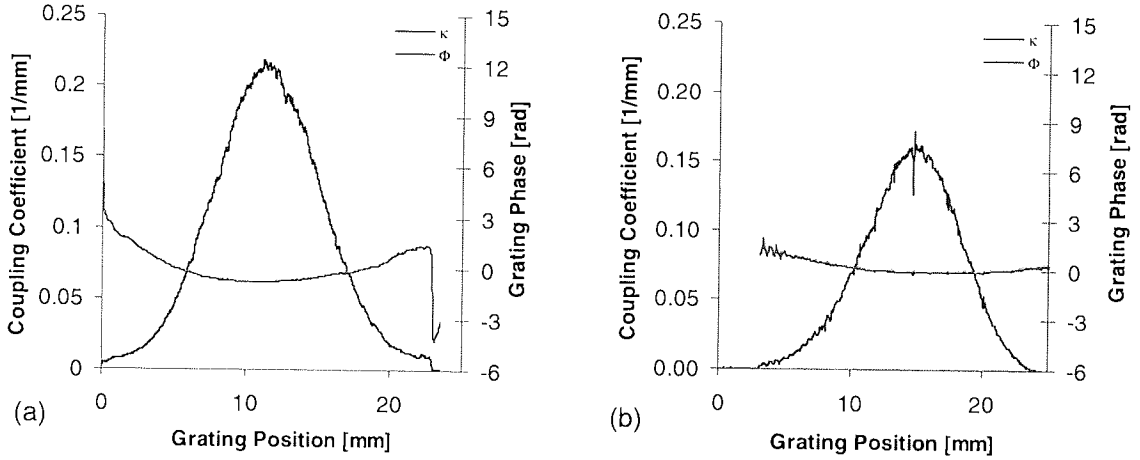

Figure 3.5-4: κ and Φ in Gaussian gratings fabricated with the polarisation control method (a) and the multiple printing in fibre method (b)

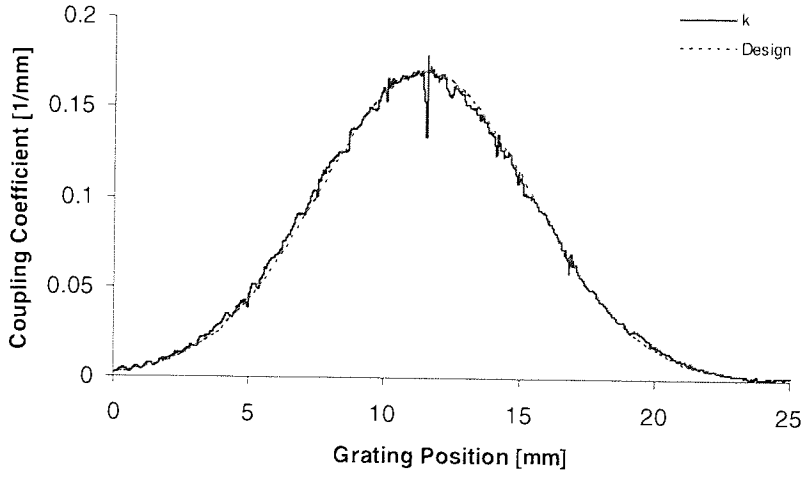

Figure 3.5-5: Comparison between designed and reconstructed apodisation function of MPF1

An overlay of the original grating design over the measured local coupling strength is shown in *Figure 3.5-5*. With the exception of some noise and several sharp dips in its course, the reconstructed κ-fits well into the shape of the Gaussian function used for the apodisation. *Figure 3.5-6* shows the match between measured grating spectrum and simulations based on the reconstruction data obtained from OFDR measurements.

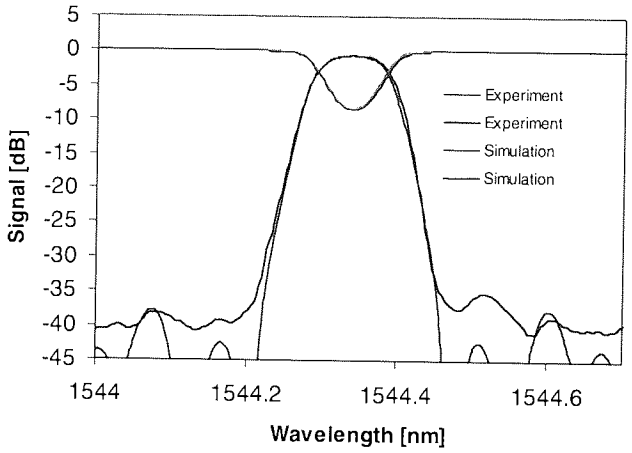

Figure 3.5-6: Measured grating spectra and spectra calculated from reconstruction data

3.5.4.2 Sinc-apodised Gratings

A similar comparison is presented for sinc-apodised gratings in *Figure 3.5-7*. The gratings were written with the different inscription methods, using the same parameters. Grating PCM4 on the left is 6.7 dB strong in transmission, whereas MPF3 on the right shows a transmission dip of 5 dB. Again this is reflected in the values of the respective coupling coefficients. The most prominent difference is the higher definition of the localised phase shifts in MPF3. The κ-values at these sites reach lower to zero, than in PCM4 and a higher number of side lobes could be resolved. In the image of the grating phase this manifests in 12 detectable, steep phase shifts of rectangular shape, which actually reach the value of 1π. In PCM4 only 7 phase shifts of rounded shape are resolved, which also are weaker.

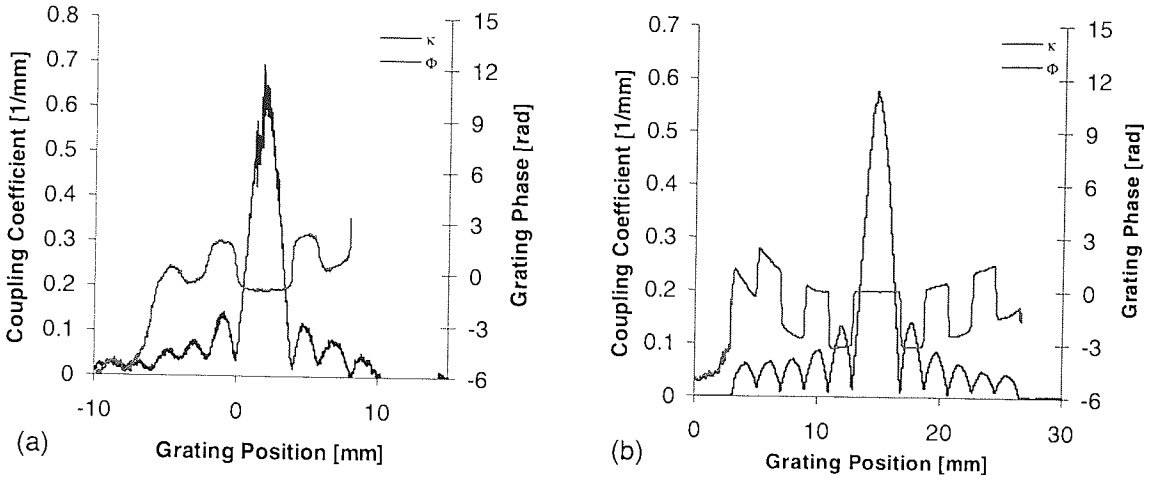

Figure 3.5-7: κ and Φ in sinc-apodised gratings fabricated with the polarisation control method (a) and the multiple print in fibre method (b).

The measured distributed grating strength fits very well with the design employed for the grating fabrication, as seen in *Figure 3.5-8*. Only discrepancies are an offset of the κ zero-level, a seeming elongation of the grating with respect to the theoretical value and a small erroneous phase shift effect, which manifests near the apex of each function lobe.

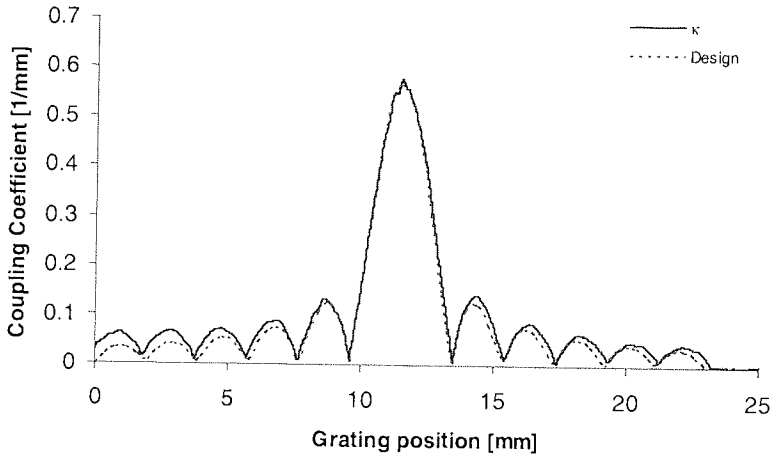

Figure 3.5-8: Comparison between designed and reconstructed apodisation function

Again measured spectra are compared to numerical calculations using the reconstructed coupling strength of the gratings, as shown in *Figure 3.5-9*.

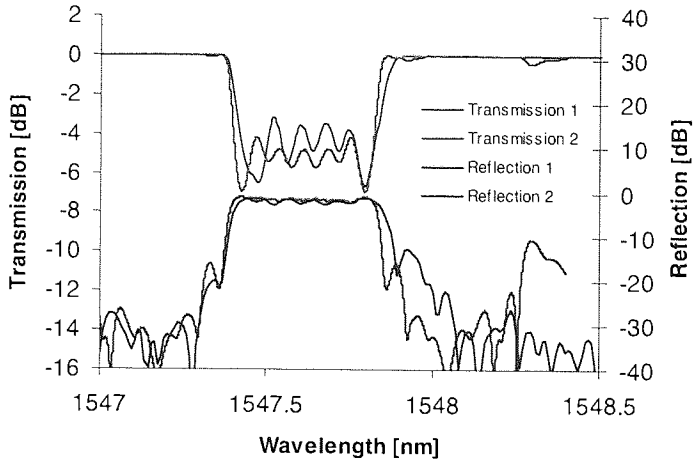

Figure 3.5-9: Measured grating spectra and spectra calculated from reconstruction data

Grating strength and bandwidth correspond very well. Also the position of the side bands fit very well. At the edges the measured spectra show a smaller slope and the symmetry of the measured spectra differs from the calculated ones. Most striking is the occurrence of 5 fringes over the grating band, as opposed to 6 fringes in the simulated spectrum.

3.5.4.3 ADC Gratings

The most complex grating design tested with OFDR is that of the ADC grating, which is highly asymmetric in its axial κ-function. In addition κ varies critically over short sections as well as in strength.

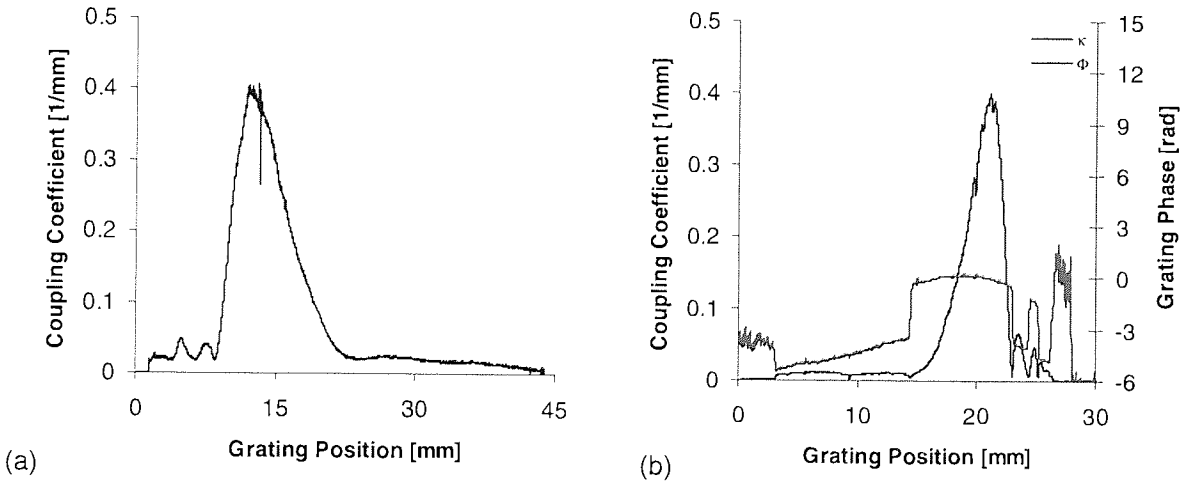

Figure 3.5-10: κ and Φ in a 23 dB strong ADC grating fabricated with the polarisation control method (a) and a 7.4 dB ADC grating written using the multiple print in fibre method (b)

Figure 3.5-10 shows the reconstruction of a 46 mm long and 23 dB strong ADC grating written with the polarisation control method PCM5 and a 23 mm long and 7.4 dB strong grating MPF5 written with the sampling beam-fibre method.

Although the first of the two gratings exceeds the specification of the OFDR set-up by over 10 dB in strength, *Figure 3.5-11* still shows a reasonable reconstruction of the grating with some of the main features. Because of the strong reflectivity in the grating centre, insufficient light power is reflected back to the detector system from the far grating end. This causes a distorted image of the reconstructed grating. The measurement on the same grating from the different direction did not yield satisfying results for this reason.

However, the grating reconstruction of MPF5 on the right hand side reveals five grating sections separated by five clear π-phase shifts. It is apparent, that either the fabrication or the characterisation method, or both reached their resolution limit at the grating position around 25 mm, where an additional phase shift is supposed to be, but is skipped.

The measured apodisation function also for ADC gratings fits the anticipated design well. Again all side-lobes appear to be stronger than the master curve. This manifests in particular in the section at the very left grating end. The often-observed fringes in the κ-function also appear.

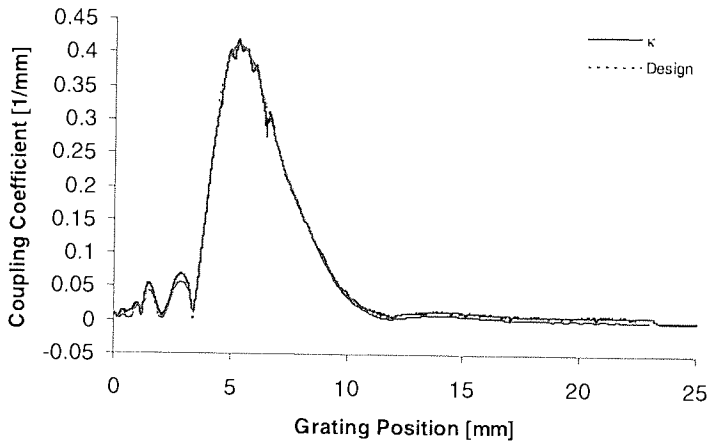

Figure 3.5-11: Comparison between designed and reconstructed apodisation function

In *Figure 3.5-12* once more a good match between measured and reconstructed data is found. One reoccurring grating error is the movement of the central phase shift towards the shorter wavelength side and the shift of the spectral centroid to the long wavelength side. This has been observed for all ADC gratings regardless of writing technique employed to fabricate them. The initial hope was to detect this systematic error using reflectometry-based grating characterisation, but its origins are still not clear.

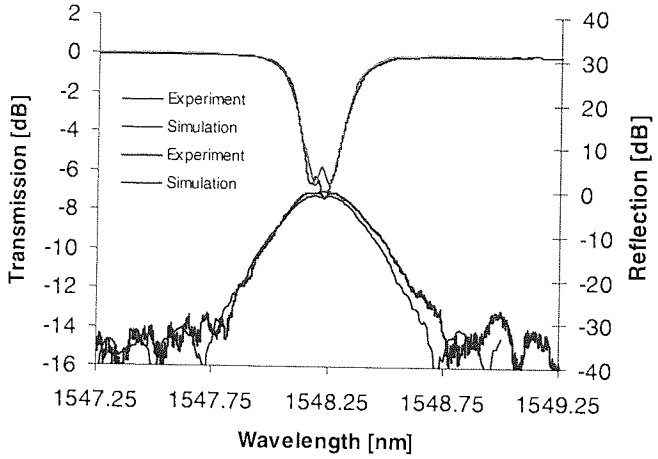

Figure 3.5-12: Measured grating spectra and spectra calculated from reconstruction data

3.5.5 Discussion

Grating characterisation on complex fibre grating structures using OFDR measurements reveal the limitations and shortcomings of the UV writing set-ups used.

One constantly re-emerging type of grating artefacts is sharp dips in the coupling coefficients of the gratings written by the Multiple Printing method. Often this effect does not reflect on the grating phase, in some cases however phase errors are detectable. The origin of these errors is most likely a mismatch between fibre translation and timing of the UV-shot at certain positions during the inscription. This leads to a slightly shift between successive interference fringes which are supposed to overlap in the same spot. Instead of an even distribution of UV-induced refractive index change in exposed sections and no exposure in others, exposed fringes may show spikes of increased and lower Δn. In particular at the edges between sections to be exposed to those left unexposed a blurring effect can take place. This can be resolved by a better positioning and faster shutter control, for example by using a stage with an integrated interferometer system.

A similar effect can explain the noise in the measurements on gratings produced by the polarisation control method, where a pulsed *KrF* laser beam of 0.7 mm beam was used for the grating writing. The energy of this type of high power single pulses naturally varies. As the writing process is not synchronised to each single grating fringe, the error is distributed evenly over the full grating and observed as noise, rather than singular errors. The choice of using an excimer laser for the fabrication set-up is a historical one and it has been pointed out repeatedly, that gratings of higher quality can be expected when using a CW source.

The phase curves are smooth and show sharp π-phase shifts for gratings fabricated with the sampling method. They appear to be noisier for the PCM gratings. Also the phase shift flanks are not as distinctive and the phase jumps vary in size, never actually reaching 1π. The

κ values of gratings from both methods however, are close to zero the locations of the phase-shifts. The positions of phase shifts and minimum coupling match excellently.
All measured κ-functions were fitted to the original apodisation design according to the main maximum. In the cases of gratings with phase-shifts this resulted in seemingly increased κ-values for the side-lobes. A possible explanation for this effect is a non-linear refractive index-change with increasing UV-fluence, leading to the opposite – an underdeveloped central grating section.
For the fitting of reconstructed grating data with measured spectra certain problems are unavoidable. Aspects like the exact grating length or centre wavelength are not trivial. A match has to be found between fabrication parameters and "absolute" grating position obtained from OFDR. Also the use of different light sources may lead to different grating wavelengths despite pre-calibration. The total refractive index change is another variable.

3.5.6 Conclusions

With the help of OFDR a detailed insight into grating fabrication with the methods of Multiple Printing in Fibre and Polarisation Control was gained. Reconstructed grating apodisation highlighted errors and noise in the distribution of the local coupling coefficient due to mismatches of grating fringes and successive UV-pulses. In both cases these errors appear to scale with local κ, supporting these assumptions.
The measurements clearly reproduce the grating design of all three grating types, which included Gaussian, sinc and ADC apodised gratings. A good match between localised minima of κ and the sites of the π-phase shifts was found, with κ reaching values close to zero. The phase-shifts were identified with great spatial and dimensional accuracy in gratings written with the sampling method. For gratings written with the Polarisation Control Method the magnitude of the phase-shifts remained below the specification and the phase change also appeared more gradual. Some phase shifts in the weaker grating sections could not be detected.
A comparison between measured grating spectra with simulations using reconstructed data for the coupling coefficients show good agreement.
The dynamic range of the OFDR method allows resolving κ down to a value of 0.01/mm for gratings of 10 dB maximum.

4 GRATINGS AND DEVICES FOR TELECOM APPLICATIONS

The great potential of fibre optic systems for data transmission was recognised since the earliest days of this technology. Glass being the material mainly used for optical fibre fabrication and the small size of these fibres make the installation of widespread optical networks a cheap and easily integrable solution. The intrinsic characteristics of optical fibres include extremely low transmission loss and sensitivity to external electro-magnetic influences.

An extremely high bandwidth capability can be achieved due to the fact that optical signal channels of different wavelengths can travel through a waveguide over long distances without interfering with each other. One limiting factor is the chromatic dispersion inherent to the waveguide material, which leads to a spreading of signals within the frequency domain, thus shifting the tails of the carrier pulses into the wavelength band of neighbouring channels. Currently, the standards for the separation between telecommunication channels are 0.8 nm (100 GHz) and 0.4 nm (50 GHz).

Grating based fibre optic devices are used to perform a multitude of functions to enable optical networks. They are used in multiplexers/demultiplexers [*80*], for short pulse generation [*72*] and pulse shaping [*98*], as dispersion compensators [*71*], modulators [*111*], chromatic filters [*82*], feedback [*83*] and switching devices [*99*], to mention the most important ones.

In the following subsections the results from work on multiplexer design and short pulse generation using a fibre Bragg grating is presented.

4.1 Novel Designs for Fibre Grating based Multiplexers

4.1.1 General Design Considerations

Multiplexers are used to launch a certain number of data channels into one single fibre. The information from all channels at one time can be obtained by filtering through a demultiplexer. To pick the data from one or a few particular channels only, add-drop filters are the most widely used devices. The vacated spectral bandwidth range can then be used to add a different data stream into the fibre, using the same carrier frequency, as the channels that have previously been dropped. These concepts are briefly explained in the course of this chapter and the concept and results from a novel filter design based on chirped apodised Bragg gratings is presented.

To exemplify the functional principle of a multiplexer, two different concepts are presented here, that were suggested at the INESC Research Centre in Porto by Rosa Romero. Both are based on combinations of optical circulators and apodised uniform Bragg gratings that were fabricated at Aston University and their concept is shown in *Figure 4.1-1* and *Figure 4.1-2*. An optical circulator is a fibre-optic integrated channelling device for guided light comprising three ports. The first port is used to launch the light into the circulator, which then passes to the second, transmission or grating port, at the end of which a reflecting filtering device is inserted. In our case this device is a fibre Bragg grating. Any light reflected by this filter is re-launched back into the circulator, and exits through port 3. In this manner optical data channels can be bundled into and separated from one single transmission fibre using an arrangement of optical circulators and gratings. A circulator is a unidirectional device, which means that light is supposed to be transmitted through it only in the way as described above. However, in practice the back-reflection of unwanted parts of the spectra is unavoidable, which affects the suppression of channels to be filtered out.

In order to obtain a demultiplexer, with the concepts shown, the input and output ports simply have to be interchanged, the circulators flipped and the light launched in the opposite direction.

Additional factors limiting the performance of these kinds of multiplexers/demultiplexers are losses within the circulators, usually of the magnitude about 1dB, and pulse degradation within the fibre gratings, for example due to the grating dispersion functions.

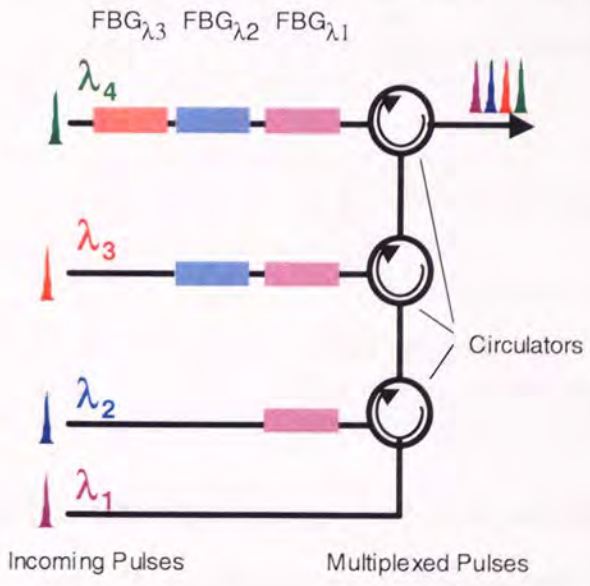

Figure 4.1-1: 4-channel multiplexer design based on 3 optical circulators and 6 apodised FBGs

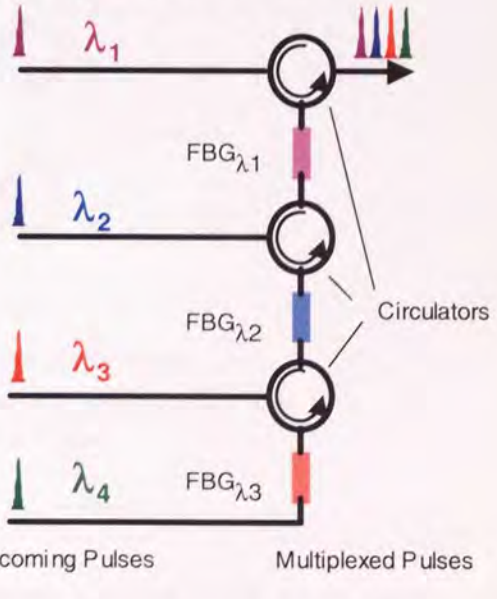

Figure 4.1-2: 4-channel multiplexer design based on 3 optical circulators and 3 apodised FBGs

Design considerations for optical circulator based multiplexers/demultiplexers include the minimisation of the number of circulators and gratings for a given number of channels to be

processed, as well as the spectral design of the gratings themselves, which is shown in the sections below.

4.1.2 Multiplexer Design using Chirped Gratings and optical Circulators

As can be seen from *Figure 4.1-1* and *Figure 4.1-2*, despite performing the same function on N=4 channels, for the second configuration only 3 apodised gratings and circulators are needed, whereas for the first configuration the number of gratings necessary is 6. This has a great impact on the total overall insertion loss on data channels when passing through a multiplexer/demultiplexer system. This loss was shown to increase linearly with the number of channels and to be more than double the magnitude for the first system compared to the latter [*112*].

To overcome this flaw of the concept shown in *Figure 4.1-1* and decrease the number of gratings, we have proposed the use of chirped fibre Bragg gratings (CFBG) covering the full wavelength bandwidth of the groups of apodised gratings, as used in the initial experiment. Another additional feature of this set-up is the linear dispersion function of chirped Bragg gratings. The set-up is shown in *Figure 4.1-3*.

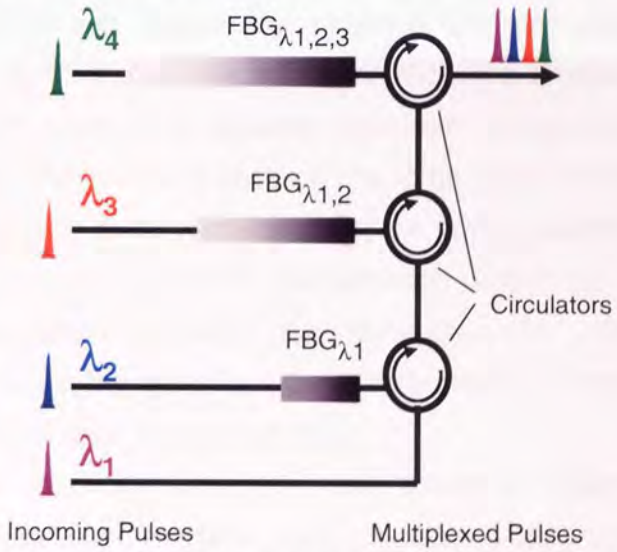

Figure 4.1-3: 4-channel multiplexer based on 3 optical circulators and 3 chirped FBGs

4.1.3 Grating Design and Fabrication

For the experiment two different sets of chirped gratings have been used – one non-apodised and one apodised. Both sets of CFBGs were fabricated using a phase mask with a chirp of 0.75 nm/cm and the exposure to ultra-violet light was achieved via a frequency-doubled argon-ion CW laser at 244 nm. *Figure 4.1-4* shows the spectra of the three non-apodised gratings.

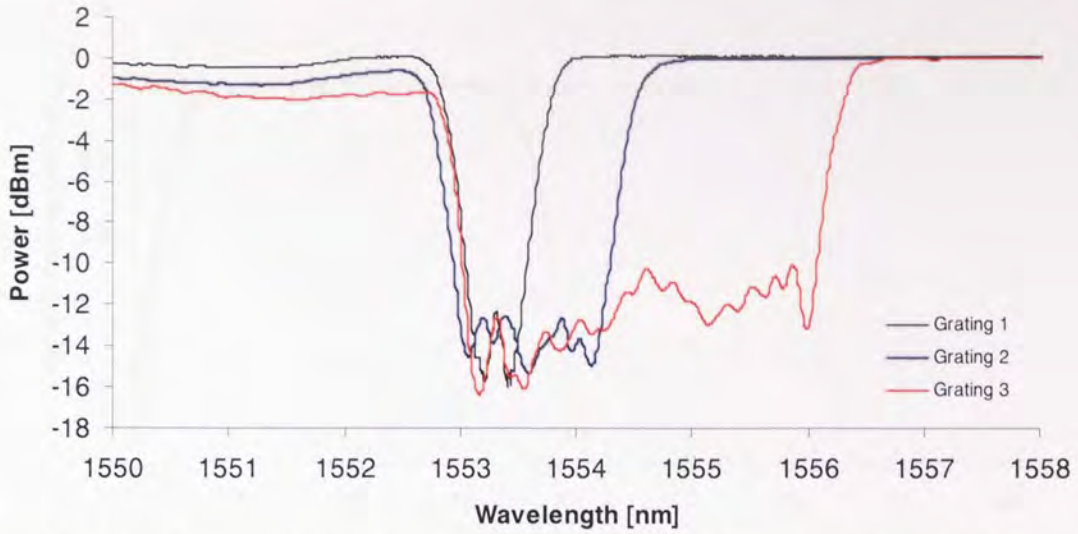

Figure 4.1-4: Transmission spectra of 3 non-apodised chirped FBGs of different lengths

In the case of the apodised CFBGs, each has a super-Gaussian apodisation profile superimposed over their refractive index modulation, which was applied using the dithering phase mask technique described in ***Chapter 2.5.4*** [*59,60*]. This was done in order to eliminate the side-lobes and reduce the crosstalk between adjacent channels in the MUX/DEMUX device. At the same time, the apodisation of a chirped fibre grating leads to a fade-out effect on both sides of its reflection spectrum, which counteracts the benefits of side-lobe suppression. That means a trade-off has to be made between maximum side-lobe suppression of each grating and the steepness of the grating spectra at their edges, both of which affected the system's cross-talk performance. Using the commercially available IFO-Gratings 3.0 simulation software, the parameters for optimised hyper-gaussian apodisation functions of each grating have been determined in order to match the slopes of their spectral profile at the short wavelength side.

The function and the according parameters are shown in *Equation 4.1-1* and listed in *Table 4.1-1*. The apodisation functions and resulting grating spectra can be seen in *Figure 4.1-5* and *Figure 4.1-6*.

Index [n]	X_{centre} [mm]	Length [mm]	Order [N]	Taper [A]
1	0	8	7	0.85
2	+5	20	10	0.85
3	+10	30	14	0.85

Table 4.1-1: Apodisation parameters of chirped FBG for novel multiplexer design

$$f_{apo}^{n} = \exp\left(-\frac{\left| x - x_{centre}^{n} \right|}{A \cdot x_{centre}^{n}} \right)^{N} \qquad \textbf{Equation 4.1-1}$$

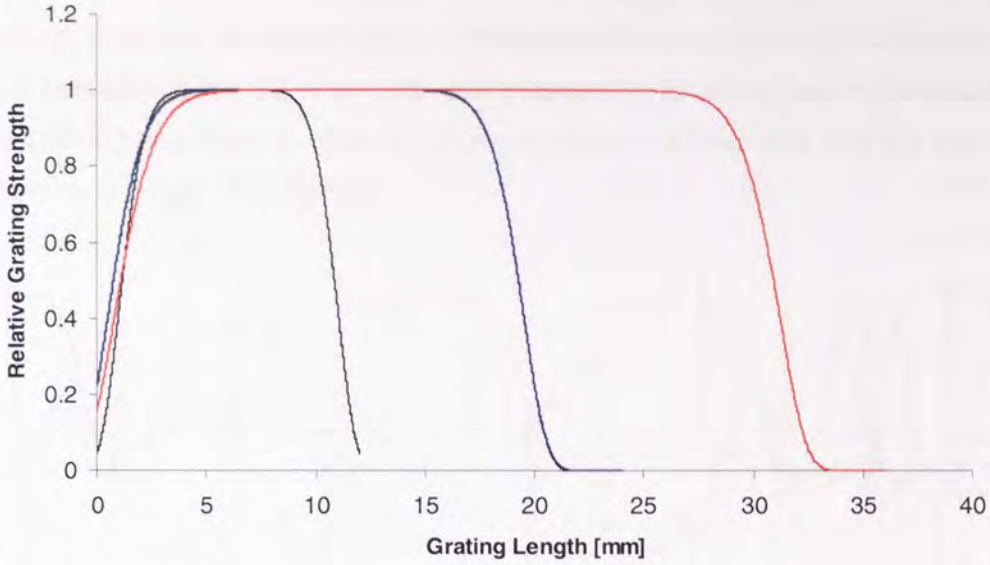

Figure 4.1-5: Apodisation functions for chirped FBG gratings used in 4-channel multiplexer/demultiplexer configuration

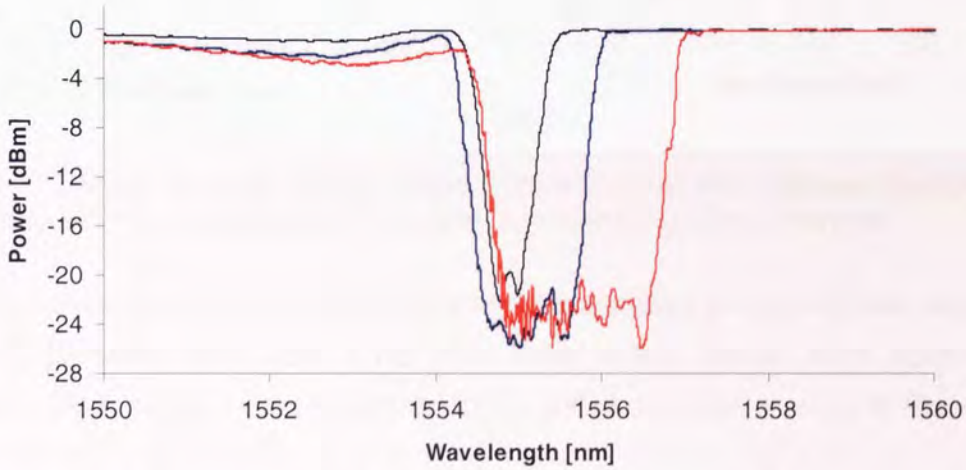

Figure 4.1-6: Transmission spectra of apodised chirped FBGs used in 4-channel multiplexer/demultiplexer configuration

CFBG1, CFBG2 and CFBG3 have a FWHM of 2.45 nm, 1.68 nm and 0.70 nm respectively, and an isolation loss of 22 dB.

4.1.4 Results and Discussion

The implementation of both grating sets into the proposed Mux/Demux setting clearly showed the benefits of using apodised CFBGs. *Figure 4.1-7* gives a direct comparison of their demultiplexing performances. The spectral responses of the multiplexer at each port are superimposed over the spectra of the corresponding channels.

Comparing the demultiplexing behaviour using the two grating sets, it is apparent that the gratings from the first set are weaker in both transmission and reflection, which undermines a

good channel separation. The reflection spectra of the apodised gratings show a better side-band reduction, lowering the noise floor for 10 dB and more. In the regions between channel 1 and 2 and between channel 3 and 4 side-lobes appear due to the spectral overlap between these neighbouring channels. In order to eliminate these, it is desirable that the steepness of the reflection band edges is increased.

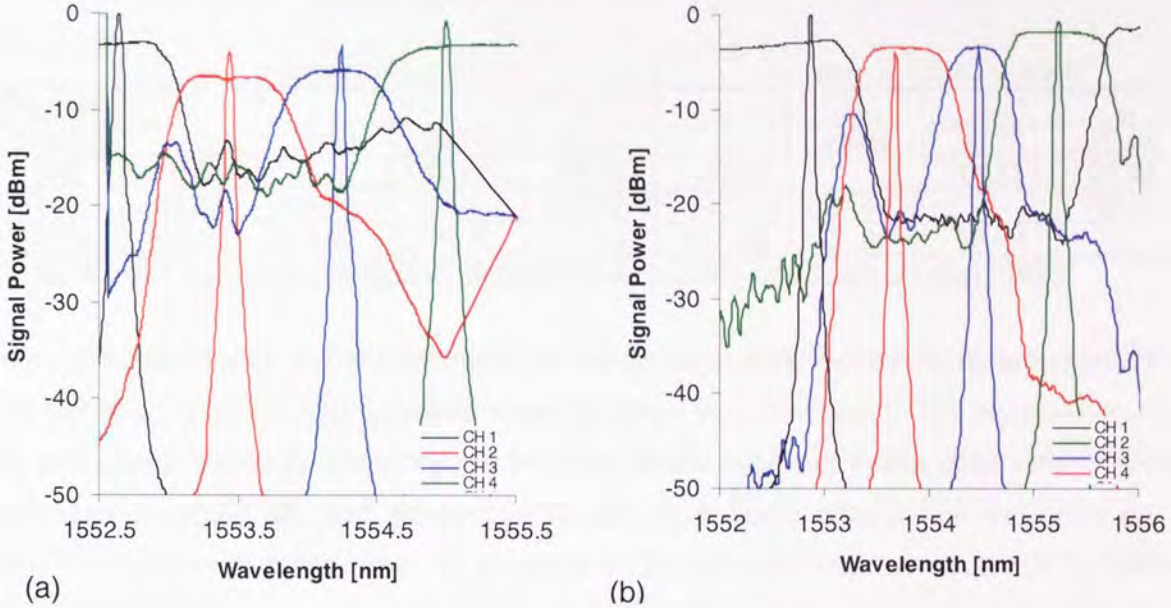

Figure 4.1-7: Spectra showing optical output from 4-channel demultiplexer design using non-apodised (a) and apodised (b) CFBGs and corresponding signal channels

The overall results showing the degree of channel separation for each of the experimental set-ups are presented in *Table 4.1-2* and *Table 4.1-3*. These were obtained from measurement data, as exemplary presented for the set of apodised gratings in *Figure 4.1-8*.

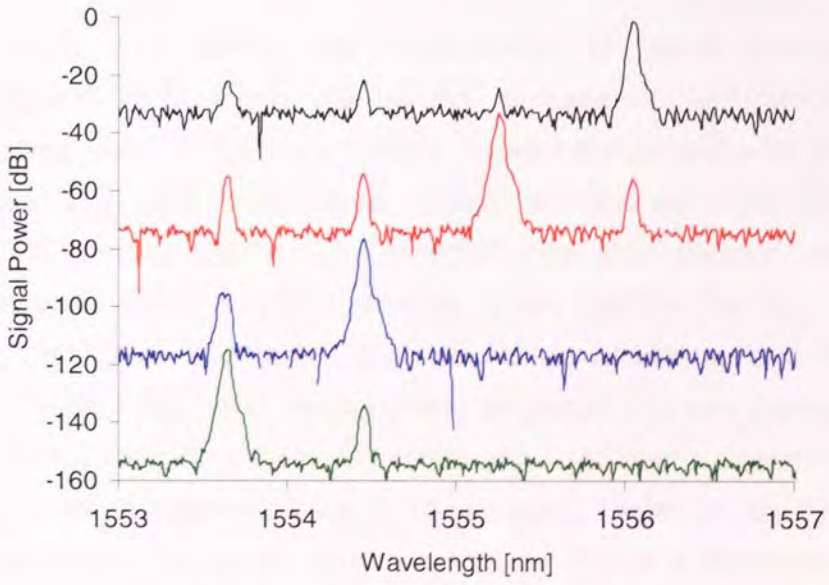

Figure 4.1-8: Signal output from each port of 4-channel demultiplexer (signal power shifted for clarity)

	Isolation in MUX-mode				Isolation in DEMUX-mode			
Channel	λ_1	λ_2	λ_3	λ_4	λ_1	λ_2	λ_3	λ_4
I [dB]	-	11.36	11.40	8.98	-	9.23	12.27	9.69
II [dB]	40.47	-	12.69	36.49	32.00	-	17.06	35
III [dB]	21.77	12.82	-	13.52	24.72	12.45	-	15.46
IV [dB]	13.71	14.11	14.28	-	11.63	14.17	14.89	-

Table 4.1-2: Channel separation in multiplexer employing non-apodised chirped FBGs

	Isolation in MUX-mode				Isolation in DEMUX-mode			
Channel	λ_1	λ_2	λ_3	λ_4	λ_1	λ_2	λ_3	λ_4
I [dB]	-	23.64	20.70	20.44	-	23.89	20.70	20.86
II [dB]	19.23	-	19.57	22.18	18.46	-	19.33	21.98
III [dB]	42.23	24.89	-	18.42	54.33	27.82	-	18.94
IV [dB]	>70.00	70.00	19.06	-	>67.90	67.90	19.00	-

Table 4.1-3: Channel separation in multiplexer employing apodised chirped FBGs

From the data above the improvement of the isolation loss values by replacement of the non-apodised gratings with apodised ones becomes very obvious. In the multiplexing mode the first set-up shows an isolation of 8.98 dB or better, whereas in the latter case this value increases to 18.42 dB and exceeding 70 dB. The same impact can be seen on the demultiplexing performance with an increase of the isolation loss from 9.23 dB or better to 18.46 dB and more.

However, these results do not fit the requirements for state of the art systems, which demand isolation levels of 30 dB or more.

4.2 Fabrication and test of a Zero-Dispersion Grating Design for WDM

The next major step towards the advancement of Dense Wavelength Division Multiplexing (DWDM) technologies will be the increase of the transmission rate in commercial systems from 10 Gbit/s to 40 Gbit/s. Besides the development of new electronic standards for their realisation, these novel systems will also set higher demands for the gratings used for channel filtering. Low insertion loss and reflection spectra of near-rectangular shape are elementary requirements for the loss-free filtering of dense optical data channels. One classical example to achieve these requirements is a sinc-apodised grating format. On the other hand the dispersion properties of these gratings also play an important role. With increasing data rates in transmission systems, dispersion related pulse degradation becomes an additional issue to be managed. Therefore, ideally a grating must have both: a near-rectangular transfer function and a low degree of dispersion. Often a trade-off between these two requirements must be made. In the past various new grating designs have been proposed to tackle this issue [*113*]. To calculate the filter function and dispersion

properties from a proposed grating design is a straightforward task. A number of standardised techniques exist, as the coupled mode theory approach [*8,9*] and transfer matrix method [*114*], both of which also are implemented in commercial software packages for grating simulation. However, in the opposite case, in which the grating apodisation function has to be determined from a given set of desired filter parameters, solutions are not as straightforward.

Constraint-based solver algorithms [*115*] are feasible tools for the design of highly complex grating structures.

This degree of complexity also adds to difficulties for the grating fabrication itself. For an optimal grating performance the fabrication method must provide a high degree of control of local coupling coefficients and the positions of discrete phase shifts.

In the case of the presented ADC gratings an iterative constraint-based solver for the modelling of the design was applied. The grating properties were defined by the spectral bandwidths at 0.5 dB, 3 dB and 30 dB in reflection and the minimum value of transmission loss within the grating band. In addition, a maximum dispersion limit was defined for the reflection signal across the 0.5 dB bandwidth and the transmitted signal across the adjacent DWDM channel bands, assuming 100 GHz channel spacing. The apodisation profile resulting from this set of restraints with the local grating strength κ over its length z is shown in *Figure 4.2-1*. It is apparent that the design his highly asymmetric with one main section of high fringe visibility and seven sections of low modulation strength alternating around the zero-line. This means that four of these sections nominally have an index modulation of negative sign. This can be compensated by introducing a π phase-shift at each position of a transition between positive and negative refractive index change during the inscription process. Although the main reflective effect stems from the main grating portion around one third of the full grating length, its overall performance strongly depends on the writing accuracy over the full length. Slight inaccuracies show significant effects within the grating spectrum and dispersion profile, which means that this design puts any writing method applied to it to an ultimate test.

Simulations based on this design predict a side-lobe suppression of 25 dB or better and a root mean square (RMS) group delay ripple of below 1 ps and varying less than 6 ps within the 3 dB reflection bandwidth. This applies to gratings of 10 to 30 dB strength if the light is launched from its left side to the right, in accordance with *Figure 4.2-1*. Both axes are described in normalised units. The abscissa is normalised with respect to the total grating length and the ordinate to the value of maximum fringe visibility, both set to unity.

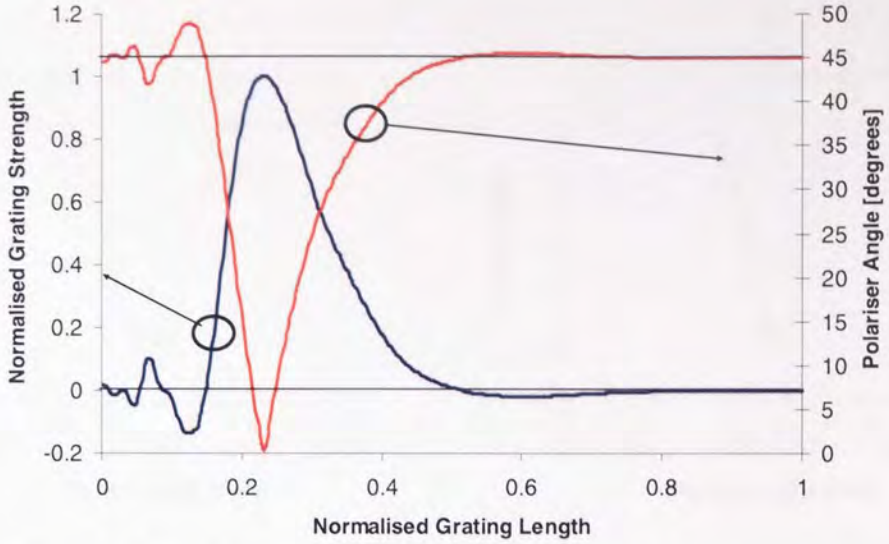

Figure 4.2-1: ADC-apodisation profile for zero-dispersion grating design (blue) with corresponding polariser angles (red)

Two gratings of this type were written within the COM research centre at the DTU in Lyngby (Denmark), using the polarisation control method, as described in ***Chapter 3.2***. Their length was 23 and 46 mm respectively, with bandwidths corresponding to 100 GHz and 50 GHz channel spacing. Measurements using a tuneable laser source and an optical spectrum analyser with a resolution of 1 pm yielded the transmission and reflection spectra as shown in *Figure 4.2-2* and *Figure 4.2-3*. The solid lines show the experimental data (red) compared to simulated spectra (blue). The experimental data fits well with the simulations, with the exception of elevated side-lobes. As is obvious from the calculated spectra, the grating design has an inherent central phase-shift, which manifests in a slight splitting of the main reflection band. The spectral measurements of all ADC gratings show a shift of this artefact towards lower wavelengths. Despite further characterisation, the reason for the second phenomenon, which is characteristic for all gratings of this type written, is not clear.

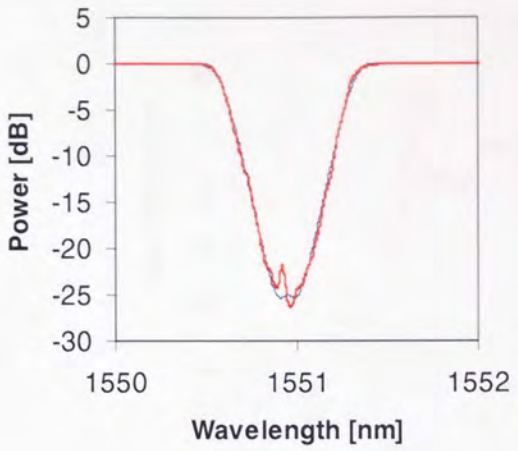

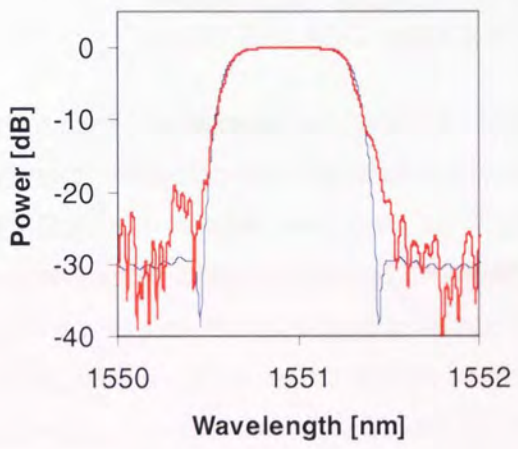

Figure 4.2-2: Measured (red) and simulated (blue) transmission and reflection spectra of 100 GHz ADC grating

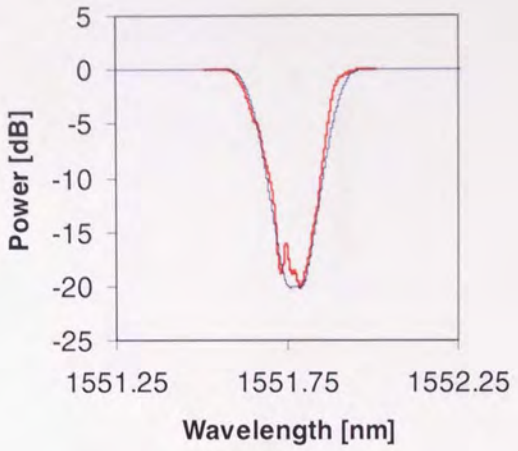

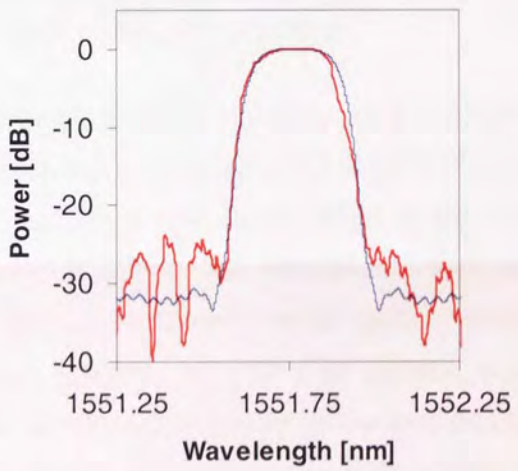

Figure 4.2-3: Measured (red) and simulated (blue) transmission and reflection spectra of 50 GHz ADC grating

The actual group delay of the 100 GHz grating within the 3 dB reflection bandwidth shows a low level of fluctuation around 10 ps. The RMS group-delay ripple is also very low at 2.5 ps. This is documented in *Figure 4.2-4*.

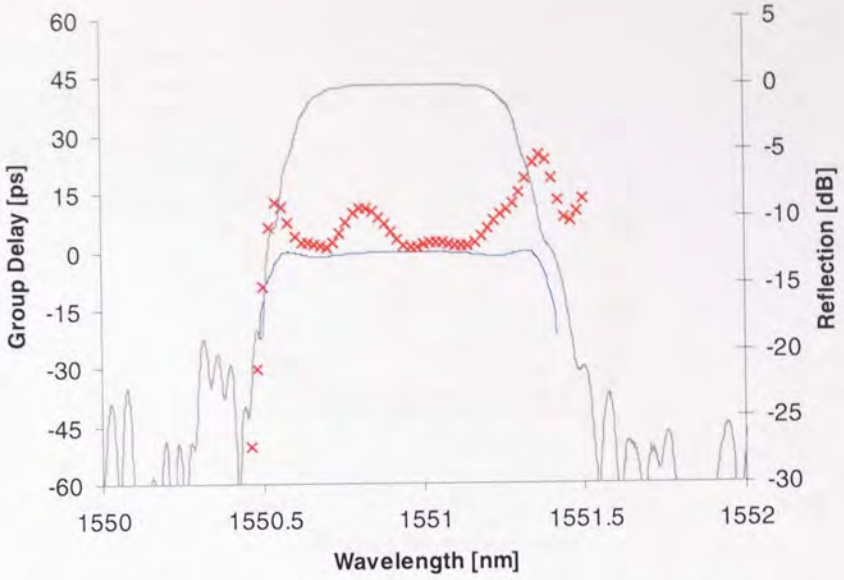

Figure 4.2-4: Measured (red) and theoretical group delay (blue) of 100 GHz ADC -grating displayed against reflection spectrum

Both gratings have been submitted to testing of their bandwidth utilisation as a function of wavelength detuning and application of different modulation formats within a DWDM set-up at 10 Gbit/s. This work was done by Christophe Peucheret and Beata Zsigri at the COM research centre of the Technical University of Denmark (DTU). The objective of their work was to investigate the influence of various signal modulation formats on the performance of an optical data transmission system, using different grating filters for their project. A CW tunable laser source was modulated with a pseudo-random bit sequence generated by using a pulse-pattern generator and a chirp free Mach-Zehnder Modulator. In a further step, the pulse train, which initially had a non return-to-zero (NRZ) format, was reshaped into a variety of return-to-zero (RZ) formats. These modulation formats included return-to-zero (RZ), carrier-suppressed return-to-zero (CS-RZ), upper and lower side-band return-to-zero (USB-RZ and LSB-RZ) formats [*116,117,118*].

Starting from the central wavelength of the grating, the channel wavelength was consecutively detuned towards shorter and longer wavelengths, while the bit-error rate was kept constant around the threshold of 10^{-9} at the same time.

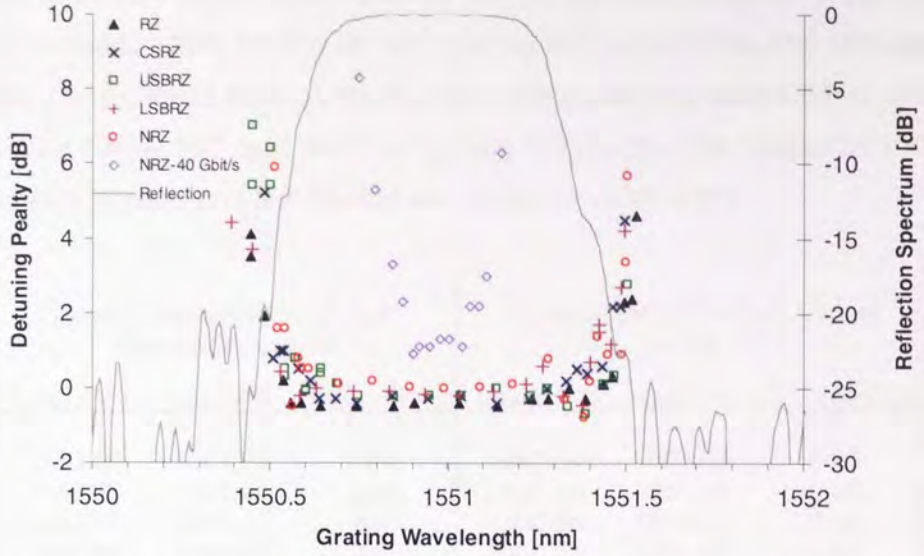

Figure 4.2-5: Optical power penalty functions at different modulation profiles (dots) of 50 GHz ADC grating compared to grating reflection spectrum (full line)

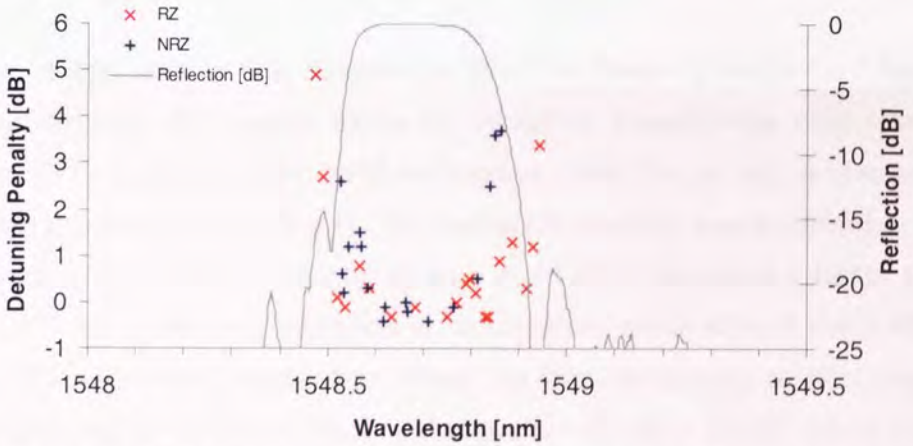

Figure 4.2-6: Optical power penalty functions at different modulation profiles (dotted lines) of 100 GHz ADC grating compared to grating reflection spectrum (full line)

Any effect of the detuning on the bit-error rate could be compensated with an increase in power of the signal pulses. Hence the quality of the grating could be measured by the degree of loss penalty against optical detuning. This experiment was repeated for each modulation profile. The results for the two gratings are shown in *Figure 4.2-5* and *Figure 4.2-6*. In addition, the reflection spectra of the gratings have been inserted in the same plots to have a direct comparison about how the wavelength detuning of the signal corresponds to the full bandwidth of the grating. With one exception, as pointed out in both graphs and Table 4.2-1, all experiments were performed at 10 Gbit/s bit-rate.

By setting the maximum acceptable value of the power penalty to be 1 dB, the useable bandwidth still exceeds 129% for the 50 GHz grating and 62% for the 100 GHz grating. The useable bandwidth is defined here as the quotient of the detuning bandwidth at which the bit-error rate remains below 10^{-9} over the 3-dB grating bandwidth. The values for the individual modulation profiles applied on each grating are shown in *Table 4.2-1*.

Modulation Profile	Grating Wavelengths of 3-dB Bandwidth Values			Wavelengths for Penalty Values >1dB			Bandwidth Utilisation [%]
	λ_{START}[nm]	λ_{END}[nm]	BW $\Delta\lambda$[nm]	λ_{START}[nm]	λ_{END}[nm]	BW $\Delta\lambda$[nm]	
100 GHz							
RZ	1550.63	1551.28	0.65	1550.54	1551.47	0.93	143
CS-RZ	1550.63	1551.28	0.65	1550.58	1551.44	0.86	132
USB-RZ	1550.63	1551.28	0.65	1550.54	1551.47	0.93	143
LSB-RZ	1550.63	1551.28	0.65	1550.53	1551.40	0.87	134
NRZ	1550.63	1551.28	0.65	1550.56	1551.40	0.84	129
NRZ 40 Gbit/s	1550.63	1551.28	0.65	1550.90	1551.04	0.10	22
50 GHz							
RZ	1548.54	1548.83	0.29	1548.52	1548.86	0.34	117
NRZ	1548.54	1548.83	0.29	1548.63	1548.81	0.18	62

Table 4.2-1: Grating bandwidth utilisation for different signal modulation formats

One setback of this work is that despite the effort to design gratings for future 40 Gbit/s systems, experimental data mainly exists for 10 Gbit/s experiments. One exemption was made for the 50 GHz grating using NRZ modulation. Here the penalty is always over 1 dB. For a detuning tolerance of 1.3 dB only 22% bandwidth usability was achieved.

From numerical simulations of this grating type in 40 Gbit/s systems a better performance was calculated, with a detuning tolerance to be expected within 60% of the 3 dB bandwidth [*101*]. At 10 Gbit/s the NRZ modulation shows the least favourable results, one fact which might be aggravated at higher bit rates. Unfortunately no other results are at hand to date. From the characterisation of ADC gratings presented in Chapter 3.5, a re-run of the experiments using gratings written with the MPF method may promise better results.

4.3 Pulse Generation using Fibre Bragg Gratings

Fibre Bragg gratings also play an important role in the generation of short optical pulses for DWDM applications. They can be implemented to fulfil tasks as wavelength selection [*73*] and tuning [*119*], spectral filtering [*82*], dispersive pulse-width suppression [*72*], and pulse shaping [*98*].

Most of these methods can be applied to manipulate the optical output from laser diodes. The simplest method for wavelength selection, for instance is the generation of an external cavity using a grating, which does not necessarily need to be an FBG [*120*]. The light is coupled directly from the output laser facet into the fibre or upon the bulk grating. Tuning can

be achieved by alteration of the grating period by rotating a transmission grating or stretching a fibre grating. Insertion of a Raman-active section, like an Ytterbium-Erbium doped fibre into an optical cavity with an FBG at either side enables the fabrication of a fibre laser, enabling a better compatibility with fibre-based systems. Recent results have shown the high quality of fibre lasers that can be achieved [*121*].

Taking advantage of the dispersive properties of FBGs, like the linear dispersion in chirped FBGs, it is possible to shorten pulses in the time-domain and narrowing their spectrum. Often however, the ideal dispersion function is not linear but of arbitrary shape, requiring gratings of complex designs and some additional tuning mechanism [*122*].

Besides for the use within DWDM and Time Division Multiplexing (TDM) systems, the spectral shape of pulses is important for applications as all-optical switches [*123*] and Code Division Multiplexing (CDMA) [*124,125,126,127*].

In some cases, certain wavelengths of the output from a light source like a laser diode are not required for a particular purpose and have to be dropped altogether. This can be done easily by employing an FBG as a chromatic filter. The filtering of higher modes and relaxation oscillations can greatly improve the temporal features of a light pulse [*128*].

4.3.1 Fibre Grating Based Injection Seeding for the Tuning of Laser Diodes

Methods for the wavelength selection of the optical output from semiconductor based on external feedback systems have been used for a long time. These include the application of bulk gratings [*129*] and mirrors [*130*], as well as fibre Bragg gratings [*121*] as reflective elements.

In the following sections, it is shown how the use of four fibre Bragg gratings within the feed-back arm of a semiconductor laser allows the simultaneous generation of pico-second pulses at different wavelengths. Moreover, the presented set-up allows the switching between single-, dual-, and triple-wavelength operation modes. Dual-wavelength operation has been presented previously, using mode-locked lasers [*131,132*] and gain-switched diode lasers [*133,134*].

Such a device is of particular interest as a laser source in WDM systems, reducing the number of required laser sources to be included in the system.

4.3.1.1 Grating Fabrication and Experimental Set-up

For the work presented a commercial *InGaAs/GaAs* single-mode ridge wave-guide emitting at 980 nm was used with a feed-back system comprising of one 1x4 coupler and 4 FBGs with different wavelengths close to that of the main mode of the diode laser.

The gratings have been fabricated in Corning SM 980 fibre using the scanning holographic method presented in ***Chapter 3.1*** with different wavelengths around 980 nm. The exact values for the wavelengths and approximate reflectivity and their spectra are shown in *Table 4.3.1-1* and *Figure 4.3.1-1*, respectively.

Grating	G1	G2	G3	G4
Wavelength [nm]	974.2	978.0	981.4	993.8
Reflection [dB]	5.0	6.5	5.1	3.0
Reflection [%]	64	73	70	47

Table 4.3.1-1: Parameters of gratings used for non-resonant injection-seeding

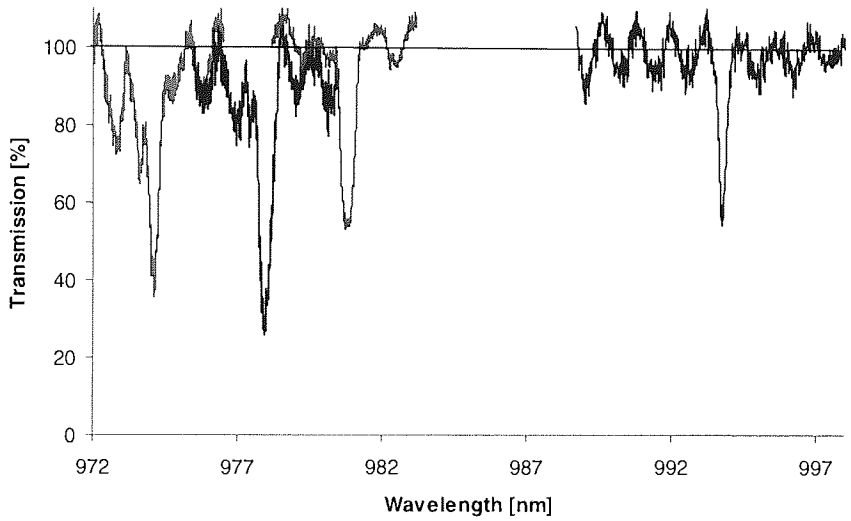

Figure 4.3.1-1: Transmission spectra of 4 FBGs written at 974 nm, 978 nm, 981 nm, and 993 nm wavelength

Because of insufficient optical power in the 980 nm region from the white light source, the noise level in the spectra is quite high. This makes an estimation of the actual grating strength difficult, especially as a resolution bandwidth of 0.5 nm had to be chosen for the same reason during the measurement with the OSA. However, by matching the measured spectra with calculated data for gratings with same length and bandwidth at 3 dB, the transmission values for the gratings *G1-G3* were estimated.

To each of the output ports, one of the four gratings was spliced, all at the same distance from the coupler. This was to assure that the light reflected from each grating took approximately the same time to reach the active layer of the laser diode, triggering the gain avalanche simultaneously, if used in a CW mode. During the experiments at St. Andrews University, the output signal from a laser was butt-coupled into the input-port of the 1x4 coupler. A schematic of the set-up is shown in *Figure 4.3-2.*

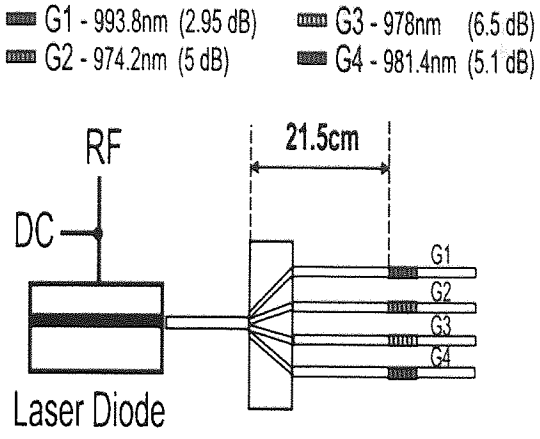

Figure 4.3.1-2: Schematic of set-up used for 4-wavelength non-resonant injection seeding of diode laser

4.3.1.2 Experimental Results

The gain dynamics for the different output wavelengths can be controlled by superimposing an RF signal over the pump current. The underlying mechanism allowing the tuning of single and simultaneous output wavelengths is thought to be non-resonant injection seeding [*135*]. Unlike in resonant self-seeding mechanisms, where the resulting wavelength is a direct result of a Fabry-Perot condition [*136*], in the non-resonant case the round-trip time, T_{ext}, in the external cavity is detuned with respect to the inverse of the modulation frequency f_{Mod} and higher modes of it.

Although it has proven difficult to find a rigid formalism for the principle of non-resonant injection seeding, experiments and qualitative theoretical analysis have shown that by controlling the modulation frequency spectral narrowing and stabilisation can be achieved alongside a tuning effect on the pulse duration. Using a multiple-wavelength cavity allows switching between the different channels. Mode hopping of the generated pulses can be induced if the phase condition of the back-reflected light is altered.

Tuning of the modulation frequency f_{Mod} in the proposed set-up between 1.80 and 2.70 GHz forced the diode laser into pulsed single, double and triple wavelength operation. *Figure 4.3.1-3* and *Figure 4.3.1-4* show the single output signals with corresponding modulation frequencies and temporal pulse shapes. Various combinations of double and triple wavelength operation with according f_{Mod} are given in *Figure 4.3.1-5* and *Figure 4.3.1-6.* The temporal characteristics for one set of singular, double and triple wavelength operation each are compared in *Figure 4.3.1-7.* The temporal offset between the three pulses is due to the optical path difference between the gratings.

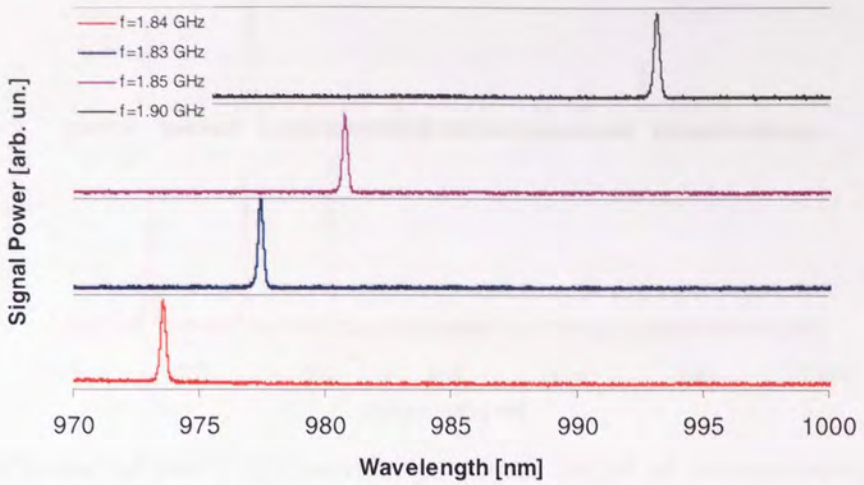

Figure 4.3.1-3: Single wavelength signal output at corresponding modulation frequencies

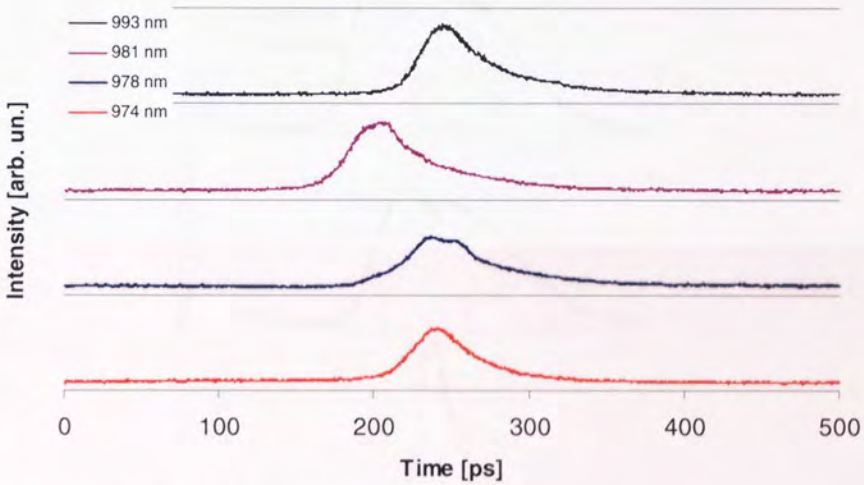

Figure 4.3.1-4: Temporal pulse shapes of single wavelength mode at corresponding wavelengths and modulation frequencies

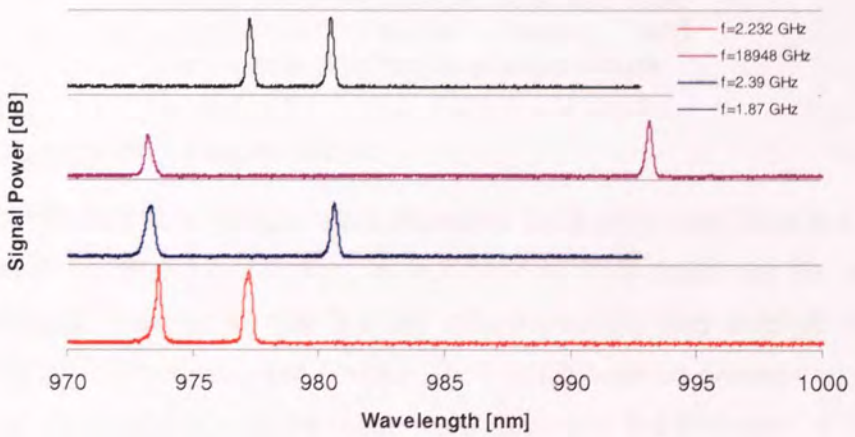

Figure 4.3.1-5: Dual wavelength signal output at corresponding modulation frequencies

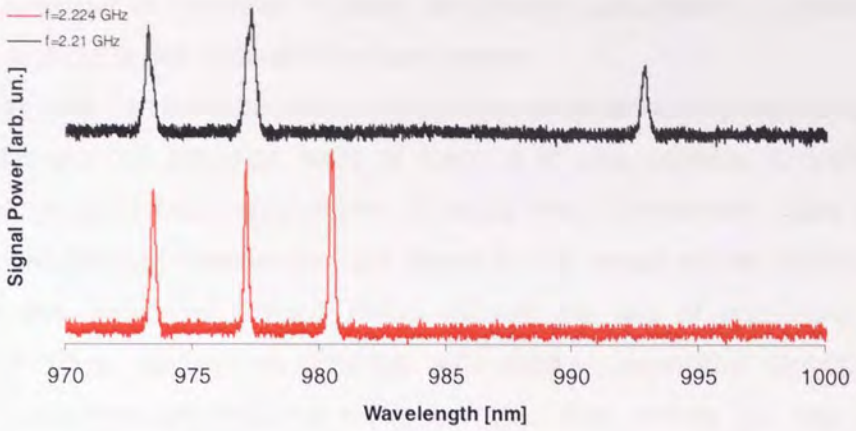

Figure 4.3.1-6: Triple wavelength signal output at corresponding frequencies

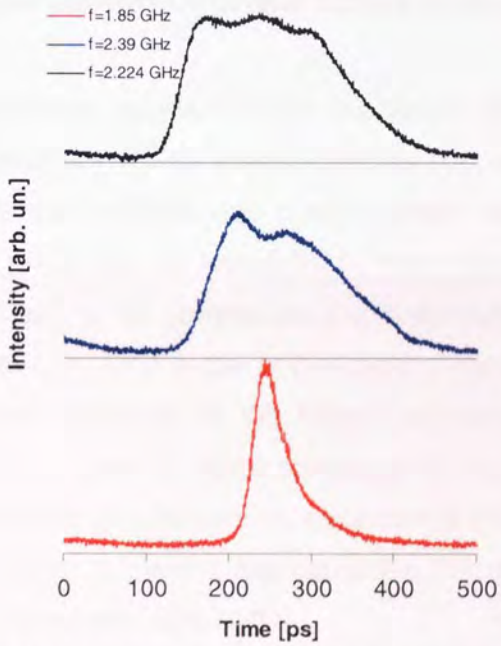

Figure 4.3.1-7: Single, dual and triple wavelength signal output and corresponding temporal pulse shape

4.3.1.3 Summary and Future Work

In theory N! different sets of signals are expected to be generated from this set-up with N being the number of different channels, in our case 4. This could not be realised in this experiment. Possible reasons for that are the differing quality and strength of the gratings used, interfering effects from the 1x4 coupler, the path difference between the gratings, the intrinsic spectral characteristics of the diode laser itself and the limitation of the modulation range.

However, the principle of tuneable multiple wavelength generation of picosecond pulses employing this technique has successfully been proven.
Further improvements can be expected using gratings of better quality regarding wavelength, bandwidth and uniformity amongst each of them. It is also possible to include a higher number of gratings, and thus wavelengths to select from. Additionally, fibre optic devices offer further possibilities of wavelength and phase tuning under stable conditions widening the options of the presented set-up. These include the use of apodised, chirped and phase-shifted gratings, as well as gratings with tailored dispersion characteristics. The application of superimposed gratings within a single fibre makes the use of a coupler obsolete and can successfully eliminate the path difference for the pulses of different wavelength.

4.3.2 Pulse-Width suppression of Diode Laser Output by Spectral Filtering

Their size, degree of technical standardisation and simple principle of operation makes gain-switched distributed feedback (DFB) lasers ideal as sources for pico-second pulses. One downside, however, is the relatively low output power, which is achieved in normal operation mode. The pulse power can be increased by overriding the diode laser, but at the cost of spectral degradation due to the generation of optical relaxation modes, which lead to a significant temporal broadening of the pulse. In the spectral domain this effect shows as an additional narrow-band peak appearing at the longer wavelength region of the original broadband laser spectrum. This peak is the direct source of the relaxation tail occurring in the time domain. It has previously been shown on a number of quantum-well DFB lasers with wavelengths around 1550 nm, that spectral filtering of the relaxation oscillation modes can successfully suppress the pulse width [*128*,*137*].

4.3.2.1 Grating Fabrication

Using fibre gratings fabricated by the scanning-holographic method, the filtering of the relaxation oscillation tail of an overridden *GaAs* gain-switched DFB laser diode emitting at 860 nm wavelength is presented. The laser is coupled straight into an optical fibre with one or a number of gratings, from which the light is incident on a detector. Using the gratings purely as loss-filter and in transmission only, the set-up does not require any circulators or other optical components, making it a simple and easy to implement solution.
The gratings were written in Newport 820 single-mode fibre, which was UV-photosensitised by high temperature high pressure H_2-loading over a period of several days.
A circular 1-inch, 836 nm uniform phase-mask was used as a beam-splitter in the set-up. The first grating, *G1* was fabricated using a stationary beam, whereas the 17 mm long *G2* was

written by a scanning beam. This resulted in the different grating bandwidths, as can be seen in *Figure 4.3.2-1.*

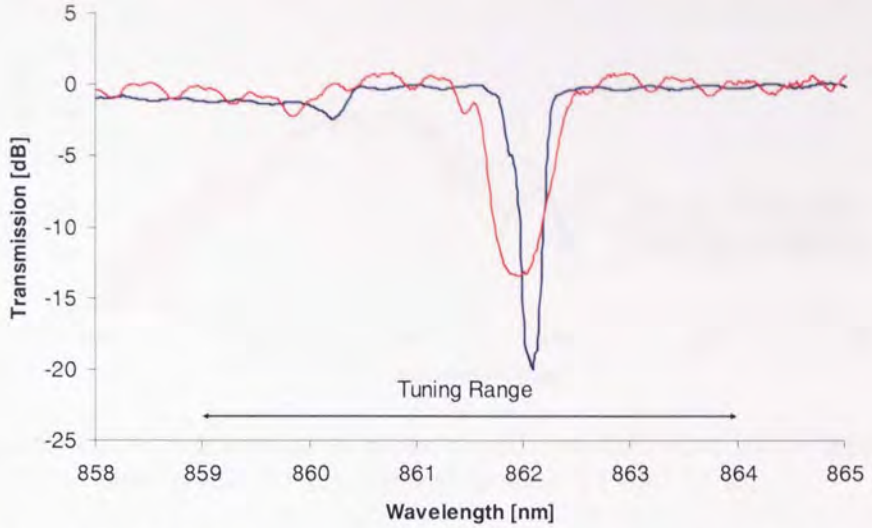

Figure 4.3.2-1: Transmission spectra of 1 mm (red) and 17 mm long (blue) uniform FBG at 862 nm wavelength with indication of tuning range

After the inscription process, the gratings were annealed at 80º C for 24 hours, during which the wavelength shifted towards the lower wavelength region for about 0.5 and 0.6 nm. The central grating wavelength was aimed to be around 860 nm, matching or being within the tuning range of the relaxation oscillation peak. In the experiment grating tuning was achieved using a tuning ring [*138*], with which the grating period was compressed down to the required value.

4.3.2.2 Experiments and Results

The laser was fabricated and provided by Glasgow University. It had a cavity length of 1400 μm and was operated by an attenuated electrical driving current with 780 V maximum peak signal. The raising and falling time of the pulses were 150 ps and 1 ns, respectively at a repetition rate of 10 kHz.

Figure 4.3.2-2 shows the initial output spectrum of the diode laser (a) and after filtering through G2 (b), and both gratings simultaneously (c). Both relaxation peaks, the larger with a 0.1 nm bandwidth around 860.8 nm, and a smaller one with a 2 nm bandwidth around the 859.5 nm wavelength, are significantly reduced after the signal passes the fibre gratings.

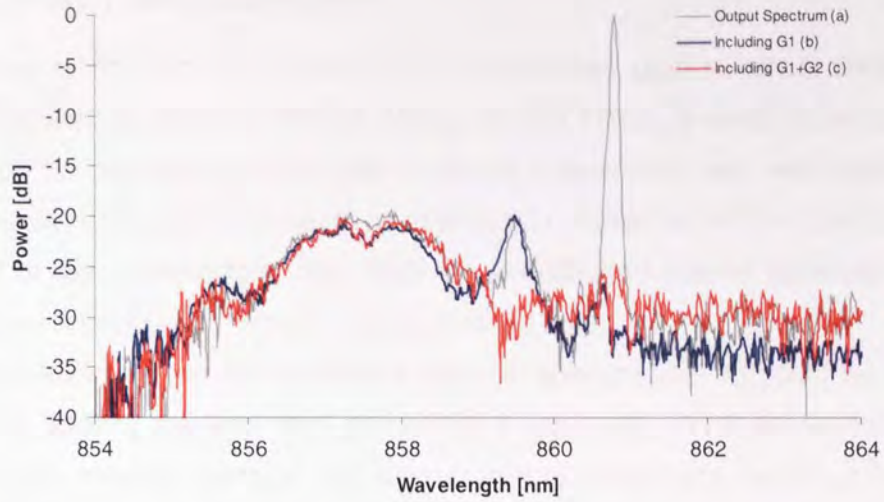

Figure 4.3.2-2: Spectrum of pulse directly emitted from diode laser (a) and after filtering with G1 (b) and both grating G1 and G2 (c)

The effect on the pulse duration can be seen in *Figure 4.3.2-3*. The pedestal of the pulse decreases in size as the gratings are tuned one after the other to match the peak wavelengths of the relaxation oscillations, showing the direct correlation between the spectral peaks and the temporal peak broadening. It also becomes evident that the peak at 860.8 nm wavelength has the greater impact on the pulse duration, compared to the peak at the short-wavelength. The filtered optical pulse had the duration of 46 ps and a peak power of 120 mW.

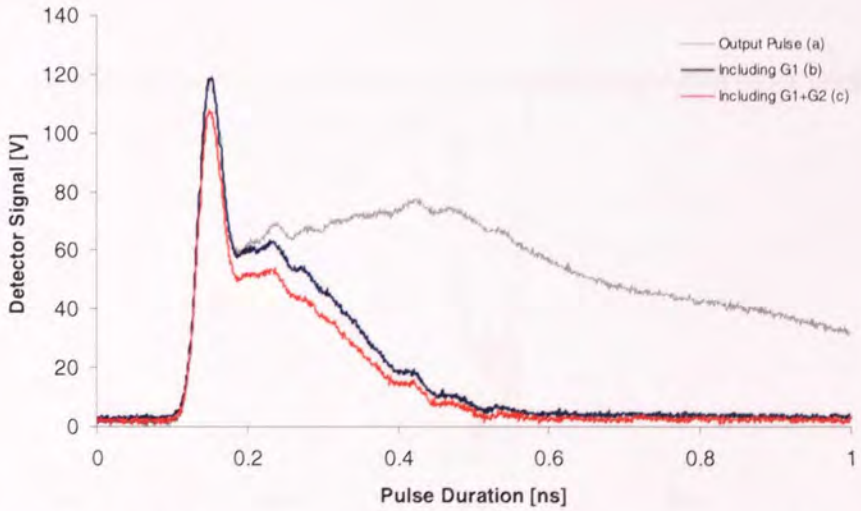

Figure 4.3.2-3: Pulse width from diode laser output without filtering (a), after filtering with G1 (b) and both grating G1 and G2 (c)

4.3.2.3 Summary and Future Work

The pulse width from the output of an overridden gain-switched DFB laser was successfully reduced by spectral filtering. Using tunable FBGs, a direct correlation between pulse-width and the out-filtering of the laser's relaxation oscillation peak was established.
However, a significant pulse tail remains even after an optimisation of the grating wavelength tuning. A part of this problem may stem from a non-optimised internal laser-diode structure, resulting in a poor distributed feedback and gain in the laser.
One second possible reason for the limited effect of spectral filtering could be the fact that despite spectral filtering the light level above 859.5 nm is still 10 dB above the noise-level, which means that stronger gratings may be required to completely suppress the unwanted side-peaks. Spectrally these features also stretch over a wider wavelength range than both gratings can cover, even if applied at the same time. The use of chirped FBGs is the most obvious response to this problem. During the course of this work chirped gratings have been written, but not yet used in any experiments. *Figure 4.3.2-4* shows the transmission spectrum of a chirped FBG at 860 nm wavelength written in a hydrogen-loaded SM 820 fibre from Newport.
The grating wavelength is well centred around 860 nm and the insertion loss exceeds 15 dB over a bandwidth of 1.5 nm. At the short wavelength side of the Bragg wavelength an additional loss band is visible with a maximum peak of 3.5 dB at 857.4 nm. This may origin from a tilt of the grating with respect to the fibre axis due to an inaccuracy of the alignment during the writing process.

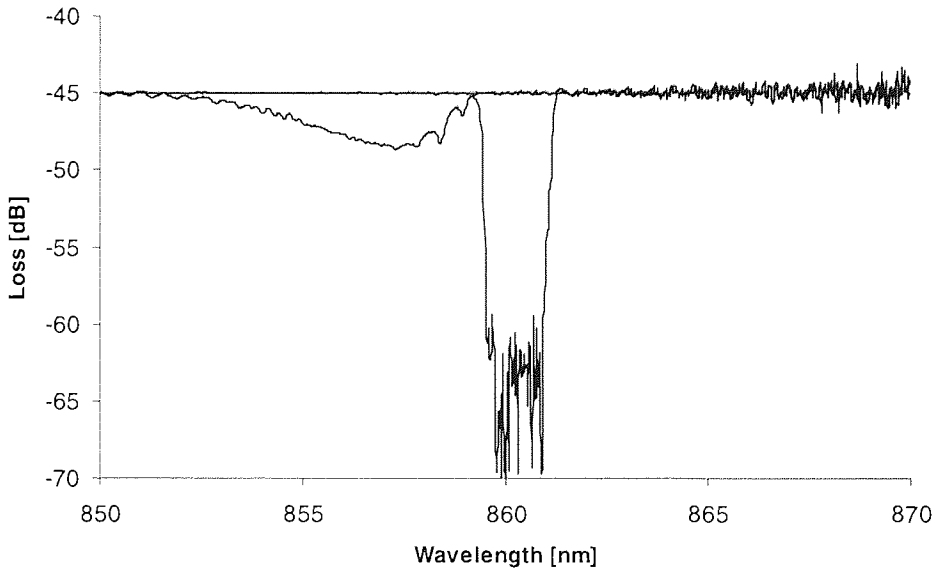

Figure 4.3.2-4: Transmission spectrum of 10 mm long self-apodised chirped FBG at 861 nm wavelength

If this grating is used as a filter in transmission this artefact will overlap with a part of the main laser output spectrum and thus weaken the signal.

Whether the benefits or drawbacks of a set-up incorporating these gratings prevail has to be proven experimentally. A second solution may be the use of the chirped gratings as a reflection filter. However this would require the use of an optical circulator, adding to the cost and complexity of the set-up. Another drawback is also that the grating bandwidth is not sufficient to cover the full spectrum of the laser signal. However one possible benefit is the linear chirp of the grating, which can lead to additional pulse suppression due to chromatic dispersion.

5 LONG PERIOD GRATING BASED SENSING DEVICES

5.1 Introduction

The basic concept of long period gratings (LPG) has been introduced in ***Chapter 2.1*** regarding their theoretical formalism and in ***Chapter 2.6*** regarding their fabrication. An LPG is a periodic refractive index perturbation in an optical fibre. Unlike in Bragg gratings, this can involve the fibre core and the cladding, which is the case for gratings written with an electric arc. In contrast to fibre Bragg gratings which have a period of typically ~500 nm, the period in a LPG may vary between 5 and 600 μm. Its principle is based on the out-coupling of power from the core mode into a multitude of co-propagating cladding modes in the grating section.
Long period gratings show high sensitivity for a large variety of measurands apart from strain and temperature, for which FBGs can also be employed. Because the waveguiding condition depends on the refractive indices of core, cladding and surrounding media, LPGs and LPG based devices are commonly used for refractive index measurements [*139*]. This is of particular interest for chemical and biological sensor applications [*140*]. Additionally, due to the tube-like geometry of the cladding instead of the cylindrical shape of the core, LPG-devices can also be used as bending and curvature sensors [*141*]. For the same reason birefringence of a fibre affects LPGs to greater extent than FBGs. This can cause the splitting of the attenuation band by 40 nm or more. Based on this effect the concept of a fibre grating based load sensor has been proposed [*65*].
Besides the use as sensors, long period grating devices can also be employed in telecommunication applications, as gain equalisers and spectral filters [*142*]. An overview over some aspects of this topic is given in a review by Vasiliev et al [*143*].
The focus of the work presented here was laid on three different scopes. The first is on vectorial bending sensors using azimuthally asymmetric fibre types or standard fibre with a modified cladding. The second topic is on an optically tuneable modulator based on a fibre Mach-Zehnder interferometer, which in return can also be used as refractive index and temperature sensor with tuneable sensitivity. The last part addresses long period structures in tapered fibres, which in particular can be used for refractive index sensing.

5.2 Towards a vectorial Curvature Sensor using Long Period Gratings

Fibre grating based strain and bending sensors nowadays are used for the monitoring of structural changes and elastic deformations in buildings, aeroplanes, ship hulls and for the automotive industry [144]. For strain measurements either FBGs or LPGs can be used. For bending using FBGs, more complex waveguide and grating structures are necessary, such as, for example, four-core fibres [*145*]. Standard long period gratings can detect bending curvature with radii of 1 m or more [*141*], but not the plane and direction in which the bending takes place.

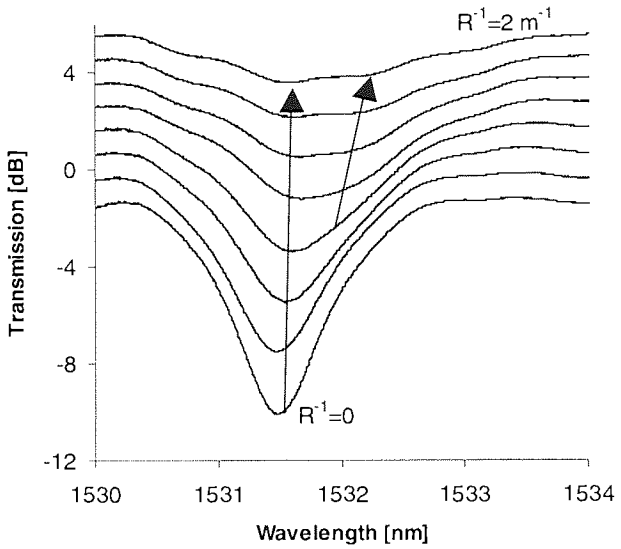

Figure 5.2-1: Wavelength shift and attenuation band splitting in FBG due to fibre bending (signal power shifted for clarity)

This is shown in Figure 5.2-1, where the bending of a fibre LPG manifests as a wavelength shift and attenuation band splitting due to a change in the mode coupling mechanism. The grating Parameters are L=50 mm, Λ=380 μm, written in a SM 28 standard fibre. Because of the circular geometry of the fibre cross-section, a bend along any azimuthal angle results in a wavelength shift of the same magnitude.

Up to a curvature of R^{-1}=2 m^{-1}, only a blue wavelength shift is observed. Above this value the attenuation band splits due to bend induced birefringence. The initial peak continues to shift towards shorter wavelength, whereas the secondary band shows a red-shift. The shown results are near constant for bending within any plane defined by the fibre core, given that the curvature is of identical magnitude.

The ability to fabricate a sensor that can detect both curvature radius and azimuthal direction of the bend opens a large field of novel applications for fibre sensors. Such three-

dimensional shape sensors can be used for diagnostics in medical applications [*146*] or as advanced formats of existing systems. Another area of interest is the defence sector [*147*].

5.2.1 Long Period Gratings in elliptical Core Fibres

In a first step, the geometry can be broken by using fibres with an elliptical core. These are speciality fibres that are commercially available, for example from FibreLogix. The boundary condition for the light guidance guiding in the core mode is changed insomuch that due to the induced birefringence two modes persist, one TE and one TM mode. These are also often referred to as "slow" and "fast" mode, reflecting the difference in their respective propagation constants. Incident on a fibre grating, each of these modes shows a separate resonance peak. Generally birefringence is an unintended side-effect due to imperfections of a waveguide. However, for some applications it can have beneficiary properties and part of the device design.

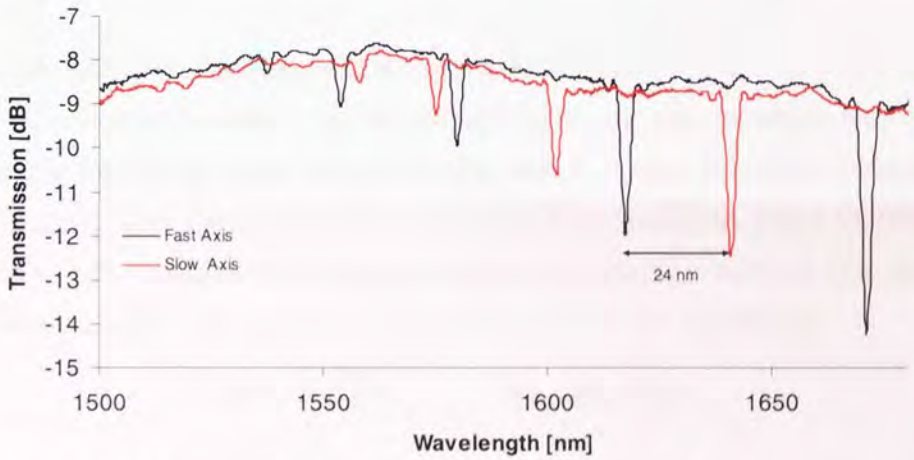

Figure 5.2-2: Spectral splitting of long period grating response in elliptic core fibre due to different propagation constants of orthogonal modes

The spectrum of a long period grating written in a fibre with elliptical core is shown in *Figure 5.2-2*. Depending on the order of cladding mode inducing the attenuation band, the wavelength separation reaches up to 24 nm over the shown range. The fibre core has large semi-axis of 5 µm and a small half-axis of 3 µm. The grating is 4 cm long and was UV-inscribed using the point-by-point method with a period of Λ=400 µm. The spectra were taken using a polarisation controller to discriminate between the two polarisation states. Additional gratings were written with at different periods, showing comparable features.

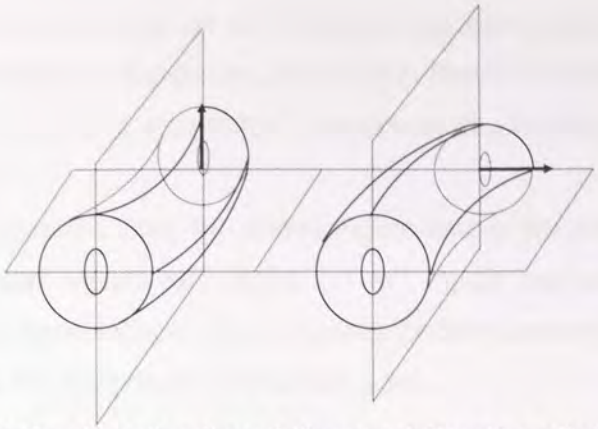

Figure 5.2-3: Bending direction of fibre as defined by elliptic semi-axes

Considering the geometry, it may seem plausible that a curvature applied to a log period grating device in an elliptical core can discriminate between bending in the planes of the two core semi-axes, as indicated in *Figure 5.2-3*. Ideally, this assumption implies that a curvature in the plane of one semi-axis will not affect the attenuation peak assigned to the mode in the other plane.

This was tested using the test apparatus described in *Figure 5.2-4*. The Fibre was clamped in a stretched condition between two mounting blocks, on one of which was placed on a one-dimensional translation stage aligned in line with the fibre. The initial distance between the fibre clamps L_0 was measured and by moving the translation stage inwards, the fibre section in the middle, containing the grating sagged by a displacement *d*. The fibre curvature was approximated to be a circular arc. The curvature R^{-1} is the defined as:

$$R^{-1} = \frac{2d}{\frac{L^2}{4} + d^2} \qquad \text{Equation 5.2-1}$$

For each set of *L* and *d* spectra were taken for the fibre in the hanging position, as well as rotated around the initial fibre axis by 90°, 180°, 270° and 360°. A schematic of the set-up is presented in *Figure 5.2-4*.

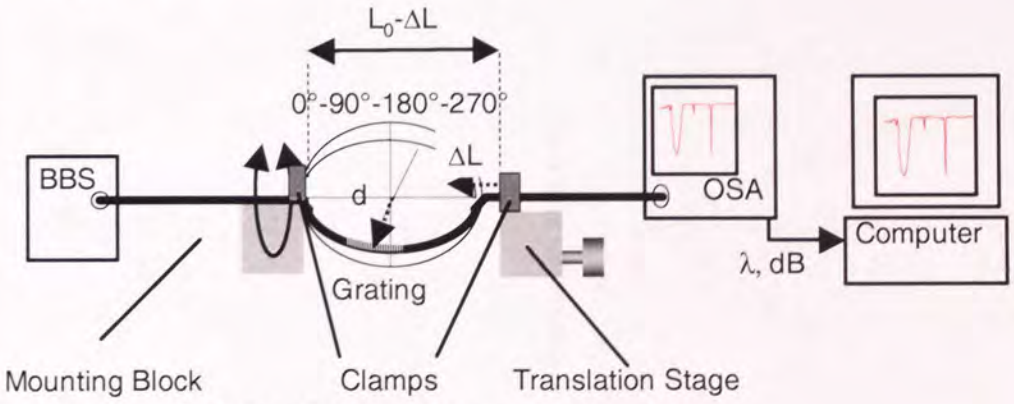

Figure 5.2-4: Bending test apparatus

All measurements were taken using an OSA with a broadband light source. An example of wavelength shift and splitting of the grating attenuation bands with increasing curvature can be seen in *Figure 5.2-5*, showing results for the resonance of light polarised along the slow axis.

In contrast to LPGs in standard fibre, the above Figure shows the splitting of the attenuation bands starting at curvature values just above 0.1 m^{-1}. Again the standard loss band shifts towards shorter, and the bend-induced band towards longer wavelengths. One notable effect is the initial red-offset of the secondary attenuation peak.

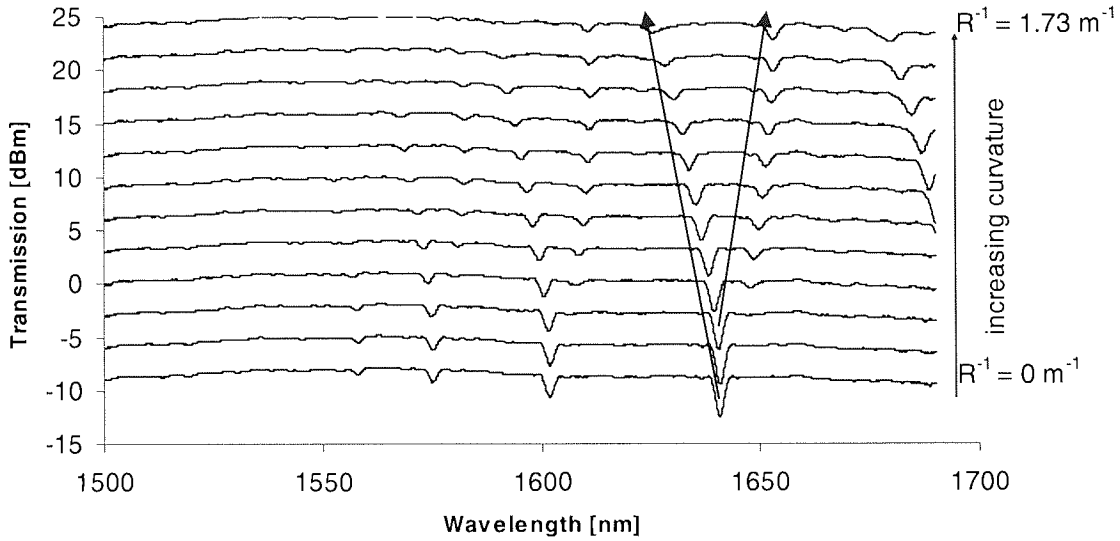

Figure 5.2-5: Spectral splitting over curvature (signal power shifted for clarity)

Here we differentiate between "standard" or "normal" and "bend-induced" attenuation peaks. The former shift continuously with increased bend curvature, whereas the latter start appearing at a threshold value for the bending radius. The bending induces new sets of phase matching conditions due to its influence on the phase and power distribution of the wave propagating through the fibre.

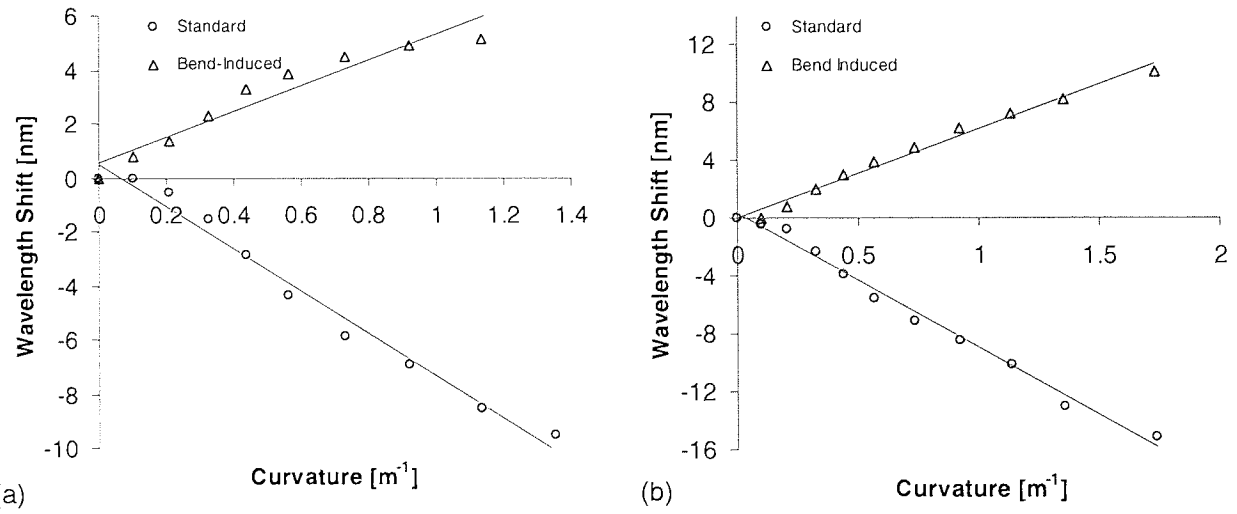

Figure 5.2-6: Bending sensitivity curves for slow (a) and fast axis (b)

The spectral curvature sensitivity for the attenuation band shown in Figure 5.2-5 at 1601 nm and the corresponding results for the fast polarisation axis are presented in Figure 5.2-6.
From linear regression curves of the spectral shift of standard and band-induced attenuation band in each respective polarisation state the spectral sensitivity values of the device $d\lambda/dR^{-1}$ were obtained. For the fast axis polarisation this is -9.4±0.5 nm·m for the normal band and 6.2±0.7 nm·m for the bend-induced loss peak.
The values for the slow axis are -8.2±0.6 nm·m for the initial loss band and 4.2±0.8 nm·m for the secondary band.
The difference can be explained as follows. A curvature on the fibre causes a distortion of the electric mode fields in the cladding sections within the inner and outer radius of the bend. This results in the splitting of the attenuation bands. As the orthogonal modes in the elliptic fibre have different electric field distributions, their phase-matching conditions also differ, resulting in different rates of wavelength shift under bending.
The above results were obtained from the configuration in which the middle fibre section was hanging between the two mounting towers. Measurements taken while the fibre grating was rotated around the fibre axis for L_0 did not yield significant changes from the sensitivities presented above. The obtained results are not strong enough to achieve a vectorial sensor system, particularly as the set-up does not provide the exact azimuthal angle of bending.
However, the large birefringence effect can be exploited for a different sensor system, like the discriminatory temperature and strain sensor described later in ***Chapter 6.5***. For a multi-parameter sensor at least the same number of spectral features is required as measurands, which have to show different ratios of their sensitivity parameters compared to each other. Therefore the LPGs in elliptical core fibres may be employed as dual temperature-bending sensors.
For the measurement of the temperature coefficients gratings were sandwiched between a 5W Peltier element and a block of Styropor. The whole arrangement was placed within a plastic box. The heating element with an integrated temperature probe was connected to a computer controlled current source and temperature indicator. The grating spectrum was continuously monitored using a broadband light source (BBS) with an OSA. This is indicated in *Figure 5.2-7*.

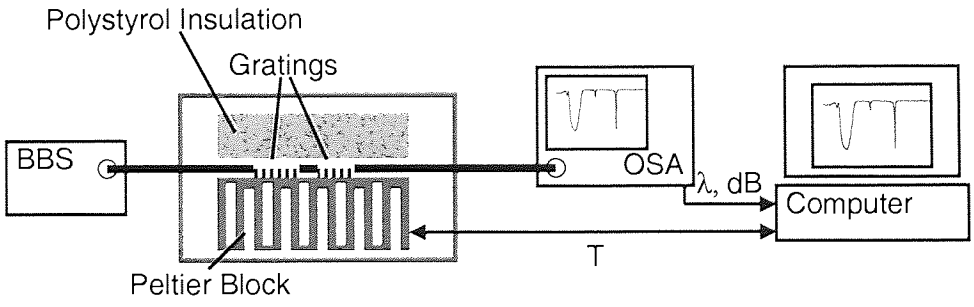

Figure 5.2-7: Measurement set-up for temperature coefficients of FTLPGs

In general the temperature was set to start from 20°C and then to rise in 5°C increments to 80°C. As soon as the temperature reached the programmed temperature and stayed stable within a margin of ±0.1°C, the actual grating spectrum was captured on the OSA and the data saved in a file.

From *Figure 5.2-8* it becomes clear that the splitting of the attenuation bands for polarisation along slow and fast axis due to strain also depends on temperature. The temperature sensitivity of normal and bend-induced peak for both polarisations is shown for the same attenuation bands as in *Figure 5.2-6*.

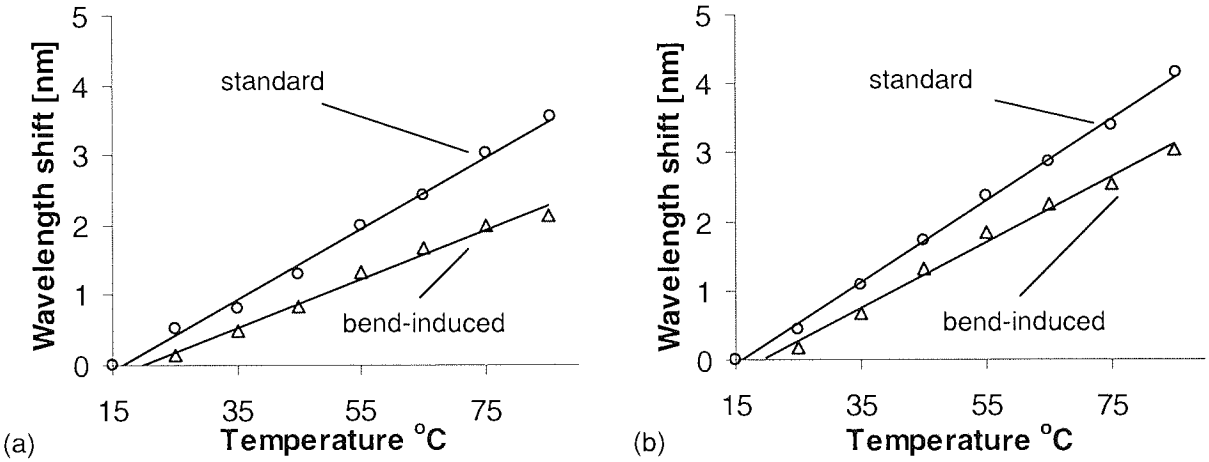

Figure 5.2-8: Temperature sensitivity curves for slow (a) and fast axis (b), measured under curvature of R^{-1}=0.2 m^{-1}

Linear regression through the measurement points yields a temperature dependent spectral sensitivity $d\lambda/dT$ of 59 ± 5 pm·°C^{-1} and 48 ± 8 pm·°C^{-1} for the standard and bend-induced attenuation bands of the fast axis polarisation. For propagation along the slow axis the values are 51 ± 8 pm·°C^{-1} for the normal peak and 35 ± 8 pm·°C^{-1} for the secondary peak. The performance of discriminatory sensors is defined by the condition number, which is 174 for the fast axis and 200 for the sow axis. These values compare well to the results obtained with other fibre grating based discriminatory sensors [*148*].

5.2.2 Directional Curvature Sensing in Standard Fibre with Modified Cladding

Besides the elliptic core concept, there are other designs to achieve fibres with asymmetric guiding properties, like D-shape [*149*] or eccentric-core fibres [*150*]. The most obvious problem is the incompatibility to standard systems and problems with coupling light into and out of the fibres. Presented here is a simple concept based on standard SM 28 fibre.

In a first step, a long period grating was UV-inscribed into the hydrogenated fibre using the point-by-point technique. The grating had a period of 400 μm and was 5 cm long. In a following process the cladding structure around the grating was altered using a focussed femtosecond beam. Unlike with standard UV lasers, modifications of the glass structure by high-power femtosecond-illumination at 800 nm do not require inherent photosensitivity of the material, hence enabling the modification of the cladding. Through a microscope objective the beam was focused down to a spot size of about 5 μm at a distance $d_{core-mod}$ from the core centre. It was then scanned at constant focus distance parallel to the fibre core. The 150 fs pulses with 1 kHz repetition rate show sufficient overlap during the scan, inscribing a continuous waveguide structure of radius R_{mod} into the cladding. The schematic in *Figure 5.2-9* shows the general idea for the resulting fibre structure.

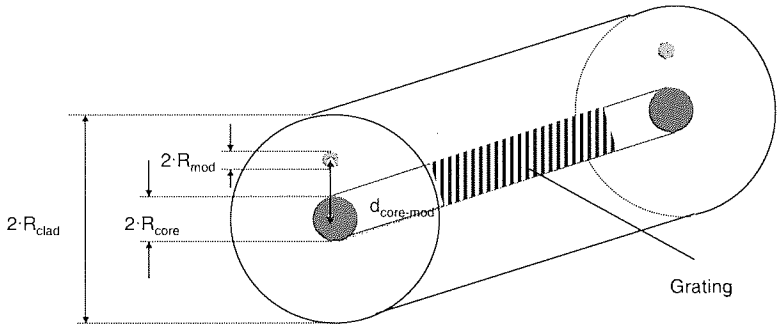

Figure 5.2-9: Cross-section of fibre with modified cladding

The bending properties of the device were tested using the same set-up as shown in *Figure 5.2-4*. The only difference is that the fibre section containing the grating was put into a tube to prevent any disorientation of the fibre curvature. The bending is defined to be convex, when the modifications in the cladding are at the outer radius of the curvature and concave in the opposite case. The bending curvature is defined by *Equation 5.2-1*, as previously.

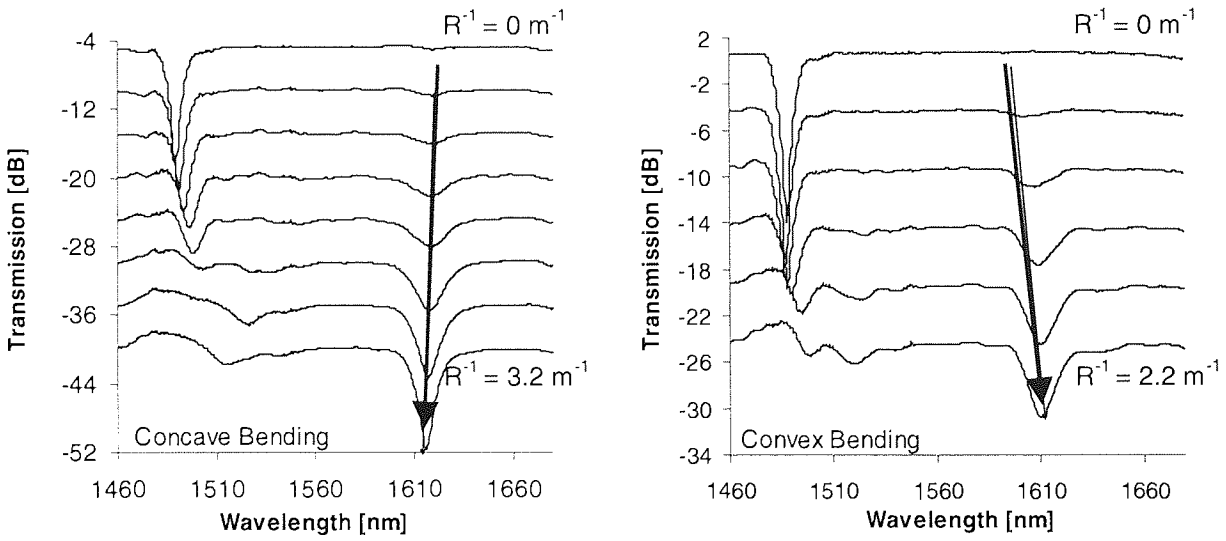

Figure 5.2-10: Spectral shifts for convex and concave bending (signal power shifted for clarity)

The spectral response of one of the grating attenuation bands to bending under convex and concave conditions is shown in *Figure 5.2-10*. The structure of this fibre grating included three regions with cladding modifications, each of radius R_{mod}=2.5 μm. Two were placed at opposite sides of the fibre core at a distance of ~6 μm, and a third one in the same plane, but at a distance of 24 μm. Here the bending is defined to be convex, if the single cladding modification is within the inner radius of the bend.

Reaching a bending curvature of R^{-1}=0.3 m^{-1} the splitting of the attenuation band can be observed, as described earlier. The normal loss peak shows a red shift for either direction of the bend, whereas the bend-induced band changes sign. The wavelength shift for both cases is displayed as a function of curvature in *Figure 5.2-11*.

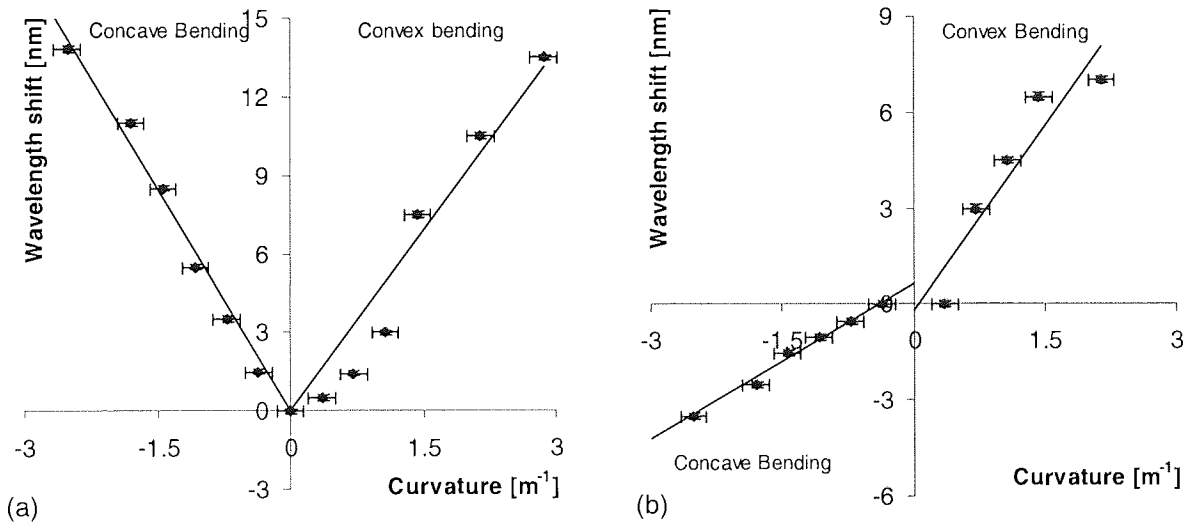

Figure 5.2-11: Spectral sensitivity graphs for standard peak (a) and bend-induced peak (b) under convex and concave bending

The sensitivity factors $d\lambda/dR^{-1}$ obtained from the regression slopes show values of 5.6±0.1 nm·m for concave bending and 4.6±0.2 nm·m for convex bending at the standard band at 1500 nm. The equivalent values for the bend-induced band are -1.6±0.1 nm·m and 3.8±0.5 nm·m for concave and convex bending, respectively. The wavelength shift of the normal band resembles the behaviour of a standard LPG in untreated SM 28 fibre, although showing higher sensitivity for small curvatures. The bend-induced band in contrast shows a break of symmetry, which allows for the distinction between the bending directions in one plane.

This is once more emphasised in *Figure 5.2-12*, where the spectral shifts due to convex and concave bending of a LPG in a standard fibre is compared to those after femtosecond laser

modification introducing one cladding waveguide of 5 μm diameter at a radial position of 9 μm.

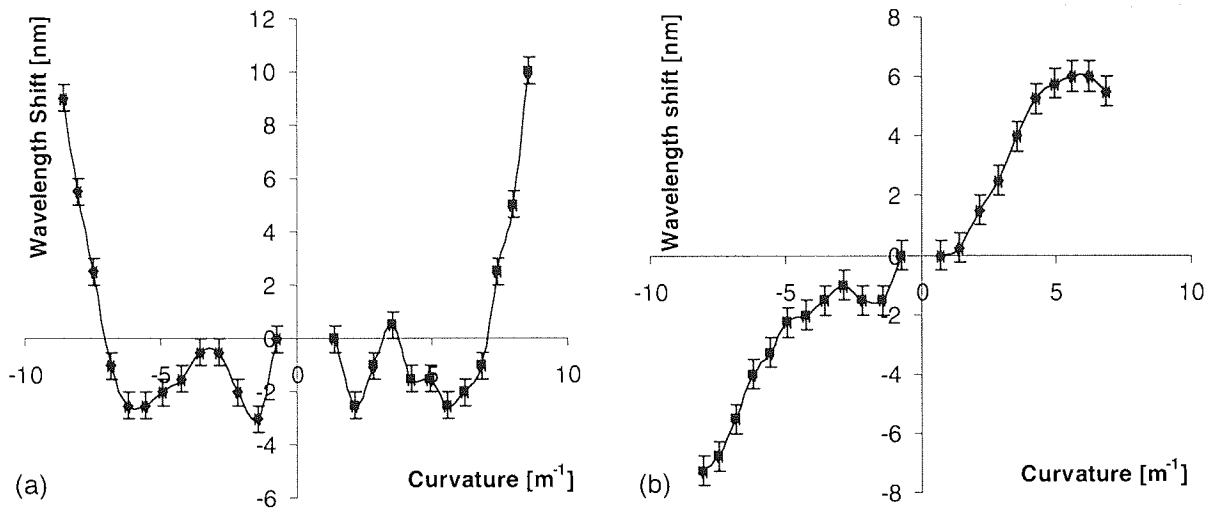

Figure 5.2-12: Spectral shift due to convex and concave bending in fibre long period grating before (a) and after cladding modification (b)

5.2.3 Conclusions and Future Work

Long period gratings were inscribed into elliptical fibres and round core fibres with modified cladding structure. Investigation of the former grating type showed attenuation band splitting of 24 nm due to the intrinsic birefringence in the fibre. Values of spectral sensitivity to bending between -9.4±0.5 nm·m and 4.2±0.8 nm·m were found, depending on the axis of polarisation and the observation of the standard or bend-induced peak. Marginal differences were found in these values for bending at different azimuthal angles, but these were insignificant and not ambiguous enough for the use as a directional bend sensor. However, the large birefringence effect and the attenuation band splitting were shown to provide a concept for the simultaneous measurement of curvature and temperature. Temperature sensitivity values between $d\lambda/dT=59\pm5$ pm·°C^{-1} and 35±8 pm·°C^{-1} were found, resulting in condition numbers between 174 and 200 defining the discriminatory performance of this kind of sensor.

A long period fibre sensor distinguishing between convex and concave bending in one plane was found by applying a uniform modification of the cladding parallel to the fibre section containing the grating. The observed wavelength shifts due to a curvature are of the magnitude of several nm per metre of bending radius, where the shift of the bend-induced attenuation band changes its sign when switching between concave and convex bending.

This principle promises the fabrication of vectorial sensors in very short time, if two cladding modifications of different parameters are applied within two perpendicular planes crossing in

the core centre. Their properties may differ in radius of the modification region, its distance to the fibre core, the total refractive index change, or any combination of these. The expected results may even be more pronounced if this technique was applied to an elliptical core fibre, along the lines defining the two half-axes.

For both fibre types the attenuation band splitting occurs at relatively low curvature values of $R^{-1} \geq 0.1\ m^{-1}$, compared to the value of $R^{-1} \geq 2\ m^{-1}$ in standard fibre.

5.3 In-Fibre Mach-Zehnder based Devices

One common application for which long period gratings are used is the concept of an in-fibre Mach-Zehnder Interferometer (MZI). These devices are based on two long period gratings separated by a section of standard fibre as cavity length [151]. After the coupling of energy from the core mode into different cladding modes, waves travelling through core and cladding will encounter different propagation constants, resulting in different optical path lengths, before being combined again by the second grating. Such devices were shown to be accurate sensors for measurements of refractive index changes in the core [*152*] or surrounding media [*153*], non-linear effects in the fibre core [*154*], temperature [*155*], strain, load and bending [*156*]. Furthermore, they can be applied in telecommunications applications, such as narrow-band multi-channel filters [*157*], isolation filters [*158*] and fibre modulators [*159*].

5.3.1 Experiments and Results

The principle of a fibre MZI is demonstrated in *Figure 5.3-1*. It reaches its maximum efficiency when two LPGs with 50%, or 3 dB, transmission are written in a fibre with an arbitrary cavity length L_{cavity} between them.

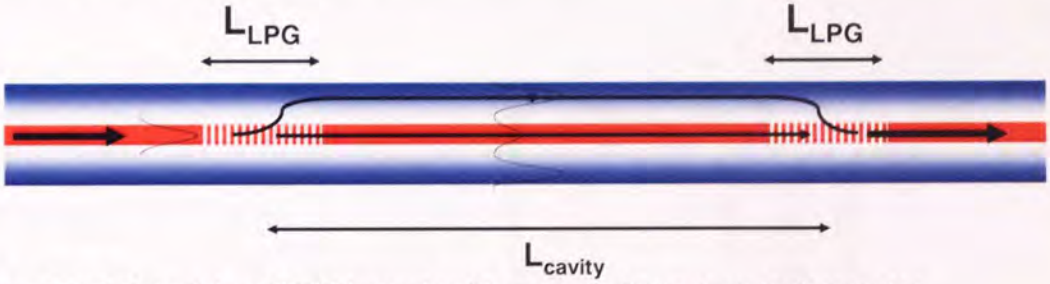

Figure 5.3-1: Principle of LPG based in-fibre Mach-Zehnder interferometer

Another crucial requirement is a good spectral overlap of both LPGs, as the grating bandwidths determine the spectral width of the response spectrum. A resulting spectrum for a fibre MZI comprising two gratings with a period of 382 μm, which are each 22 mm long and separated by 13.7 mm from centre to centre, is shown in *Figure 5.3-2* overleaf.

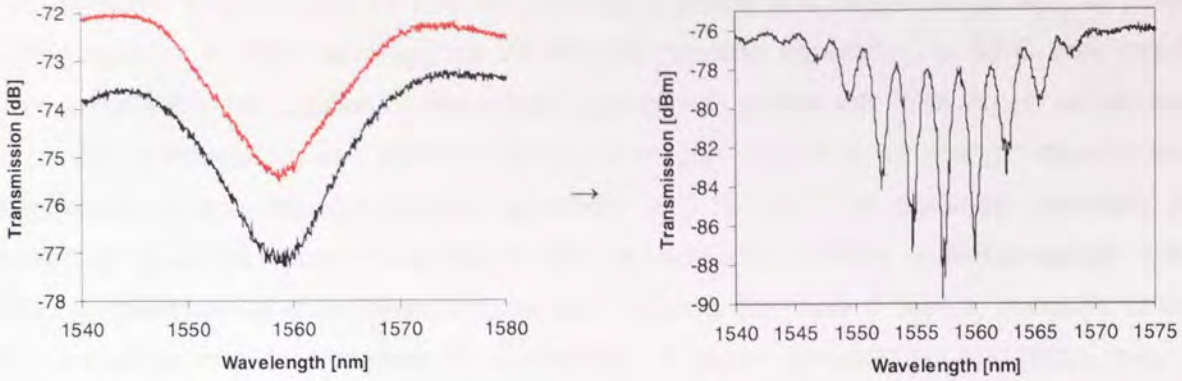

Figure 5.3-2: Combination of two 3 db LPGs (a) into in-fibre Mach-Zehnder interferometer (b) with $l_{grating}$=22 mm, l_{cavity}=13.7 cm

From considerations of the phase relations of the core and cladding modes, the fringe separation S within a fibre MZI can be approximated by a function of the spectral wavelength and the cavity length [*160*].

$$S \approx \frac{\lambda^2}{\Delta m L_{cavity}} \qquad \textbf{Equation 5.3-1}$$

The term Δm is the spectrally varying function of the refractive effective index difference between core and cladding modes Δn_{eff} defined by *Equation 5.3-2*.

$$\Delta m = \Delta n_{eff} - \lambda \frac{d}{d\lambda} \Delta n_{eff} \qquad \textbf{Equation 5.3-2a}$$

$$\Delta n_{eff} = n_{eff}^{core} - n_{eff}^{clad} \qquad \textbf{Equation 5.3-2b}$$

One convenience of Mach-Zehnder devices is the fact that the described configuration can be used for both sensing and switching/modulation applications. One example for how it can be used as temperature sensor is given in *Figure 5.3-3*. For the measurement a set-up like the one described previously in *Figure 5.2-7* was used.

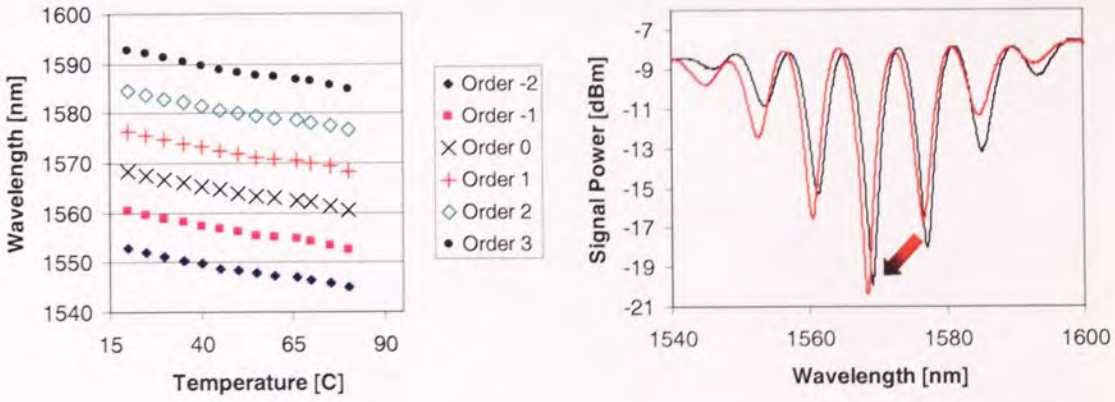

Figure 5.3-3: Wavelength shift of MZI spectrum at temperatures between 19°C and 80°C (left) and showing phase shift of almost 2π (right)

A temperature change from 19°C to 80°C shows a phase shift of almost 2π with all peaks shifting towards shorter wavelengths. At the end position equivalent to 80°C they nearly overlap with the initial position of their neighbouring peak to their left. This effect can be used for temperature sensing in a passive device. From the slopes of wavelength change with temperature, a spectral temperature sensitivity of 0.12 nm/°C is obtained. Inversely by controlling the temperature of the MZI, it can be used as a tunable multi-wavelength filter. Using temperature as a switching mechanism is not a convenient choice, because of the slow response and the problem of maintaining a given temperature accurately over a prolonged time.

One possible tuning mechanism is using the polarisation dependency of such a set-up if an intrinsically birefringent Erbium-Ytterbium doped fibre is inserted into the interferometer cavity [*161*].

A similar set-up is shown in *Figure 5.3-4*, in which the tuning of the response spectrum results from non-linear photorefractive effects in the Er/Yb doped section due to optical pumping with a 980 nm diode.

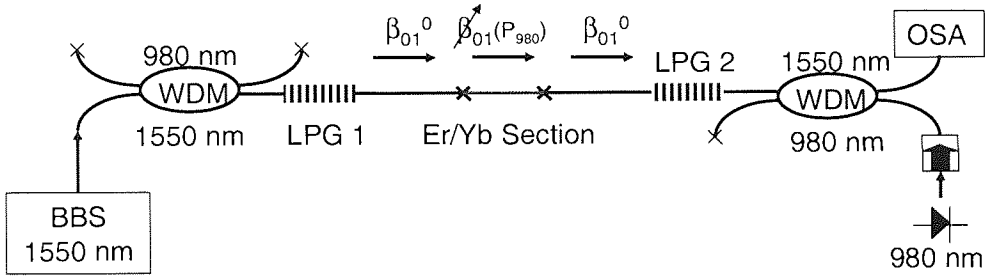

Figure 5.3-4: Experimental set-up for optically tunable in-fibre Mach-Zehnder interferometer

By optically pumping the active fibre section, the core refractive index is changing due to non-linear optic and thermal effects. The resulting change in the propagation constant for the core mode causes a wavelength offset of the Mach-Zehnder spectrum. This is shown in *Figure 5.3-5* for pump currents between 0 mA and 150 mA.

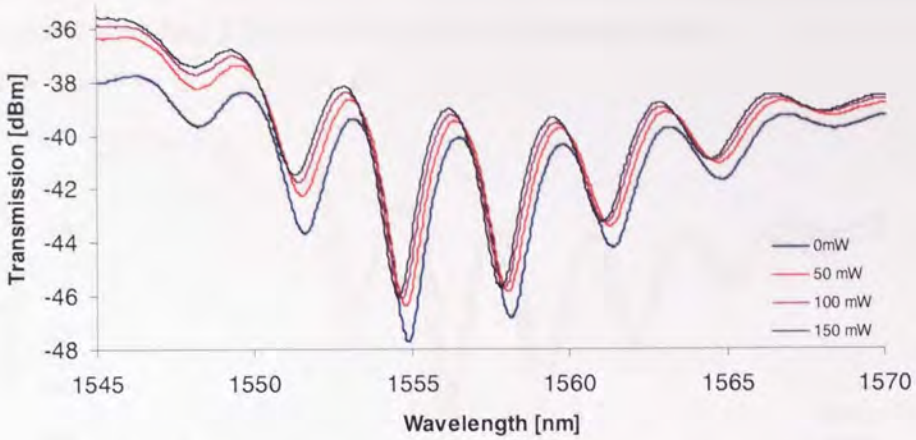

Figure 5.3-5: Wavelength shift of MZI configuration operated in air due to refractive index shift in ErYb doped fibre caused by optical pumping

The Mach Zehnder interferometer is based on the same set of gratings, like the one shown in *Figure 5.3-2*. The total cavity length is 13 cm, of which 8 cm is the optically active fibre. Due to a core mismatch between standard and Er/Yb fibre, the spectrum of the Mach-Zehnder interferometer is slightly degenerated when compared to *Figure 5.3-2*. With increasing pump current the spectral fringes show blue wavelength shift of up to 0.9 nm. The rate of wavelength shift with pumping current varies between $d\lambda/dI$=2.0 nm/mA and 2.7 nm/mA.

The absorption of the pump laser light decreases exponentially with propagation through the Er/Yb fibre and so the refractive index change is not uniform. With L_1 the length of the Er/Yb fibre the wavelength shift can be described as

$$\Delta\lambda = \frac{1}{\lambda} S \int_0^{L_1} \Delta n_{core} dL_1' \qquad \textbf{Equation 5.3-3}$$

The parameter S is the spectral separation of neighbouring fringes. By observation of the pump-induced luminescence in the fibre, it seems that absorption takes place in only around 2 cm of the Er/Yb fibre. Assuming a change of the core refractive index n^{core} only, from the observed wavelength shift an averaged Δn^{core} can be estimated to be between 2×10^{-6} and 8×10^{-6} over 8 cm and 2 cm, respectively. The rate of wavelength shift achieved in each of the set-ups is increasing with the length of active fibre inserted into the MZI.

Alternative measurements were performed using a different grating pair separated by 22 mm. In that case Er/Yb-sections of 1 cm and 5.5 cm were inserted. In these cases the wavelengths shifted with $d\lambda/dI$=1.2 nm/mA, and $d\lambda/dI$=1.6 nm/mA.

In subsequent experiments, the active section of the former MZI was immersed in water. *Figure 5.3-6* shows the resulting wavelength shift as a function of pump power. Because of

the changed refractive index difference at the outer cladding interface the whole spectrum at zero pump current is shifted 2.5 nm to the shorter wavelength side.

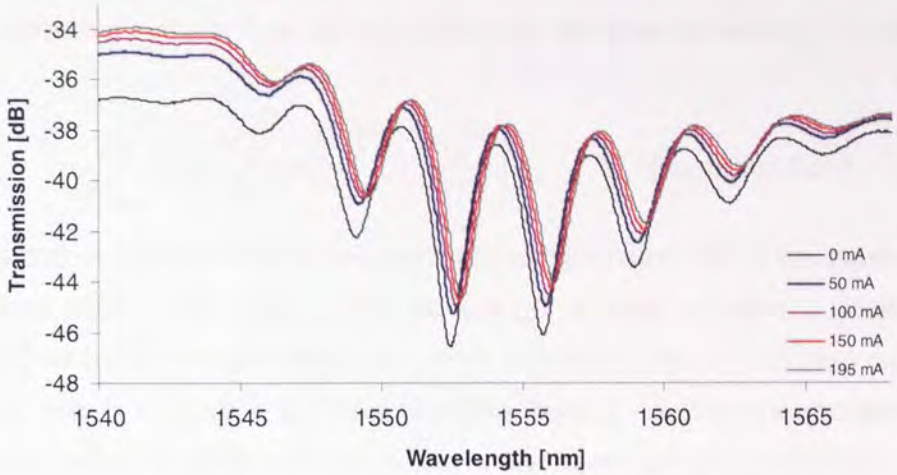

Figure 5.3-6: Wavelength shift of MZI configuration with active fibre section immersed in water as a function of optical pumping

With increasing optical pumping however, the fringes start shifting to the longer wavelength side, as opposed to the results with the MZI in air. A comparison of the pump-induced wavelength shift for the band around 1555 nm is given in *Figure 5.3-7*. The linear relation between pump current and wavelength shift is apparent, as is the change of sign if the MZI device is run in water. A maximum tunable wavelength shift of 0.42 nm is achieved.

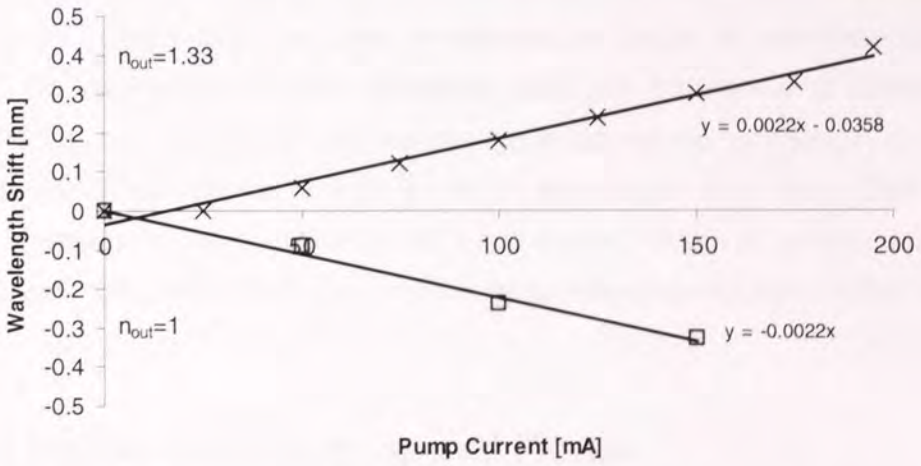

Figure 5.3-7: Wavelength response of MZI device in air and water shown for 1555 nm resonance band

The spectral sensitivity coefficients are found to be -2.2±0.25 pm/mA in air and 2.2±0.35 pm/mA in water.

The change of argument in the response spectrum is unexpected. One possible explanation may be the approach to treat the effect as a function of two mechanisms that occur at the same time. The spectral wavelength is depending on the effective refractive index difference

Δn_{eff} between the core mode and the cladding modes interfering. During the pumping of the Er/Yb section its core refractive index changes due to a non-linear optical effect. At the same time both core and cladding can be subjected to thermal effects changing their respective refractive indices. The spectral response can then be written in a simplified way as

$$\frac{\partial \lambda}{\partial I_{Pump}} \propto \left(\frac{\partial n_{eff}^{core}}{\partial I} + \frac{\partial n_{eff}^{core}}{\partial T} - \frac{\partial n_{eff}^{clad}}{\partial T} \right) \qquad \textit{Equation 5.3-4}$$

It is obvious that as long as the first two parts of the right hand side in the equation are larger than the contribution of the cladding, the wavelength change will have a positive sign. This can be achieved by a heat-sink effect the water immersion has on the fibre cladding. In air, however, the heat is trapped in the fibre because there is no effective transport mechanism to cool down the outer fibre region. In this case fibre core and cladding experience a temperature increase, which has a greater effect on the effective refractive index for the cladding modes.

5.3.2 Discussion

It has been shown that optical pumping of fibre section with an active core material within the cavity of a LPG Mach-Zehnder pair can be used as a tuneable multi-channel filter. With the set-up presented, wavelength tuning of up to 0.42 nm has been shown, but this value can probably be increased in the future. The channel spacing is determined by the free spectral range of the MZI device and the tuning mechanism is based on non-linear and thermal changes of the differential effective refractive index for the core and cladding modes involved. This has been highlighted by the change in sign of the wavelength shift, between the cases in which the device is kept in air or submerged in a water bath. The total wavelength change can be controlled by the pump current, length of optically active fibre in the cavity, surrounding refractive index and the temperature conductivity of the surrounding medium.

5.4 Long Period Gratings in tapered Fibres

Fibre tapers are integrated optical devices obtained when the radius of a fibre is reduced over a certain length. This has the effect that the guiding properties of the fibre vary, leading to concentration of optical power in the core or scattering losses [*162*]. Tapers are being used in telecoms and sensing applications, as tuning devices in ring lasers [*163*], biomedical sensors [*164*] and fibre based gas detectors [*165*].

Bragg gratings in tapered fibres show an altered phase due to the changing effective refractive index [*166*]. The change in the waveguide properties directly affects the grating

coupling coefficient by changes of electric field distribution of propagating modes and the area of mode overlap.

A study has been carried out to investigate the spectral response of long period gratings in tapered fibres to external factors as surrounding refractive index, temperature change and bending. As is presented here, fibre taper long period gratings (FTLPG) show interesting results for the former due to the high spectral sensitivity in the refractive index region of 1.3. To date most results were presented for liquid carbon-hydrate compounds. The ability to measure the constitutions of aqueous solutions offers the perspective of future fibre based bio-medical applications.

5.4.1 Fabrication of Fibre Taper Long Period Gratings

A series of LPGs was written into grating tapers obtained by Rosa Romero from INESC in Porto and Kazimierz Jedrzejewski from the Fibre Optic Research Centre at Warsaw University of Technology. The first were fabricated by applying strain to a fibre while it was subjected to an electric arc, which gradually moved along the fibre axis. For the later a flame was used instead of the arc to soften the fibre material. The tapered sections were up to 3.2 cm long and had a minimal waist of ~34 µm. The tapers are considered to be adiabatic, which means loss free. The rate of change in radius is slow over length, so no light is scattered outside from the cladding.

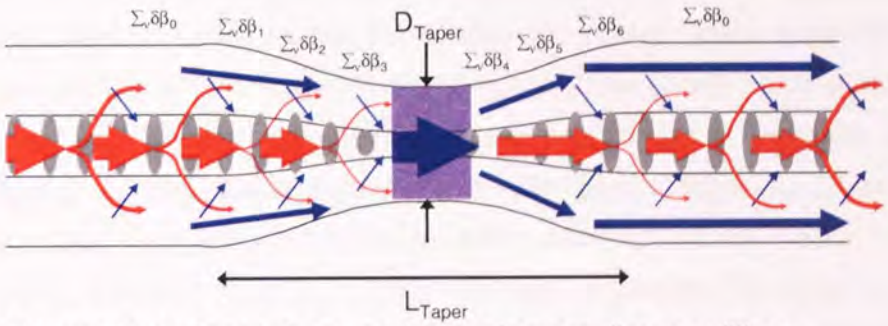

Figure 5.4-1: Taper shape and changing coupling conditions

The shape of a taper including a long period grating is sketched in Figure 5.4-1, also indicating the changing coupling conditions over the section.

LPGs were written into the tapers after hydrogenation of the fibre samples, using an Ar-Ion laser emitting UV light at 244 nm wavelength. The period of the different gratings was varied between 250 µm and 500 µm, using increments of 50 µm. All measurements were taken using an OSA with a broadband light source.

Figure 5.4-2 shows the spectrum of a LPG in a fibre taper. The grating period is Λ=500 µm and the length L_{LPG}=5 cm. The grating shows a strong attenuation band around 1370 nm

wavelength and a wide Mach-Zehnder like response between 1550 nm and 1660 nm wavelength with weaker discrete features in-between and at lower wavelengths.

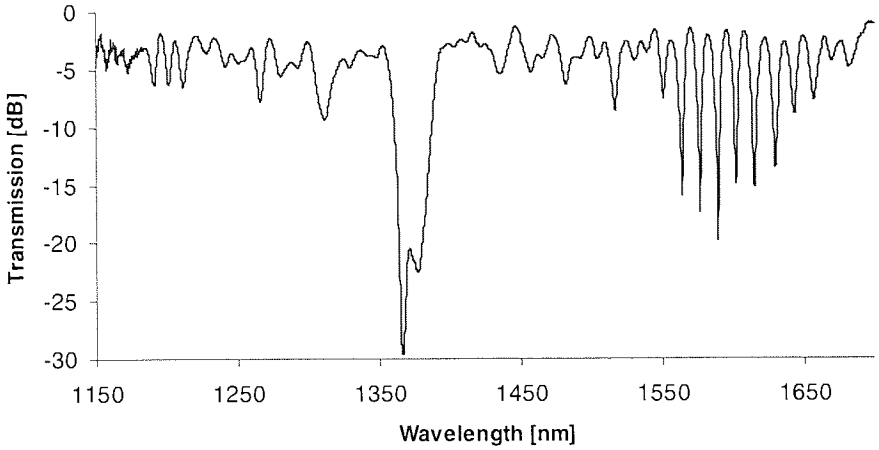

Figure 5.4-2: Long period grating spectrum in taper (L=5cm, Λ=500µm)

The Mach-Zehnder effect was observed in all gratings with periods between 350 µm and 500 µm, whereas no distinctive features could be observed in gratings with periods of 300 µm or below. The comb-like structure is believed to be a genuine Mach-Zehnder effect, which can be explained as follows.

With decreasing fibre radius in the taper the core cross-section decreases accordingly, therefore the main electric field contributions of the propagating modes are coupled into the fibre cladding. The coupling between modes is defined by the overlap integral of their electric field in the perturbation region of the fibre core and scales down accordingly with the transversal core area. This is indicated in *Figure 5.4-1.* In the shaded area at minimum fibre diameter no coupling between the modes occurs. The length of the fibre section with negligible coupling coefficients is equivalent to the cavity length L_{cavity}, as defined in *Equation 5.3-1.* This hypothesis has been tested by washing out the grating fringes in the tapered section of smallest radius by a static UV-beam exposure. No effect on the grating spectrum was observed, meaning that the grating structure in this section has no effect on the mode evolution.

The high number of broad discrete attenuation bands can be explained by the changing coupling mode conditions in the tapering fibre sections. In a standard long period grating only a limited number of cladding modes fit the phase matching condition with the core mode, as indicated by $\sum_{\nu}\delta\beta_{\mu}$ in *Figure 5.4-1.* This leads to distinctive, narrow attenuation bands around the resonance wavelengths. With changing waveguide properties the propagation constants β of core and cladding modes change continuously, enabling different sets of cladding modes to couple to the core mode, exemplified with the indices 1 to 6 of the same term. The

result is an increased number of transmission peaks, some of which overlap, showing the broad spectral features as seen in *Figure 5.4-2*.

5.4.2 Refractive Index Sensitivity Measurements

For measurements of their sensitivity to surrounding refractive index the tapered fibre LPGs were placed in a V-grove machined into an Aluminium plate and successively immersed in certified refractive index liquids.

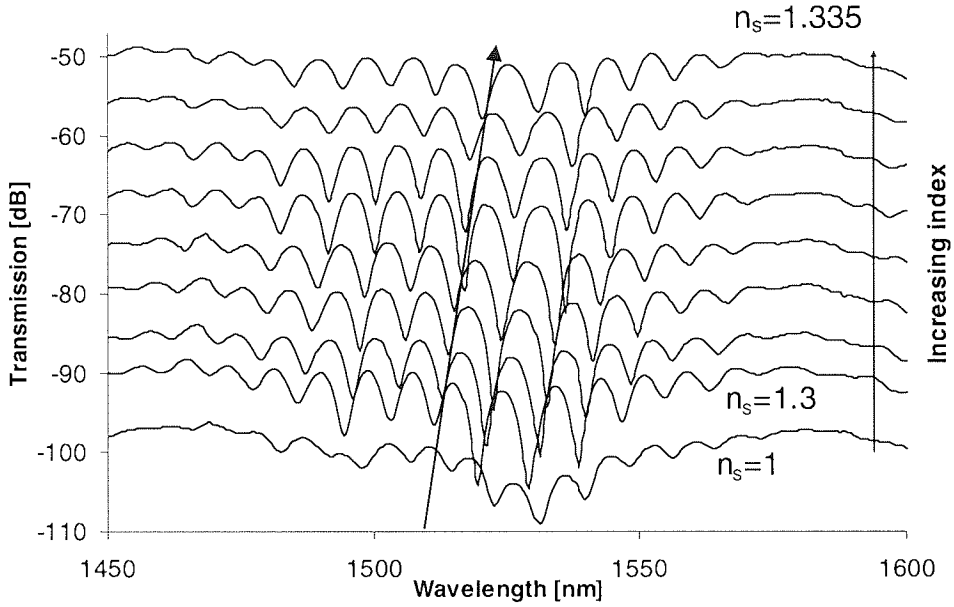

Figure 5.4-3: Refractive index calibration by measuring the sensitivity of MZI (signal power shifted for clarity)

After each spectrum was taken, the devices were washed step by step in a cleaning procedure, using methanol and deionised water. The set-up was placed on an optical bench, which acted as heat sink keeping the grating at constant temperature. In a first step a calibration was carried out on the spectral shift of the Mach-Zehnder fringes. *Figure 5.4-3* shows this process using a 5 cm long LPG of 400 μm period written in one of the fibre tapers. Please note that between the first and second spectrum from the bottom a wavelength jump from n=1 to 1.3 occurs, whereas all following spectra are taken for a refractive index increment of 0.05. The resulting sensitivity curve is presented in *Figure 5.4-4*, showing an approximately linear change of wavelength with surrounding refractive index.

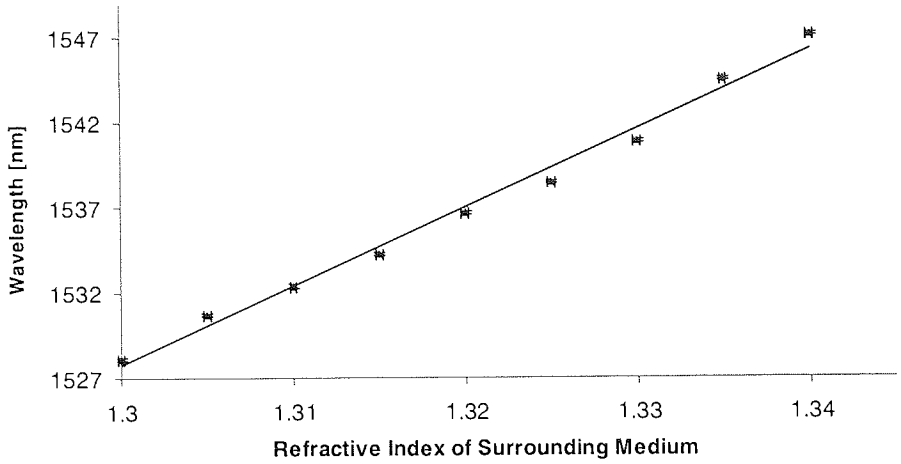

Figure 5.4-4: Refractive index calibration of MZI structure in FTLPG

After this series of measurements, the same tapered fibre grating was immersed into a tank containing 500 ml deionised water, the refractive index of which is given as between 1.3 and 1.33. Into the tank containing the grating, a 2-molar NaCl solution was added in increments of 10 ml. The corresponding wavelength shift of the MZI was monitored to identify the correlation between NaCl concentration and refractive index, using the assumption of its linearity to refractive index change obtained from *Figure 5.4-4*. The result from this experiment is displayed in *Figure 5.4-5*, where it can be observed that the correlation of wavelength shift to NaCl concentration is linear, too.

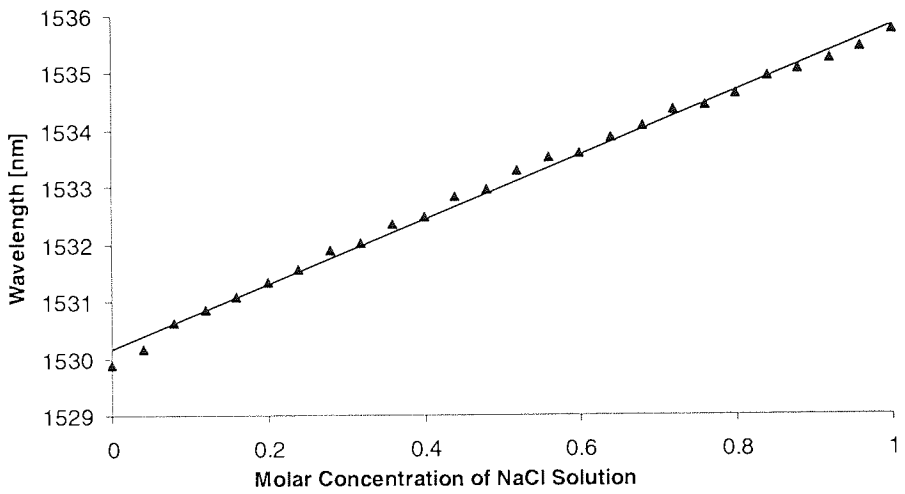

Figure 5.4-5: Calibration of refractive index with respect to molar concentration of NaCl solution

Besides measuring spectral sensitivity of MZI resonators, attention has also been paid to the spectral evolution of selected discrete attenuation bands, as shown in *Figure 5.4-6* for a FTLPG with 350 μm period immersed in refractive index matching fluids of increasing *n*.

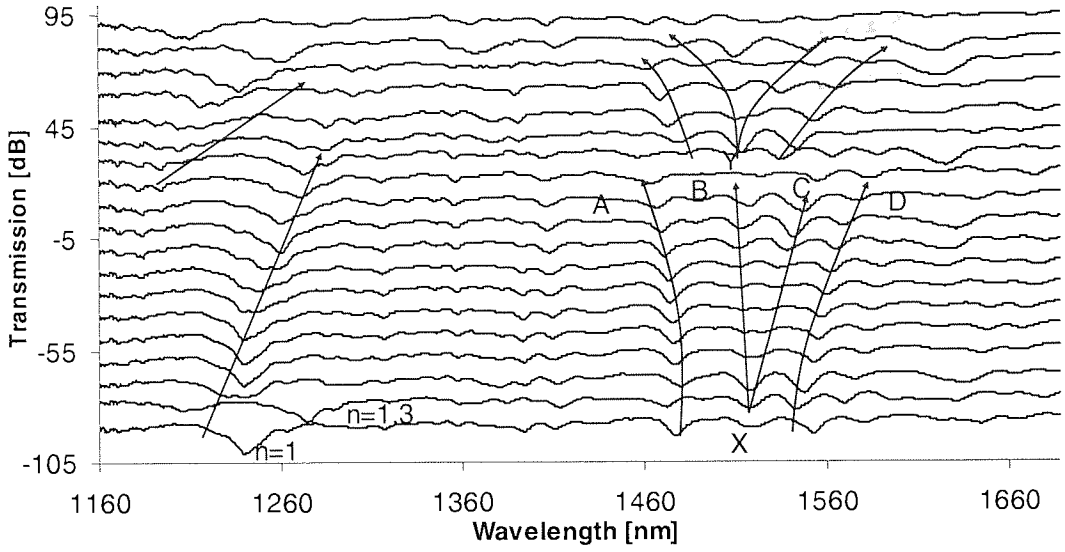

Figure 5.4-6: Spectral shifts of discrete attenuation bands to changes of surrounding refractive index (signal power shifted for clarity)

One interesting result is the shift of different attenuation bands towards longer and shorter wavelengths, like the bands denoted A and D in the graph. Even more so, some attenuation bands split in two, showing this same behaviour, like in the cases for bands B and C. This spectral splitting effect is also referred to as spectral bifurcation in the following.

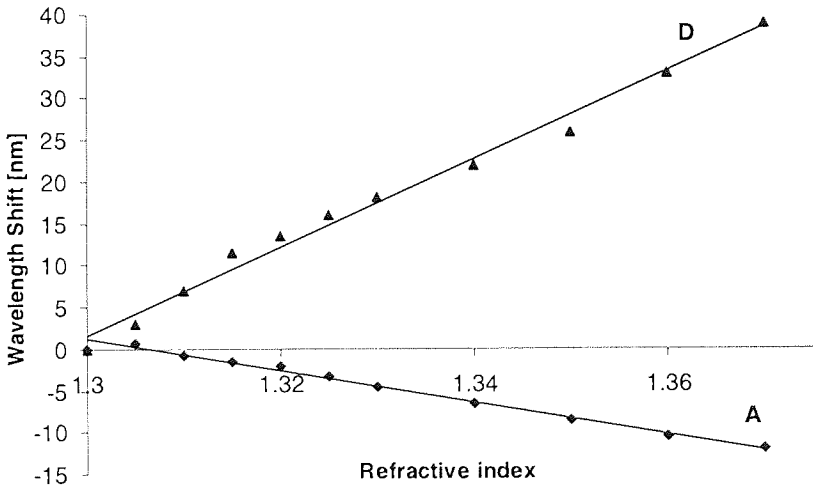

Figure 5.4-7: Spectral sensitivity as function of refractive index

The wavelength shift of band A and D over refractive index is plotted in *Figure 5.4-7.* Again the curves are fairly linear in the region between n=1.3 and 1.36. Above that value, the attenuation bands drift apart too far and wash out, making it difficult to follow their further development as indicated as position Y in *Figure 5.4-6.*

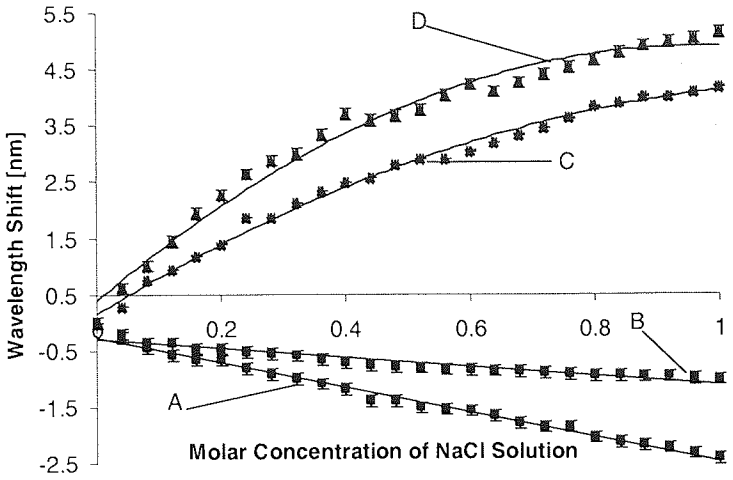

Figure 5.4-8: Spectral sensitivity drawn over refractive index of NaCl solution

The spectral sensitivity to the molar concentration of a NaCl solution is shown in *Figure 5.4-8*. It shows fairly linear wavelength shifts of negative sign for the bands A and B and a curved function for bands C and D of positive increments. Applying the calibration function obtained from *Figure 5.4-5* to this data yields the function of spectral refractive index sensitivity, as shown in *Figure 5.4-9*.

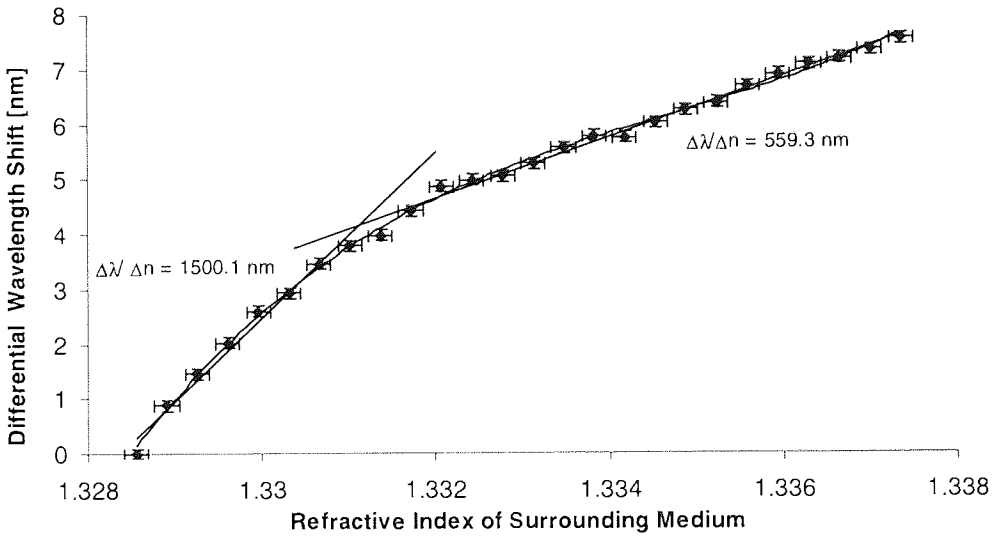

Figure 5.4-9: Spectral sensitivity of bifurcating attenuation band over surrounding refractive index

The spectral sensitivity is given by the slope of the two lines approximating the above curve, leading to a sensitivity of $d\lambda/dn=1500\pm36$ nm in the range between $n=1.33$ and 1.331 and $d\lambda/dn=559\pm55$ nm for the region between $n=1.331$ and 1.338.

5.4.3 Temperature Sensitivity

In further experiments the temperature sensitivity of the tapers was investigated. *Figure 5.4-10* and *Figure 5.4-11* show the temperature drift of the Mach-Zehnder Fringes and selected discrete attenuation bands of the grating shown in *Figure 5.4-1* for a grating with Λ=400 µm and L=5 cm.

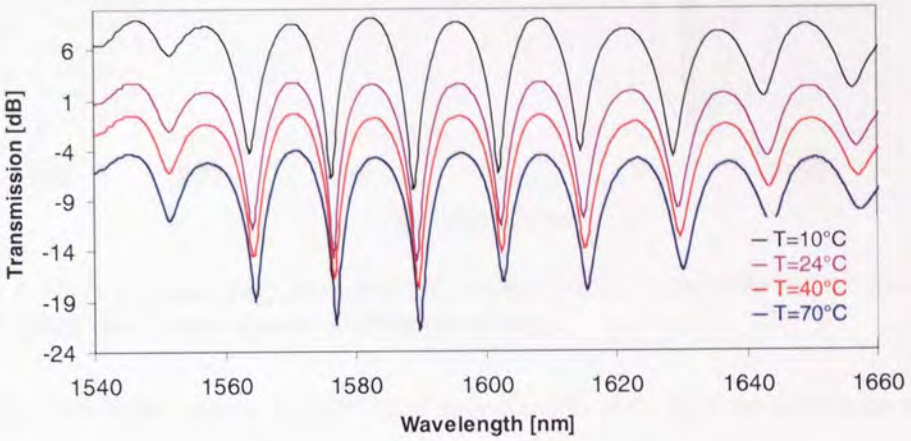

Figure 5.4-10: Temperature shift of MZI section in 5 cm long FTLPG with L=400 µm

The fringe spectrum in *Figure 5.4-10* uniformly shifts to shorter wavelengths with increasing temperature, supporting the above assumption that a real Mach-Zehnder effect is the underlying mechanism leading to the spectrum between 1540 nm and 1660 nm. The rate of shift is ~ -10 pm/°C, leaving the fringe separation fairly constant. The total wavelength shift is less than 1 nm for any of the resonance. Because of the limited bandwidth resolution of the OSA covering the large spectral range, the temperature sensitivity of the Mach-Zehnder section could not be determined with higher accuracy.

In contrast to that, the discrete bands show larger wavelength shifts, partly in connection with bifurcation effects, as seen in *Figure 5.4-6*, which are marked by circles and denoted with A, B and C.

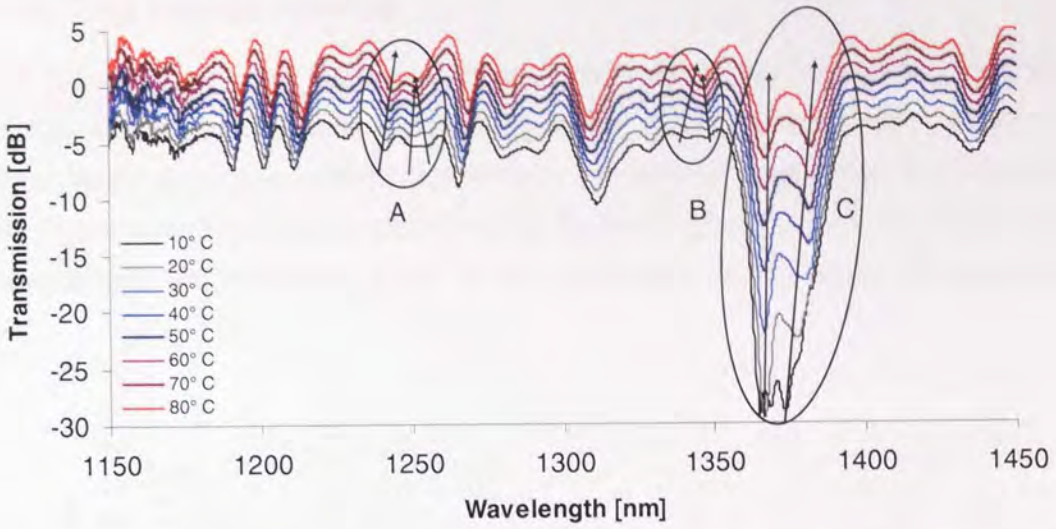

Figure 5.4-11: Temperature shift and bifurcation effect in discrete attenuation bands over temperature (signal power shifted for clarity)

For the double and triple peaks A and C the wavelength shift over temperature is displayed in *Figure 5.4-12*.

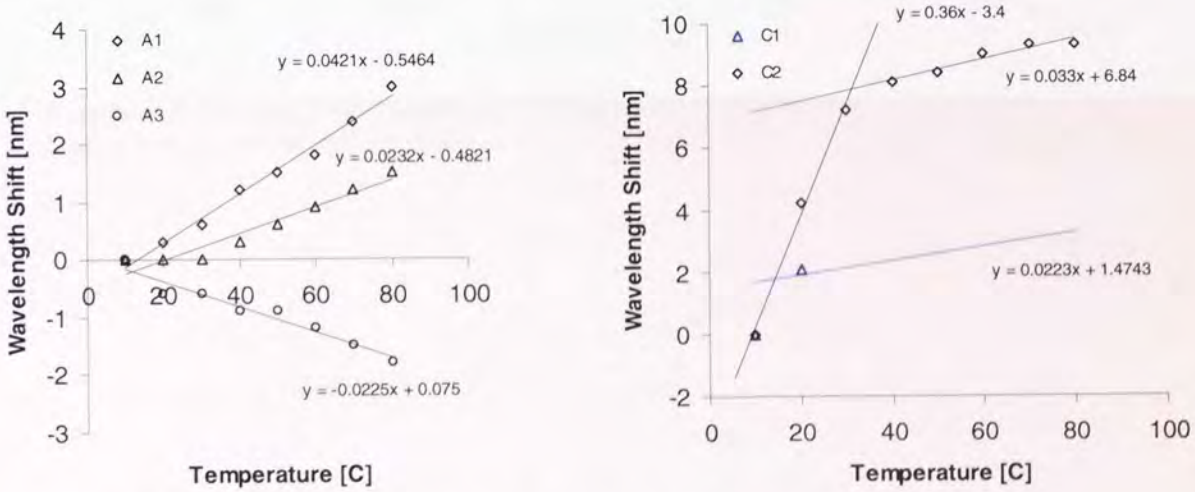

Figure 5.4-12: Temperature sensitivity curve for loss bands A and C

Starting at a temperature of 10°C, with increasing temperature two of the attenuation Bands in A show positive and the third one negative wavelength shift. Spectral sensitivities of -22.5±2.3 pm/°C, 23.2±3.8 pm/°C, and 42.1±6.4 pm/°C are found. The peaks in attenuation band C show two linear regimes, the first up to a temperature of ~20 °C and a second above that value. The sensitivity in the latter case is 33±5 pm/°C for one attenuation band and -22.3±3 pm/°C for the other. The seemingly steep increase of the wavelength shift in the temperature range between 10°C and 25°C may be the result of the switch from one disappearing attenuation band to an emerging one, which has previously been covered by overlapping with the main attenuation band. In the first curve this appears as a shoulder on the right-hand side of the initial spectrum.

5.4.4 Bending Characteristics

For the bending experiments the same measurement apparatus was used, as shown in *Figure 5.2-5*. To prevent the fibre from kinking in the taper region, it was inserted into a plastic tube, which ensured a continuous curvature, as defined by *Equation 5.4-1* over its full length. In *Figure 5.4-13* the results are shown for the same grating, as used for the refractive index experiments. As indicated, some of the attenuation bands again show bifurcation effects.

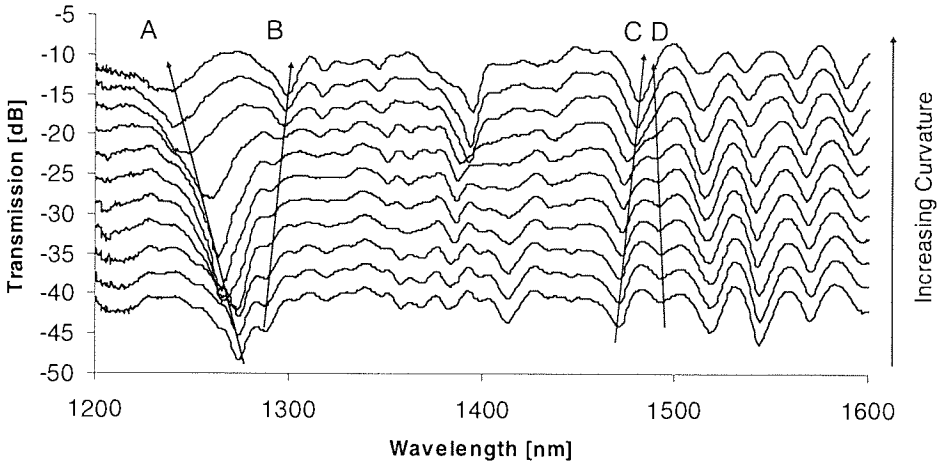

Figure 5.4-13: Spectral changes in FTLPG due to bending (signal power shifted for clarity)

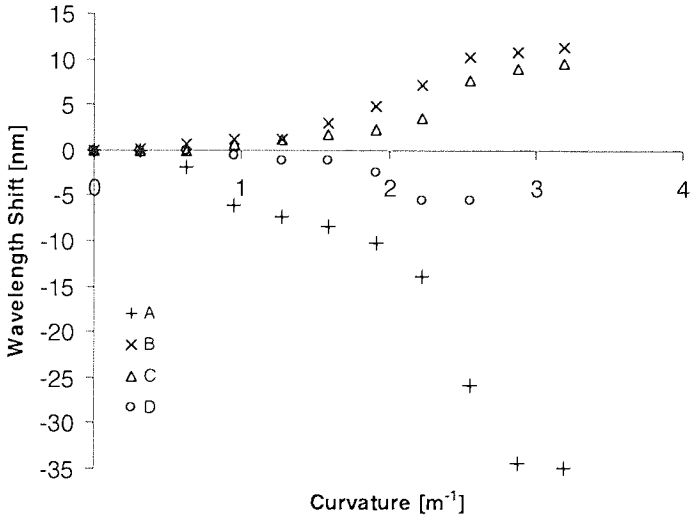

Figure 5.4-14: Spectral Sensitivity of FTLPG to bending curvature

From the shift of the selected attenuation bands, the spectral sensitivity of the tapered fibre LPG was obtained, as shown in *Figure 5.4-14*. Up to a curvature of 0.5 m^{-1} no obvious response is detected, followed by a linear regime up to a value of about 2 m^{-1}. The wavelength shifts of all bands except C appear to reach an asymptotic regime. As in the case of

temperature measurements the erratic behaviour of curve C may be due to the disappearance or blending of the measured band with neighbouring bands and the emerging of new bands from previously overlapping spectra.

In the linear domains the differential spectral sensitivity of bands A and B is 2.56±0.18 nm·m and 9.31±1.22 nm·m for bands C and D. The latter value is in good agreement with the maximum bending sensitivity for step-index fibre reported by Allsop et al. [*64*].

5.5 Conclusions

Various novel concepts of long period grating based devices have been presented with potential applications in sensing and telecommunications.

First steps were undertaken in an approach to the fabrication of vectorial curvature sensors, using elliptical core fibre and standard SM 28 fibre with an asymmetrically modified cladding. With the latter a successful discriminatory device for convex and concave bending was achieved and a concept is proposed to combine both approaches into a 3-dimensional directional sensor suitable for applications ranging from civil and mechanical engineering over medical technologies to the use in the defence sector.

Furthermore, an active sensor/switch concept based on a fibre-Mach-Zehnder interferometer is proposed. The spectral response of the device can be controlled by optically pumping an Erbium-Ytterbium doped fibre section in the interferometer cavity. In addition, the sensitivity response changes dramatically if the device is subjected to changed refractive index and heat conductivity properties of the surrounding medium, allowing the tailoring of its sensitivity parameters.

Finally, results from long period grating devices written into tapered fibres are presented. These show spectral response based on Mach-Zehnder effects, as well as discrete resonances between core mode and a high number of cladding modes.

The observation of the latter show bifurcation effects with the change of any sensing parameters, which manifest in the splitting and merging of discrete attenuation bands in the course of measurements.

The most promising results were obtained from refractive index measurement, where the tapered fibre gratings show very high sensitivity for materials with a refractive index in the range of around 1.3. This offers the possibility of bringing forward a fibre based sensor concept for aqueous solutions, with potential in the area of bio-chemistry.

Additional measurements exhibited temperature sensitivity coefficients of typically 30 pm/°C, which is very low for long period grating based sensors. On the other hand the bending sensitivity reaches values of nearly 10 nm·m.

6 TYPE IA GRATINGS

6.1 Introduction

Depending on fibre composition, pre-treatment with deuterium or hydrogen and the parameters used for the inscription process itself, it is possible to classify UV-gratings into various types with different properties [*21,36,42*]. The models explaining the photorefractive effects leading to the formation of type I, II and IIA gratings have been introduced in ***Chapter 2.1***.

Investigations into the effect causing the suppression of type IIA grating formation in hydrogen-loaded boron-germanium fibre [*37*] lead to the discovery of a fourth grating type. It has been shown that during long term UV-exposure in these fibres often a partial or full erasure of the initial type I grating is observed, followed by the evolution of a secondary grating. Unlike type IIA gratings, these regenerated gratings evolve showing a red wavelength shift of up to 20 nm in total compared to where the first grating appeared. Because of the apparent analogy to type IIA gratings, these regenerated gratings have been called type IA gratings [*167*].

For the original experiment a Coherent FRED 300 frequency-doubled Ar-Ion laser at 244 nm wavelength was used in a power regime around 100 mW and the process took up to 2 hours in total.

From further investigations it has been shown that type IA gratings exhibit a significantly lower temperature coefficient but identical strain sensitivity compared to type I and IIA gratings. In the most extreme case, the difference in temperature coefficient reached 55% in comparison to type IIA gratings. It was shown that type IA gratings applied in combination with one of the other grating types are useful for a simultaneous dual strain-temperature sensor concept [*168,169*].

The duration of two hours for the inscription time of one type IA grating is not acceptable if these gratings were to be used for commercial purposes. Therefore the first objective after their discovery was to minimise the inscription time by choosing UV-sources of higher optical output and suitable *B-Ge* fibres.

A more thorough investigation of the influence of fibre materials and fabrication conditions on type IA grating formation has been undertaken and summarised by my colleague George Simpson for his Ph.D. thesis [170]. His comprehensive work on type IA gratings elaborates the effects certain factors that can have on the grating writing process and grating properties. Covered aspects are the impact of boron and hydrogen content, the hydrogenation method

itself, temperature, beam fluence and applied strain during inscription, the duration of the grating writing and the writing method itself. For these experiments a Coherent Sabre FRED *Ar*-ion laser system of 244 nm wavelength and maximum output power of 800 mW was used. The findings of Liu [*167*] and Shu [*168*] were confirmed. Similar grating evolution spectra and temperature coefficients significantly lower than those from any other fibre type were found. Another crucial result, providing the motivation to conduct the research presented here, was the fact that by using high power UV-light for the fabrication of type IA gratings, the writing time could be reduced down to 8-10 minutes for one grating [*171*].

In the following sections and in particular for the discussion of results from the present work some of these latest results will be used as a reference.

The main objective of the work presented here is to identify whether type IA gratings can be written using an Oxford Lasers copper-vapour laser emitting at 255 nm wavelength and to investigate the properties of these. Lasers based on *Cu*-vapour technology offer a high power UV-source. Initially designed for the micromachining of metals, their applicability for device inscription into optical glass waveguides has gradually been recognised. Previous work on fibre grating fabrication has shown good results [*172*] and proven that this concept is an alternative contender for the fibre optics industries.

The most significant difference is the slightly higher wavelength and the pulsed output from this laser set-up, as opposed to the CW operation of *Ar*-ion lasers. Using a number of samples of different fibre types, the aim was also to establish the influence of beam fluence and writing time on the formation and properties of type IA gratings.

The potential application of type IA gratings is treated as a second objective to establish whether the writing process at 255 nm is a viable approach for the fabrication of commercially useable sensors.

6.2 Methodology

The work was divided into three sections. Sets of gratings were written in three different boron-germanium fibre types, namely a commercially available Verillion *B-Ge* fibre and two types of non-commercial Nortel C3 fibre (batch numbers CA-3555 and CA-3513). For reference reasons, gratings were written under identical writing conditions in Corning SM 28 single-mode standard fibre and in Stocker Yale CMS-1550-R1 fibre. One aim of this work was to identify fibre dependent differences in the characteristics of the type IA grating.

After fabrication, 6 to 8 gratings were annealed simultaneously at 80º C in a Sanyo-Gallenkamp heating chamber for 65 hours or longer. Using a 1x8 coupler and an EXFO IQ-12004 measurement kit comprising of a tuneable laser source and 8 power meters, the annealing effect with time could be measured on each grating of the batch at the same time. The spectra for all gratings were taken in regular intervals. After the experiments the central

wavelength shift and change in strength of all grating peaks with time could be extracted from the spectrum data.

Between the fabrication process and the annealing test, all gratings presented here were kept in a freezer at -30º C.

Temperature and strain sensitivity of the gratings were measured in a final step, using a broadband light source with an HP 8142 optical spectrum analyser. The gratings were subjected to temperature changes using a 5W Peltier within a thermally insulated environment and the spectral response measured for a set of temperature values.

For the strain measurement the gratings were subsequently fixed to an aluminium block on one side and a one-dimensional translation stage of micrometer precision on the other. Both ends of the fibre were rested in V-grooves on either block and fixed by aluminium clamps with rubber pads to prevent damaging and slippage of the fibre. By knowledge of the initial distance between the edges of the clamping blocks the strain could be calculated as a function of the linear translation of the stage.

6.3 Grating Inscription

All of the type IA gratings were fabricated using the Oxford Lasers Copper Vapour laser emitting pulsed UV light at 255 nm wavelength with a repetition rate of 6 kHz. Depending on the coherence requirements, this system can reach an averaged maximum laser power between 300 mW and 800 mW. In the present case, the high coherence and moderate power mode was used. With the model available at Aston University the coherence and beam power are controlled by a set of aperture plates inside the laser system and can not be manipulated externally.

In order to achieve different exposure conditions, a set of neutral density filters was inserted on a revolver wheel into the beam path. The set included filters of 30, 40 and 50% transmission and one filter with 3% transmission that was used for beam alignment on the fibre. The laser power was measured before each writing process using a light power meter from Ophir, which was inserted into the beam path directly after the laser output aperture and behind the neutral density filter. This was done for monitoring reasons.

The fabrication conditions were kept as closely as possible to those from previous work. Nevertheless certain differences were unavoidable. Despite the high repetition rate and a rather moderate peak power of 1 kJ, the writing conditions using a *Cu*-Vapour laser can only be considered an approximation to those using a CW *Ar*-Ion system.

In the past three different writing methods were tested for type IA grating fabrication. Two of these are the holographic method and the static beam inscription through a phase mask. In both cases an expanded beam can be used for the fabrication of long gratings. However, the most adapted method was found to be the repetition of scans though a phase mask.

One of the reasons for this is the Gaussian beam profile, common for all standard UV lasers. Any non-uniform power distribution along the beam cross-section reflects directly on the local photorefractive effect in the fibre. Sections exposed to low levels of UV power, as prominent in the beam tail, will never develop beyond the state of a type I grating, whereas grating sections subject to high beam power mature into a type IA grating structure.

For static beams a partial levelling of beam power can be achieved using a telescopic set-up with the falling edges cut off. This problem can be solved simpler using an aperture slit placed on the phase mask side facing an incoming scanning beam. The slit automatically determines the grating length. If the full width of the beam passes over both edges of the slit during each scan, a uniform distribution of accumulated beam fluence in every part of the grating is ensured.

Often a splitting of the transmission band with a second peak appearing half way between the wavelengths associated to type I, and type IA gratings, can be observed. In some cases this can be explained by a non-uniform distribution of UV power, leading to a grating section, which has not fully evolved to a type IA grating. Under idealised fabrication conditions it is more likely that a dramatic increase of the fibre's *V*-number due to the average refractive index change contributes to the appearance of these "ghost" peaks [*173*].

Because of the long fabrication times the long-term stability of the set-up and beam condition is crucial. One of the drawbacks of the method favoured here is the travel of the beam and the increase in writing time due to off-times of the beam.

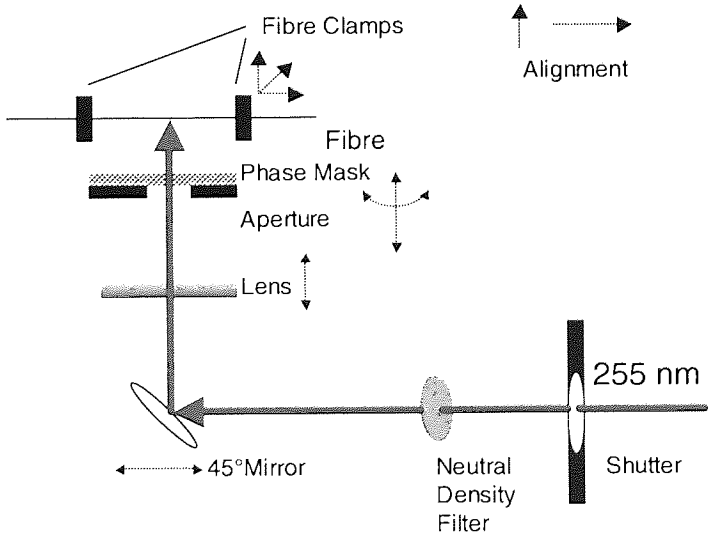

Figure 6.3-1: Writing set-up for type IA grating inscription

A schematic of the grating writing set-up used is shown in *Figure 6.3-1*. The beam diameter from the Cu-vapour laser was approximately 3 mm. By using a periscope set-up, the beam is brought at level with the fibre height. After passing through a computer controlled shutter and a neutral density filter the beam hits a 45º mirror, which is mounted on a computer-controlled

Aerotech U500 translation stage and is reflected towards the phase mask and fibre. Additionally in front of the phase mask cylindrical lens with 80 mm distance is inserted, focussing the beam in the fibre core. The fibre is clamped on a massive aluminium block on one side and a 3-dimensional translation tower on the other side. The phase mask can be tilted around the axis, as defined by the incoming beam and also moved closer to and further away from the fibre by a manual micrometer translation stage.

First of all one set of reference parameters for the grating inscription was defined and applied to at least one grating in each fibre type. The controlled parameters were the scanning speed and the optical power of the laser beam. The latter could only be set with a coarse accuracy, as the laser model installed at Aston University has no tuning mechanism for the output power, so that the inscription power was tuned by neutral density filters of discrete transmission values. In addition, the laser output varied from one day of the experiments to the other because of optical detuning inside the laser casing due to temperature fluctuations in the laboratory and mechanical instabilities.

Each grating set consists of the reference grating and at least two more gratings for the fabrication of which in one case the scanning speed was altered under the same beam power conditions and in the other case the beam power was changed, using the same scanning speed as for the reference gratings. This was done with the aim to investigate in which way beam fluence and writing speed affect the properties of the gratings written.

During the writing process the fibres were repetitively scanned, whilst the scanning conditions were kept constant. After each scan cycle the grating spectra were taken along with the raw data displaying the central wavelength and transmission loss value of up to three peaks in the spectra. The inscription process was manually aborted as soon as no longer a significant wavelength change could be measured. The data were then saved in two separate files after the abortion of the writing procedure.

The different rates with which the saturation of the type IA gratings took place resulted in different gratings being subjected to differing levels of UV-exposure and final wavelengths.

As a reference, the number of accumulated fluence has been defined as "normalised" fluence η in order to give the possibility of direct comparisons between gratings written at different light power and scan numbers. In this case it is defined as the total beam energy distributed per unit length of fibre and it is calculated by the ratio between light power P_{UV} and scanning speed v_{scan} applying after a number n of scans, as given in *Equation 6.3-1.*

$$\eta = n\frac{P_{UV}}{v_{scan}} \qquad \textbf{Equation 6.3-1}$$

This calculation is valid under the assumption that between neutral density filter and fibre the loss in UV power is always proportionate to the output power, and that the alignment of the set-up ensures that the fibre is always illuminated by the same fraction of the beam, which is

of unchanging width. For that reason the result has to be treated with caution and as a number of arbitrary units rather than an actual power density. This helps to overcome the problem, that the diameters of the cores in the different fibre types, and thus the lateral cross-sections and volumes are not known. The same problem also occurs for the exact shape and energy distribution of the beam in the position where it is incident on the fibre core.

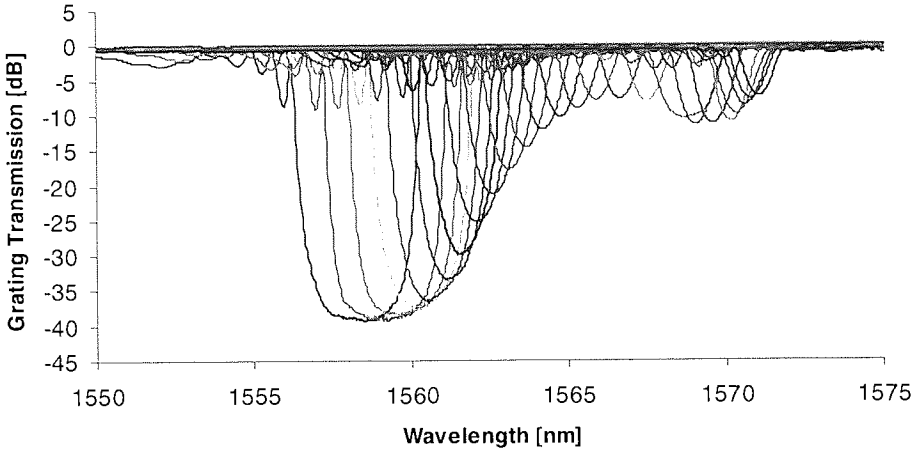

Figure 6.3-2: Type IA grating evolution over the course of 375 scans

A typical example for the partial erasure and regeneration of a grating under successive scans of UV-exposure is given in *Figure 6.3-2*. The 1 mm long grating was written in a Verillion sample, using an UV-power of 96 mW with a scan speed of 1 mm/s [*Verillion Sample 2*]. The Graph shows the first spectrum and following spectra taken after each 15th scan. The initial type I gratings are likely to be stronger, than shown in the figure, but could not be fully resolved either due to strong background light in the fibre or because of the set dynamic range of the OSA. The type IA grating also peaks at a maximum value before starting to decrease in strength.

In all fibre samples except the CA 3555 batch an additional type I grating was written alongside the IA grating. In this way the growth and annealing parameters, as well as strain and temperature coefficients measured later in the process could directly be compared for gratings written in the same piece of fibre. For grating fabrication a phase-mask with a period of Λ_{PM}=1070 nm from QPS was used.

Table 6.3-1 gives a comprehensive overview over the fabrication parameters for all type IA gratings presented here.

Fibre Type	Sample	Laser Power [mW]	Grating Length [mm]	Scan Velocity [mm/s]	Number of Scans	Normalised Fluence [arbitrary units]	Comment
Verillion	1	190	1	1	60	11.4	
	2	96	1	1	375	36	
	3	188	1	1	132	24.8	
	4	95	1	0.2	100	47.5	
	5	180	1	0.2	21	10.5	Reference condition
CA-3513	1	175	1	0.2	85	74.4	Reference condition
	2	175	8	0.2	23	20.1	Reference condition
	3	90	8	0.2	95	42.8	
	4	171	8	1	103	17.6	
CA-3555	1	150	10	0.2	87	65.3	Reference condition
	2	166	10	0.2	61	50.6	Reference condition
	3	87	10	0.2	131	56.99	
	4	160	10	1	200	32	
SM 28	9	180	1	0.2	60	54	Reference condition
	10	184	1	0.2	47	43.2	Reference condition
	11	180	1	0.2	56	50.4	Reference condition
Stocker Yale	1	181	8	0.2	58	52.5	Reference condition

Table 6.3-1: Writing conditions for Type IA gratings in diverse B/Ge-fibre types

In the parameter set defined the reference condition the scan velocity is 0.2 mm/s, with a laser output power of close to 180 mW. Two additional parameter sets have been applied to write gratings in the three sets of *B/Ge* fibre. In one the light power was halved, maintaining the same scan velocity, in the other the power was kept at high level and the scan velocity was increased to 1 mm/s.

The only parameter not kept constant is the grating length. The grating length in some of the fibres was set to a smaller value if the inscription process was found to be too lengthy. The limited number of samples and time did not allow for the rerun of experiments.

All graphs were taken using a broadband light source and HP-8142 OSA running at a 0.1 nm bandwidth resolution. The data points for grating wavelength and strength after each scan were directly acquired by the software controlling the writing program. For the definition of the wavelength, the software contained an algorithm calculating the centroid fit of the loss peak.

In the following the grating evolution curves are presented using this condensed data, charted over the accumulated UV-fluence. *Figure 6.3-3* depicts this representation, showing the formations of three different IA type gratings.

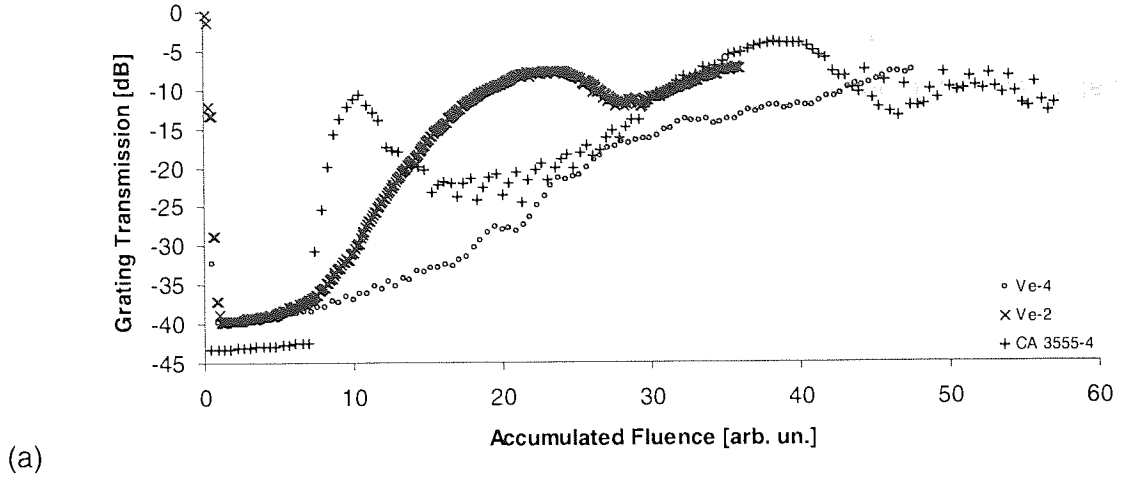

(a)

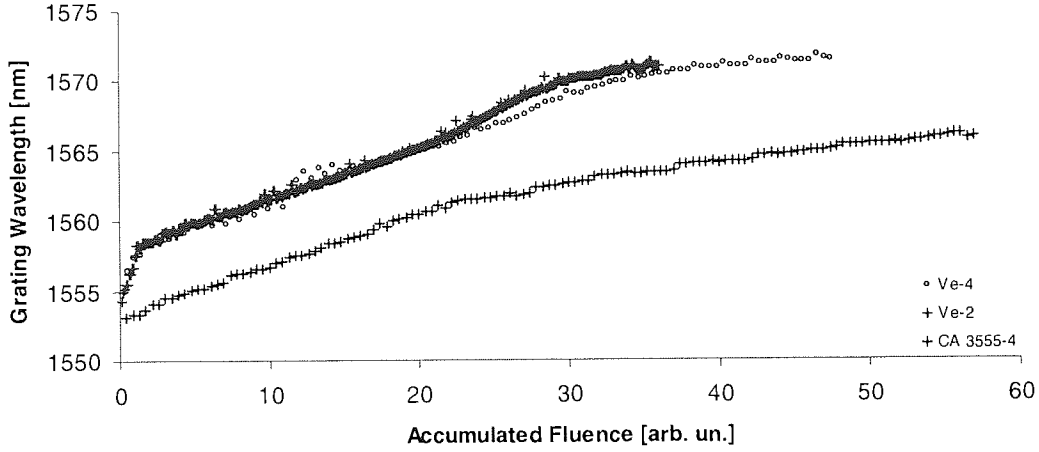

(b)

Figure 6.3-3: Examples of three characteristic Type IA grating formation curves with respect to optical transmission (a) and wavelength shift (b)

It is apparent that the formation of type IA gratings is no uniform process. *Figure 6.3-3* shows three typical evolution curves. In the first case, [*Ve-4*], the type IA grating does not form after an erasure of the initial grating. Instead the original peak steadily decreases. The second case has already been shown in *Figure 6.3-2*, where the final grating emerges from the regeneration of the first [*Ve-2*]. In some cases, however the secondary grating too decreases in strength and a second regeneration process can be observed [*CA 3555-4*]. To cover the grating development from the earliest stages, while the initial type I gratings are very strong, the sensitivity of the OSA was set to a very high level, which meant a decrease in the scan speed.

What determines the full transition to type IA grating in all cases is the saturation effect of the average refractive index. This can be seen in Figure 6.5-3(b). The wavelength saturation curve of grating CA 3555-4 shows two slopes, one to a value of accumulated fluence of 20, and another beyond, before converging to the final wavelength. The Verillion samples, in

contrast show three slopes: the first for the initial 5-10 scans, a second to a fluence value of 20, and a third between 20 and thirty, before starting to converge, too.
For the CA 3555 fibre this change coincides with the maximum value of the first regenerated grating. In the case of the Verillion-2 sample the first phase is the expected red-shift for a type-I grating. The second rate change appears at the maximum erasure of the first grating, whereas the second break comes in effect after the peak of the regenerated grating.
In order to minimise the time of the grating writing process, the writing scan cycle was not paused to allow for a full spectral scan before the resuming of the writing process, which was in no way synchronised with the duration of one writing step. Depending on the temporal match of the two scans, at the time of the OSA passing the grating wavelength region, the UV beam could be hitting central sections of the grating, causing a thermally-induced shift of the grating spectrum. This explains the periodical appearance of spikes in the data, which for example is seen as noise in the CA-3555-4 curve in *Figure 6.5-3(a).*

6.3.1 Grating Evolution in Verillion Fibre

The grating written under reference conditions was Verillion-5. As expected, *Figure 6.3-4* shows a decrease in rate of wavelength shift with an increase in writing speed [Verillion-1; Verillion-3], decrease in UV-power [Verillion 4], or both [Verillion-2].

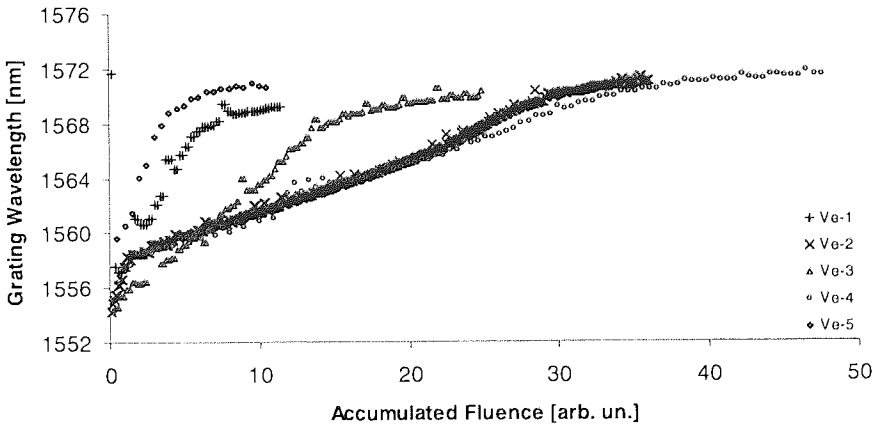

Figure 6.3-4: Growth dynamics of type IA gratings in Verillion fibre

A halving of the UV-power requires a 4-5 fold number of scans in order to reach the same level of effective refractive index saturation. Assuming a near-constant UV-power level, an increase in scanning speed from 0.2 mm/s to 1 mm/s results in the necessity to increase the number of scans by a factor between 3 and 6.5. This significant discrepancy can be seen by comparison of Verillion 1 and Verillion 3, showing two gratings fabricated under identical conditions. The fact that Verillion 2 shows a higher rate of wavelength change compared to

Verillion 4, despite being fabricated using the higher scanning speed, requires additional explanation.

The total wavelength shift, if measured from the nominal central wavelength of 1552 nm given by the phase mask pattern reaches 19 nm.

The wavelength shift in Verillion 2 and Verillion 4 appears to happen in three phases. For the other three gratings this cannot be observed, possibly due to the fact, that the number of measurements taken in the first part of the experiment is not sufficient to document this behaviour.

Regarding the transmission data, the gratings 2 and 3 show the effect of partial erasure and regeneration. In all other cases the initial grating strength decays steadily until the refractive index saturation sets it.

6.3.2 Gratings in CA-3513 Fibre

Of the gratings shown in *Figure 6.3-5*, number CA 3513-2, CA3513-3 and CA 3513-4 are of identical length, with grating 2 as reference.

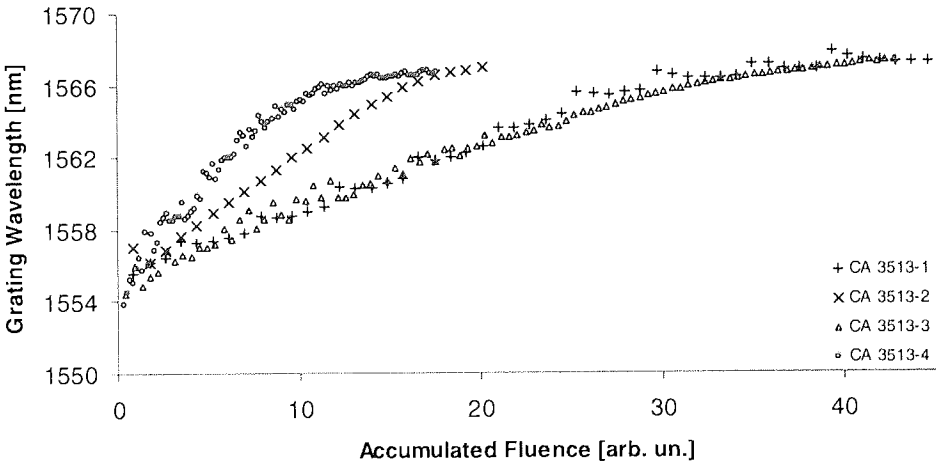

Figure 6.3-5: Growth dynamics of type IA gratings in CA 3513 fibre

As for the Verillion fibre, a decrease of laser power under constant scanning conditions leads to a slower effective refractive index growth [CA 3513-3]. Again, a reduction of the power to 50% of the initial value leads to a 4-fold exposure time. In contrast, an increase of scanning speed under constant UV power lead to a faster saturation of the refractive index [CA 3513-4]. Most significantly, the growth dynamic of grating 1 differs greatly from those of grating 2. Both gratings were fabricated under identical conditions with the only difference in the grating length. Grating 1 is 1 mm in length and grating 2 is 8 mm long. The most substantial difference between the two fabrication processes are the time intervals between two scans after which the beam repeatedly returns to the same fibre section and the fabrication time in total. It has been pointed out by George Simpson that out-diffusion of the

hydrogen from the fibre core have a great impact on the type IA grating writing process [*171*]. When stored outside of a cooled environment, a shorter writing time ensures a more rapid grating evolution. The evolution of the average refractive index is smoother than for any other fibre types. Only the wavelength curve for grating 2 displays a tendential transition through three phases of different slopes. The first ends almost instantly at 1554 nm wavelength, followed by a longer linear period until reaching 1565 nm after 15 units of fluence. This growth finally abates to zero, reaching its final wavelength at 1568 nm, equivalent to a shift of 16 nm.

Not shown here is the variation of grating strength with exposure. Only grating 2 showed a twofold grating regeneration. The transmission dip of all other gratings decreased in a uniform manner.

6.3.3 Gratings in CA-3555 Fibre

Using CA 3555 fibre, the two reference gratings CA 3555-1 and CA 3555-2 were written under similar conditions. Although the laser power for the exposure of those gratings differed only by 10%, their wavelength evolution graphs are inconsistent. This can be seen in *Figure 6.3-6.*

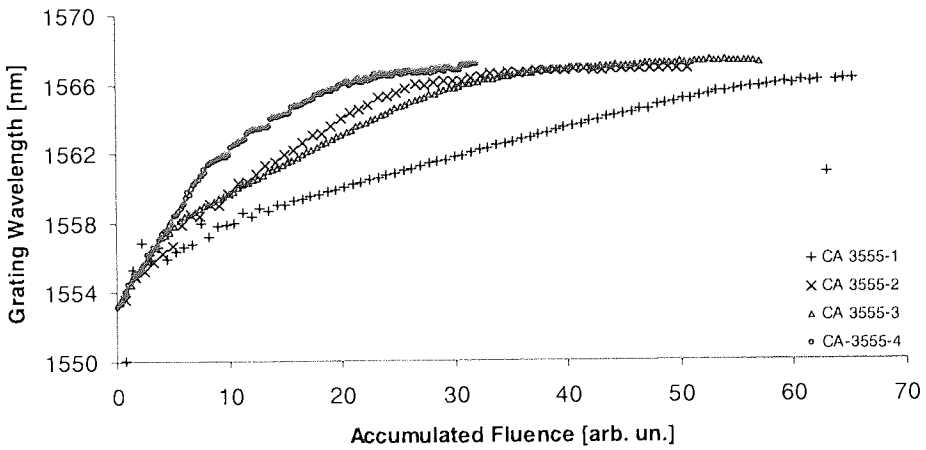

Figure 6.3-6: Growth dynamics of type IA gratings in CA 3555 fibre

The slope of refractive index change of grating 1 is smaller than for grating 2. The wavelength curve for CA 3555-3, which was written at the same speed, but with lower power, follows the curve of grating 1. In comparison with the two previous fibre types, a halving of the power level resulted only in a double number of scans required.

An increase of scanning speed under retention of the laser power, as used for CA3555-2, again displayed a faster saturation of the refractive index, as reported for gratings in CA 3513 fibre.

Total wavelength shifts of over 15 nm were observed. With the exception of grating 4, the wavelength curve can again be approximated by three linear slopes for each of the gratings. This behaviour is most prominent for grating 3. Each grating 1 and 4 shows the regeneration effect after partial erasure at fluence values around 20 and 50, respectively. Grating 3 shows regeneration effects in both these fluence domains. This is not presented here.

6.3.4 Gratings in Corning SM 28 Standard Fibre

A number of type IA gratings have been written in Corning SM 28 standard fibre for comparison reasons. During inscription wavelength shift and grating strength have been monitored in the same manner as for the Type IA gratings. For all fibre samples the saturation of refractive index allowed for a wavelength shift of below 8 nm, describing a continuous curve. This is shown in *Figure 6.3-7*. All three gratings were written under identical conditions and their growth dynamics match well. The noise in the curve of the SM 28-9 sample is a periodical occurring error, which stems from the effect described in ***Chapter 6.3***, caused by measuring the spectrum simultaneously during the writing process.

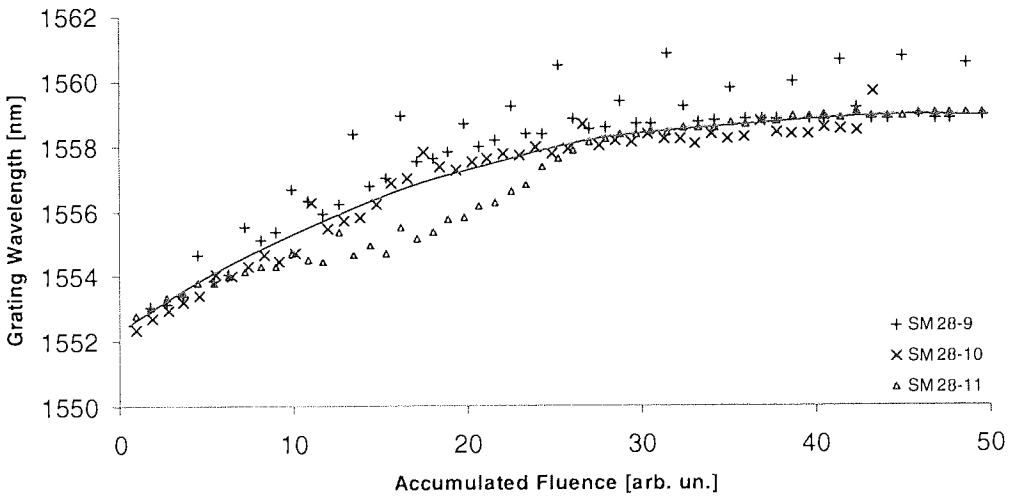

Figure 6.3-7: Growth dynamics of type I gratings in standard SM 28 fibre

Grating evolution has been monitored using UV power between 82 mW and 220 mW using a writing speed of 0.2 mm/s. The results in *Figure 6.3-8* show a decline in the rate of effective refractive index change with decreasing power. It is apparent that the writing time increases with decreasing UV-power.

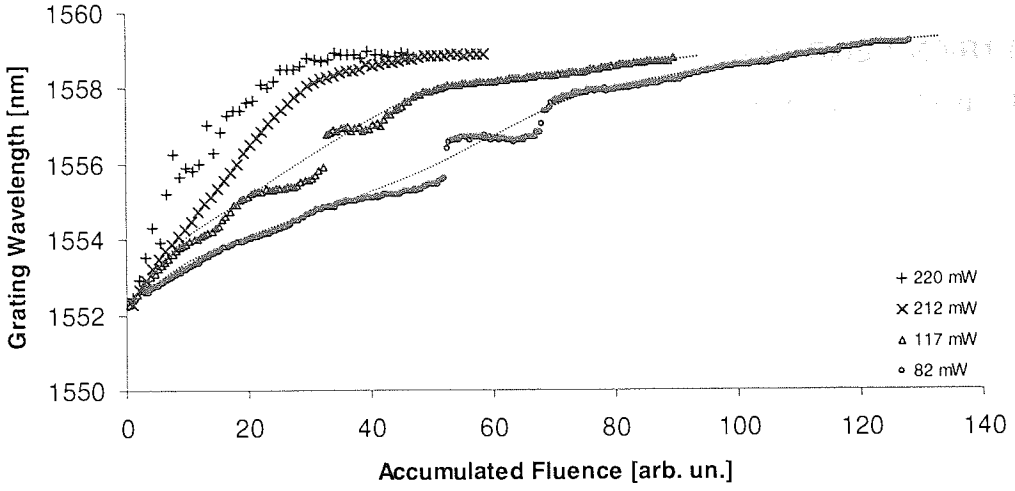

Figure 6.3-8: Wavelength shift over accumulated fluence for type I gratings written in SM 28 standard fibre using different levels of UV-power

To demonstrate the non-linear behaviour of the refractive index change, the multiplicative factor denoting the increase in writing time is plotted against normalised power, where 220 mW is set as 1. This is shown in *Figure 6.3-9*. The time factors have been obtained by rescaling the accumulated fluence axis for each grating in such a way, that their wavelength change curves match the one for the grating written using 220 mW. The increase in writing time with decreasing UV power can roughly be approximated by a second order polynomial function, as indicated in the graph.

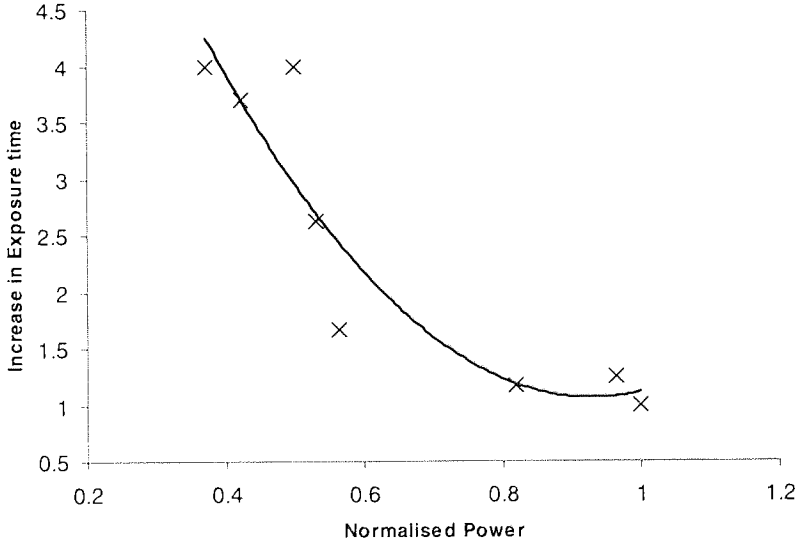

Figure 6.3-9: Effect of change in UV power on writing time

6.3.5 Gratings in Stocker-Yale Fibre

In *Figure 6.3-10* the evolution of a grating written in Stocker-Yale CMS-1550-R1 fibre is shown. This is an intrinsically photosensitive cladding suppressing fibre, yet nothing is known about the dopants in the glass of the fibre core.

The wavelength curve suggests that the grating inside this type of fibre I generated by photosensitivity processes that differ from those in the above-presented fibres. After an initial increase, the central grating wavelength drops and continues to decrease linearly. This data is based on a centriod fit of the grating peak, which is cut-off at the maximum value of the optical dynamic range. No change of grating strength can be observed, which is stronger than 80 dB at all times, which exceeds the measurement sensitivity of the OSA used.

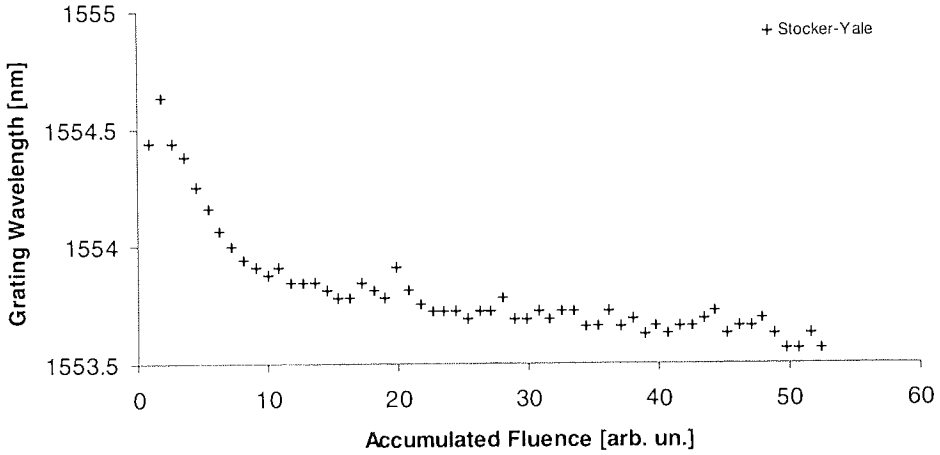

Figure 6.3-10: Growth dynamics of type I gratings in Stocker-Yale fibre

6.3.6 Discussion

As previously reported [*167,168,172*], Bragg grating fabrication in *B-Ge* doped silicate fibres under high UV fluence yields highly complex growth behaviour. In contrast to this, grating growth in standard germanium-silicate fibres in approximation follows a power law, as presented in *Equation 6.3-2* [*51,53*].

$$\Delta n = Ct^{b} \qquad \textbf{Equation 6.1-2}$$

The refractive index change Δn is a function with time t, in which the factors C and b are determined experimentally for each fibre type, using the reflection data from the grating being written. Strictly speaking, this function only applies to grating writing with a stationary beam. It also becomes apparent that as the total refractive index change is established from the grating strength and thus the refractive index modulation, any increase of the average refractive index due to non-modulated parts is neglected. In the case of type IA gratings however, this simplification is not possible. Despite a decrease of grating reflectivity due to decreasing refractive index modulation, the continuing shifting of the central grating

wavelength indicates an increase of the refractive index in the fibre section containing the grating. This behaviour is illustrated in Simpson's work where the dc part of the refractive index is estimated to reach $1.8x10^{-2}$ compared to typical index modulations of the magnitude about 10^{-4} [*171*].

A very likely explanation for these observations considers the function of the boron content and the fluence regime applied to the fibre during grating inscription. In the case of type IIA gratings in boron-germanium fibres, two different mechanisms are assumed to be responsible for the positive and subsequent refractive index change [*34,36*]. Hydrogenation of this type of fibre possibly may trigger the formation of an unidentified defect type, leading to a secondary photorefractive effect of positive sign. This secondary effect may occur at a slower rate, than the effect leading to type I grating evolution. The partial erasure of the first grating may stem from a combined effect due to the limited diffraction efficiency of the phase mask and the refractive index change in the nominally unexposed perturbation minima catching up with the refractive index of the saturated type I maxima. The occurrence of a secondary effect observed in the fibre type used for the experiment also qualitatively matches well with predictions based on the UV dipole-quadrupole model by Kristensen [*174*].

Simpson reported an increase of transmission loss at the 1400 nm absorption band associated with the Bragg wavelength shift during the transition from type I to type II grating [*175*]. The growth and saturation of the absorption band under UV exposure has previously been reported [*176*]. An additional red-shift and broadening of the band suggests that the contributions from *SiOH* (1390 nm) and *GeOH* (1410) are offset in favour of the latter. Convolution of the loss band from a boron-germanium fibre after UV-exposure revealed the formation of a third band around 1424 nm, which to date has not yet been assigned to any known defect.

It is also conceivable that once the hydrogen is completely out-diffused from the fibre, the type IIA photosensitivity effect pays a contribution to the growth dynamics.

Monitoring the *SiOH* - *GeOH* absorption band during blank UV-exposure allows the controlled pre-treated of hydrogenated fibres, in which the type IA gratings can be written subsequently [*175*]. This allows shorter writing times resulting in better control of the modulation index within the fibres, in particular because stability issues of the writing set-up become less critical. Because these results were obtained during the course of the work presented here, this technique was not applied for the grating fabrication.

The regeneration of the gratings and the evolution of the grating wavelength in three stages of different slopes, which both were also observed earlier [*171*], support these assumptions. In this work that effect could not be observed in all gratings. The reason for the latter can be the non-sufficient dynamics of the OSA for the power measurement and the small number of

measurements, as opposed to the requirements to monitor the rapid grating development in the first instants of the fabrication process.

The UV fluence during the grating inscription appears to play an important role for the observation of the erasure and regeneration effect of gratings. This appears in all gratings written in *G/Ge* fibre at low power except Verillion 4. Using 180 mW, it takes place preferentially at higher scanning speeds, as seen in Verillion-1, CA 3513-4 and CA 3555-4.

Hydrogen out-diffusion and grating self-annealing due to heating effects from the laser beam may indicate the existence of additional, thermally unstable photorefractive processes taking place during type IA grating fabrication.

A decrease of UV power while maintaining all other fabrication parameters constant consistently shows the trend of a slowed down grating evolution. For the Verillion, CA 3513 and SM 28 fibre, the trend of a parabolic increase of exposure time with decreasing UV power is observed.

Still, there are great discrepancies in the grating fabrication process, as seen in the cases where gratings written under seemingly identical conditions exhibit largely different growth dynamics. This is most obvious for the gratings 1 and 3 in Verillion fibre, as well as the respective samples 1 and 2 from the CA 3513 the CA 3555 batch.

All inconsistencies occur in cases, in which high laser power was used for grating inscription and in which the scanning speed or time was changed, as described above, in particular for the gratings 2 and 4 in CA 3513 fibre. Heating effects in the fibre core could play an important role in the occurrence of these discrepancies.

It is more likely that a set of factors affects the apparently incoherent results. For conclusive results more attention has to be paid to experimental conditions as air temperature and total duration of the inscription process. Hydrogen out-diffusion may be one of the main error sources. Another factor is the accelerated self-annealing of the fibres at elevated UV power levels.

One indicator to support the last assumption is the similarity between the growth curves for gratings 2 and 4 in the Verillion fibre. For moderate laser power the definition of the accumulated fluence allows the normalisation of the refractive index change for different beam powers. The accelerated refractive index saturation, achieved by increase of the scanning velocity for the gratings CA 3513-4 and CA 3555-2 can also be explained by a reduced out-hydrogenation and annealing effect if the photorefractive effect is assumed to happen on a faster time scale than the heating effect in the fibre core.

For an explanation of these surprising results, further experiments under more constrained experimental conditions will be necessary. The number of samples for the work presented here is too low for a conclusive statement. The spread of results from 12 gratings in SM 28

fibre written under constant and varying UV-power suggests a high possibility of outliers amongst the data for the boron-germanium fibres.

Only the writing of gratings in Stocker-Yale fibre contradicts all findings from the other fibre samples. The grating wavelength stays fairly constant during the inscription process. With continuous UV-exposure the grating strength exceeds the measurement range of the OSA. Based on centroid fits of the visible spectrum this fibre type even shows a tendential reverse trend, a decrease of grating wavelength.

6.4 Annealing Experiments

When subjected to high temperatures, UV-written gratings proved to be far from permanent structures of refractive index modulation. Instead the grating spectra shift towards shorter wavelengths [*177*] and a decrease in reflection is observed [*178*]. The glass structure of the fibre core is found to recombine into its initial state, showing the defect centres, as present before UV-illumination.

Nowadays the annealing of UV-written FBGs is used as a standard method for the determination of grating lifetime cycles and temperature stability , as well as the identification of the defect types responsible for the photo-induced refractive index change [*179,180,181,182*].

To ensure a good stability of UV gratings under temperatures complying with the operational conditions, fibre gratings are usually subjected to an accelerated annealing process directly after inscription [*183*]. The occurring changes in reflectivity and wavelength have to be taken into account.

6.4.1 Experimental setup

After writing, all gratings presented here were stored in a freezer at -30° C before being annealed at 80° C in a Sanyo-Gallenkamp environmental chamber over a period of at least 65 hours. Each end of the fibres containing a grating was spliced to a pigtail cable. Up to eight gratings at one time were fixed on an even surface inside of the heating chamber. One pigtail end of each fibre was connected to the output of a 1x8 coupler, connected to the laser output port of an EXFO IQ-12004 measurement kit. The other ends were plugged into the input ports of the power metres of the same equipment. This is illustrated in *Figure 6.4-1.*

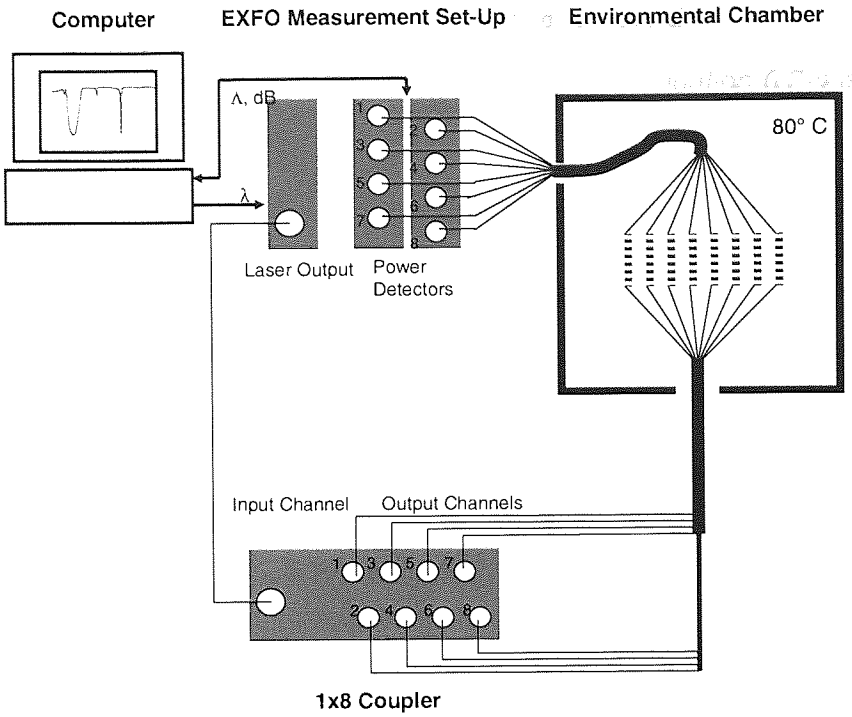

Figure 6.4-1: Measurement arrangement for monitoring the annealing process of type IA gratings

The spectra of all gratings were taken simultaneously in intervals of 20 minutes and saved in a corresponding file for each grating. After abortion of the annealing test the data on grating wavelength and strength were extracted from these files using special Labview software. The wavelength was determined by centroid fit of the loss peak, whereas the grating strength was directly measured from the minimum value of the light transmission.

6.4.2 Methodology

As pointed out in the previous chapter, the analysis of the data from gratings in hydrogenated boron-germanium fibre is not straightforward. The first and most general formalisms for the description of annealing processes in optical fibres are the power-law approach and the ageing curve approach, proposed by Erdogan et al. [*179*]. The appeal of the former lies in the simplicity of approximating the refractive index decay by *Equation 6.4-1.*

$$\kappa = \frac{1}{1 + A\left(\frac{t}{t_1}\right)^{\alpha}} \qquad \textit{Equation 6.4-1}$$

The dimensionless factors A and α are temperature dependent and have to be determined from the experimental data, whereas the time t is given in relation to a reference constant t_1 of the same dimension.

Factor A shows good correspondence with experimental data, if plotted in form of *Equation 6.4-2*, with T being the annealing temperature in Kelvin and A_0 and α constants.

$$A = A_0 \exp(aT) \qquad \textbf{Equation 6.4-2}$$

From work done by Erdogan the definition of α according to *Equation 6.2-4* is only accurate for temperatures of 600 K or higher.

$$\alpha = \frac{T}{T_0} \qquad \textbf{Equation 6.2-3}$$

The normalised refractive index κ has also been introduced as the relative fringe visibility in ***Chapter 4.2***. It is defined as the integrated coupling constant (*ICC*) scaled to unity. For gratings of reflectivity up to 96% *ICC* can be derived from the grating spectrum following *Equation 6.4-4*, in which *R* is the normalised reflectivity.

$$ICC = a \tanh\left(\sqrt{R}\right) \qquad \textbf{Equation 6.2-4}$$

It has been pointed out however, that the grating lifetime prediction from this method is only valid for non-hydrogenated germanium-silicate fibres.

More general formalisms for lifetime estimations [*181,182*] are based on the ageing curve approach [*179*] and require annealing test over a range of temperatures exceeding 300°C.

Data on boron-germanium co-doped fibres specifically has been presented on long term-stability in fibres from hydrogen-loaded performs [*183*] and on annealing effects originating from material decay exceeding 100°C [*184*].

The experimental set-up used for this work does not fit any of the special cases described above. As will become evident below, the decrease in the *ICC* is not the only effect on the refractive index of the gratings. Shifts of central grating wavelength are found to be partly independent from the grating decay.

6.4.3 Results

The power law approach gives a good approximation of the refractive index decay curves observed. From least square value fits of the differences between the function in *Equation 6.4-1* and the actual decay curves the parameters *A* and α were determined for all gratings. *Figure 6.4-2* exemplary shows the three different types of annealing curves exhibited by the gratings and compared to the theoretical fit. In all cases the annealing temperature was 80ºC. The obtained parameters are presented in *Table 6.4-1*, alongside some initial grating properties and fabrication parameters. In the case of (a) the decay of modulated refractive index fits well into the power law model, whereas in case (b) some discrepancies are visible, which mainly manifest as oscillations of κ at the earlier stage of the annealing process. A similar behaviour of annealing curves was observed by Simpson [*170*] for gratings written in fibres that were under strain during the UV-exposure. The strain had no obvious effect on the grating evolution and could not be correlated to the shape of the annealing curves.

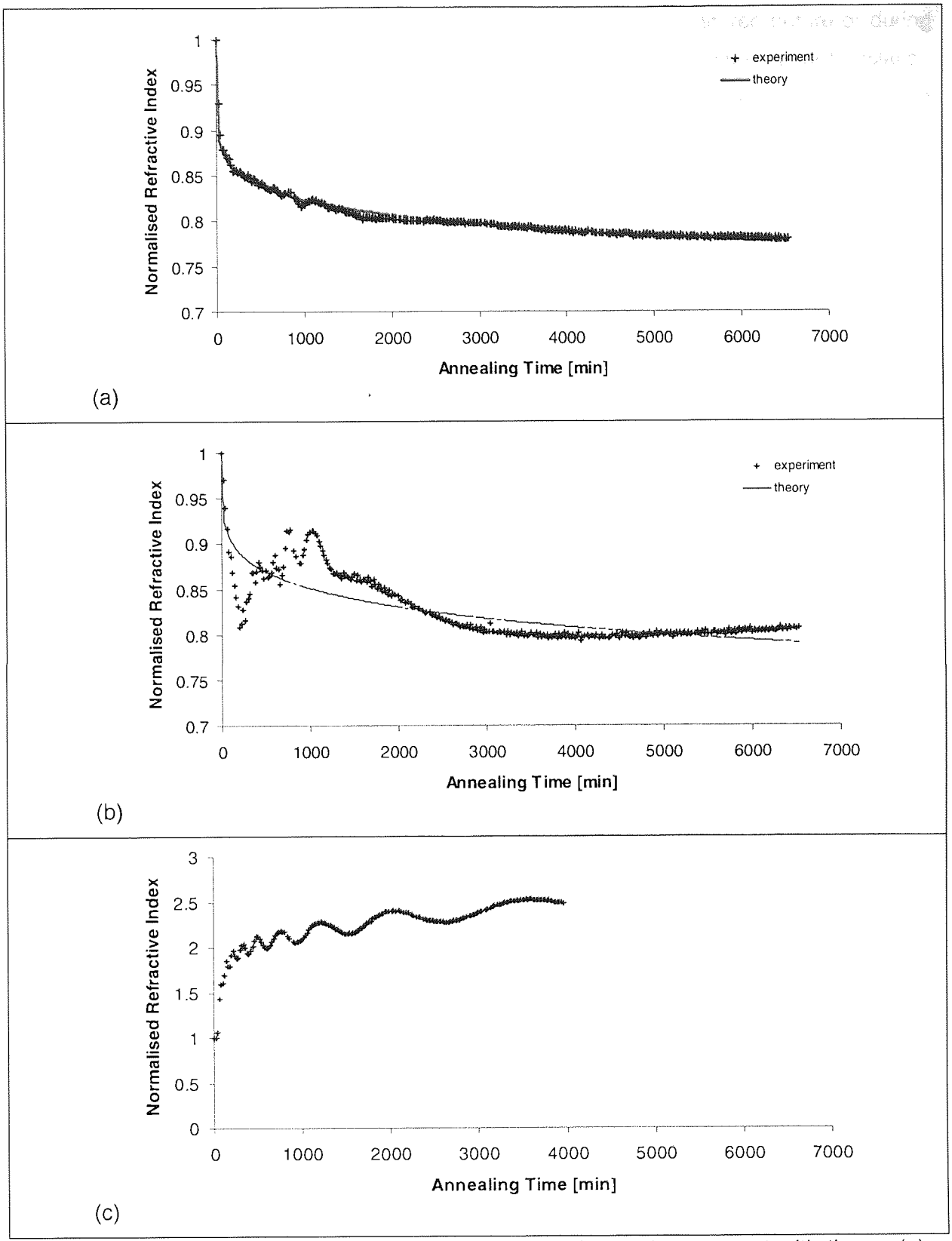

Figure 6.4-2: Example of grating decay curves in good agreement with theory (a), fair agreement (b), and without converging result (c)

The increase of refractive index modulation as shown in *Figure 6.4-2 (c)* can be seen for the gratings 1 and 4 in CA 3555 fibre and in grating 3 in CA 3513 fibre. To my knowledge such

an effect has not been reported yet. It is possible that it is an extreme case of the effect seen in section (b) of the same figure. The strain of the fibre was not monitored before or during the inscription, although the fibres have been stretched using the 3-dimensional translation tower on one side of the fibre mount. This was done to prevent the bowing of the fibre in the centre and to ensure the UV beam hits the fibre core in each section.

Fibre Type	Sample	Grating Type	A	α	Convergence	Reflection	Inscription Power [mW]	Scan Velocity [mm/ s]	Accumulated Fluence
Verillion	1	IA	0.1125	0.2039	A	0.71	190	1	11.4
	2	IA	0.0718	0.1584	A	0.71	96	1	36
	3	IA	0.1620	0.1957	A	0.72	188	1	24.8
	4	IA	0.1019	0.1186	B	0.73	95	0.2	47.5
	5	IA	0.2376	0.1498	A	0.56	180	0.2	10.5
	1	I	0.0390	0.2663	A	0.29	190		
	2	I	0.0275	0.2217	A	1.00	96		
	3	I	0.0277	0.2087	B	0.98	188		
	4	I	0.0435	0.1343	B	0.83	95		
	5	I	0.0291	0.1827	A	0.84	180		
CA 3513	1	IA	0.0652	0.2532	B	0.14	175	0.2	74.4
	2	IA	0.2410	0.1415	A	0.99	175	0.2	20.1
	3	IA	N/A	N/A	C	0.99	90	0.2	42.8
	4	IA	N/A	N/A	C	0.98	171	1	17.6
	1	I	0.0381	0.2207	B	0.18	175		
	2	I	0.0442	0.1767	A	0.99	175		
	3	I	0.0474	0.1727	A	0.92	90		
	4	I	0.0323	0.2131	A	0.98	171		
CA 3555	1	IA	N/A	N/A	C	0.15	150	0.2	65.3
	2	IA	0.2883	0.0492	B	0.99	166	0.2	50.6
	3	IA	0.1358	0.2180	B	0.85	87	0.2	57
	4	IA	N/A	N/A	C	0.82	160	1	32
SM 28	9	I(a)	0.0738	0.0718	B	0.10	180	0.2	54
	10	I(a)	0.0180	0.1402	B	0.69	184	0.2	43.2
	11	I(a)	0.0164	0.1771	A	0.08	180	0.2	50.4
	9	I	0.0357	0.1235	A	0.09	180		
	10	I	0.0178	0.1796	B	0.36	184		
	11	I	0.0133	0.2370	A	0.96	180		

Table 6.4-1: Overview of annealing parameters affecting index modulation

Due to the large spread of the A and α values, obtained from the annealing curves, it is difficult to link the results with any of the fabrication parameters or other grating properties. Only the standard and saturated type I gratings in SM 28 and Stocker Yale fibre were fabricated under controlled conditions. All other type I gratings were fabricated for reasons of reference of central wavelength, temperature and strain coefficients only. The annealing curves of type IA gratings 3 and 4 in CA 3513 fibre and type IA gratings in 1 and 4 in CA 3555 do not fit the theoretical model and neither do any of the gratings in the CA 3629 and

Stocker-Yale fibre. In these gratings an increase of grating strength is observed either directly at the beginning of the annealing process or after a certain period of decay. The latter trend is also visible in *Figure 6.4-2 (b)*. Strain on the fibre samples during the inscription process is a possible explanation. In the case of the Stocker-Yale fibre, the effect is more likely to be due to the material composition of the fibre itself, showing good grating stability with respect to strength and wavelength.

Neither the A and α values, nor the convergence condition of the annealing curves of the different gratings can be correlated to the fluence during the exposure or their initial reflectivity. Most of the α values are between 0.15 and 0.25 with a few outliers in between. The validity of the α factors for annealing temperatures as low as the ones used here has been put in question since the first formulation of the power law approach [*179*]. The coefficients found here correspond well in magnitude with the results reported.

As a general trend, all A factors tend to be larger for the type IA and saturated type I gratings than those for the standard type I gratings. In the case of type IA gratings in Verillion fibre, the value of A increases with increasing UV power and decreasing speed. The same trend continues for the data obtained from the CA 3555 fibre.

In the models describing the decay of refractive index in UV written fibre gratings changes in the mean refractive index are not considered. This is because of the general assumption that most of the refractive index change during the writing process is effectively turned into the index modulation of the grating. To the behaviour seen in this work an analogy can be found to annealing effects in gratings written in fibres that were treated with a hot hydrogenation process or photosensitivity locking [185]. Considering the fabrication parameters, in particular the UV-power and fluence used for the fabrication of type IA gratings, this analogy becomes plausible. Because of the large wavelength shifts observed during the fabrication of type IA gratings under constant or even decreasing grating strength, a second set of data is required considering this effect.

Figure 6.4-3 shows the spectrum of the CA 3513-2 sample before and after annealing. Besides the larger decrease of the transmission dip, it can also be seen that the type IA grating shifts over a larger wavelength range than the type I grating.

The full annealing data for all gratings in the different fibre samples is displayed in the following *Figure 6.4-4* to *Figure 6.4-8*.

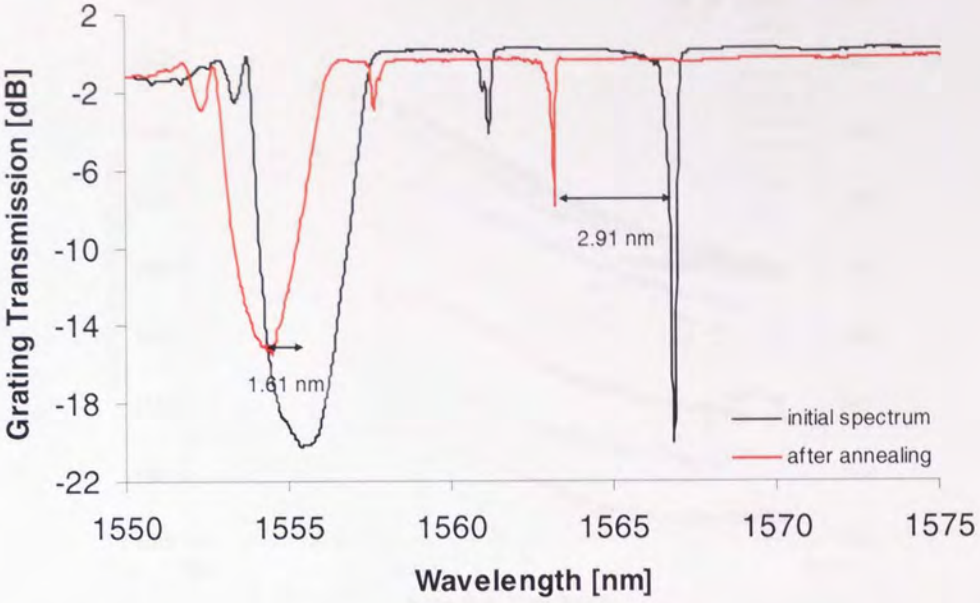

Figure 6.4-3: Exemplary spectra of type I and type IA gratings in fibre sample CA 3513-2 before and after annealing

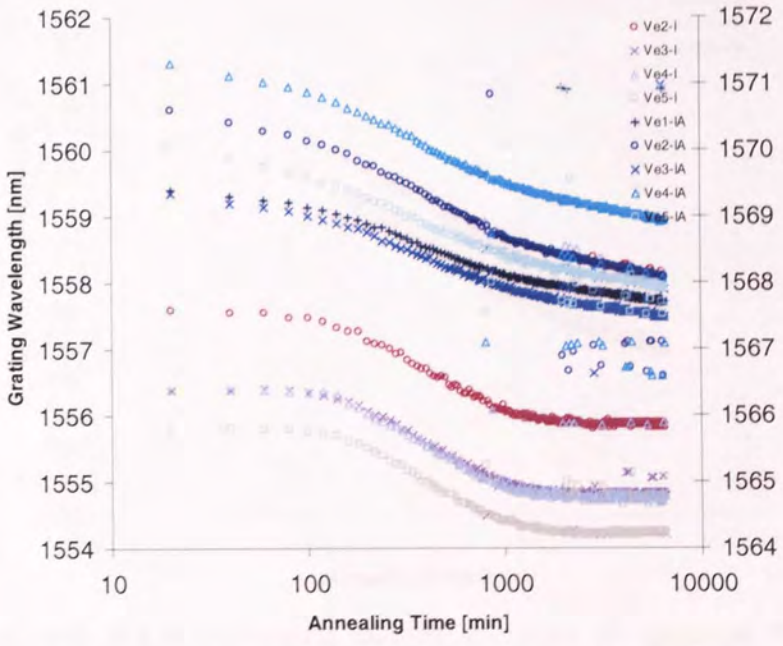

Figure 6.4-4: Annealing curves for type IA and type I gratings in Verillion fibre

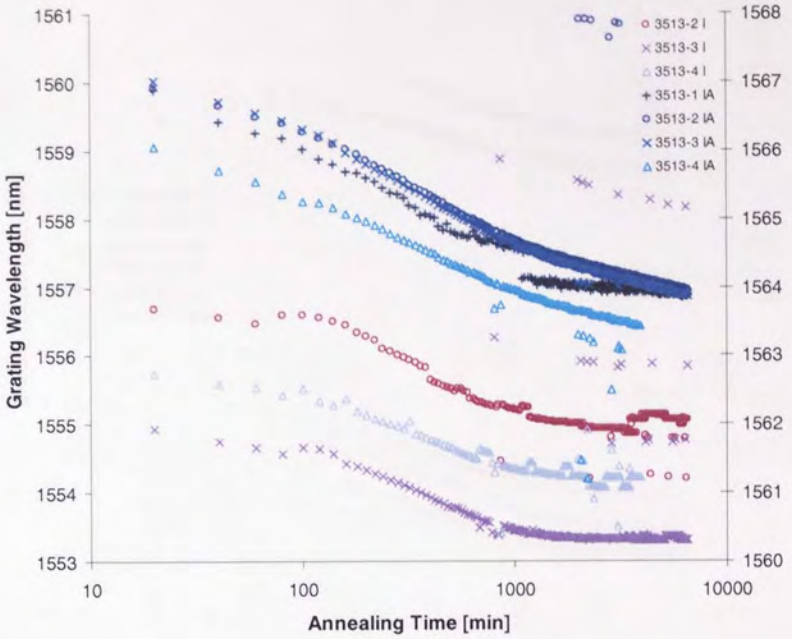

Figure 6.4-5: Annealing curves for type IA and type I gratings in CA 3513 fibre

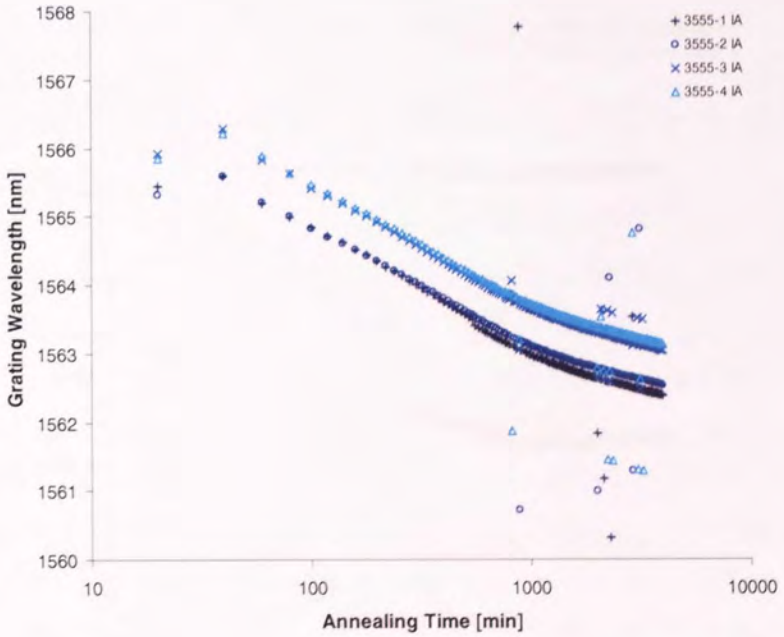

Figure 6.4-6: Annealing curves for type IA gratings in CA 3555 fibre

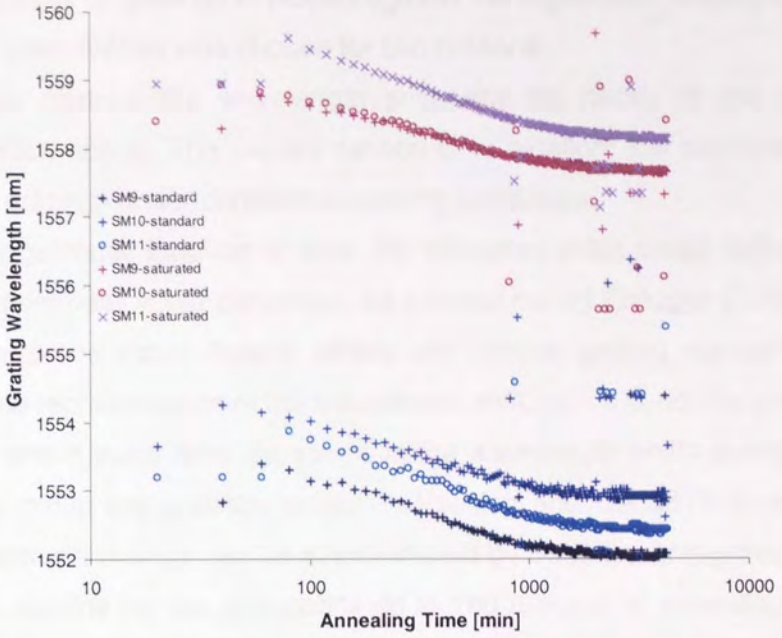

Figure 6.4-7: Annealing curves for saturated and non-saturated type I gratings in Corning SM 28 standard fibre

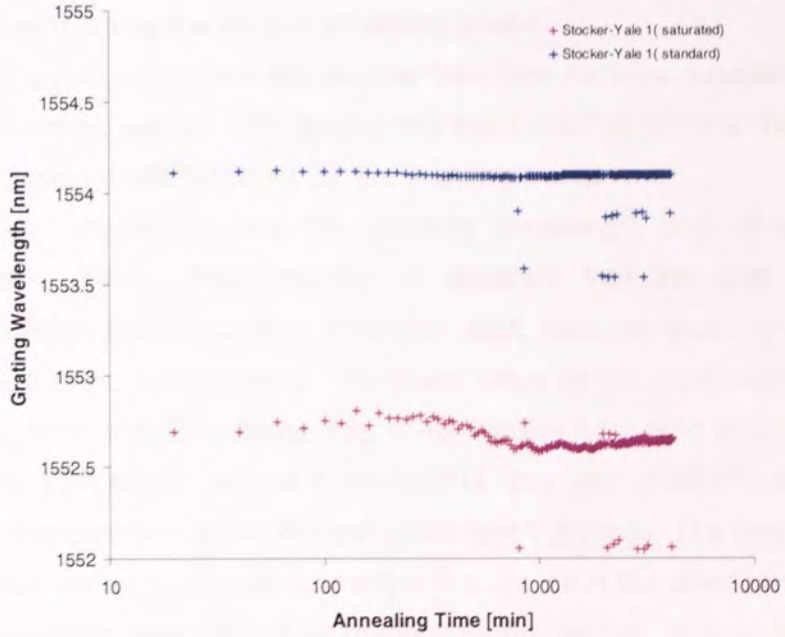

Figure 6.4-8: Annealing curves for saturated and non-saturated type I gratings in Stocker-Yale CMS fibre

The wavelength shift of all gratings is plotted against the logarithmic display of the annealing time. This form of presentation was chosen for two reasons.

Firstly, in order to contrast the wavelength shift with the decay of the refractive index modulation presented above. The second reason is to highlight the continuous wavelength shift if the type IA gratings under constant annealing conditions.

Plotted over the logarithmic function of time, the refractive index decay following the power law function will show near linear behaviour, as pointed out by Erdogan [*179*]. If we assume that the mean refractive index linearly affects the central grating wavelength, the same should apply for the representation of the wavelength shift, which is not the case here.

From the figures above three different trends in the wavelength shifts during annealing are found. In the first group are gratings written in Verillion and CA 3513 fibre. In logarithmic display their wavelength change can be approximated by three linear regression curves: one with a low or zero decline for the data points up to 160 minutes of annealing, a steeper one for the period between 160 and 1000 minutes and a third one of lower steepness after that. In the first and third phase the slope of the type IA gratings is higher than that of the type I gratings. Here the slopes of the type I gratings are zero. For the central section no clear conclusion can be made.

The evolution of the gratings in CA 3555, CA 3629 and Corning SM 28 fibre takes place in two phases, the first having the higher decrement. In the case of the boron-germanium fibres the slope changes after 900 minutes of annealing, whereas for the standard fibre this happen after 1000 minutes. Little difference can be observed between the annealing curves of the standard and saturated type I gratings in the SM 28 fibre. The slopes of the latter again reach values close to or zero during the second annealing phase.

The wavelength of gratings written in the Stocker-Yale fibre remains constant throughout the whole annealing process. Around 900 minutes into the annealing process the wavelength of the overexposed grating drops for about 0.2 nm in a single step.

The initial and final wavelength and the resulting wavelength shift of all gratings are compared in ***Table 6.4-2***. From there it is apparent that the type IA gratings in boron-germanium fibres show a larger wavelength shift, than the type I gratings, which in turn are more stable in the standard fibre. The typical value for the wavelength shift of type IA gratings in the CA 3513 and 3555 fibres after 6540 minutes annealing at 80°C is 3 nm. The lower value of only 2.63 nm for sample 4 in CA 3513 fibre after 3960 minutes confirms the continuous annealing process, as in contrast to the type I gratings. The type I grating in the same sample shows the same wavelength shift of 1.6 nm, as in the other samples after 6540 minutes. The wavelength shifts of type IA gratings in the Verillion fibre scatter over a large range between 1.7 nm and 2.52 nm. This may be caused by the rapid wavelength shift in the initial moments of the annealing process, which was not monitored using 20-minute intervals.

Fibre Type	Sample	λ_{start}^{I} [nm]	λ_{start}^{IA} [nm]	λ_{end}^{I} [nm]	λ_{end}^{IA} [nm]	$\Delta\lambda^{I}$ [nm]	$\Delta\lambda^{IA}$ [nm]	t [min]
Verillion	1	No Data	1569.40	No Data	1567.70	-	1.70	6540
	2	1557.54	1570.60	1555.85	1568.08	1.69	2.52	6540
	3	1556.39	1569.34	1554.79	1567.46	1.60	1.88	6540
	4	1556.40	1571.31	1554.77	1568.92	1.63	2.39	6540
	5	1555.81	1570.04	1554.21	1567.91	1.60	2.13	6540
CA 3513	1	No Data	1566.89	No Data	1563.91	-	2.98	6540
	2	1556.68	1566.91	1555.07	1563.95	1.61	2.96	6540
	3	1555.73	1567.01	1554.22	1563.87	1.51	3.14	6540
	4	1554.93	1566.05	1553.31	1563.42	1.62	2.63	3960
CA 3555	1	No Data	1565.59	No Data	1562.38	-	3.21	3960
	2	No Data	1565.59	No Data	1562.53	-	3.06	3960
	3	No Data	1566.27	No Data	1563.04	-	3.23	3960
	4	No Data	1566.21	No Data	1563.13	-	3.08	3960
SMF 1300	9	1553.38	(1558.76)	1551.98	(1557.64)	1.40	1.12	4220
	10	1554.24	(1558.93	1552.88	(1557.65)	1.36	1.28	4220
	11	1553.86	(1559.59)	1552.42	(1558.13)	1.44	1.46	4220
Stocker-Yale	1	1554.23	(1552.83)	1554.12	(1554.10)	0.11	-1.27	4220

Table 6.4-2: Wavelength shifts in type I and type IA gratings due to annealing

In the SM fibre the standard type I gratings show average values of around 1.4 nm, similar to those in the saturated gratings, varying between 1.12 nm and 1.46 nm. The results from the Stocker-Yale fibre showing a wavelength increase for the overexposed grating are not ambiguous, as the wavelength fluctuates randomly in the early stage of the annealing. There is hardly any difference in wavelength for the standard grating.

For the type IA gratings, a comparison between *Table 6.4-2* with *Table 6.3-1* indicates a trend, according to which the wavelength shift tends to be lower for higher writing powers.

6.4.4 Discussion

The grating annealing procedure presented here was mainly aimed to stabilise the gratings before the measurements of temperature and strain coefficients and to highlight the different properties of type I and type IA gratings. As pointed out earlier, for a valid prediction of grating lifetime a larger number of samples would have been necessary and additional data from experiments at significantly higher temperatures are needed. This can be done as a future project. It is also questionable whether existing models can be applied to describe the stability of type IA gratings. All approaches so far only deal with isolated aspects of grating inscription, as are the impact of hydrogenation or the boron content.

Although the power law approach could be used to fit most of the grating annealing curves with good or fair approximation, the incoherence of the resulting A and α coefficients indicate

more complex underlying mechanisms and the requirement of better controlled fabrication conditions.

A first approach to ensure a better fit of the annealing curves with theory is the control of fibre strain during inscription. A better control of temperature conditions, writing time and annealing at higher temperatures may help to achieve more coherent A and α values.

The possibility of auto-annealing effects from heat effects during the UV inscription process has been pointed out in the literature [*182,170*]. This becomes even more critical in the case of gratings written through overexposure and using high UV power. However, from the data available from this work no clear trend is observed indicating the impact of UV power or total accumulated fluence during inscription.

The most evident problem is the fact, that all annealing methods for life time prediction use the effective refractive index decay, whereas it has been shown here that in type IA gratings the dc value of UV-induced refractive index change becomes important. During the writing process the grating is not defined by its strength, but by the maximum shift in wavelength. This automatically leads to large differences in the reflectivity values of the gratings. One possibility to tackle this problem and control the grating strength is the blank beam pre-exposure method suggested by Simpson [*171*].

In reality the grating wavelength shift $\Delta\lambda_{Bragg}$ due to a change in refractive index δn follows the *Equation 6.2-5*.

$$\Delta\lambda_{Bragg} = \lambda_{Bragg}\frac{\kappa\delta n}{n_{eff}} \qquad \textbf{Equation 6.2-5}$$

It becomes apparent that the effective refractive index n_{eff} and the relative integrated coupling coefficient κ have to be known at the same time. It is possible including the first in the equation for each measurement point during the annealing process, as described above. The determination of the effective refractive index n_{eff} is not so straightforward. For an accurate measurement of the change in dc refractive index an interferometer set-up can be used. Therefore the relative change in time delay of a recombined coherent laser signal needs to be measured after travelling through a fibre treated by blank UV-inscription or an annealing process, and a length of reference fibre [*186*].

As a first step the wavelength shift of the gratings monitored during annealing was plotted against the logarithm of annealing time, assuming a near-linear relation between wavelength and mean refractive index. Depending on the fibre type, in this representation the wavelength showed two or three quasi-linear regimes of decline. The phase of steep decline can be considered to be the main thermal depopulation effect of meta-stable states induced by UV-exposure. In the type I gratings the complete depletion of these centres, which can be achieved at the given temperature, is reached after 900-1000 minutes, showing no or only

small subsequent changes in wavelength. This is different for the type IA gratings, where the wavelength continues to fall linearly, but with a lower decrement.

A possible explanation for this is the existence of two separate defects in the latter fibre type, which decay at different rates. This is analogous to the assumption of different colour centres competing during UV inscription. These may differ in activation energy and population numbers. As the first defect sites completely deplete, the second type may still be prevalent. In that case the slope of the steep refractive index decline is the superposition of two effects, which after the saturation of the first takes the value of the remaining one.

Hypothetically the slowed wavelength shift in the Verillion and CA 3513 fibre during the first annealing phase could be explained by a third annealing effect with positive refractive index change and shortest saturation time. This has been reported in boron-germanium fibres and explained by material decay due to the boron content of the fibre [*184*]. For short annealing times at temperatures below 150°C this effect appears to be negligible, but it has not been investigated in hydrogenated fibres yet.

6.5 Sensing Parameters of 255 nm written Type IA Gratings

Besides the anomalies of their evolution during UV-inscription and annealing, it has been reported, that Type IA gratings exhibit a temperature coefficient that is significantly lower than any other grating type. The difference in temperature sensitivity reaches values of 55%, if compared to Type IIA gratings, showing great potential for applications as simultaneous measurements of multiple measurands [*168, 169*]. In contrast to the temperature coefficients, the strain coefficients for all grating types are fairly constant.

The concept of a Type IIA-IA double-grating sensor head has been suggested for that purpose, with which wavelength shifts from temperature can be discriminated from those due to strain.

Therefore, the Type IA and Type I gratings written for this work were tested with respect to their temperature and strain sensitivity.

The discrimination between temperature and strain in a dual-grating set-up can be obtained using the respective sensitivity matrix, as shown in *Equation 6.5-1.*

$$\begin{bmatrix} \Delta\lambda_1 \\ \Delta\lambda_2 \end{bmatrix} = \begin{bmatrix} \kappa_{T1} & \kappa_{\varepsilon 1} \\ \kappa_{T2} & \kappa_{\varepsilon 2} \end{bmatrix} \begin{bmatrix} \Delta T \\ \Delta\varepsilon \end{bmatrix} \qquad \textit{Equation 6.5-1}$$

The wavelength shifts $\Delta\lambda_1$ and $\Delta\lambda_2$ of two distinctive gratings subjected to a change of temperature ΔT and strain $\Delta\varepsilon$ are a function of their respective temperature and strain coefficients, κ_T and κ_ε. The coefficients are determined from independent temperature and strain measurements on each grating.

For strain-temperature discrimination the vectors inside the sensitivity matrix have to be independent. By inversion of the matrix multiplication, temperature and strain can be obtained from the wavelength shifts of the two gratings.

6.5.1 Temperature Sensitivity Measurements and Results

For the measurement of the temperature coefficients, both gratings were sandwiched within a heat-sink paste between a 5W Peltier element and a block of Styropor ©. The whole arrangement was placed within a plastic box. The heating element with an integrated temperature probe was connected to a computer controlled current source and temperature indicator. The grating spectrum was continuously monitored using a broadband light source (BBS) with an OSA. This is indicated in *Figure 6.5-1*.

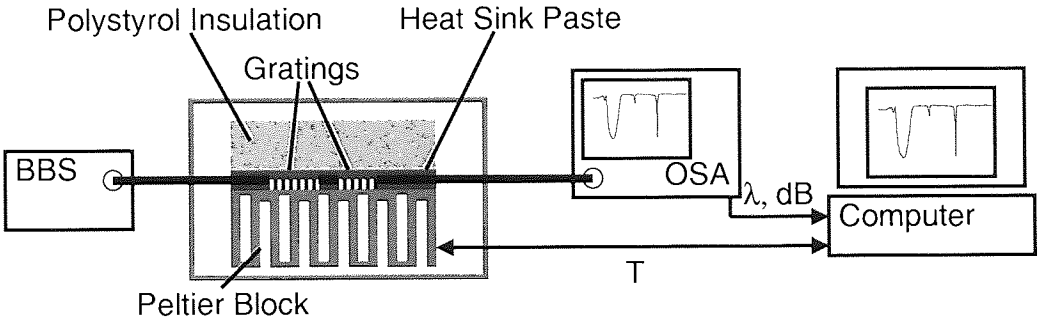

Figure 6-5.1: Measurement set-up for temperature coefficients of type I and IA gratings

In general the temperature was set to start from 20°C and then to rise in 5°C increments to 80°C. As soon as the temperature reached the programmed temperature and stayed stable within a margin of ±0.1°C, the actual grating spectrum was captured on the OSA and the data saved in a file. In addition, the software controlling the process determined the grating wavelength by centroid-fit. The result from one Type I-IA grating pair is presented in *Figure 6.5-2*.

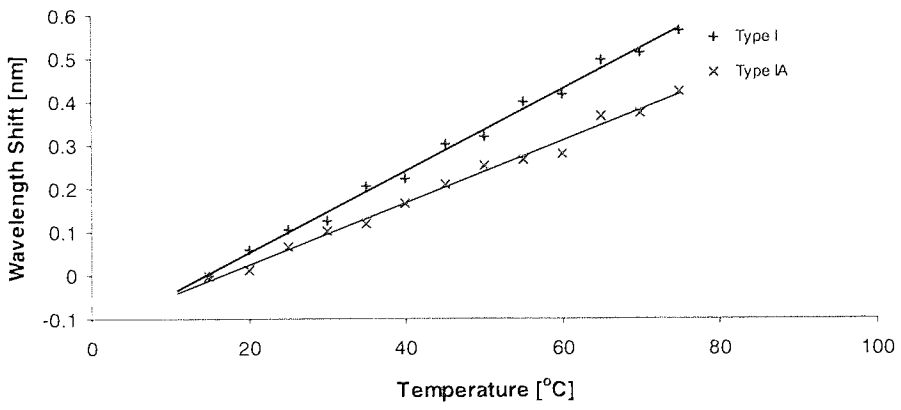

Figure 6.5-2: Temperature dependent wavelength shifts of type I and type IA gratings in CA 3513-3

The linear regression for the wavelength shift against temperature for the gratings yields κ_T values of 9.4 pm/K for the type I grating and 7.1 pm/K for the type IA grating. In the same manner the temperature coefficients for all other gratings have been established. The results are summarised in *Table 6.5-1*.

Fibre Type	Sample	κ_T(I) [pm/K]	κ_T(IA) [pm/K]	Difference [%]
Verillion	1	8.7	8.1	-7.4
	2	8.7	8.2	-6.1
	3	8.9	8.1	-9.9
	4	8.5	7.9	-7.6
	5	8.6	8.0	-7.5
CA 3513	1	8.9	7.8	-14.1
	2	9.3	8.9	-4.5
	3	9.4	7.1	-32.4
	4	9.6	8.2	-17.1
CA 3555	1	(8.4)	7.9	(-6.3)
	2	(8.6)	8.1	(-6.2)
	3	N/A	8.5	N/A
	4	N/A	8.6	N/A
SM 28	9	10.1	(10.0)	(-1.0)
	10	10.1	(9.9)	(-2.0)
	11	9.5	(10.0)	(+5.0)
Stocker-Yale	1	9.5	(9.5)	(0)

Table 6.5-1: Temperature coefficients of type I and IA gratings

The data for the Verillion and CA 3513 samples is obtained from grating of both types. A clear trend towards smaller κ_T for type IA gratings is observed. In the case of the Verillion fibre, the average value for type I gratings is (8.7±0.2) pm/K and (8.05±0.15) pm/K for type IA gratings. This results in a difference of κ_T ranging between 6% and 10%.

The values for the CA 3513 gratings are spread over a larger range with the median κ_T=(9.25±0.35) pm/K for type I gratings and (8.35±0.55) pm/K for type IA gratings. For the individual fibre samples κ_T varies between 4.5% and 32.4%. The extremely low value for the sample number 2 is likely to be due to a measurement error. Possible reasons may be the lack of contact between fibre and Peltier element or slippage of the fibre.

Comparison data does not exist for the other fibre types. In the case of CA 3555 fibres no type I gratings were inscribed along the type IA gratings into the fibre samples. For all other fibres the gratings resulting from the overexposed writing step cannot be considered to be Type IA gratings. This is reflected in the red wavelength shifts of 6 nm at best. For the latter group of fibre samples the temperature coefficients differ less that 5% for the overexposed gratings in comparison to standard Type I gratings. This is shown in parentheses. Both

increased as well as decreased coefficient values are observed. On average, the coefficient of type I gratings is by 10% lower that the one in the fibres of high boron content.
In two of the CA 3555 fibres, the splitting of the main wavelength loss peak is observed. This has previously been reported in Type IA gratings. The peak at lower wavelength is believed to be the effect from a higher order mode in the fibre due to the increased V-number. In both cases tested here their κ_T-value is found to be 6% higher than for the type IA grating.

6.5.2 Strain Sensitivity Measurement and Results

After the temperature measurements all fibres were clamped with padded metal clamps inside V-groves, which were on metal holders fixed on a massive aluminium block and a one dimensional translation stage, respectively. The aluminium block and the translation stage were clamped on an optical table. A schematic of this set-up is shown in *Figure 6.5-3*.

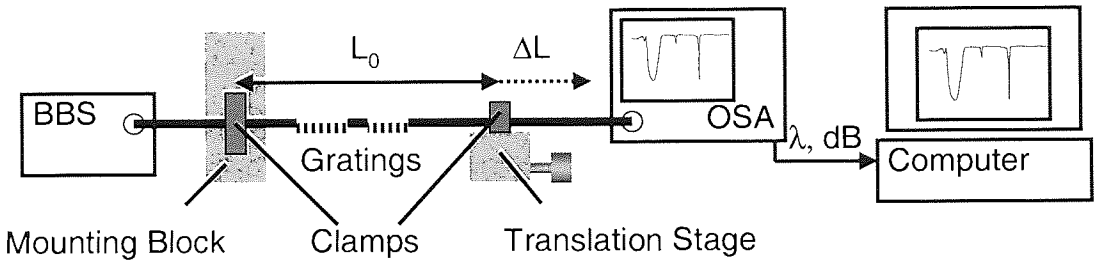

Figure 6.5-3: Measurement set-up for strain coefficients in type I and IA gratings

Using the adjustment screw of the translation stage, the fibre was then stretched to a point before being strained. Using a ruler, the distance between the centres of the two metal clamps was measured and defined as the reference fibre length at zero strain. After an initial waveform capture, the fibre was stretched in equidistant intervals, using the micrometer screw of the translation stage. Labview software calculated the applied strain using *Equation 6.5-2* and determined the central wavelength of the grating applying a centroid fit.

$$\varepsilon = \frac{\Delta L}{L_0} \qquad \textbf{Equation 6.5-2}$$

The strain ε is a simple division of the cumulative increase in length ΔL by the initial fibre length L_0. *Figure 6.5-4* shows an example for the resulting wavelength over strain curves.
An overview of all results is given in *Table 6.5-2*.

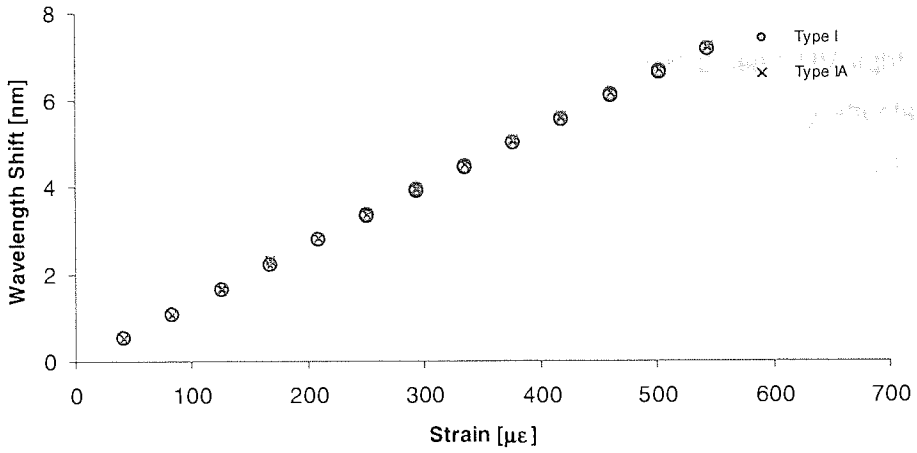

Figure 6.5-4: Wavelength shifts of type I and type IA gratings in CA 3513-3 under Strain

Nevertheless, the data proves a good match between the κ_ε values for type I and IA gratings, with deviations of typically less than 2%. Due to the higher peak wavelength of the type-IA gratings the strain sensitivity coefficient tends to be slightly higher than that for the type I gratings. A difference of 10 nm between the peak wavelengths of two gratings in the 1550 nm region corresponds to a relative value of 0.66%, which is in good approximation with the difference in κ_ε obtained.

Fibre Type	Sample	κ_ε(I) [$^{pm}/_{\varepsilon}$]	κ_ε(IA) [$^{pm}/_{\varepsilon}$]	Difference [%]
Verillion	1	10.0	10.2	+1.7
	2	9.9	10.0	+0.8
	3	10.1	10.2	+0.8
	4	10.1	10.2	+0.8
	5	No Data	No Data	N/A
CA 3513	1	11.5	11.7	+1.5
	2	10.9	10.8	-0.8
	3	11.1	11.3	+1.5
	4	11.3	11.3	0
CA 3555	1	(10.9)	11.0	(+0.8)
	2	(10.7)	11.2	(+4.7)
	3	No Data	11.1	N/A
	4	No Data	11.8	N/A
SMF 1300	9	8.8	9.0	(+1.9)
	10	9.5	(9.6)	(+0.9)
	11	8.8	(8.8)	(+1.0)
Stocker-Yale	1	9.3	(9.4	(+0.9)

Table 6.5-2: Strain sensitivity coefficients for Type I and IA gratings

6.6 Future Work and Conclusions

The properties of Type IA gratings written with high power pulsed UV light of 255 nm wavelength were investigated with respect to growth dynamics, annealing effects and strain and temperature sensitivity. The gratings were written in hydrogen loaded boron-germanium co-doped fibres and their results compared to those from fibre samples without boron content.

The grating evolution was monitored with respect to central wavelength and depth of the transmission band and the inscription was aborted with the fading effect of wavelength shift.

As for gratings written using 244 nm light from a CW Argon-Ion laser, the characteristic wavelength red-shift of 15-19 nm from the initial wavelength was observed.

During the writing of some of the gratings in boron-germanium fibre a one-fold or two-fold partial erasure and regeneration of the refractive index modulation was observed. This is another characteristic property of type IA gratings, which is believed to be due to two or more different photosensitivity effects taking place at the same time at different rates of refractive index change.

The results from the writing experiments failed to provide conclusive data about the influence of fluence and scanning speed on the writing process. The only trend observed was an increase of rate in grating wavelength change with higher beam power. To clarify this point, further experiments will be necessary with a larger number of samples written under more constraint experimental conditions. This applies in particular for the temperature and strain on the fibre, hydrogenation level and total exposure time. A two-step grating fabrication process with a preceding blank beam pre-exposure is to be favoured for the inscription of type IA gratings.

This may also help reduce the discrepancies found in the data of the annealing experiments. The α and A coefficients as defined in the power law for the description of the refractive index modulation amplitude are spread over a large range of values. Annealing at significantly higher temperatures may improve the results. It is also likely that a new annealing model has to be formulated for type IA gratings. The UV-induced refractive index increase during writing and the decrease during annealing need to be measured and decoupled into their ac and dc parts. The first can be obtained by measuring the integrated coupling constant κ; the latter by an interferometer method.

As a first approximation for the decay of dc refractive index the grating wavelength was plotted over the annealing time. At 80°C, all type I gratings were found to be completely annealed after 1000 minutes, with an average in total wavelength shift of around 1.4 nm in the case of SM 28 fibre and 1.6 nm for the boron-germanium fibres. All type IA gratings showed continuing wavelength shift at the time the annealing was aborted. In

CA 3555 fibre a wavelength shift was reached after 4000 minutes and in CA 3513 fibre a shift of 2.6 nm after the same duration and 3 nm after 6500 minutes. The values for the Verillion fibre spread greatly, possibly due to instantaneous refractive index decay in the very beginning of the annealing, providing incorrect figures for the starting wavelengths.

Displayed against a logarithmic x-scale, the wavelength data shows linear decrease in two and three stages. Only the sample in Stocker-Yale fibre shows no significant change in the central grating wavelengths.

The temperature coefficients in type IA gratings were found to be lower than those of type I gratings in the same fibre samples, the relative differences varying between 6% and 32%. The temperature coefficients of gratings in all other fibre types were found to be 10-15% above the values of the type I gratings in boron-germanium fibre and no significant differences were found between the standard and the overexposed gratings in these fibre types.

Except for one case, the strain sensitivity coefficients vary less than 2% within each sample, demonstrating the applicability of 255 nm written type IA gratings for temperature-strain sensor applications.

7 THESIS CONCLUSIONS

The pivotal basis of the presented work is UV-photosensitivity of silicate glasses for optical telecommunications and sensor applications. New methods have been elaborated to exploit these effects for the writing of grating structures into optical waveguides and, although far from complete, a representative selection of possible applications for these devices is given.

For the realisation of waveguide gratings different laser systems have been used as UV-sources, like continuous-wave argon-ion lasers, pulsed argon-fluoride excimer lasers and a copper-vapour UV laser with a high pulse repetition rate, all operating at different wavelengths. The latter is of particular interest, as it has been used for optical device inscription since recently only. Its feasibility for this kind of application has been shown by the successful writing of Bragg and long period gratings in a variety of different fibre types. Using the copper-vapour laser, the influence of fibre type on photosensitivity effects during the inscription of type IA gratings in boron-germanium fibres has been investigated. The results with respect to growth dynamics, grating stability and sensitivity to certain measurands are compared to those from previous experiments using argon-ion lasers and a good agreement is found between them.

The exact origins of the photosensitivity effect leading to IA grating formation could not be established and more work needs to be invested to do so. What has become evident is that the underlying mechanisms are more complex than for standard photosensitivity processes. One main reason for this is the high susceptibility of the growth dynamics to minor changes in the fabrication conditions. Therefore, for the reproducible writing of type IA gratings, factors such as strain and temperature during the fabrication, storage temperature and time between writing and annealing, etc. will require a high degree of control.

New Bragg grating inscription methods have been developed for both fibres and planar waveguides. For fibre grating writing a holographic Talbot-interferometer based technique is presented, enabling the fabrication of chirped gratings of lengths up to 1 cm at arbitrary wavelength. In addition, such gratings display self-apodisation, which has been supported by the demonstration of side-lobe suppression in their reflection spectra and small ripples in their time-delay functions. Using this set-up, chirped and uniform gratings were written over wavelengths between 860 nm and 1562 nm, which were also tested and used for various applications.

The Polarisation Control Method (PCM) for fabrication of complex Bragg gratings has successfully been transferred from fibre optic technology to planar technology during a 4-month project at the DTU in Lyngby/Denmark. The reduction of sidelobe-suppression in planar waveguide gratings shows the effective writing of Gaussan gratings. Still some inadequacies have to be tackled, mainly concerning the control of the alignment procedure. Nevertheless this method has great potential as a future technique for the writing of complex planar waveguide gratings, as the available methods to date are restricted in comparison to writing techniques in fibres.
In addition, uniform gratings have been written in integrated planar waveguide chips, showing the way for future solutions of integrated photonics circuits to be used in telecommunications and sensing. A combination of integrated chip design and advanced grating fabrication techniques in near future can offer feasible results.

For the monitoring of the performance and accuracy of Polarisation Control Method and the Multiple Print in Fibre method, gratings written with these set-ups were send to the TUHH in Hamburg/Germany for characterisation with Optical Frequency Domain Reflectometry, showing the strengths of these methods, as well how they can be still improved. For the former, the control of phase-shift strength is one crucial issue, which may be tackled by switching from Excimer to continuous-wave laser, whereas for the latter the stitching-overlap of subsequent UV-bursts may still be improved.

Fibre Bragg gratings for a number of different telecoms applications have been written and tested in collaboration with some research partners. A novel multiplexer / demultiplexer configuration based on apodised chirped fibre Bragg gratings is presented. Underlying is the idea to reduce the total number of gratings in a multiplexer and demultiplexer in order to reduce power loss. In addition, the chirped characteristics reduce pulse broadening due to residual dispersion in standard fibres. The apodisation function had to satisfy a trade-off between side-lobe suppression and definition of the spectral filter function. The performance of devices with apodised and non-apodised gratings has been tested in both configurations, as multiplexer and demultiplexer, showing channel separation of 20 dB or better when using apodised gratings.

Using the Polarisation Control Method a novel design for low-dispersion gratings has been employed and tested in gratings for channel filtering by measuring their detuning tolerance. In numerical simulations the proposed ADC design showed high potential as a band rejection filter of high detuning tolerance, which was partially confirmed by experimental data at 10 Gbit/s transmission rates. However, at 40 GBit/s these expectations were not matched. Subsequent characterisation of equivalent gratings written with the same method revealed that the actual grating structure may not reach the quality necessary for measurements under such demanding conditions.

Another essential application for fibre Bragg gratings in telecoms is the generation of picosecond pulses and modulation of semiconductor lasers. Two methods have been presented, both using fibre Bragg gratings written with the Talbot interferometer set-up, with wavelengths at 980 nm and 860 nm. In the first case single-, dual- and triple-pulse operation from a diode laser was obtained by non-resonant injection seeding under varying modulation frequencies using four gratings of different wavelengths within the gain spectrum. In the second case, significant reduction in the duration of a pulse from an over-ridden diode laser was achieved by purely spectral filtering of the relaxation oscillation modes using two Bragg gratings.

Sensing applications of optical fibre devices were shown using long period gratings. For the application of a vectorial curvature sensor long period gratins were written in rotationally asymmetric fibres, namely elliptic core fibre and standard fibre with a modified core section. The former showed no significant difference in response to bending within various azimuthal planes, but emerged as a dual temperature and bend sensor instead, showing reasonable discrimination between both measurands. Using the modified cladding fibre, the difference between convex and concave bending in one plane could clearly be measured. In the near future, the combination of both techniques has the potential to turn into a real vectorial sensor measuring curvature and azimuthal angle of the bend at the same time.

Using an in-fibre Mach-Zehnder interferometer with an Erbium/Ytterbium section in its cavity has proven to be applicable as an active device for both switching and sensing. Optical pumping of the active zone changes the refractive index configuration of the core-cladding waveguide, manifesting as a wavelength shift of the fringe spectrum. Depending on the refractive index and heat conductance of the surrounding medium the direction of wavelength shift due to the non-linear optical pump effect can be changed.

Further experiments were carried out using tapered fibre long period gratings with respect to their temperature, refractive index and bending sensitivities. Due to the continuous change in the phase-matching conditions a high number of distinguishable narrow- and overlapped broad attenuation bands are found. In some devices, an intrinsic Mach-Zehnder effect was observed. Changes of measurands repeatedly show bifurcation effects of overlapping and neighbouring attenuation bands, giving rise to a high utilisable spectral sensitivity. This effect proves to be of particular importance for refractive index measurement of saline and/or organic solutions with a refractive index of around 1.3, around which the devices show extremely high sensitivity.

And finally, the temperature and strain sensitivity of type IA fibre Bragg gratings written with the Copper-vapour laser were obtained and found in good agreement with former results based on experiments with Argon-ion lasers. Depending on the fibre type used, significant

differences in the temperature coefficients, but identical strain sensitivities were measured for type I and type IA gratings. In combination, these two grating types can be used as a feasible dual-sensor for simultaneous strain and temperature measurements.

8 Publications

8.1 Patents

1. X. Shu, Y. Liu, D. Zhao, L. Zhang, I. Bennion, B.A.L. Gwandu, F. Floreani. "Dual-parameter optical waveguide grating sensing device and sensor". European Patent EP1324082, published 02.07.2003

8.2 Journal Publications

1. X. Shu, Y. Liu, D. Zhao, B. Gwandu, F. Floreani, L. Zhang, I. Bennion. "*Dependence of temperature and strain coefficients on fiber grating type and its application to simultaneous temperature and strain measurement*". Optics Letters **9** (27). 701-703 (2002).
2. X. Shu, K. Sugden, D. Zhao, F. Floreani, L. Zhang, I. Bennion. "*Complex Growth Behaviour of hybrid-type Fibre Bragg Gratings*". Electronics Letters **39** (3). 274-276 (2003).
3. F. Floreani, A. Gillooly, L. Zhang, I. Bennion, X. Shu, K. Sugden. "*A simple method for the fabrication of intrinsically apodised Chirped Fibre Bragg Gratings*". IOP Journal of Optics A **5**. 59-62 (2003).
4. H.-J. Deyerl, C. Peucheret, B. Zsigri, Student Member, F. Floreani, N. Plougmann, S. J. Hewlett, M. Kristensen, and P. Jeppesen. *"A compact low dispersion fiber Bragg grating with high detuning tolerance for advanced modulation formats"*. Opt. Comm. (2004). – *in press* -
5. H.-J. Deyerl, N. Plougmann, J.B. Jensen, F. Floreani, H. R. Sørensen and M. Kristensen. *"Fabrication of advanced Bragg gratings with complex apodization profiles using the polarization control method"*. Appl. Opt. **43** (17). 3513-3522 (2004).
6. R. Romero, O. Frazão, F. Floreani, L. Zhang, P.V.S. Marques, H.M. Salgado. *"Chirped Fibre Bragg Grating Based Multiplexer and Demultiplexer for DWDM Applications"*. SPIE Journ. Optics and Lasers in Engineering (2004) – *in press* -
7. E.U. Rafailov, I.G. Cormack, F. Floreani, L. Zhang, I. Bennion, W. Sibbett. *"Tunable and multiple-wavelengths/temporal output from gain-switched diode laser and a four Bragg-grating fibre"*. Appl. Phys. Lett. **85** (6). 861-862 (2004).
8. T. Allsop, F. Floreani, K.P. Jedrzejewski, R. Romero, D.J. Webb, I. Bennion. *"A discriminatory sensor for temperature and curvature based upon a Long period Grating written in an Optical fibre Taper"*. Submitted to Electron. Lett. (2005)
9. T. Allsop, M. Dubov, A. Martinez, F. Floreani, I. Khrushchev, D.J. Webb, I. Bennion. *"Long period grating directional bend sensor based on asymmetric index modification of cladding"*. Electron Lett. 41 (2). 59-60 (2005).
10. T. Allsop, F. Floreani, K. Jedrzejewski, P. Marques, R. Romero, D. Webb, I. Bennion. *"Refractive index sensing with a Long Period Grating fabricated in a biconical tapered fibre"*. Accepted for publication in Electron. Lett. (2005).

8.3 Conference Publications

1. X. Shu, D. Zhao, Y. Liu, B. Gwandu, F, Floreani, L. Zhang, I. Bennion. *"Effectively Simultaneous Temperature and Strain Measurement Utilising a Dual-grating Sensor Formed by Type IA and Type IIA FBGs"*. IEEE Sensors 2002 Coference Techical Digest. 1740-1745 (2002).
2. X. Shu, Y. Liu, D. Zhao, B. Gwandu, F. Floreani, L. Zhang, I. Bennion. *"Fiber Grating Type Dependence of Temperature and Strain Coefficients and Application to simultaneous Temperature and Strain Measurement"*. IEEE 15th Optical Fiber Sensors Conference Technical Digest. OFS 2002. Vol.1. 83-86 (2002).
3. F. Floreani, A. Gillooly, L. Zhang, I. Bennion, X. Shu, K. Sugden. *"Fabrication of Chirped Gratings of arbitrary Wavelength and intrinsic Apodisation Profile using scanning holographic Set-up"*. Proceedings for POWAG 2002. 31-33 (2002).
4. F. Floreani, A. Gillooly, D. Zhao, L. Zhang, I. Bennion, X. Shu, K. Sugden. "*Effects of intrinsic Apodisation in Chirped Fibre Bragg Gratings fabricated using Scanning Holographic Set-up*". Photon 2002 Abstract Book and Programme. 7-8 (2002).
5. F. Floreani, A. Gillooly, D. Zhao, L. Zhang, I. Bennion, X. Shu, K. Sugden. "*Investigation of intrinsically apodised Chirped Fibre Bragg Gratings fabricated using scanning holographic Set-up*". IEEE Proceedings for WFOPC 2002. 80-85 (2002).
6. I.G. Cormack, E.U. Rafailov, W. Sibbett, F. Floreani, L. Zhang, I. Bennion. "*Tunable and multiple-Wavelengths/temporal Output from Gain-switched Diode Laser and a four Bragg-Grating Fibre*". CLEO Europe 2003. Munich (Germany).
7. R. Romero, O. Frazao, F. Floreani, L. Zhang, P.S.B. Andre, P.V.S. Marques, H.M. Salgado, J.L. Santos. "*Chirped Fiber Bragg Gratings for Optical Communications and Sensor Applications*". Conftele 2003 Aveiro/Portugal.
8. R. Romero, O. Frazao, R. A. Ibbotson, A. Gray, F. Floreani, L. Zhang, P. V. S. Marques, H. M. Salgado. *"Chirped Fiber Bragg Gratings for Optical Dispersion Compensation at10Gbit/s"*. I. Symposium on Enabling Optical Networks 2003 Aveiro/Portugal.
9. F. Floreani, Hans-Jürgen Deyerl, Nikolai Plougmann, Haiyan Ou, Jesper Bo Jensen, Martin Kristensen. *"A flexible Approach for the Apodization of planar Waveguide Bragg Gratings"*. BGPP 2003 Monterey/USA.
10. R. Romero, O. Frazao, F. Floreani, L. Zhang, P.V.S. Marques, H.M. Salgado. "*Multiplexer and Demultiplexer based on Fibre Bragg Gratings and Optical Circulators for DWDM Systems*". HSNMC 2003 Estoril/Portugal.
11. T. Allsop, F. Floreani, K.P. Jedrzejewski, R. Romero, P.V.S. Marques, D.J. Webb, I. Bennion. "*Tapered Fibre LPG Device as a Sensing Element for Refractive Index*". Accepted for OFS 2005. Bruges / Belgium.
12. T. Allsop, F. Floreani, D.J. Webb, I. Bennion, "*The Bending and Temperature Characteristics of Long Period Gratings written in Elliptical Core Step-Index Fibre*". Accepted for OFS 2005. Bruges / Belgium.
13. T. Allsop, M. Dubov, A. Martinez, F. Floreani, D.J. Webb, I. Bennion. "*A Long Period Grating directional Bend Sensor incorporating Index Modification of the Cladding*". Accepted for OFS 2005. Bruges / Belgium.
14. T.D.P. Allsop, F. Floreani, D.J. Webb, I. Bennion, K.P. Jedrzejewski, R. Romero, P.V.S. Marques. "*Investigation of Mach-Zehnder Effects in Tapered Fibre Long Period Gratings*". Accepted for CLEO Europe 2005. Munich / Germany.
15. T.D. Allsop, M. Dubov, A. Martinez, F. Floreani, I. Khrushchev, D.J. Webb, I. Bennion. *"Directional Bend Sensor Based on an Asymmetric Modification of the Fiber Cladding by Femtosecond Laser". Accepted for CLEO-2005, Baltimore, USA, May 22 - May 27, 2005.*

9 REFERENCES

[1] K.O. Hill, F. Fujii, D.C. Johnson, B. S. Kawasaki, *"Photosensitivity on optical fiber waveguides: application to reflection filter fabrication"*, Appl. Phys. Lett. **32** (10), 647-649 (1978).

[2] A. Suzuki, X. Wang, Y. Ogawa, S. Nakamura, "10x320Gb/s (3.2Tb/s) DWDM/OTDM transmission in C-band by semiconductor-based devices", Proc. ECOC 2004, Paper Th4.1.7 (Postdeadline) (2004).

[3] M.A. Powers, S.T. Koev, A. Schleunitz, H. Yi, V. Hodzic, W.E. Bentley, G.F. Payne, G.W. Rubloff, R. Ghoddzi, "*A fabrication platform for electrically mediated optically active bifunctionalized sites in BioMEMS*", Lab Chip **5**, 583-586 (2005).

[4] A. Unamuno, L. Li, D. Uttamchandani, "*Fiber Bragg Grating Demodulator Based on Hybrid Optical MEMS*", IEEE Journ. Sel. Top. Quant. Electron. 10 (3), 598-603 (2004).

[5] R.D. Smith, P. Liu, S.H. Lee, E. Tracy, R. Pitts, "Interfacial Stability of Thin Film Fiber-Optic Hydrogen Sensors", Proc. 2002 U.S. DOE Program Rev. (2002).

[6] Gerd Keiser, *"Mode Theory for Circular Waveguides"* in Optical Fiber Communications, Chapter 2.4, 33-51, Mc Graw Hill, 1983, Second Edition (1991).

[7] John A. Buck, "Weakly-Guiding Fibers with Step Index Profiles" in Fundamentals of Optical Fibers, Chapter 3, 51-91, Wiley, New Jersey (2004).

[8] A. Yariv, "*Coupled-Mode Theory for Guided-Wave Optics*", IEEE Journ. Quant. Electron. **9** (9), 919-934 (1973).

[9] T. Erdogan, *"Cladding-Mode resonances in short- and long-period fiber grating filters"*, Journ. Opt. Soc. Am. **A 14** (8), 1760-1773 (1997).

[10] C. Tsao, Optical Fibre Waveguide Analysis (Oxford, New York,1992).

[11] H.S. Cross, H. Kogelnik, *"Sidelobe suppression in corrugated-waveguide filters"*, Opt. Lett. **1** (1), 43-45 (1977).

[12] K.O. Hill "*Aperiodic Distributed-Parameter Waveguides for Integrated Optics"*, Appl. Opt. **13** (8), 1853-1856 (1974).

[13] M. Yamada, K. Sakuda, *"Analysis of almost-periodic distributed feedback slab waveguides via a fundamental matrix approach"*, Appl. Opt. **26** (16), 3474-3478 (1987).

[14] H. Kogelnik, *"Filter Response of Nonuniform Almost-Periodic Structures"*, Bell Syst. Techn. Journ. **55** (1), 109-126 (1976).

[15] S. Radic, N. George, G.P. Agrawal, *"Analysis of Nonuniform Nonlinear Distributed Feedback Structures: Generalized Transfer Matrix Method"*, IEEE Journ. Quant. Electron. **31** (7), 1326-1336 (1995).

[16] J. Hong, W. Huang, T. Makino, *"On the Transfer Matrix Method for Distributed-Feedback Waveguide Devices"*, Journ. Lightwave Technol. **10** (12), 1860-1868 (1992).

[17] M.J. Yuen, *"Ultraviolet absorption studies of germanium silicate glasses"*, Applied Optics **21** (1), 136-140 (1982).

[18] V.M. Marchenko, *"Photoinduced transformations of oxygen-deficient centers in silica and germanosilicate glasses"*, Glass Phys. Chem. **21** (4), 263-271 (1995).

[19] D.P. Hand, P.S.J. Russell. "*Photoinduced refractive-index changes in germanosilicate fibers*". Opt. Lett. **15** (2), 102-104 (1990).

[20] R.M. Atkins, V. Mizrahi. *"Observations of Changes in UV Absorption Bands of Singlemode Germanosilicate Core Optical Fibres on Writing and thermally Erasing Refractive Index Gratings"*. Electron. Lett. **28** (18), 1743-1744 (1992).

[21] V. Mizrahi, S. LaRochelle, G.I. Stegeman, J.E. Sipe. *"Physics of photosensitive-grating formation in optical fibers"*. Phys. Rev. **A 43** (1), 433-438 (1991).

[22] K.S. Chiang, M.G. Sceats, D. Wong, "*Ultraviolet photolytic-induced changes in optical fibers: the thermal expansion coefficient*", Opt. Lett. **18** (12), 965-967 (1993).

[23] M.G. Sceats, P.A. Krug, *"Photoviscous annealing: dynamics and stability of photorefractivity in optical fibers"*, Proc. SPIE Vol. **2044**, 113-120 (1993).

[24] D. Wong, S.B. Poole, M.G. Sceats, "Stress-birefringence reduction in elliptical-core fibers under ultraviolet irradtiation", Opt. Lett. **17** (24), 1773-1775 (1992).

[25] M.G. Sceats, G.R. Atkins, S.B. Poole, *"Photolytic Index Changes in Optical Fibers"*, Annu. Rev. Mater. Sci. **23**, 381-410 (1993).

[26] P.Y. Fonjallaz, H.G. Limberger, R.P. Salathé, F. Cochet, B. Leuenberger, *"Tension increase correlated to refractive index change in fibers containing UV-written Bragg gratings"*, Opt. Lett. **20** (11), 1346-1348 (1995).

[27] H.G. Limberger, P.Y. Fonjallaz, R.P. Salathé, F. Cochet, *"Compaction- and photoelastic-induced index changes in fiber Bragg gratings"*, Appl. Phys. Lett. **68** (22), 3069-3071 (1996).

[28] P.J. Lemaire, R.M. Atkins, V. Mizrahi, W.A. Reed, *"High Pressure H_2 Loading as a Technique for Achieving ultrahigh Photosensitivity and thermal Sensitivity in GeO_2 doped optical Fibers"*, Electron. Lett. **29** (13), 1191-1193 (1993).

[29] A. Iino, M. Kuwabara, K. Kokura, *"Mechanisms of Hydrogen-Induced Losses in Silica-Based Optical Fibers"*, Journ. Lightw. Technol. **8** (11), 1675-1679 (1990).

[30] G.R.Atkins, P.J. Lemaire, *"Effects of elevated temperature hydrogen exposure on short-wavelength optical losses and defect concentrations in germanosilicate optical fibers"*, Journ. Appl. Phys. **72** (2), 344-348 (1992).

[31] R.M.Atkins, P.J.Lemaire, T.Erdogan, V.Mizrahi, *"Mechanisms of enhanced UV Photosensitivity via Hydrogen Loading in Germanosilicate Glasses"*, Electron. Lett. **29** (14), 1234-1245 (1993).

[32] H. Patrick, S.L. Gilbert, A. Lidgard, M.D. Gallagher, *"Annealing of Bragg gratings in hydrogen-loaded optical fiber"*, Journ. Appl. Phys. **78** (5), 2940-2945 (1995).

[33] J. Rathje, M. Kristensen, J.E. Pedersen, *"Continuous anneal method for characterizing the thermal stability of ultraviolet Bragg gratings"*, Journ. Appl. Phys. **88** (2), 1050-1055 (2000).

[34] W.X. Xie, P. Niay, P. Bernage, M. Douay, J.F. Bayon, T. Georges, M. Monerie, B. Poumellec. *"Experimental evidence of two types of photorefractive effects occurring during photoinscriptions of Bragg gratings within germanosilicate fibres"*. Opt. Comm. **104**, 185-195 (1993).

[35] P. Niay, P. Bernage, S. Legoubin, M. Douay, W.X. Xie, J.F. Bayon, T. Georges, M. Monerie, B. Poumellec, *"Behaviour of spectral transmissions of Bragg gratings written in germania-doped fibres: writing and erasing experiments using pulsed or cw uv exposure"*, Opt. Commun. **113**, 176-192 (1994).

[36] L. Dong, W.F. Liu, L. Reekie. *"Negative-index gratings formed by a 193-nm excimer laser"*. Opt. Lett. **21** (24), 2032-2034 (1996).

[37] I. Riant, S. Borne, P. Sansonetti. *"Dependence of fiber Bragg grating thermal stability on grating fabrication process"*. OSA Technical Digest Series, Optical Fiber Communications Conference Vol. **9**, 86-87 (1996).

[38] M.Kristensen, *"Ultraviolet-light-induced processes in germanium-doped silica"*, Phys. Rev. **B 64**, 4201-4208 (2001).

[39] Martin Kristensen, *"Refractive Index Engineering in Silica Glass"*, Doctoral Dissertation, Technical University of Denmark (DTU), COM Center - Glass Components & Materials, ISBN 87-90974-41-7 (2003).

[40] J.L. Archambault, L. Reekie, P.S.J. Russell, *"High reflectivity and narrow bandwidth fibre gratings written by single excimer pulse"*, Electron. Lett. **29** (1), 28-29 (1993).

[41] B. Malo, D.C. Johnson, F. Bilodeau, J. Albert, K.O. Hill, *"Single-excimer-pulse writing of fiber gratings by use of a zero-order nulled phase mask: grating spectral response and visualisation of index perturbations"*, Opt. Lett. **18** (15), 1277-1279 (1993).

[42] J.L. Archambault, L. Reekie, P.S.J. Russell, *"100% Reflectivity Bragg Reflectors produced in Optical Fibres by single Excimer Pulses"*, Electron. Lett. **29** (5), 453-455 (1993).

[43] A. Martinez, M. Dubov, I. Khrushchev, I. Bennion, *"Direct writing of fibre Bragg gratings by femtosecond laser"*, Electron. Lett. 40 (19), 1170-1172 (2004).

[44] Y. Kondo, K. Nouchi, T. Mitsuyu, M. Watanabe, P.G. Kazansky, K. Hirao, *"Fabrication of long-period fiber gratings by focused irradiation of infrared femtosecond laser pulses"*, Opt. Lett. **24** (10), 646-648 (1999).

[45] A. Dragomir, D.N. Nikogosyan, K.A. Zagorulko, P.G. Kryukov, E.M. Dianov, *"Inscription of fiber Bragg gratings by ultraviolet femtosecond radiation"*, Opt. Lett. **28** (22), 2171-2173 (2003).

[46] S.J. Mihailov, W. Smelser, D. Grobnic, R.B. Walker, P. Lu, H. Ding, J. Unruh, *"Bragg Gratings Written in All-SiO2 and Ge-Doped Core Fibers With 800 nm Femtosecond Radiation and a Phase Mask"*, Journ. Lightw. Technol. **22** (1), 94-100 (2004).

[47] G. Rego, O. Okhotnikov, E. Dianov, V. Sulimov, *"High temperature stability of long-period fiber gratings produced using an electric arc"*, Journ. Lightw. Technol. **19** (10), 1574-1579 (2001).

[48] G. Meltz, W.W. Morey, W.H. Glenn, *"Formation of Bragg gratings in optical fibers by a transverse holographic method"*, Opt. Lett. **14** (15), 823-825 (1989).

[49] D.Z. Anderson, V. Mizrahi, T. Erdogan, A.E. White, *"Production of In-Fibre Gratings using a diffractive optical Element"*, Electron. Lett. **29** (6), 566-568 (1993).

[50] J. Albert, S. Thériault, F. Bilodeau, D.C. Johnson, K.O. Hill, P. Sixt, M.J. Rooks, *"Minimization of phase errors in long fibre Bragg grating phase masks made using electron beam lithography"*, IEEE Photon. Technol. Lett. **8** (10), 1334-1336 (1996).

[51] H. Patrick, S.L.Gilbert, "*Growth of Bragg gratings produced by continuous-wave ultraviolet light in optical fiber*", Opt. Lett. **18** (18), 1484-1486 (1993).

[52] Q. Zhang, D.A. Brown, L. Reinhart, T.F. Morse, *"Simple prism-based scheme for fabricating Bragg gratings in optical fibers"*, Opt. Lett. **19** (23), 2030-2032 (1994).

[53] B.J. Eggleton, P.A. Krug, L. Poladian, K.A. Ahmed, H.F. Liu, *"Experimental demonstration of compression of dispersed optical pulses by reflection from self-chirped optical fiber Bragg gratings"*, Opt. Lett. **19** (12), 877-879 (1994).

[54] R. Kashyap, J.R. Armitage, R. Wyatt, S.T. Davey, D.L. Williams, *"All-Fibre narrowband Reflection Gratings at 1500 nm"*, Electron. Lett. **26** (11), 730-731 (1990).

[55] B. Malo, K.O. Hill, F. Bilodeau, D.C. Johnson, J. Albert, *"Point-by-Point Fabrication of Micro-Bragg Gratings in photosensitive Fibre using single Excimer Pulse refractive Index Modification Techniques"*, Electron. Lett. **29** (18), 1668-1669 (1993).

[56] L. Poladian, "*Understanding profile-induced group-delay ripple in Bragg gratings*", Appl. Opt. **39** (12), 1920-1923 (2000).

[57] J. Albert, K.O. Hill, B. Malo, Thériault, F. Bilodeau, D.C. Johnson, L.E. Erickson, *"Apodisation of the spectral response of fibre Bragg gratings using a phase mask with variable diffraction efficiency"*, Electron. Lett. **31** (3), 222-223 (1995).

[58] B. Malo, S. Thériault, D. C. Johnson, F. Bilodeau, J. Albert, K. O. Hill, *"Apodised in-fibre Bragg grating reflectors photoimprinted using a phasemask"*, Electron. Lett. **31** (3), 223-225 (1995).

[59] W.H. Loh, M.J. Cole, M.N. Zervas, S. Barcelos, R.I. Laming, *"Complex grating structures with uniform phase masks based on the moving fiber-scanning beam technique"*, Opt. Lett. **20** (20), 2051-2053 (1995).

[60] W.H.Loh, M.J.Cole, M.N.Zervas, R.I.Laming, *"Compensation of imperfect phase mask with moving fibre-scanning beam technique for production of fibre gratings"*, Electron. Lett. **31** (17), 1483-1485 (1995).

[61] A. Asseh, H.Storoy, B.E. Sahlgren, S. Sandgren,R.A.H. Stubbe, *"A writing technique for long fiber Bragg gratings with complex reflectivity profiles"*, Journ. Lightw. Technol. **15** (8), 1419-1423 (1997).

[62] M.J. Cole, W.H. Loh, R.I. Laming, M.N. Zervas, S. Barcelos, *"Moving fibre/phase mask-scanning beam technique for enhanced flexibility in producing fibre gratings with uniform phase mask"*, Electron. Lett. **31** (17), 1488-1490 (1995).

[63] L. Poladian, B. Ashton, W. Padden, *"Interactive Design and Fabrication of Complex FBGs"*, Proceedings OFC 2003, Vol. **1**, 378-379 (2003).

[64] Yu Liu, *"Advanced Fibre Gratings and their Applications"*, Ph.D. Thesis, Aston University, Birmingham, United Kingdom (2001)

[65] Private correspondence with Paulo Marques from INESC Porto.

[66] T. Allsop, D.J. Webb, I. Bennion, *"A comparison of the sensing characteristics of long period gratings written in three different types of fiber"*, Opt. Fibre Technol. **9**, 210-223 (2003).

[67] L. Zhang, Y. Liu, L. Everall, J.A.R. Williams, I. Bennion, "*Design and Realization of Long-Period Grating Devices in Conventional and High Birefringence Fibers and Their Novel Applications as Fiber-Optic Load Sensors*", IEEE Journ. Sel. Top. Quant. Electron. **5** (5), 1373-1378 (1999).

[68] Y. Zhu, P. Shum, C. Lu, B.M. Lacquet, P.L. Swart, S.J. Spammer, "*EDFA gain flattening using phase-shifted long-period grating*", Microw. Opt. Technol. Lett. **37** (2), 153-157 (2003).

[69] S. James, R.P. Tatam, *"Optical fibre long-period grating sensors: characteristics and application"*, Meas. Sci. Technol. **14**, R49-R61

[70] K.P. Chen, P.R. Hermann, R. Taylor, C. Hnatovsky, *„Vacuum-Ultraviolet Laser-Induced Refractive-Index Change and Birefringence in Standard Optical Fibers"*, Journ. Lightw. Technol. **21** (9), 1969-1977 (2003).

[71] W.H. Loh, R.I. Laming, N. Robinson, A. Cavaciuti, F. Vaninetti, C.J. Anderson, M. Zervas, M.J. Cole, *"Dispersion Compensation Over Distances in Excess of 500 km for 10-Gbit/s Systems Using Chirped Fiber Gratings"*, IEEE Photon. Technol. Lett. **8** (7) 944-946, (1996).

[72] J.A.R. Williams, I. Bennion, K. Sugden, N.J. Doran, *"Fibre dispersion compensation using a chirped in-fibre Bragg grating"*, Electron. Lett. **30** (12), 985-987 (1994).

[73] M. Ibsen, M.K. Durkin, I. Laming, *"Chirped Moiré Fiber Gratings Operating on Two-Wavelength Channels for Use as Dual-Channel Dispersion Compensators"*, IEEE Photon. Technol. Lett. **10** (1), 84-86 (1998).

[74] M. Ibsen, M.K. Durkin, M.N. Zervas, A.B. Grudinin, R.I. Laming, *"Custom Design of Long Chirped Bragg Gratings: Application to Gain-Flattening Filter with incorporated Dispersion Compensation"*, IEEE Photon. Technol. Lett. **12** (5), 498-500 (2000).

[75] R.W. Fallon, L. Zhang, A. Gloag, I. Bennion, *"Multiplexed Identical Broad-Band-Chirped Grating Interrogation System for Large-Strain Sensing Applications"*, IEEE Photon. Technol. Lett. **9** (12), 1616-1618 (1997).

[76] K. Ennser, M.N. Zervas, R.I. Laming, *"Optimization of Apodized Linearly Chirped Fiber Gratings for Optical Communicatios"*, IEEE Journ. Quant. Electron. **34** (5), 770-778 (1998).

[77] M.C. Farries, K. Sugden, D.C.J. Reid, I. Bennion, A. Molony, M.J. Goodwin, *"Very broad reflection bandwidth (44nm) chirped fibre gratings and narrow bandpass filters produced by the use of an amplitude mask"*, Electron. Lett. **30** (11), 891-892 (1994).

[78] Y. Wang, J. Grant, A. Sharma, G. Myers, *"Modified Talbot Interferometer for Fabrication of Fiber-Optic Grating Filter Over a Wide Range of Bragg Wavelength and Bandwidth Using a Single Phase Mask"*, Journ. Lightw. Technol. **19** (10), 1569-1573 (2001).

[79] P.Y. Cortès, H. Fathallah, S. LaRochelle, L.A. Rusch, P. Loiselle, *"Writing of Bragg Gratings with Wavelength Flexibility using a Sagnac Type Interferometer and Application to FH-CDMA"*, Proceedings ECOC'98, Vol. **1**, 411-412 (1998).

[80] P.-Y. Cortès, F. Oullette, S. LaRochelle, *"Intrinsic apodisation of Bragg gratings written using UV-pulse interferometry"*, Electron. Lett. **34** (4), 396-397 (1998).

[81] J.M. Jouanno, D. Zauner, M. Kristensen, *"Low Crosstalk planar add-drop multiplexer fabricated with UV-induced Bragg gratings"*, Electron. Lett. **33** (25), 2120-2121 (1997).

[82] J. Hübner, D. Zauner, M. Kristensen, *"Strong Sampled Bragg Gratings for WDM Applications"*, IEEE Photon. Techn. Lett. **10** (4), 552-554 (1998).

[83] S. Guldberg-Kjær, J. Hübner, M. Kristensen, C. Laurent-Lund, M. Rysholt Poulsen, M.W. Sackerl, *"Planar waveguide laser in Er/Al-doped germanosilicate"*, Electron. Lett. **35** (4), 1-2 (1999).

[84] C. Riziotis, M. N. Zervas, *"Performance comparison of Bragg grating-based optical add-drop multiplexers in WDM transmission systems"*, IEE Proc. Circuits Dev. Syst. **149** (3), 179-186 (2002).

[85] R. Kashyap, A. Swanton, D.J. Armes, *"Simple technique for apodising chirped an unchirped fibre Bragg gratings"*, Electron. Lett. **32** (13), 1226-1228 (1996).

[86] J.B. Jensen, N. Plougmann, H-J. Deyerl, P. Varming, J. Hübner, M. Kristensen, *"Polarization control method for ultraviolet writing of advanced Bragg gratings"*, Opt. Lett. **27** (12), 1004-1006 (2002).

[87] H.J. Deyerl, N. Plougmann, J.B. Jensen, F. Floreani, H.R. Sørensen, M. Kristensen, *"Fabrication of advanced Bragg gratings with complex apodization profiles using the polarization control method"*, Appl. Opt. 43 (17), 3513-3522 (2004).

[88] Jesper Bo Jensen, "UV *Writing of Advanced Bragg Gratings in Optical Waveguides*", Ph.D. Thesis, COM Research Cente, DTU Lyngby, Denmark (2002).

[89] M. Svalgaard, *"Direct writing of planar waveguide power splitters and directional couplers using a focused ultraviolet laser beam"*, Electron. Lett. **33** (20), 1694-1695 (1997).

[90] L. *Geppert, "A quantum leap for photonics"*, IEEE Spectrum 41 (7), 16-17 (2004).

[91] K.B. Mogensen, H. Klank, J.P. Kutter, *"Recent developments in detection for microfluidic systems"*, Electrophoresis **25**, 3498-3512 (2004).

[92] D. Zauner, K. Kulstad, J. Rathje, M. Svalgaard, *"Directly UV-written silica-on-silicon planar waveguides with low insertion loss"*, Electron. Lett. **34** (16), 1582-1584 (1998).

[93] S. Kieckbusch, C. Knothe, E. Brinkmeyer, *"Fast and Accurate Characterization of Fiber Bragg Gratings with High Spatial and Spectral Resolution"*, Proc. OFC 2003, Vol. **1**, 379-381 (2003).

[94] P. Giaccari, H.G. Limberger, R.P. Salathé, *"Local coupling-coefficient characterization in fiber Bragg gratings"*, Opt. Lett. **28** (8), 598-600 (2003).

[95] M. Ibsen, R. Feced, J.A.J. Fells, W. S. Lee, *"40 Gbit/s high performance filtering for DWDM networks employing dispersion-free fibre Bragg gratings "*, Proc. ECOC 2001, 594-595 (2001).

[96] J.A.J. Fells, P.J. Bennett, R. Feced, P. Ayliffe, J. Wakefield, H.F.M. Priddle, V. Baker, S.E. Kanellopoulos, C. Boylan, S. Sahil, W.S. Lee, S.J. Clements, A. Hadjifotiou, *"Widely tunable twin fiber grating dispersion compensator for 80 Gbit/s"*, Proc. CLEO/QELS 2001.

[97] A. Grunnet-Jepsen, A.E. Johnson, E.S. Maniloff, T.W. Mossberg, M.J. Munroe, J.N. Sweetser, *"Demonstration of All-Fiber Sparse Lightwave CDMA Based on Temporal Phase Encoding"*, IEEE Photon. Technol. Lett. **11** (10),1283-1285 (1999).

[98] P. Petropoulos, M. Ibsen, A.D. Ellis, D.J. Richardson, *"Rectangular Pulse Generation Based on Pulse Reshaping Using a Superstructured Fiber Bragg Grating"*, IEEE Journ. Lightw. Technol., 19 (5), 746-752 (2001).

[99] M.C. Cardakli, A.E. Willner, *"Synchronization of a Network Element for Optical Packet Switching Using Optical Correlators and Wavelength Shifting"*, IEEE Photon. Technol. Lett. **14** (9), 1375-1377 (2002).

[100] *C. Knothe, E. Brinkmeyer, "Reset-free phase shifter in a Sagnac-type interferometer for control of chirp and apodization of Bragg gratings"*, Proc. BGPP 2003, Paper TuB3 (2003).

[101] H.J. Deyerl, C. Peucheret, B. Zsigri, F. Floreani, N. Plougmann, S. J. Hewlett, M. Kristensen, and P. Jeppesen, "*A compact low dispersion fiber Bragg grating with high detuning tolerance for advanced modulation formats*", Opt. Comm. –in press-

[102] A joint comparison study between OFDR and OLCR has been conducted by research groups from DTU (Denmark), TUHH (Germany), EFFL (Switzerland) and Aston University (United Kingdom) under the aegis of the ODUPE Network by the European Comission. Results suggest a good agreement between both methods, but have not been published to date.

[103] P.A. Krug, R. Stolte, R. Ulrich, *"Measurement of index modulation along an optical fiber Bragg grating"*, Opt. Lett. **20** (17), 1767-1769 (1995).

[104] E. Brinkmeyer, *"Simple Algorithm for reconstructing fiber gratings from reflectometric data"*, Opt. Lett. **20** (8), 810-812 (1995).

[105] R. Feced, M.N. Zervas, M.A. Muriel, *"An Efficient Inverse Scattering Algorithm for the Design of Nonuniform Fiber Bragg Gratings"*, IEEE Journ. Quant. Electron. **35** (8), 1105-1115 (1999).

[106] P. Beaud, J. Schütz, W. Hodel, H.P. Weber, H.H. Gilgen, R.P. Salathé, *"Optical reflectometry with micrometer resolution for the investigation of integrated optical devices"*, *IEEE J. Quant. Electron.* **25** (4), 755-759 (1989).

[107] U. Glombitza, E. Brinkmeyer, *"Coherent Frequency-Domain Reflectometry for Characterization of Single-Mode Integrated-Optical Waveguides"*, IEEE Journ. Lightw. Technol. **11** (8), 1377-1384 (1993).

[108] IFO_Grating, Version 3.0 by Optiwave Corporation. Available: http://www.optiwave.com

[109] Andrew Gillooly, *"Advanced Fibre Bragg Grating Fabrication Systems and Devices"*, Ph.D. Thesis, Aston University, Birmingham, United Kingdom (2005).

[110] Private Correspondence with John Mitchell. Details about this work are due to be published within a following Ph.D. Thesis at Aston University.

[111] N.A. Olsson, C.H. Henry, R.F. Kazarinov, H.J. Lee, K.J. Orlowski, *"Performance characteristics of a1.5μm single frequency semiconductor laser with an external waveguide Bragg reflector"*, IEEE Journ. Quant. Electron. **43** (2), 143-147 (1988).

[112] R. Romero, O. Frazão, F. Floreani, L. Zhang, P.V.S. Marques, H. M. Salgado, "*Chirped Fibre Bragg Grating based Multiplexer and Demultiplexer for WDM Applications*". IASTED International Conference on Communication Systems and Networks. Marbella / Spain, September 2004.

[113] G. Nykolak, B.J. Eggleton, G. Lenz,T.A. Strasser, *"Dispersion Penalty Measurements of Narrow Fiber Bragg Gratings at 10 Gb/s"*, Phot. Technol. Lett. **10** (9), 1319-1321(1998).

[114] B.G. Kim, E. Garmire, *"Comparison between the matrix method and the coupled-wave method in the analysis of Bragg reflector structures"*, Journ. Opt. Soc. Am **9** (1), 132-136 (1992).

[115] L. Poladian, *"Simple grating synthesis algorithm"*, Opt. Lett. **25** (11), 787-789 (2000).

[116] A. Hodzic, B. Konrad, K. Petermann, *"Alternative Modulation Formats in N x 40 Gb/s WDM Standard Fiber RZ-Transmission Systems"*, Journ. Lightw. Techol. **20** (4), 598-607 (2002).

[117] F. An, M. Marhic, L. Kazovsky, Y. Akasaka, D. Harris, R. Huang, *"Comparison of linear fiber impairments tolerance among 40 Gb/s modulation formats"*, Proc. OFC 2003, Vol. **2**, 657-658 (2003).

[118] G. Bosco, A. Carena, V. Curri, R.Gaudino, P. Poggiolini, *"On the use of NRZ, RZ, and CSRZ Modulation at 40 Gb/s With Narrow DWDM Channel Spacing"*, Journ. Lightw. Technol. **20** (9) 1694-1704 (2002).

[119] C.S. Goh, M.R. Mokhtar, S.A. Butler, S.Y Set, K. Kikuchi, M. Ibsen, *"Wavelength Tuning of Fiber Bragg Gratings Over 90 nm Using a Simple Ttuning Package"*, IEEE Photon. Technol. Lett. **15** (4), 557- 559 (2003).

[120] K.S. Repasky, J.D. Williams, J.L. Carlsten, E.J. Noonan, G.W. Switzer, *"Tunable external-cavity diode laser based on integrated waveguide structures"*, Opt. Eng. **42** (8), 2229-2234 (2003).

[121] D. Pudo, L.R. Chen, D. Giannone, L. Zhang, I. Bennion, *"Actively Mode-Locked, Tunable Dual-Wavelength Erbium-Doped Fiber Laser"*, IEEE Photon. Technol. Lett. **14** (2), 143-145 (2002).

[122] D. Giannone, Y.W. Lee, I.Y. Khruschev, I. Bennion, *"Tuneable compensator of dispersion and slope using non-uniformly strained chirped fibre grating"*, Proc. CLEO 2002, Vol. **1**, 527-528 (2002).

[123] J.H. Lee, P.C. Teh, P. Petropoulos, M. Ibsen, D.J.Richardson, *"Timing jitter tolerant all-optical modulator and demultiplexing systems incorporating pulse-shaping fiber Bragg gratings"*, OFC 2001, PD30-1 (Postdeadline) (2001).

[124] X. Fang, D.N. Wang, S. Li, *"Fiber Bragg grating for spectral phase optical code-division multiple-access encoding and decoding"*, Journ. Opt. Soc. Am. **B 20** (8), 1603-1610 (2003).

[125] P.C. Teh, M. Ibsen, J.H. Lee, P. Petropoulos, D.J. Richardson, *"A 4-channel WDM/OCDMA system incorporating 255-chip 320 Gchip/s quaternary phase coding and decoding gratings"*, OFC 2001 PD37-1 (Postdeadline) (2001).

[126] P.C. Teh, P. Petropoulos, M. Ibsen, D.J. Richardson, *"A 10 Gbit/s 160Gchip/s coding:decoding system based on superstructured fiber gratings"*, OFC 2000 PD9-1 (Postdeadline) (2000).

[127] P.C. Teh, P. Petropoulous, M. Ibsen, D.J Richardson, *"Phase Encoding and Decoding of Short Pulses at 10 Gb/s Using Superstructured Fiber Bragg Gratings"*, IEEE Phot. Technol. Lett. **13** (2), 154-156 (2001).

[128] M.V. Dubov, D. Giannone, I.Y. Khrushchev, I. Bennion, *"Pulse tail suppression in a laser diode output by tuneable notch filter"*, Electron. Lett. **37** (23), 14041405 (2001).

[129] K.C. Harvey, C.J. Myatt, *"External-cavity diode laser using a grazing-incidence diffraction Grating"*, Opt. Lett. **16** (12), 910-912 (1991).

[130] J. Sacher, W. Elsäßer, E.O. Göbel, "Nonlinear dynamics of Semiconductor Laser Emission Under Variable Feedback Conditions", IEEE Journ. Quant. Electron. **27** (3), 373-379 (1991).

[131] B. Zhu, I.H. White, *"Variable delay dual wavelength picosecond optical pulse generation using an actively mode-locked multichannel grating cavity laser"*, Appl. Phys. Lett. **65** (23), 2928-2930 (1994).

[132] D. Burn, G. Hay, W. Sibbett, *"Dual-wavelength external-cavity semiconductor lasers"*, Techn. Digest, CLEO, Baltimore, MD, 444, JThA2 (1993).

[133] C. Shu, Y.H.Lee, *"Tunable Dual-Wavelength Picosecond Optical Pulses Generated from a Self-Injection Seeded Gain-Switched Laser Diode"*, IEEE Journ. Qant. Electron. **32** (11), 1976-1980 (1996).

[134] D.N. Wang, C. Shu, "Tunable Dual-Wavelength Picosecond Pulse Generation Using Multiple-Optical-Path Self-Seeding Approach", IEEE Photon. Technol. Lett. **9** (9), 1211-1213 (1997).

[135] E. Rafailov, D.J.L. Birkin, W. Sibbett, E.A. Avrutin. *"Nonresonant Self-Injection Seeding of a Gain-Switched Diode Laser"*. IEEE Journ. Sel. Top. Quant. Electron. 7 (2), 287 (2001).

[136] D. Huhse, M. Schell, J. Kaessner, D. Bimberg, I.S. Tarasov, A.V. Gorbatchov, D.Z. Garbuzov. *"Generation of electrically wavelength tunable (DI = 40 nm) single-mode laser-pulses from a 1.3mm Fabry-Perot laser by self-seeding in a fibre-optic configuration"*. Electron. Lett. **30** (2), 157-158 (1994).

[137] S. Vainshtein, G. Simin, J. Kostamovaara, *"Deriving of single intensive picosecond optical pulses from a high-power gain-awitched laser diode by spectral filtering"*, Journ. Appl. Phys. 84 (8), 4109-4113 (1998).

[138] B.A.L. Gwandu, L. Zhang, K. Chisholm, Y. Liu, X. Shu, I. Bennion, *"Compact FBG array structure for high spatial resolution distributed strain sensing"*, Meas. Sci. Technol. **12**, 918-921 (2001).

[139] V. Bhatia, *"Applications of long-period gratings to single and multi-parameter sensing"*, Opt. Expr. **4** (11), 457-466 (1999).

[140] T. Allsop, L. Zhang, I. Bennion, *"Detection of organic aromatic compounds in paraffin by a long-period fiber grating optical sensor with optimized sensitivity"*, Opt. Comm. **191**, 181-190 (2001).

[141] H.J. Patrick, C.C. Chang, S.T. Vohra, *"Long-period gratings for structural bend sensing"*, Electron. Lett. **34** (18), 1773-1775 (1998).

[142] G.D. van Wiggeren, T.K. Gaylord, D.D. Davis, M.I. Braiwish, E.N. Glytsis, E. Anemogiannis, *"Tuning, attenuating and switching by controlled flexure of long-period gratings"*, Opt. Lett. **26** (2), 61-63 (2001).

[143] S.A. Vasiliev, O.I. Medvekov, *"Long-period refractive index fiber gratings: properties, applications, and fabrication techniques"*, Proc. SPIE, Vol. **4083**, 212-223 (2000).

[144] Portfolio of Smartfibres (Photonics Cluster), www.smartfibre.com

[145] D. Zhao, L.Zhang, I.Bennion, X. Shu, G.M.H. Flockhart, W.N. MacPherson, J.S. Barton, J.D.C Jones, *"Implementation of Vector Bending Sensors Using Long-Period Gratings UV-Inscribed in Flat-Clad and 4-Core Fibres"*, Proc. OFS 2003, Paper Fr 2-4, 794-797 (2003).

[146] T.D. Allsop, T. Earthrowl, R. Revees, D.J. Webb, M. Miller, B.W. Jones, I. Bennion, *"Application of long-period grating sensors to respiratory function monitoring"*, Proc. SPIE, Vol. **5588**, 148-156 (2004).

[147] W.N. MacPherson, G.M.H. Flockhart, R.R.J. Maier, J.S. Barton, J.D.C Jones, D. Zhao, L.Zhang, I.Bennion, *"Pitch and roll sensing using fibre Bragg gratings in multicore fibre"*, Meas. Sci. Technol. **14**, 1642-1646 (2004).

[148] P. Sivanesan, J.S. Sirkis, Y. Murata, S.G. Buckley, *"Optimal wavelength pair selection and accuracy analysis of dual fiber grating sensors for simultaneously measuring strain and temperature"*, Opt. Eng. **41** (10), 2456-2463 (2002).

[149] T. Allsop,V. Mezentsev, A. Gillooly, T. Earthgrowl-Gould, R. Neal, D.J. Webb, I. Bennion, *"The Spectral Characteristics of Long Period Gratings written in D-Shaped Optical Fibre as a Bending Sensors"*, Proceed. OFS 2003, TuP-8, 88-91, (2003).

[150] H.J. Patrick, *"Self-aligning, bipolar bend transducer based on long period grating written in eccentric core fibre"*, Electron. Lett. **36** (21), 17631764 (2000).

[151] E.M. Dianov, S.A. Vasiliev, A.S.Kurkov, O.I. Medvekov, V.N. Protopopov, *"In-Fiber Mach-Zehnder Interferometer based on a Pair of Long-Period Gratings"*, Proc. ECOC 1996, Paper MoB.3.6, (1996)

[152] T.-J. Ahn, B.H. Kim, B.H. Lee, Y. Chung, U.C. Paek, W..T. Han, *"Measurement of refractive-index change upon UV irradiation of optical fiber using a LPG pair"*, Techn. Dig. 5th Optoelectronics and Communications Conference, Tokyo, Paper 12P-45 (2000).

[153] T. Allsop, R. Reeves, D.J. Webb, I. Bennion, *"A high sensitivity refractometer based upon a long period grating Mach-Zehnder interferometer"*, Rev. Sci. Instrum. **73** (4), 1702-1705 (2002).

[154] Y.H. Kim, B.H. Lee, Y. Chung, U.C. Paek, W.T. Han, *"Measurement of the pump-induced phase change in Yb3+/Al3+ co-doped optical fibers using a long-period grating pair"*, Proc. OFC 2002, 564-565 (2002).

[155] B.H. Lee, J. Nishii, *"Self-interferenc of long-period fibre grating and its application as temperature sensor"*, Electron. Lett. **34** (21), 2059-2060 (1998).

[156] Y.G. Han, B.H. Lee, W.T. Han, U.C. Paek, Y.Chung, *"Fibre-optic sensing applications of a pair of long-period fibre gratings"*, Meas. Sci. Technol. **12**, 778-781 (2001).

[157] L. Tallone, L. Boschis, L.Cognolato, E. Emelli, E. Riccardi, O. Rossotto, *"Narrow-band rejection filters through fabrication of in-series long-period gratings"*, Proc. OFC 1997, Vol. **6**, 175 (1997).

[158] X.J. Gu, *"Wavelength-division multiplexing isolation fiber filter and light source using cascaded long-period fiber gratings"*, Opt. Lett. **23** (7), 509-510 (1998).

[159] D.S. Starodubov, V. Grubsky, A. Skorucak, J. Feinberg, X.J. Cai, K.M. Feng, A.E. Willner, *"Novel fiber amplitude modulators for dynamic channel power equalization in WDM systems"*, Proc. OFC 1998, Vol. **2**, PD8-1, (1998).

[160] B. Ha Lee, Junji Nishii. *"Dependence of fringe spacing on the grating separation in a long-period fiber grating pair"*, Appl. Opt. **33** (16), 3450-3459 (1999).

[161] Y.W. Lee, B. Lee, *"Polarization-Sensitive Interference Spectrum of Long-Period Fiber Grating Pair Separated by Erbium-Doped Fiber"*, IEEE Photon. Technol. Lett. **14** (9), 1312-1314 (2002).

[162] Optical Waveguide Theory, A.W. Snyder and J.D. Love, Kluwer Academic Publishers (Norwell), (2000).

[163] M. Melo, O. Frazão, A.L.J. Teixeira, L.A. Gomes, J.R. Ferreira da Rocha, H.M. Salgado, *"Tunable L-band erbium-doped fibre ring laser by means of induced cavity loss using a fibre taper"*, Appl. Phys. **B 77** (1), 139-142 (2003).

[164] Rabbany SY, Donner BL, Ligler FS,*"Optical Immunosensors"*, Crit. Rev. Biomed. Eng. **22** (5,6), 307-346 (1994).

[165] Candido Bariain, Ignacio R. Matias, Francisco J. Arregui, and Manuel Lopez-Amo, *"Experimental results toward development of humidity sensors by using a hygroscopic material on biconically tapered optical fiber"*, Proc. SPIE 3555, 95-105 (1998).

[166] N.Q. Ngo, S.Y. Li, R.T. Zheng, S.C. Tjin, P. Shum, *"Electrically tunable dispersion compensator with fixed center wavelength using fiber Bragg grating"*, Journ. Lightw. Technol. **12** (6), 1568-1575 (2003).

[167] Y. Liu, J.A.R. Williams, L. Zhang, I. Bennion. *"Abnormal spectral evolution of fiber Bragg gratings in hydrogenated fibers"*. Opt. Lett. **27** (8), 586-588 (2002).

[168] X. Shu, Y. Liu, D. Zhao, B. Gwandu, F. Floreani, L. Zhang, I. Bennion. *"Dependence of temperature and strain coefficients on fiber grating type and its application to simultaneous temperature and strain measurement"*. Opt. Lett. **27** (9), 701-703 (2002).

[169] X. Shu, D. Zhao, Y. Liu, B. Gwandu, F. Floreani, L. Zhang, I. Bennion, *"Effectively Simultaneous Temperature and Strain Measurement Utilising a Dual-grating Sensor Formad by Type IA and Type IIA FBGs"*, Techn. Dig. IEEE Sensors 2002 Coference, 1740-1745 (2002).

[170] George Simpson, *"Title"*, Ph.D. Thesis, Photonics Research Group, Aston University, Birmingham, United Kingdom (2004).

[171] A.G. Simpson, K. Kalli, K. Zhou, L. Zhang, I. Bennion. *"Formation of type IA fibre Bragg gratings in germanosilicate optical fibre"*. Electron. Lett. **40** (3), 163-164 (2004).

[172] E.K. Illy, H.J. Booth, G. Rutterford, M.R.H. Knowles, *"Laser processing of photonics components with copper vapor lasers"*, Proceedings of SPIE Vol. **4941**, 26-34 (2003).

[173] Unpublished data. Private correspondence with A.G. Simpson

[174] Private Correspondence

[175] A.G. Simpson, K. Kalli, K. Zhou, L. Zhang, I. Bennion. *"Blank beam fabrication of regenerated type IA gratings"*. Meas. Sci. Technol. **15**, 1-5 (2004).

[176] J. Canning, M. Aslund, and P. Hu., *"Ultraviolet-induced absorption losses in hydrogen-loaded optical fibres and in presensitized optical fibres"*, Opt. Lett. **25** (22), 1621-1623 (2000).

[177] M. Douay, E. Fertein, W.X. Xie, P. Bernage, P. Niay, J.F. Bayon, T. Georges, *" Thermal Hysteresis of Bragg Wavelengths of Intra-core Fiber Gratings"*, Photon. Technol. Lett. **5** (11), 1331-1334 (1993).

[178] R.M. Atkins, V. Mizrahi, *"Observations of Changes in UV Absorption Bands of Singlemode Germanosilicate Core Optical Fibres on Writing and thermally erasing refractive Index Gratings"*, Electron. Lett. **28** (18), 1743-1743 (1992).

[179] T. Erdogan, P.J. Lemaire, D. Monroe, *"Decay of ultraviolet-induced fiber Bragg gratings"*, Journ. Appl. Phys.**76** (1), 73-80 (1994).

[180] S. Kannan, J.Z.Y. Guo, P.J. Lemaire, *"Thermal Stability Analysis ov UV-Induced Fiber Bragg Gratings"*, IEEE Journ. Lightw. Technol. **15** (8), 1478-1483 (1997).

[181] I. Riant, B. Poumellec, *"Thermal decay of gratings written in hydrogen-loaded germanosilicate fibres"*, Electron. Lett. **34** (16), 1603-1604 (1998).

[182] J. Rathje, M. Kristensen, J.E. Pedersen, *"Continuous method for characterizing the thermal stability of ultraviolet Bragg gratings"*, Journ. Appl. Phys. **88** (2), 1050-1055 (2000).

[183] D.L. Williams, R.P. Smith, *"Accelerated lifetime tests on UV written intra-core gratings in boron germania codoped silica fibre"*, Electron. Lett **31** (24), 2120-2121 (1995).

[184] K.E. Chisholm, K. Sugden, I. Bennion, *"Effects of thermal annealing on Bragg fibre gratings in boron/germania co-doped fibre"*, Journ. Phys. **D 31**, 61-64 (1998).

[185] M. Åslund, J. Canning, "*Anneal properties of gratings written into UV-presensitized hydrogen-outdiffused optical fiber*", Opt. Lett. 25 (10), 692-694 (2000).

[186] B. Malo, K.A. Vineberg, F. Bilodeau, J. Albert, D.C. Johnson, K.O. Hill, *"Ultraviolet photosensitivity in Ge-doped silica fibers: wavelength dependence of the light-induced index change"*, Opt. Lett. **15** (17), 953-955 (1990).